Methods Development for Forward and Adjoint Thermal Neutron Scattering in the Presence of Background Media in Motion

By

Eli C. Moll

A dissertation submitted in partial fulfillment of

the requirements for the degree of

Doctor of Philosophy

(Nuclear Engineering and Engineering Physics)

at the

UNIVERSITY OF WISCONSIN-MADISON

2019

Date of final oral examination: 5/03/2019

The dissertation is approved by the following members of the Final Oral Committee:

Douglass L. Henderson, Professor, Engineering Physics
Carl Sovinec, Professor, Engineering Physics
Paul Wilson, Professor, Engineering Physics
Gregory Moses, Professor, Engineering Physics
Bryan Bednarz, Assistant Professor, Engineering Physics

Acknowledgments

This work was performed in part under appointment to the Nuclear Regulatory Commission Fellowship program at the University of Wisconsin - Madison Department of Engineering Physics. Specifically this work was supported by Department of Energy grants: DE-FG99ER54513 and DE-F02-04ER54751, the DOD Navy grant N00173-08-1-G902, and the Domestic Nuclear Detection Office: Academic Research Initiative grant 2015-DNARI00013-04-00.

Table of Contents

List of Tables

List of Figures

Abstract

A new method for forward and adjoint neutron transport in the presence of a free gas monatomic background media at thermal equilibrium has been developed and implemented. For the forward development improvements hinge upon the removal of assumptions on the form of the angular scattering probability in the center of mass (CM) frame and the form of the zero temperature elastic scattering cross section. Further, the derivation has been converted to ($\hat{I}\pm$, $\hat{I}^2$) space to allow for easier integration and derivation of the adjoint. Forward results show good agreement with theoretical models for the continuous energy transport of neutrons in a free gas at a specified equilibrium temperature. The adjoint derivation applies the Principle of Detailed balance to arrive at an independent cross section for adjoint transport which is also calculated from first principles, rather than the existing forward free gas cross section. At the time of writing, no professional radiation transport codes have continuous energy thermal adjoint neutron scattering. This work develops and implements such scattering as well as including the impact of a Maxwellian distribution of background velocities. The adjoint free gas scattering cross section displays an interesting behavior, wherein neutrons do not tend toward equilibrium as they do in the forward case, but experience some fraction of downscattering due to the presence of the equilibrium background distribution. Thus, more scattering events are required for adjoint particles to upscatter through the thermal energy region. The adjoint energy transfer function shows good agreement with theory. A forward and adjoint self-adjoint problem has been constructed to study the analogue transport in both cases, and the results show good agreement. All of this work has been implemented in the FRENSIE (Framework for Research in Nuclear ScIence and Engineering) software code, a radiation transport code developed at the University of Wisconsin Madison which handles forward and adjoint continuous energy transport for neutrons, photons, and electrons.

Chapter 1

Introduction

The Monte Carlo method may be described as a statistical approach to solving differential and integro-differential equations [1]. While it is often associated with the random walk processes in radiation physics, the Monte Carlo method is capable of application in a much broader sense, ranging from the physical sciences to economics. In general, the Monte Carlo method works by randomly sampling event states from known, or assumed, probability density functions (PDF). For a single step process this seems highly unnecessary, but when multiple events occur in series it can be difficult or even impossible to accurately represent the intricate relationship between the steps when assessing the outcome of the situation. Take the example of economics, wherein the Monte Carlo method is used in the prediction of the valuation of securities. With the Monte Carlo method one is able to define probabilities for asset prices, interest rates, etc. and therefrom sample these state variables and calculate an expected cash flow for the investment. This can be done numerous times in order to calculate nearly all possible interactions between the state variables, and the end result will yield a distribution of cash flows from which one can infer the most likely return on investment, general risk, volatility, amongst other important features [2].

In the field of radiation sciences the Monte Carlo method is utilized to simulate radiation transport, from particle generation to termination. In much the same way as in economics, the application of Monte Carlo in radiation transport allows one to understand the likelihood of various outcomes from an intricate and highly interdependent problem. Monte Carlo methods application to radiation transport was first proposed in the 1940s by various researchers such Von Neumann, Metropolis, and Fermi [3]. At the time, full scale Monte Carlo simulations were far too costly, as the computational time required to simulate the requisite number of individual particles for statistically sound findings was impractical. Further, handling continuous energy cross sections and intricate geometrical models was ungainly due to both computational and memory capabilities. The situation as of the writing of this work is starkly different, as the access to vast computational resources with ample memory has become a staple of the scientific community. Thus Monte Carlo problems can now be solved with high fidelity in all variables of interest [4]. Such capabilities have

made the Monte Carlo method the gold standard in radiation transport problems, as one can sample physics in a continuous energy space as well as resolve geometrical entities to nearly machine precision. With the constant growth of computational resources, as well as the development of new methods such as GPU computing, Monte Carlo is likely to continue its meteoric rise to prominence as the most relied upon method of radiation transport.

1.1 Description of the Monte Carlo Method

It is often easiest to understand the Monte Carlo solution method in contrast with deterministic methods. Many individuals in the physical sciences have studied finite difference and finite element techniques at some point in their career, and thus the contrast to a known method may assist one in grasping the salient features of the stochastic nature of the Monte Carlo method. There exist various deterministic methods for solving differential and integro-differential equations, but a key feature of such methods is the requirement to discretize the phase space in state variables (space, energy, time, angle, etc.). Take for example the simple case of solving a first order differential equation using finite difference techniques:

$$f'(x) + f(x) = 0. \tag{1.1}$$

A natural finite difference definition of the first derivative might be a central difference, which states that the derivative at any point should behave as the slope between the nearest neighbors. For a relatively smooth function and a refined discretization step the following equation is a reasonable approximation of the derivative:

$$f'(x) \approx \frac{f(x + \delta x) - f(x - \delta x)}{2\delta x}. \tag{1.2}$$

Substituting Equation 1.2 into Equation 1.1 one would find a series of algebraic expressions which describes the relationship between the function $f(x)$ at various points in the solution space. This can be solved via matrix methods and the resulting solution is a vector $\bar{F}(x)$ which satisfies the previous equations at the discretization points. The upside of such discretization is that problems can be solved with relatively low computational effort and memory requirements [5]. However, the downsides include error imbued from the discretization, lack of granularity in the resulting quantities, as well as the inability to resolve heterogeneities that are smaller

than the discretization, an issue of pivotal importance when dealing with very fine physical structures [6].

In contrast to deterministic methods, the Monte Carlo method is referred to as a stochastic method. Variables are randomly sampled based on known probability laws, and one acquires statistical data from the aggregation of all samples. This data can then be utilized to predict the quantities of interest to within a statistical uncertainty associated with the pool of samples [7].

In radiation transport the sampled value at the highest level is the random walk which a particle undergoes while within the system. The set of all possible random walks is described by the probability laws which govern the behavior of particles within the system. More specifically, a random walk is determined by sampling the particle state and interactions based on known information such as the geometry, source profile, and material properties (cross section and density). A particle is *born*, so to speak, by randomly sampling the position, energy, and direction from the user supplied source profile. From this point on the reader should assume that the term *sampling* in relation to probability distributions implies an unbiased, random sampling technique. The transport of the particle along the selected ray is then sampled in mean free paths using both the macroscopic cross section and geometry information. Upon arriving at a collision site, a reaction is sampled from the cross section data, outgoing particle states are sampled from the selected reaction, and the particle repeats the transport process. This continues until the particle exits the geometry permanently or is lost through an absorption reaction.

Due to the nature of the transport a common misconception is that each particle transported represents a particle that would have been transported in a physical experiment. The reality is that each particle random walk represents a statistical probability that said random walk would occur. By aggregating a large population of possible walks one can then begin to infer the behavior of the population as a whole. Based on the nature of the process, the overall accuracy of a Monte Carlo simulation is directly tied to the number of particles run. Further, the resulting quantities of interest describe the probability that any given source particle will contribute to the selected response. This assumes that the geometry and material data are known with absolute certainty, an assumption which is false in practice due to mechanical tolerancing, density fluctuations, temperature variatins, cross section uncertainty, and various other sources of imperfection. A detailed derivation of the random walk process and the determination of quantities of interest are discussed later in this work.

1.2 Motivations for Adjoint Methods Development

The previous section described forward Monte Carlo radiation transport. That is to say, radiation transport wherein particles are birthed at a source location and are transported to their eventual termination sites, possibly contributing to various finite detector regions along the way. This is the most efficient method of solution for processes in which the source is localized relative to the detection region. For example, imagine a localized system which emits radiation which is situated within a facility (i.e. a nuclear reactor). Often one wishes to determine the leakage of radiation outside of the containment and biological shielding to ensure that the levels are within radiation safety standards. In this example the source region is localized while the detector region is the entire space outside of containment. Thus it is most efficient to generate particles in the source and transport them to all locations outside of containment, as most particles which leave the source will interact with the detector phase space.

With this in mind it is not difficult to construct a counterexample wherein the detector region is localized with respect to the source distribution. Imagine now that a patient is undergoing proton beam therapy. There are many possible ways in which one can orient the beam and the patient in three-dimensional space in order to deliver the maximum dose to the tumor while sparing the sensitive tissues. In the forward case one would need to run a parametric study over various possible configurations to determine which orientation produces the best results. However, if one could generate particles at their absorption points within the tumor and then transport them back through their interactions to the source one would quickly find the optimal source orientation in a single simulation. While this is an overgeneralization, the process of sampling a particle starting point within a detector and transporting it to a source is known as the adjoint transport process and is of great interest to this work [8]. Figure 1.1 depicts the difference between the forward and adjoint schemes when the detector region is small compared to the source region.

While the physics and sampling techniques behind the adjoint process will be discussed in a later section, it is of use to understand what the response from an adjoint simulation represents. For a forward simulation, the response in a detector represents the probability that a given source particle will contribute to the detector. This is often in terms of a physical quantity per source particle (i.e. flux, current, reaction rate, etc.). In an adjoint simulation the response describes the importance or sensitivity of a given source location to the detector. Dr. Henderson's research group

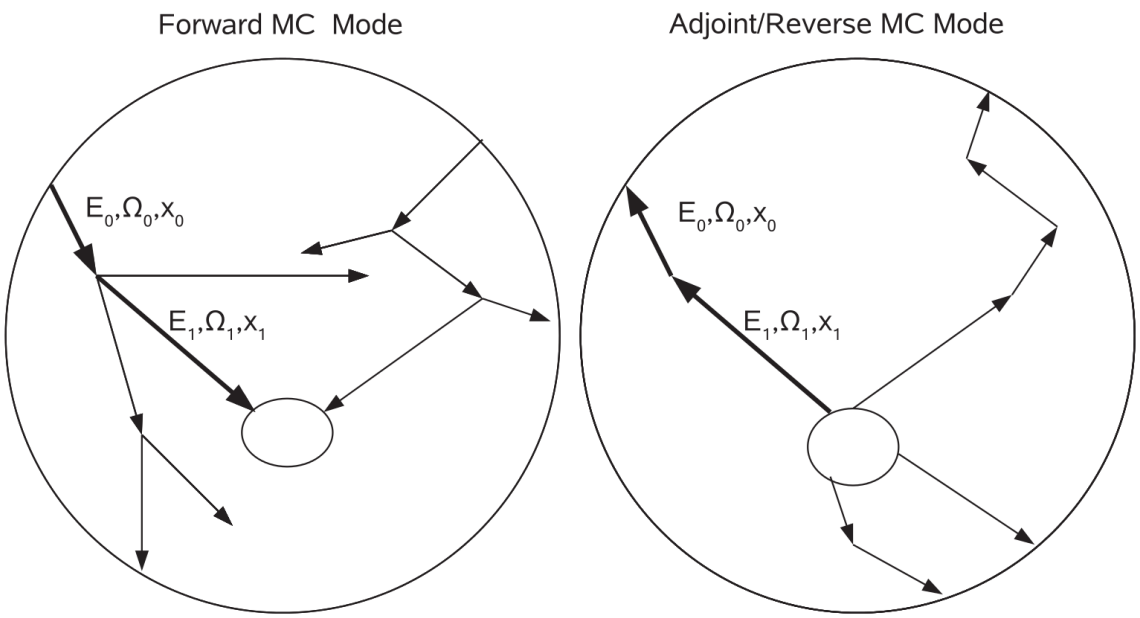

Figure 1.1: **Comparison of Monte Carlo forward and adjoint transport.** *In forward transport particles are generated at the source location (outer circle) and transported through the detector region (inner circle). In adjoint transport particles are generated at the detector location (inner circle) and are transported through the source region (outer circle). In this way, only tracks which contributed to the detector are transported and thus the method is computationally efficient [9].*

has historically developed treatment planning optimization routines for prostate brachytherapy. By applying the adjoint transport to the prostate and sensitive structures, one finds a sensitivity map which describes how sensitive these structures are to a source placed in any given location. This allows for one to select optimal locations which have maximum dose delivery to the prostate while sparing the urethra, rectum, and surrounding tissues [10–12]. Figure 1.2 depicts the sensitivity field at a specific slice of the prostate. This would be convolved with sensitivity fields for the sensitive structures to select ideal brachytherapy seed locations which maximize the dose to the prostate and minimize the dose to the sensitive structures.

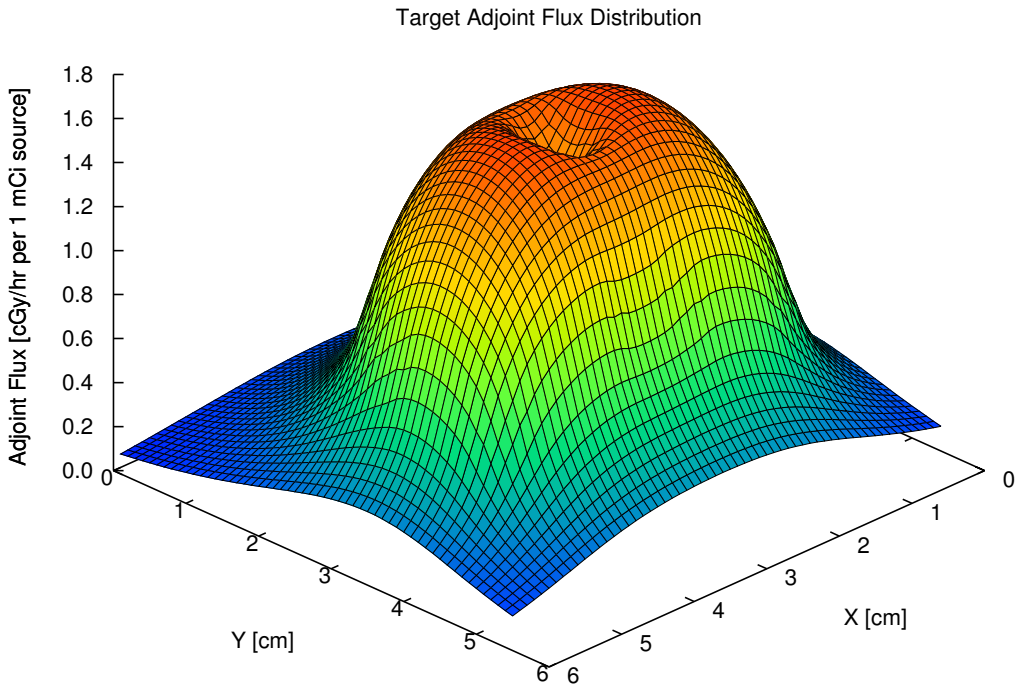

Figure 1.2: **Prostate Adjoint Flux at Midplane.** *The adjoint flux depicts the sensitivity of the prostate to a brachytherapy seed location. That is to say, regions of high adjoint flux would receive large doses if a brachytherapy seed were to be placed there. Convolving this with adjoint fluxes of the sensitive tissues allows for one to select the optimal seed locations for achieving the prescribed prostate dose while minimizing dose to sensitive tissues [13].*

1.3 Thermal Neutron Transport

While the previous sections have discussed the importance of Monte Carlo radiation transport in general for both forward and adjoint physics it should be noted that this work focuses on the treatment of neutron transport. At a basic level neutron transport aims to simulate the interactions of neutrons with the nuclei of the target media. Unlike electrons and photons, neutrons do not interact with the atomic structure of the target atoms but rather with the nucleus [6]. Due to the interaction with the nucleus, the transport behavior of neutrons is somewhat different than that of photons and electrons. Photons and electrons are stopped primarily by the electron interactions, and thus materials with high electron density tend to be effective at stopping photons and electrons [14]. Conversely, neutrons interactions

are dependent upon the neutron-nucleus interaction and the likelihood of interaction is characterized by a quantity referred to as the cross section. This leads to interesting physics where low A materials, such as hydrogen, tend to be far more opaque to neutrons than materials such as lead or steel [6]. Chapter 5 dives in to the mathematics of neutron transport theory, but it is important to understand that the interaction parameter for neutron reactions is highly energy dependent. Figure 1.3 depicts the cross section for nuclear fission for Uranium-235 [15]. Notice how the cross section is orders of magnitude higher in the low energy region (below 1 eV) than it is in the higher energy regions.

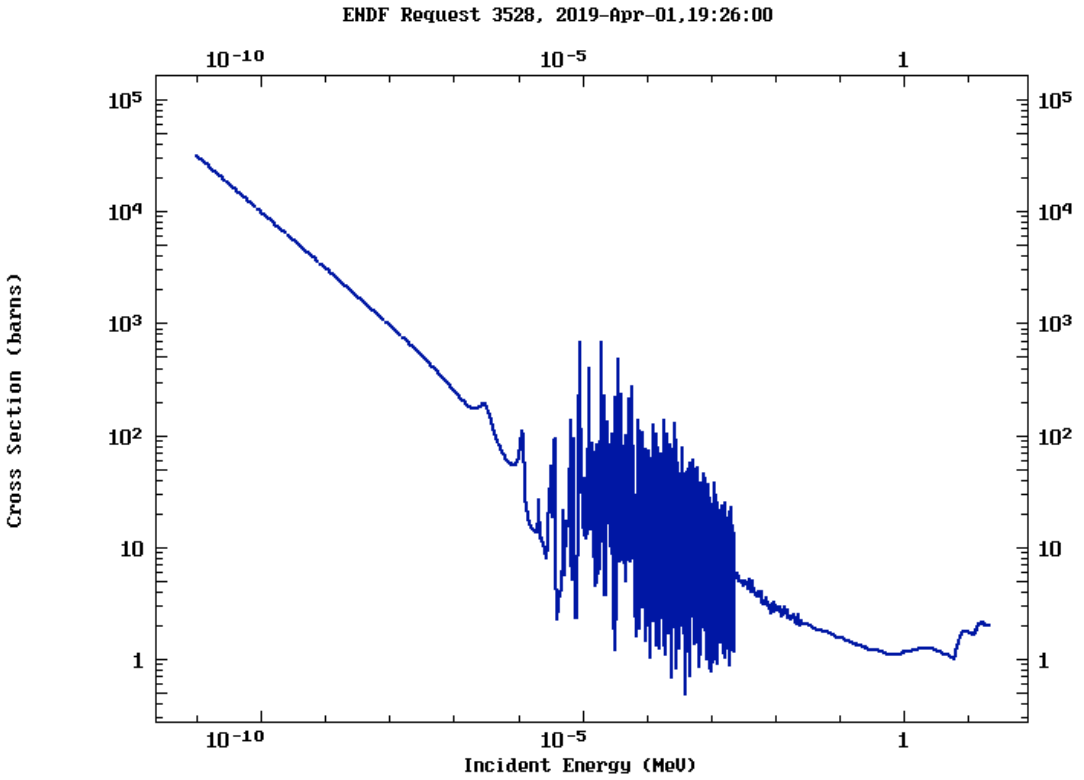

Figure 1.3: **Uranium-235 Fission Cross Section.** *The Uranium-235 cross section for fission is plotted between* 1×10^{-10} *and* 20 *MeV. Notice that the cross section increases as the energy decreases, especially in the thermal region (i.e. below approximately 1 eV). Such behavior is common for neutron interactions, and thus many reactions may be observed more readily through the use of thermal neutrons [15].*

There are many applications for neutronics which span the entire energy range of known cross sections, but this work will further focus on low energy neutron applications and the physics that drive them. One such example of the utilization of thermal neutrons is in the detection of improvised explosive devices (IED) in

combat zones. Thermal neutrons have a high absorption cross section for isotopes such as ^{1}H and ^{14}N which are often found abundantly in IEDs [15]. Further, the capture mechanism for these isotopes is the $X(n,\gamma)Y$ absorption reaction which emits a photon of a characteristic energy which may be detected and flagged for the presence of an explosive. While this is a simple example, Figure 1.3 depicts the general trend for neutron reactions, which is that the cross section increases for low energy neutrons. Due to this behavior, the energy of the neutrons in the thermal region is then incredibly important to the ability to detect explosives, as a change in energy directly translates to a change in the reaction rate of interest and thus the likelihood of detection.

While this is a simple example, the importance of thermal neutrons for many applications including nuclear reactors is one reason that thermal neutron physics have been so heavily studied and several methods have been developed to accurately model the forward thermal neutron scattering reaction. These consist of free gas scattering methods which consider the temperature of the background scattering media as well as models for the coherent and incoherent scattering from molecules and crystalline structures [16, 17]. This work seeks to extend existing forward free gas scattering methods by removing implicit assumptions allowing for improved accuracy.

1.4 Neutron Modeling in Modern Monte Carlo Codes

Many current Monte Carlo codes deal primarily with the forward transport process, and as such most forward neutron physics can be modeled with few approximations. However, the adjoint transport process has not received nearly the same development time. This has led to very few codes containing adjoint physics, and those that do are often hampered by series of approximations. Table 1.4 shows neutron, photon, and electron forward and adjoint capabilities in modern Monte Carlo codes. This work is primarily concerned with the neutronics and the development of neutron transport methods. Other researchers in Dr. Henderson's group are working on the transport of photons and electrons for forward and adjoint continuous energy Monte Carlo simulations.

MCBEND, a commercial radiation transport code in the United Kingdom, is one of the only Monte Carlo codes available today which contains adjoint neutron physics. While this is an impressive achievement in pushing adjoint physics and adjoint Monte Carlo transport forward, one of the major downfalls of the implementation

Table 1.1: **Continuous Energy Capabilities of Monte Carlo Codes Available Today.** *The final column shows the proposed capabilities of the Forward-Adjoint Continuous Energy Monte Carlo (FACEMC) code. Note that GEANT4 electron adjoint capabilities are currently incomplete, and MCBEND does not have continuous energy adjoint neutron transport for the entire energy range [modified from [18]].*

Code	n	γ	e	$n^\dagger$	$\gamma^\dagger$	$e^\dagger$
EGS4	-	$\surd$	$\surd$	-	-	-
EGSnrc	-	$\surd$	$\surd$	-	-	-
ITS6	-	$\surd$	$\surd$	-	-	-
PENELOPE	-	$\surd$	$\surd$	-	-	-
MCNP5/6	$\surd$	$\surd$	$\surd$	-	-	-
MCNPX	$\surd$	$\surd$	$\surd$	-	-	-
GEANT4	$\surd$	$\surd$	$\surd$	-	$\surd$	-
MCBEND	$\surd$	$\surd$	$\surd$	$(\surd)^*$	-	-
FACEMC	$\surd$	$\surd$	$\surd$	$\surd$	$\surd$	$\surd$

is the lack of treatment of low energy adjoint neutronics. In MCBEND the thermal energy region is treated as a single group much as it would be treated in forward multigroup physics [19]. For problems which are not reliant upon the thermal energy region, this proves unimportant and induces little error. However, there are numerous cases where thermal neutrons are the primary energy region of importance, and an inability to resolve within that energy space renders these problems incalculable in MCBEND.

Beyond MCBEND's lack of continuous energy adjoint thermal neutronics, there has been no development of continuous energy adjoint thermal neutron scattering cross sections in the presence of a background media in motion. Adjoint neutron scattering on static scattering centers has been derived by Hoogenboom, but the temperature dependent counterpart has not [20]. The primary drive of this work is to utilize the same novel method for the development of a forward free gas thermal neutron scattering cross section to develop an adjoint equivalent. In doing so the ability to model temperature dependent adjoint thermal neutronics has been gained which was not previously derived or implemented in existing Monte Carlo transport codes.

1.5 The Development of a New Research Framework and Monte Carlo Code

A Framework for Research in Nuclear ScIence and Engineering (FRENSIE) has been developed to address two key issues in the radiation transport community. The first issue is that radiation transport is largely unable to model adjoint physics today. The second issue is that many of the existing codes today are proprietary or export controlled and contain significant amounts of legacy code. To the first issue, adjoint radiation transport requires entirely new cross sections and physics to be implemented. It would be possible to work in existing codes such as GEANT4, however it was determined that the development cost to develop for GEANT4 would likely be too great. It was also unclear if the necessary components for adoption of new data sets was present. For that reason the Forward-Adjoint Continuous Energy Monte Carlo (FACEMC) code has been developed and is a key component of FRENSIE. All forward and adjoint physics are implemented in FACEMC. Going forward, FRENSIE and FACEMC will both be used at times to describe the Monte Carlo radiation transport code developed by Dr. Henderson's research group.

In addressing the second issue, the goal of the FRENSIE research group has been open source development with collaboration ever since the project began. The nuclear industry has been plagued by proprietary and export controlled radiation transport codes for some time. Further, many of the codes in use today are comprised of large quantities of legacy code, being written in older languages like Fortran. FRENSIE has been developed from the ground up to use updated programming practices in C++11 and to allow collaborative development with little overhead by adopting a high-level black-box approach to software design. The design strategies and thought processes for the FRENSIE software development team are discussed in more depth in Appendix J.

1.6 Report Outline

This report will discuss the physics necessary to model forward and adjoint neutron transport in FRENSIE, as well as the derivation of a new thermal neutron treatment. The focus will be primarily on thermal neutronics, but much of the derivation of the generalized adjoint elastic and inelastic neutron scattering will be applicable to the entire energy space. Chapter 2 will focus primarily on the application of the

Monte Carlo method to Fredholm Equations of the Second Kind (FIESK) as this will be necessary to understand the underlying sampling routines which make up the Monte Carlo method and how a random walk process can approximate the solution to a mathematical equation. Chapter 3 will focus on the development of the forward and adjoint transport equation and various methods for solution, as well as define important quantities such as the Monte Carlo estimator. Following the general derivation of the forward and adjoint transport equations, Chapter 5 will focus on the theory and sampling techniques required for simulating forward neutron reactions, as well as the adjoint elastic and inelastic scattering reactions in the presence of fixed background media. Chapter 6 depicts the forward neutron transport work which has been implemented in FRENSIE and testing against the ACE implementation of the $S(\alpha, \beta)$ ENDF data for low energy coherent and incoherent neutron scattering. For readers with a comprehensive understanding of transport theory, it is suggested to begin with Chapter 6 and progress therefrom.

Chapter 7 will discuss a novel method developed for free gas thermal neutron scattering. This method allows for a forward free gas thermal neutron scattering cross section which is not hampered by historical assumptions. Further, the method allows for an independent calculation of the adjoint cross section, and the development of an adjoint scattering cross section in the presence of background media in motion. Not only does this fill the need for a continuous energy adjoint scattering cross section in the thermal region, but it adds the accuracy and additional physics present from allowing the background media to be a free gas in thermal equilibrium. Chapter 8 depicts the numerical calculation of the forward and adjoint cross sections from the newly derived method. This includes the transport probabilities, cross sections, and infinite media transport models.

Appendix J provides the reader with a general overview of FRENSIE to further inform the decision to produce a new radiation transport code and research framework. Finally, Chapter 9 provides a brief summary of each chapter as a reference and reminder for what has been discussed in this work. Chapter 9 also summarizes the salient features of the new methods developed herein and the importance to the field of computational neutron transport.

Chapter 2

Monte Carlo Application to Solving Fredholm Integral Equations

It is not immediately apparent why the application of Monte Carlo methods to Fredholm Integral Equations of the Second Kind (FIESKs) will be of importance. However, it will be shown in Chapters 3 and 4 that both the transport equation and the adjoint transport equation can be transformed in to FIESKs. Thus, understanding how the Monte Carlo method applies mathematically to FIESKs will help to inform the method by which the random walk processes are able to solve the radiation transport equation, as well as extract quantities of interest through estimators.

2.1 Fredholm Integral Equations of the Second Kind - FIESK

The FIESK is an equation of the following form:

$$f(t) = \lambda \int_a^b K(t,s) f(s) ds + g(t). \tag{2.1}$$

Here the integral kernel $K(t,s)$ and the external forcing function $g(t)$ are known, and the function $f(t)$ is the unknown and desired quantity. It may be easiest to envision the integral kernel $K(t,s)$ as a function which describes the transition of some function from state s to state t. State transition is a very common occurrence in radiation transport equations, and as such the notation will be amended to more clearly indicate the transition. As such the notation $K(s \to t)$ will be equivalent to the notation $K(t,s)$ herein, and the former will be used for clarity. It should be noted that the bounds of integration for the FIESK are fixed values a and b.

A slight modification to the FIESK can be found when the upper limit of integration is a variable as opposed to a fixed value as shown here:

$$f(t) = \lambda \int_a^t K(s \to t) f(s) ds + g(t). \tag{2.2}$$

This type of equation is referred to as the Volterra Integral equation. The Volterra Integral equation is of interest in radiation transport in situations where there exists a functional limit on the independent variable. One such example would be a particle scattering off of a nearly infinite-mass target at rest. It can be shown with conservation of momentum and energy that the maximum energy of the particle must be bounded by its incoming energy [18]. One may redefine the Volterra Integral equation as a FIESK by defining a kernel which contains the Volterra kernel within the region of interest, and a zero value kernel outside of it [21]. For example:

$$K'(s \to t) = \begin{cases} K(s \to t) & \text{if } s < t \\ 0 & \text{if } s > t. \end{cases} \tag{2.3}$$

Thus, a generalized notion of solving FIESKs using Monte Carlo methods will be sufficient to solve both FIESKs and Volterra Integral equations. The remainder of this work will focus on FIESK solutions.

While there are numerous methods to solve FIESKs, the most relevant method to the Monte Carlo discussion is that of the method of successive approximations. The method of successive approximations is an iterative method which aims to calculate the solution to the integral equation by recursively generating approximate solutions. For a FIESK, the zeroth order approximation is simply set equal to the forcing function $g(t)$. Then, assuming the zeroth order approximation is sufficiently accurate, a first order approximation is generated by substituting the zeroth order approximation into the right hand side of the equation. This continues as follows:

$$\begin{aligned}
f_0(t) &= g(t) \\
f_1(t) &= \lambda \int_a^b K(s \to t) f_0(s) ds + g(t) = \lambda \int_a^b K(s \to t) g(s) ds + g(t) \\
f_2(t) &= \lambda \int_a^b K(s \to t) f_1(s) ds + g(t) = \lambda \int_a^b K(s \to t) \left(\lambda \int_a^b K(\nu \to s) g(\nu) d\nu + g(s) \right) ds \\
&\vdots \\
f_n(t) &= \lambda \int_a^b K(s \to t) f_{n-1}(s) ds + g(t).
\end{aligned} \tag{2.4}$$

Assuming the required conditions are met, as the order of the approximation grows to infinity, the final term will converge to the exact solution of the FIESK as

$$f(t) = \lim_{n \to \infty} f_n(t). \tag{2.5}$$

As could be seen in Equation 2.4 for the terms f_1 and f_2, an expansion was provided which substituted in the previous terms. This produces a nested system of integrals. One may represent this succinctly via a Neumann series by defining the first order and following order terms in a new function $h_n(t)$:

$$h_n(t) = \begin{cases} \int_a^b K(s \to t) f(s) ds & n = 1 \\ \int_a^b K(s \to t) h_{n-1}(s) ds & n > 1. \end{cases} \tag{2.6}$$

This allows one to rewrite the successive approximations infinite order term from Equation 2.5 in a simplified manner in terms of $h_i(x)$:

$$f(t) = g(t) + \sum_{i=1}^{\infty} \lambda^i h_i(t). \tag{2.7}$$

It can be seen that this process lends itself to continually using the integral operator $\int_a^b K(s \to t) ds$ on the function of interest. In order for convergence to be guaranteed, one must ensure that application of the integral operator does not cause the function to grow, as an infinite number of applications would then lead to divergence. Technically, the spectrum of the integral operator must be contained within the open unit disk [8]. Doing so ensures that the series will converge to the exact solution to the FIESK given an infinite number of operations.

2.2 Application of the Monte Carlo Method to Solve FIESK

Of interest to this work is the manner by which the Monte Carlo method can be used to solve FIESKs. From the discussion in the previous section, it is clear that there are ways by which iterative processes are capable of solving FIESKs given infinite iteration. Even without infinite iteration, one is capable of calculating the error contained in the approximation from truncating the summation at any given step. This section will focus on showing that the Monte Carlo random walk process describing the process of transitioning an entity from state to state recovers the solution to the FIESK. Note that the discussion herein will be somewhat brief and is based on the work done by Spanier and Gelbard which goes in to much greater depth in Chapter 2.4 of their text, *Monte Carlo Principles and Neutron Transport Problems* [8].

Application of the random walk process to solving a FIESK is defined by the

following probability density functions (PDFs) [8]:

$$\begin{aligned} p^1(t) &= P(t_1 = t), \\ p(t,s) &= p(s \to t) = P(t_{n+1} = t | t_n = s \text{ and } k > n), \\ p(t) &= P(k = n | t_n = t), \end{aligned} \tag{2.8}$$

subject to the requirements that

$$\begin{aligned} p^1(t) &\geqslant 0, \\ p(s \to t) &\geqslant 0, \\ \int_\Gamma p^1(t) dt &= 1, \\ \int_\Gamma p(s \to t) dt &= 1 - p(s) \leqslant 1 \quad \forall\, t \in \Gamma. \end{aligned} \tag{2.9}$$

Here x represents the state of a particle in some continuous phase space Γ. The PDFs listed in Equation 2.8 detail the behavior of generation, transition, and termination probabilities. The PDF $p^1(t)$ describes the likelihood that the initial event in any random walk occurs in state t. This could be analogously thought of as the PDF describing birth state of a particle. Based on the third requirement shown in Equation 2.9 it is clear that $p^1(t)$ is a normalized PDF, and thus a random walk must begin somewhere in the phase space Γ.

The PDF $p(s \to t)$ describes the probability of transitioning from an initial state s in Γ to an final state t in Γ. That is to say, it is the probability that the next state t_{n+1} is state t given that the previous state t_n was state s. The final PDF $p(t)$ describes the probability that state t will be the termination state for the random walk. The termination is stated to happen on event k, such that if $k = n$, then t_n describes termination state of the random walk. This informs the final requirement in Equation 2.9, as it states that the probability of transitioning from s to any other state t is unity minus the probability that s itself is a termination state.

Now, the probability of undergoing an n^{th} event in some state t can be written as follows:

$$P^n(t) = P(t_n = t | k > n-1, n \geqslant 2), \tag{2.10}$$

given that the first order term $P^1(t)$ is equal to $p^1(t)$ which is merely sampling the initial state of the random walk. This can be simplified even further using a recursive algorithm, wherein the n^{th} event is dependent on the likelihood of state transition

from the $(n-1)^{st}$ event as follows:

$$P^n(t) = \int_\Gamma p(s \to t) P^{n-1}(s) ds. \tag{2.11}$$

Further, one may define a discrete random variable $T(t)$ which describes the density of events that occur in state t. An example of the event density $T(t)$ could be a localized reaction rate, or the number of particles that occur with reaction χ at location $\bar{r}$ and energy E. This expected value of $T(t)$ is merely the cumulative probability of any event at stage n occurring in state t,

$$< T(t) >= P^1(t) + P^2(t) + P^3(t) + \ldots = \sum_{n=1}^{\infty} P^n(t). \tag{2.12}$$

Now that one has defined the expectation value of the event density at state t, one may proceed to define a continuous quantity which captures the likelihood of collisions occurring at any state $t \in \Gamma$. This new term, $P(t)$ will be referred to as the continuous event density and will describe the probability that any event occurs in state t. Again following Spanier and Gelbard, it can be shown that the Monte Carlo random walk process discussed herein is capable of recovering the solution to FIESKs, assuming that $g(t)$ and $k(s \to t)$ satisfy the same properties as the birth and transfer probabilities $p^1(t)$ and $p(s \to t)$,

$$\begin{aligned} P(t) &= \sum_{n=1}^{\infty} P^n(t) \\ &= p^1(t) + \sum_{n=2}^{\infty} \left(\int_\Gamma p(s \to t) P^{n-1}(s) ds \right) \\ &= p^1(t) + \int_\Gamma p(s \to t) \sum_{n=2}^{\infty} P^{n-1}(s) ds. \end{aligned} \tag{2.13}$$

Now one may observe that the index $n-1$ may be shifted, such that the term within

the summation may be rewritten in a form that has been seen previously:

$$\begin{aligned} P(t) &= p^1(t) + \int_\Gamma p(s \to t) \sum_{n=2}^{\infty} P^{n-1}(s) ds \\ &= p^1(t) + \int_\Gamma p(s \to t) \sum_{n=1}^{\infty} P^{n}(s) ds \\ &= p^1(t) + \int_\Gamma p(s \to t) P(s) ds. \end{aligned} \tag{2.14}$$

Equation 2.14 clearly states that the Monte Carlo random walk method recovers the solution to the FIESK. As the theoretical underpinning has been developed, it is now of use to discuss how the Monte Carlo random walk method is practically applied. One begins by sampling the initial state of the walk, t_1, using the PDF $p^1(t)$ which was defined for the purpose of generation sampling. Assuming the initial state is not also a termination state, the random walk will need to sample the transfer probability. At this point one must sample the transfer probability with respect to the incoming state. That is to say, the probability that state t_2 will be selected given existing state t_1 can be sampled from:

$$p(t|t_1) = \frac{p(t_1 \to t)}{\int_t p(t_1 \to t) dt}. \tag{2.15}$$

This states that the probability of transferring to any state t from existing state t_1 is the probability of that specific state transition occurring over the probability that any state transition occurs. Recall that it is possible for states to be termination states, and thus the probability of transferring out of t_1 and into another state is not necessarily unity. The random walk proceeds in this manner until a termination state t_k is selected. At this point the random walk ends and the set of sampled states which describe the random walk can be written as $\alpha = (t_1, \ldots, t_{k-1}, t_k)$. While this is interesting from a mathematical standpoint, one still needs to be able to extract useful information from the set of sampled random walks in order for the Monte Carlo random walk method to be applicable for computational radiation transport.

2.3 Discussion of Monte Carlo Inner Product Estimators

The previous section confirmed that the Monte Carlo random walk process is capable of solving FIESKs. This section will deal with how useful information regarding the population of sampled walks may be extracted from the data. As one is often seeking the neutron flux, fluence, or reaction rates in nuclear engineering, it is of importance to be able to derive these quantities from the set of sampled random walks. In actuality one will find that an estimation of a quantity of interest along with its uncertainty in the phase space is what will be done. The quantity of interest will be represented as the inner product of a known function $h(t)$ and the unknown solution to the FIESK $f(t)$:

$$I = \int_{\Gamma} h(t)f(t)dt. \tag{2.16}$$

Imagine that one wishes to calculate the fission rate within a given fuel rod in a system. Recalling that the reaction rate may be represented as $R = \int_E \Sigma(E)\phi(E)dE$, one will know the macroscopic cross section of the material, as this must be supplied prior to the simulation. Therefore, $\Sigma(E)$ is a known quantity for all energies E. The unknown quantity is the energy-dependent neutron flux distribution $\phi(E)$. The ultimate goal of this section is to discuss how the random walk method can estimate the value for I, for which two methods will be shown. As these methods seek to estimate the value of I they will be referred to as estimators henceforth.

The Termination Estimator

The first and most basic estimator described will gather data about every event in a random walk and will contribute to the estimation of I only when the entire walk has terminated. For this reason it is referred to as a *termination estimator*. In order to use the random walk method one must first construct the PDFs $p^1(t)$ and $p(s \to t)$ by normalizing the forcing function and transfer kernel $g(t)$ and $K(s \to t)$ respectively. One may now construct the termination estimator $\epsilon(\alpha)$ for random walk α as follows:

$$\epsilon(\alpha) = \frac{g(t_1)}{p^1(t_1)} w(t_1 \to t_2) \dots w(t_{k-1} \to t_k) \frac{h(t_k)}{p(t_k)}, \tag{2.17}$$

where the weighting function $w(s \to t)$ is merely the normalized transfer probability assuming that the state transition does not result in termination:

$$w(s \to t) = \begin{cases} \dfrac{K(s \to t)}{p(s \to t)} & \text{if } p(s \to t) \neq 0 \\ 0 & \text{if } p(s \to t) = 0. \end{cases} \tag{2.18}$$

From the previous statement about normalization, without variance reduction techniques the weighting function after each event will be unity, as $K(s \to t)$ is equal to $p(s \to t)$ by design. Further, the constant in front can be reduced by recognizing the following:

$$\frac{g(t_1)}{p^1(t_1)} = \int_\Gamma g(t)dt = C. \tag{2.19}$$

This yields the simplified expression for the analogue termination estimator:

$$\epsilon(\alpha) = C\frac{h(t_k)}{p(t_k)}. \tag{2.20}$$

In order to verify the accuracy of this result it will be shown that the estimator in Equation 2.20 is in fact equivalent to the value of the inner product. This serves as proof of an unbiased estimator for the quantity I given $h(t)$ [8]. The calculation of the expectation value of the termination estimator is shown below:

$$\begin{aligned} < \epsilon(\alpha) > &= \sum_\alpha P(\alpha)\epsilon(\alpha) \\ &= \sum_{k=1}^{\infty} \int \dots \int dt_1 \dots dt_k \left[p^1(t_1)p(t_1 \to t_2) \dots p(t_{k-1}) \to p(t_k) \cdot \right. \\ &\quad \left. \frac{g(t_1)}{p^1(t_1)} w(t_1 \to t_2) \dots w(t_{k-1} \to t_k) \frac{h(t_k)}{p(t_k)} \right]. \end{aligned} \tag{2.21}$$

Utilizing the Neumann series solution to the FIESK one may simplify this expression to arrive at:

$$\begin{aligned} < \epsilon(\alpha) > &= \sum_{k=1}^{\infty} \int \dots \int dt_1 \dots dt_k \left(g(t_1)K(t_1 \to t_2) \dots k_(t_{k-1} \to t_k)h(t_k) \right) \\ &= \int_\Gamma h(t)F(t)dt. \end{aligned} \tag{2.22}$$

It may be seen that if $h(t)$ exists only in a sub-region Γ_h of Γ that the termination estimator will be zero outside of that sub-region. Thus the termination estimator

will only contribute if the random walk terminates in the sub-region Γ_h. While this is a very straight-forward estimator it is also problem dependent and often inefficient. This is especially the case as the domain Γ_h shrinks in comparison to Γ, making it less likely that any given particle will terminate in the region of interest. For this reason it is profitable to discuss an alternate estimator which does not suffer from this behavior.

The Event Estimator

The termination estimator only contributes to the estimation of I if a random walk α terminates in the sub-region Γ_h over which the known function $h(t)$ exists. This is problematic from a computational standpoint, as many random walks will not be contributing to the estimation of the quantity of interest. A better estimator would be capable of contributing to the estimation of I every time an event occurs within the sub-region Γ_h. This estimator will be referred to as the *event estimator* will be shown below briefly. For the interested reader a verbose derivation may be found in the previously mentioned text by Spanier and Gelbard [8]. The estimator may be written as:

$$\begin{aligned}\eta(\alpha) &= \sum_{m=1}^{k} \frac{g(t_1)}{p^1(t_1)} w(t_1 \to t_2) \dots w(t_{k-1} \to t_k) h(t_k) \\ &= \sum_{m=1}^{k} W_m(\alpha) h(t_m). \end{aligned} \tag{2.23}$$

The variable $W_m(\alpha)$ may be thought of as the current weight, or the weight of the particle after undergoing event m in the random walk. As before, for an analogue calculation without variance reduction this value will be unity and the ratio of the forcing function to the birth probability will be described by the constant shown in Equation 2.19. This will yield an estimator of the following form:

$$\eta(\alpha) = C \sum_{m=1}^{k} h(t_k). \tag{2.24}$$

Now as the size of Γ_h shrinks with respect to Γ, the event estimator will grow increasingly efficient with respect to the termination estimator, as each random walk will have more opportunities to contribute to the estimation of I. However, it should be noted that both of these estimators will become ineffective when the

sub-region Γ_h reduces to a point, and thus $h(t)$ reduces to a delta function. This case may be addressed by analyzing the dual of the FIESK to develop a method for the estimation of quantity I at a point.

Estimator Accuracy

Before moving on to the dual of the FIESK and the estimation of quantities of interest at a delta detector phase space, it is helpful to understand the difference between a theoretical estimator and an estimator in a simulated problem consisting of a finite quantity of random walks. In the previous derivations one may note that the summations over random walks are always taken to infinity in order to be the exact solution to the FIESK. Yet, it is impractical to imagine taking an infinite number of samples, in the same way that it is impractical to imagine taking an infinite number of terms in the successive approximations solution to the FIESK. Thus, one must develop an understanding for the inherent error associated with the truncation the solution after any number of sampling events.

One may define the estimation of I as the average of the individual random walk estimations

$$\bar{I} = \frac{1}{N} \sum_{i=1}^{N} i(\alpha_i), \tag{2.25}$$

where $i(\alpha_i)$ is the i^{th} random walk estimation of I.

From here the uncertainty of $\bar{I}$ may be quantified by calculating the sample standard deviation. This is often referred to as the standard error of the quantity and is as follows:

$$S = \left[\frac{1}{N-1} \sum_{i=1}^{N} i(\alpha_i)^2 - \frac{N}{N-1} \bar{I} \right]^{1/2}. \tag{2.26}$$

Thus the uncertainty in the simulation behaves as the inverse square root of the number of random walks,

$$S \propto \frac{1}{\sqrt{N}}. \tag{2.27}$$

If one obtains an estimate S_1 of the standard error for some N_1, it is then easy to calculate an estimate of the required number of random walks N_2 which will result in the desired error S_2. While the term error is being used it should be noted that this is statistical uncertainty, not systematic error associated with round-off or discretization. For the remainder of this work the meaning of the term error shall coincide with uncertainty when referring to estimators.

It should briefly be noted that the ability to estimate $\bar{I}$ from random walks is predicated on the assumption that random walks terminate in a finite number of steps (i.e. that random walks are not the zero-variance walk). As this work focuses primarily on neutron transport, this means that only strictly subcritical systems can be analyzed, as there is a guaranteed limit to the number of steps any given random walk can undergo. Due to the constraints associated with achieving open-source licensing without export-control, critical and super-critical modeling capabilities are not currently planned for FRENSIE, and this constraint is always satisfied in the work laid out herein.

2.4 The Dual FIESK for Point Estimators

As stated in the previous sections, the random walk estimators are ineffective at estimating I when the sub-region over which the known function $h(t)$ operates shrinks to a single point. In order to be able to analyze this case, one must assess the dual FIESK and its solution [22]. To begin, one must consider an operator H which has the following property:

$$H \cdot f(t) = f(t) - \int_{\Gamma} K(s \to t) f(s) ds. \tag{2.28}$$

This can be rearranged into a FIESK of the following form:

$$f(t) = \int_{\Gamma} K(s \to t) f(s) ds + H \cdot f(t). \tag{2.29}$$

If one assumes that $H \cdot f(t) = g(t)$ this is of the form of the original FIESK shown in Equation 2.1. It can be shown that if $f(t)$ is strictly a real-valued function, the adjoint operator $H^{\dagger}$ is defined by the following equality [22]:

$$\int_{\Gamma} f^{\dagger}(t) H \cdot f(t) dt = \int_{\Gamma} f(t) H^{\dagger} f^{\dagger}(t). \tag{2.30}$$

It can also be shown that the newly defined quantity $f^{\dagger}(t)$ is the solution to a separate FIESK which will be referred to as the dual FIESK [22]. Further, one may

determine the form of the adjoint operator $H^\dagger$ as

$$\begin{aligned}
\int_\Gamma f^\dagger(t) H \cdot f(t)\,dt &= \int_\Gamma f^\dagger(t)\left(f(t) - \int_\Gamma K(s \to t) f(s)\,ds\right) dt \\
&= \int_\Gamma \left(f^\dagger(t) f(t) - f^\dagger(t) \int_\Gamma K(s \to t) f(s)\,ds\right) dt \\
&= \int_\Gamma f^\dagger(t) f(t)\,dt - \int_\Gamma \left[\int_\Gamma K(s \to t) f^\dagger(t) f(s)\,ds\right] dt \qquad (2.31) \\
&= \int_\Gamma f^\dagger(t) f(t)\,dt - \int_\Gamma f(s) \left[\int_\Gamma K(s \to t) f^\dagger(t)\,dt\right] ds \qquad (2.32) \\
&= \int_\Gamma f^\dagger(t) f(t)\,dt - \int_\Gamma f(t) \left[\int_\Gamma K(t \to s) f^\dagger(s)\,ds\right] dt \qquad (2.33) \\
&= \int_\Gamma f(t) H^\dagger \cdot f^\dagger(t), \qquad (2.34)
\end{aligned}$$

where

$$H^\dagger \cdot f^\dagger(t) = f^\dagger(t) - \int_\Gamma K(t \to s) f^\dagger(s)\,ds. \qquad (2.35)$$

Now one may set the function $H^\dagger \cdot f^\dagger(t)$ equal to the known function $h(t)$ in Equation 2.16 to obtain the dual FIESK:

$$f^\dagger(t) = h(t) + \int_\Gamma K(t \to s) f^\dagger(s)\,ds. \qquad (2.36)$$

What is of interest in the dual FIESK is that the forcing function is now the known parameter $h(t)$ which defines the region of response Γ_h for the estimation of I. It should also be noted that while the kernel K is functionally the same, the integration is taking place over final states rather than initial states as it did in the original FIESK. In order to show that these two FIESKs are in fact duals, the functional form for I must be calculated as follows:

$$\begin{aligned}
I &= \int_\Gamma f(t) h(t)\,dt \\
&= \int_\Gamma f(t) H^\dagger \cdot f^\dagger(t)\,dt \\
&= \int_\Gamma f^\dagger(t) H \cdot f(t)\,dt \\
&= \int_\Gamma f^\dagger(t) g(t)\,dt. \qquad (2.37)
\end{aligned}$$

FIESK and Dual FIESK Comparison

It may not be immediately apparent where the FIESK and the dual FIESK are of primary use, however a brief analysis of their forcing functions, $g(t)$ and $h(t)$ respectively, will provide insight. As was discussed first, if $h(t)$ is a delta function the sub-region Γ_h over which the estimator exists vanishes to a single point and thus the likelihood of any given random walk contributing to it is identically zero. In this case only dual FIESK will be able to produce an estimate for I, as $h(t)$ appears only as a forcing function in the FIESK. This describes the case where a detector exists only at a single point, more commonly referred to as a point detector.

Conversely, if $g(t)$ is a delta function then only the original FIESK is capable of producing an estimate for I. This describes the case where the source is a single point in space, and thus the dual FIESK is incapable of resolving this response. In general, the choice between the FIESK and dual FIESK often comes down to the relative sizes of the source and detector regions in phase space. The following general rule describes where the FIESK and dual FIESK are most efficient:

$$\text{Efficient Method} = \begin{cases} \text{FIESK} & \text{if } \Gamma_d > \Gamma_s \\ \text{Dual FIESK} & \text{if } \Gamma_s > \Gamma_d. \end{cases} \tag{2.38}$$

Where Γ_d and Γ_s describe the detector and source regions respectively. Due to this rule of thumb there are many cases in radiation transport in which the detector region is small with respect to the source, and thus the dual FIESK is significantly more efficient at estimating I. In support of this reasoning this work will focus on the development of methods of adjoint thermal neutron transport for more efficient neutronics calculations.

2.5 Chapter Summary

Several points from this chapter must be emphasized before moving on to the next chapter. They are summarized in the following list:

- As the number of variables increases, solving a FIESK using the method of successive approximations can become cumbersome or impractical analytically.
- The Monte Carlo random walk process is capable of solving FIESKs and is often

a much simpler solution methodology when there are many interdependent variables.

- Both the termination and event estimators are capable of estimating inner product quantities of interest with calculable uncertainty arising from the finite set of random walks.
- Problems with a delta source can only be solved using the FIESK, while problems with a delta detector can only be solved using the dual of the FIESK.
- If the source region is larger than the detector region the dual of the FIESK may become more computationally efficient.

Chapter 3

Forward Radiation Transport Theory

The previous chapter focused on the application of the Monte Carlo random walk method to the solution of the FIESK and dual FIESK at a high level. The goal of this chapter is to define precisely how the Monte Carlo random walk process is applied in relation to radiation transport modeling. It has been alluded to that the random walk process simulates the transport of particles from source to termination, but this behavior must be grounded in both mathematics and nuclear physics. Thus, this chapter will seek to apply the general thought processes from Chapter 2 to the specific equation governing radiation transport.

3.1 The Forward Transport Equation

The primary work in this chapter will discuss the forward transport equation and its methods of solution. Chapter 4 will revisit this discussion in the context of the adjoint transport equation.

The Integro-Differential Transport Equation

The radiation transport equation is fundamental to nuclear science and engineering. The canonical form of the transport equation is the integro-differential form seen below:

$$\begin{aligned}\frac{1}{\nu}\frac{\partial\varphi(\vec{r},E,\hat{\Omega},t)}{\partial t}+\hat{\Omega}\cdot\vec{\nabla}\varphi(\vec{r},E,\hat{\Omega},t)+\Sigma_T(\vec{r},E)\varphi(\vec{r},E,\hat{\Omega},t)=\\ S(\vec{r},E,\hat{\Omega},t)+\int\int\Sigma_T(\vec{r},E'\rightarrow E,\hat{\Omega}'\rightarrow\hat{\Omega})\varphi(\vec{r},E',\hat{\Omega}',t)dE'd\hat{\Omega}'.\end{aligned} \tag{3.1}$$

Where $\vec{r}$ is position, E is energy, $\hat{\Omega}$ is direction, t is time, and ν is speed. The transport equation characterizes the expected behavior of radiation in a system. While this governs both photon and neutron transport, this work deals only with neutron transport, and thus it will be said that the transport equation characterizes the *neutron* behavior, or neutronics, of a system [6]. In Equation 3.1, φ represents the angular neutron flux as a function of space, direction, energy, and time. Therefore, the units on φ are the neutron flux per unit energy per unit solid angle. Note that

this is different from the scalar flux ϕ which can be found when angular dependence is integrated out and which describes the total flux of particles in any direction at a given location in phase space.

The first term on the left hand side (LHS) in Equation 3.1 describes the time rate of change of the angular flux in the system. The second term on the LHS describes the transport of neutrons into and out of the volume of interest. The third term on the LHS is the total collision density. Σ_T is the total cross macroscopic cross section, which describes the probability per unit path length that a neutron will undergo any reaction. Therefore, the product of Σ_T and φ yields the density of neutrons which collide within the phase space.

The first term on the right hand side (RHS) is the generic source term which describes the production of neutrons within the phase space. While it is written here as a function $S(\vec{r}, E, \hat{\Omega}, t)$, it will often be a mixture of external sources and flux dependent sources such as multiplication, fission, and radioactive decay. The final term on the RHS describes the the transfer of particles from any other state to the state of interest, and thus is an additional source of neutrons.

The final term on the RHS contains what is referred to as the double differential cross section $\Sigma_T(\vec{r}, E^{'} \rightarrow E, \hat{\Omega}^{'} \rightarrow \hat{\Omega})$. The double differential cross section describes the probability per unit path length per unit energy per unit solid angle that a particle will undergo a collision at point $\vec{r}$, transferring from energy E' to E and direction $\hat{\Omega}'$ to $\hat{\Omega}$. Note that the double differential total cross section can be written as the product of the total cross section and the probability of transferring from state $(E', \hat{\Omega}')$ to state $(E, \hat{\Omega})$ as follows:

$$\Sigma_T(\vec{r}, E^{'} \rightarrow E, \hat{\Omega}^{'} \rightarrow \hat{\Omega}) = \Sigma_T(\vec{r}, E')f(\vec{r}, E^{'} \rightarrow E, \hat{\Omega}^{'} \rightarrow \hat{\Omega}). \tag{3.2}$$

Further, the total cross section can be broken up as the sum of the individual reaction cross sections as

$$\Sigma_T(\vec{r}, E^{'} \rightarrow E, \hat{\Omega}^{'} \rightarrow \hat{\Omega}) = \sum_i \Sigma_i(\vec{r}, E')c_i(\vec{r}, E')f_i(\vec{r}, E^{'} \rightarrow E, \hat{\Omega}^{'} \rightarrow \hat{\Omega}). \tag{3.3}$$

The term $c_i(\vec{r}, E')$ refers to the number of neutrons emitted after undergoing reaction

i. This value will be determined by the type of reaction that is sampled as follows:

$$c_i(\vec{r}, E') = \begin{cases} 0 & \text{for absorption reactions: } (n,\gamma),(n,p),(n,d),(n,\alpha),\ldots \\ 1 & \text{for elastic and inelastic scattering} \\ x & \text{for } (n,xn) \text{ multiplication reactions} \\ \nu(E') & \text{for fission reactions.} \end{cases}$$

Using this definition of $c_i(\vec{r}, E')$, one may determine the normalization for the total double differential transfer function:

$$\begin{aligned} \int\int \Sigma_T(\vec{r}, E^{'}) f(\vec{r}, E^{'} \to E, \hat{\Omega}^{'} \to \hat{\Omega}) dE d\hat{\Omega} &= \int\int \sum_i \Sigma_i(\vec{r}, E^{'}) c_i(\vec{r}, E^{'}) \\ &\quad \cdot f_i(\vec{r}, E^{'} \to E, \hat{\Omega}^{'} \to \hat{\Omega}) dE d\hat{\Omega} \\ \int\int f(\vec{r}, E^{'} \to E, \hat{\Omega}^{'} \to \hat{\Omega}) dE d\hat{\Omega} &= \frac{\sum_i \Sigma_i(\vec{r}, E^{'}) c_i(\vec{r}, E^{'})}{\Sigma_T(\vec{r}, E')} \\ &= c(\vec{r}, E^{'}). \end{aligned} \tag{3.4}$$

Here $c(\vec{r}, E')$ is the cross section weighted average of the reaction emission values and describes the average number of neutrons that will be emitted from a collision at point $\vec{r}$ and energy E'. From a theoretical standpoint, it is interesting to understand the total double differential transfer function. However, in order to implement the Monte Carlo random walk process one must develop a double differential transfer function for each specific reaction in the problem, such that once a reaction is sampled the appropriate outgoing state distributions may also be sampled.

Conversion of the Forward Transport Equation to Integral Form

The above discussion was designed to familiarize the reader with the standard integro-differential form of the neutron transport equation. The discussion of FIESK solutions in Chapter 2 should suggest that the solution methodology employed herein will be in regards to an integral equation. Thus, the conversion from the integro-differential to integral form of the neutron transport equation must be undertaken. The derivation shown herein generally follows those found in numerous nuclear engineering texts and resources [5, 23–25].

To aid in the conversion to the integral form a simplifying assumption and a redefinition will be made. First, steady state physics are of primary importance to this work, and thus the time dependence of the transport equation will be ignored.

Second, the RHS of Equation 3.1 will be combined into a single term which captures both the sources and the in-transfer terms and will be referred to as the emission density $\chi(\vec{r}, E, \hat{\Omega})$:

$$\chi(\vec{r}, E, \hat{\Omega}) = S(\vec{r}, E, \hat{\Omega}) + \int\int \Sigma_T(\vec{r}, E' \to E, \hat{\Omega}' \to \hat{\Omega})\varphi(\vec{r}, E', \hat{\Omega}')dE'd\hat{\Omega}'. \tag{3.5}$$

Removing the time dependence and substituting in the emission density on the RHS yields the simplified integro-differential transport equation,

$$\hat{\Omega} \cdot \vec{\nabla}\varphi(\vec{r}, E, \hat{\Omega}) + \Sigma_T(\vec{r}, E)\varphi(\vec{r}, E, \hat{\Omega}) = \chi(\vec{r}, E, \hat{\Omega}). \tag{3.6}$$

At this point the method of characteristics will be implemented in order to transform the simplified transport equation into the integral transport equation. Assume that the characteristic line for the method of characteristics is the line from point $\vec{r}$ along direction $\hat{\Omega}$ parameterized by distance R given as:

$$\vec{r}' = \vec{r} - R\hat{\Omega}. \tag{3.7}$$

One may now determine the directional derivative along the characteristic line by taking the partial derivatives with respect to the characteristic as follows:

$$\begin{aligned}\frac{d}{dR} &= \frac{dx'}{dR}\frac{\partial}{\partial x} + \frac{dy'}{dR}\frac{\partial}{\partial y} + \frac{dz'}{dR}\frac{\partial}{\partial z} \\ &= -\Omega_x\frac{\partial}{\partial x} - \Omega_y\frac{\partial}{\partial y} - \Omega_z\frac{\partial}{\partial z} = -\hat{\Omega} \cdot \vec{\nabla}.\end{aligned} \tag{3.8}$$

Thus the transport term can be reduced to a single derivative along the characteristic, transforming the problem into a first order ordinary differential equation (ODE) of the form

$$-\frac{d}{dR}\varphi(\vec{r}', E, \hat{\Omega}) + \Sigma_T(\vec{r}', E)\varphi(\vec{r}', E, \hat{\Omega}) = \chi(\vec{r}', E, \hat{\Omega}). \tag{3.9}$$

The resultant first order ODE can be solved by utilizing an integrating factor of the form:

$$\exp\left[-\int_0^R \Sigma_T(\vec{r} - R'\hat{\Omega}, E)dR'\right]. \tag{3.10}$$

The integrating factor is multiplied by both sides of the equation and the equation is then integrated on $R \in [0, \infty]$. Here a physical assumption must be made which states that the flux is a physical quantity describing the motion of particles in phase space and thus must be bounded as $R \to \infty$. Slightly more strictly it is stated that it

is not only bounded but that $\varphi \to 0$ as $R \to \infty$. Application of this methodology yields an integral version transport equation,

$$\varphi(\vec{r}, E, \hat{\Omega}) = \int_0^{\infty} \chi(\vec{r} - R\hat{\Omega}, E, \hat{\Omega}) \exp\left[-\int_0^{R} \Sigma_T(\vec{r} - R'\hat{\Omega}, E) dR'\right] dR. \tag{3.11}$$

At this point the integral is along the characteristic. However, one would prefer to have the integral be over an arbitrary differential volume dV'. In order to do this one must convert back from the characteristic to the original coordinate system using the following identities:

$$R = |\vec{r} - \vec{r}'|, \tag{3.12}$$

$$\hat{\Omega} = \frac{\vec{r} - \vec{r}'}{|\vec{r} - \vec{r}'|}, \tag{3.13}$$

$$dV' = R^2 dR d\hat{\Omega}. \tag{3.14}$$

Substituting these identities into the integral transport equation with respect to a characteristic yields the integral transport equation wherein the integration is performed over a differential volume dV' rather than along a characteristic line as shown:

$$\varphi(\vec{r}, E, \hat{\Omega}) = \int \chi(\vec{r}', E, \hat{\Omega}) \exp\Big[-\int_0^{|\vec{r} - \vec{r}'|} \Sigma_T(\vec{r} - R'\hat{\Omega}, E) dR'\Big] \frac{\delta\left(\hat{\Omega} - \left[\frac{\vec{r} - \vec{r}'}{|\vec{r} - \vec{r}'|}\right]\right)}{|\vec{r} - \vec{r}'|^2} dV'. \tag{3.15}$$

One final definition will be made to yield the simplified integral transport equation. The following term τ will be defined as:

$$\tau(\vec{r}', \vec{r}, E, \hat{\Omega}) = \exp\left[-\int_0^{|\vec{r} - \vec{r}'|} \Sigma_T(\vec{r} - R'\hat{\Omega}, E) dR'\right] \frac{\delta\left(\Omega - \left[\frac{\vec{r} - \vec{r}'}{|\vec{r} - \vec{r}'|}\right]\right)}{|\vec{r} - \vec{r}'|^2}. \tag{3.16}$$

Substituting this into the integral transport equations yields the simplified integral transport equation. While it is not yet in the form of a FIESK, the following sections will discuss the methods by which it may be converted and the various benefits and drawbacks of each method. The simplified integral transport equation is now of the form:

$$\varphi(\vec{r}, E, \hat{\Omega}) = \int \chi(\vec{r}', E, \hat{\Omega}) \tau(\vec{r}', \vec{r}, E, \hat{\Omega}) dV'. \tag{3.17}$$

3.2 Definition of the Transport FIESKs

This section will propose three possible FIESKs that can be constructed from the simplified integral transport equation using different variables of interest.

The Angular Flux FIESK

The most conceptually straight-forward FIESK to develop revolves around the angular flux, φ. In nuclear engineering the flux or fluence of a system is frequently the quantity of interest, and thus it is common to think of neutrons in terms of flux. This is further reinforced by the fact that deterministic solutions often focus on solving for the neutron flux [5]. To begin, one must expand the simplified expression found in Equation 3.17 with the previous definition for the emission density found in Equation 3.5:

$$\begin{aligned}\varphi(\vec{r}, E, \hat{\Omega}) = &\int S(\vec{r}', E, \hat{\Omega})\tau(\vec{r}', \vec{r}, E, \hat{\Omega})dV' + \\ &\int\int\int \tau(\vec{r}', \vec{r}, E, \hat{\Omega})\Sigma_T(\vec{r}', E' \to E, \hat{\Omega}' \to \hat{\Omega})\varphi(\vec{r}', E', \hat{\Omega}')dE'd\hat{\Omega}'dV'.\end{aligned} \tag{3.18}$$

As Equation 3.18 is in the form of a FIESK for the angular flux, one may apply the methodology put forth in the previous chapter to simulate the angular flux via the Monte Carlo random walk method. The birth or source PDF can be constructed as follows:

$$p^1(\vec{r}, E, \hat{\Omega}) = \frac{\int S(\vec{r}', E, \hat{\Omega})\tau(\vec{r}', \vec{r}, E, \hat{\Omega})dV'}{\int\int S(\vec{r}', E, \hat{\Omega})\tau(\vec{r}', \vec{r}, E, \hat{\Omega})dV'dVdEd\hat{\Omega}}. \tag{3.19}$$

Further, the transfer PDF can be split up into the product of a PDF which governs the spatial transport from $\vec{r}$ to $\vec{r}'$ and a PDF which governs the phase space transfer from an initial energy-angle state $(E', \hat{\Omega}')$ to a final energy-angle state $(E, \hat{\Omega})$ as shown:

$$\begin{aligned}p(s \to t) &= p(\vec{r}' \to \vec{r}, E' \to E, \hat{\Omega}' \to \hat{\Omega}) \\ &= p(\vec{r}' \to \vec{r}|E, \hat{\Omega}) \cdot p(E' \to E, \hat{\Omega}' \to \hat{\Omega}|\vec{r}').\end{aligned} \tag{3.20}$$

The spatial transport PDF is merely the transport function $\tau(\vec{r}', \vec{r}, E, \hat{\Omega})$ after

normalization. Thus,

$$p(\vec{r}' \rightarrow \vec{r} \quad |E, \hat{\Omega}) = \frac{\tau(\vec{r}', \vec{r}, E, \hat{\Omega})}{\int \tau(\vec{r}', \vec{r}, E, \hat{\Omega}) dV}. \tag{3.21}$$

What is typically done in this derivation is to write the normalization constant as a weighting factor [8]. That is to say:

$$w(\vec{r}', E, \hat{\Omega}) = \int \tau(\vec{r}', \vec{r}, E, \hat{\Omega}) dV. \tag{3.22}$$

This more clearly demonstrates that the normalization constant herein acts as a weighting function. The particle weight is multiplied by the weighting function after each collision, and it may be seen that weight is not bounded by the region $[0, 1]$ meaning that the weight of the particle can grow or shrink dramatically over the random walk process [8]. This unbounded variation in particle weights will tend to increase the variance of any estimator used and is thus detrimental to achieving the necessary statistics for converged results [24].

Perhaps the largest issue with the transport PDF derived from the flux FIESK is that the macroscopic collision cross section is absent. What this means practically is that a collision event can be sampled in a vacuum, which is due to the physical property that the flux itself is allowed to be non-zero in a vacuum. The final issue is computational in nature and arises from the fact that the source is represented as an integral. Depending on the nature of the source term, this may be difficult to accurately evaluate and sample in general. It is due to these issues that the direct application of the Monte Carlo method to a flux FIESK is rarely done and will not be attempted in this work [8].

The Emission Density FIESK

In order to derive the emission density FIESK one need only substitute the expression for the flux from Equation 3.18 into the equation for the emission density in Equation 3.5 [24] yielding the following expression:

$$\chi(\vec{r}, E, \hat{\Omega}) = S(\vec{r}, E, \hat{\Omega}) + \int_{V'} \int_{E'} \int_{\hat{\Omega}'} \frac{\Sigma_T(\vec{r}, E' \rightarrow E, \hat{\Omega}' \rightarrow \hat{\Omega})}{\Sigma_T(\vec{r}, E')} \Sigma_T(\vec{r}, E') \tau(\vec{r}', \vec{r}, E', \hat{\Omega}') \cdot \chi(\vec{r}', E', \hat{\Omega}') dV' dE' d\hat{\Omega}'. \tag{3.23}$$

The expression in Equation 3.23 can be greatly simplified by the inclusion of two

new terms which will be referred to as the collision kernel and the transport kernel. The collision kernel will handle the probability that particle at position $\vec{r}$, energy E', and direction $\hat{\Omega}'$ will undergo a collision which leaves it at energy E and direction $\hat{\Omega}$,

$$C(\vec{r}, E^{'} \rightarrow E, \hat{\Omega}^{'} \rightarrow \hat{\Omega}) = \frac{\Sigma_T(\vec{r}, E^{'} \rightarrow E, \hat{\Omega}^{'} \rightarrow \hat{\Omega})}{\Sigma_T(\vec{r}, E')}. \tag{3.24}$$

The transport kernel represents the probability that a particle at $\vec{r}'$, energy E', and direction $\hat{\Omega}'$ will have its next collision in a differential volume dV about point $\vec{r}$,

$$T(\vec{r}^{'} \rightarrow \vec{r}, E, \hat{\Omega}) = \Sigma_T(\vec{r}, E)\tau(\vec{r}^{'}, \vec{r}, E, \hat{\Omega}). \tag{3.25}$$

Each of these kernels captures a component of the transition kernel. The collision kernel captures the behavior of transferring between one energy-angle state to another, while the transport kernel captures the behavior of transporting a particle in space. The product of these two kernels yields the complete transition kernel $K(s \rightarrow t)$ for the emission density FIESK,

$$K(s \rightarrow t) = C(\vec{r}, E^{'} \rightarrow E, \hat{\Omega}^{'} \rightarrow \hat{\Omega})T(\vec{r}^{'} \rightarrow \vec{r}, E^{'}, \hat{\Omega}^{'}). \tag{3.26}$$

Substituting equations 3.24 and 3.25 into equation 3.23 yields the following result:

$$\chi(\vec{r}, E, \hat{\Omega}) = S(\vec{r}, E, \hat{\Omega}) + \int\int\int C(\vec{r}, E^{'} \rightarrow E, \hat{\Omega}^{'} \rightarrow \hat{\Omega})T(\vec{r}^{'} \rightarrow \vec{r}, E^{'}, \hat{\Omega}^{'}) \cdot \chi(\vec{r}^{'}, E', \hat{\Omega}^{'})dV^{'}dE^{'}d\hat{\Omega}^{'}. \tag{3.27}$$

The Collision Density FIESK

While the flux and emission density were apparent throughout the derivation, another quantity of interest referred to as the collision density can be constructed which is often of use. The collision density is, as the name implies, the density of collisions occurring in a phase space. One might also think of this as a total reaction rate density, and thus it is defined as the product of the total cross section and the angular flux,

$$\psi(\vec{r}, E, \hat{\Omega}) = \Sigma_T(\vec{r}, E)\varphi(\vec{r}, E, \hat{\Omega}). \tag{3.28}$$

By simple manipulation using equations 3.25 and 3.17 one can rewrite the collision density in terms of the transport kernel and emission density [24],

$$\psi(\vec{r}, E, \hat{\Omega}) = \int T(\vec{r}' \rightarrow \vec{r}, E, \hat{\Omega}) \chi(\vec{r}', E, \hat{\Omega}) dV'. \tag{3.29}$$

The collision density FIESK can be obtained by substituting Equation 3.27 into Equation 3.29, yielding the following expression:

$$\begin{aligned}\psi(\vec{r}, E, \hat{\Omega}) = &\int S(\vec{r}', E, \hat{\Omega}) T(\vec{r}' \rightarrow \vec{r}, E, \hat{\Omega}) dV' + \\ &\int\int\int T(\vec{r}' \rightarrow \vec{r}, E, \hat{\Omega}) C(\vec{r}', E' \rightarrow E, \hat{\Omega}' \rightarrow \hat{\Omega}) \psi(\vec{r}', E', \hat{\Omega}') dE' d\hat{\Omega}' dV'.\end{aligned} \tag{3.30}$$

The first term on the RHS can be thought of as the source term. However, it should be noted that the source term in the collision density FIESK is actually a first collided source term in comparison to the source term in the emission density FIESK. This is due to the fact that the source term and the transport kernel are now multiplied and the product is integrated over the volume.

Again the transition kernel can be extracted from within the integral as follows:

$$L(s \rightarrow t) = T(\vec{r}' \rightarrow \vec{r}, E, \hat{\Omega}) C(\vec{r}', E' \rightarrow E, \hat{\Omega}' \rightarrow \hat{\Omega}). \tag{3.31}$$

3.3 Salient Features of the State Transition Kernels

The state transition kernels for the emission and collision density FIESKs have interesting properties that should be investigated before proceeding with the application of the Monte Carlo random walk process. Recall that the collision kernel was found to be equal to the total double differential transfer probability, or the total double differential cross section divided by the total cross section. Thus, integrating the collision kernel over energy and angle produces the normalization factor for the collision kernel,

$$\int\int C(\vec{r}, E' \rightarrow E, \hat{\Omega}' \rightarrow \hat{\Omega}) dE d\hat{\Omega} = c(\vec{r}, E'). \tag{3.32}$$

Here $c(\vec{r}, E')$ represents the average number of neutrons emitted per collision. It should be noted that this does not necessarily imply that there is multiplication. If no multiplication is present, $c(\vec{r}, E')$ will take on a value less than unity due to

absorption, and the integrated double differential total cross section will reduce to the scattering cross section. This ratio of the scattering to total cross section is often referred to as the survival (or non-absorption) probability P_{NA}, or the likelihood that any given interaction will be a scattering reaction [6]. Thus $c(\vec{r}, E')$ may be written as

$$\int\int C(\vec{r}, E' \rightarrow E, \hat{\Omega}' \rightarrow \hat{\Omega}) dE d\hat{\Omega} = \frac{\Sigma_s(\vec{r}, E')}{\Sigma_T(\vec{r}, E')} = P_{NA}(\vec{r}, E'). \tag{3.33}$$

The transport kernel must also be investigated. Again it is important to calculate the value of the transport kernel when integrated over all space for an infinite medium, as the normalization of the transport kernel will be important in the adjustment of particle weights throughout the random walk transport process. It can be shown that for an infinite system the transport kernel normalizes to unity. The basic method for this proof is to revert the integral over volume to one over the characteristic line previously defined and then apply the Liebniz rule of integration to reduce the term outside of the exponential. At this point one may evaluate the integral on the region $[0, \infty)$ which will yield the aforementioned result of unity. This is an ideal result as it allows one to disregard a weighting factor in the transport step [24], as the expression is already normalized to unity:

$$\int T(\vec{r}' \rightarrow \vec{r}, E, \hat{\Omega}) dV = 1. \tag{3.34}$$

However, as computational resources are finite there will never be a true infinite geometry representation and thus the transport kernel will always normalize to a value less than unity. This can be remedied by including a bounding box of infinitely absorbing material surrounding the entire geometry which terminates any random walk which enters it. This is commonly referred to as a *graveyard* in Monte Carlo simulations and is defined as an area which immediately terminates any history which enters it. It can also be shown that the inclusion of the graveyard recovers the original normalization of the transport kernel to unity [24].

Emission Density State Transition Kernel

At this point one may reconstruct the state transition kernels for both the emission density and collision density FIESKs and calculate the normalization for each. For the emission density state transition kernel one must substitute equations 3.33 and 3.34 into Equation 3.26 and the expression must be integrated over all possible final

states $t \in \Gamma$ to yield:

$$\begin{aligned}\int K(s \to t)dt &= \int\int\int C(\vec{r}, E' \to E, \hat{\Omega}' \to \hat{\Omega})T(\vec{r}' \to \vec{r}, E', \hat{\Omega}')dEd\hat{\Omega}dV \\ &= \int c(\vec{r}, E')dV \int T(\vec{r}' \to \vec{r}, E, \hat{\Omega})dV \\ &= \int c(\vec{r}, E')dV \\ &= \bar{c}(\vec{r}', E'). \end{aligned} \tag{3.35}$$

Here the normalization produces the function $\bar{c}(\vec{r}', E')$ which is closely related to the previously defined $c(\vec{r}, E')$. The term $\bar{c}(\vec{r}', E')$ represents the average number of particles emitted per collision at energy E' along a line from points $\vec{r}$ to $\vec{r}'$. Again recall that without multiplication the meaning of the net number of particles emitted reduces to a modified survival probability of particles at energy E' a line from points $\vec{r}$ to $\vec{r}'$. Thus, without multiplication one would find the following expression:

$$\bar{c}(\vec{r}', E') = \overline{P}_{NA}(\vec{r}', E'). \tag{3.36}$$

By inspection it can be seen that the minimum value for $\bar{c}(\vec{r}', E')$ is bounded by the modified survival probability, and thus the minimum value of the state transition kernel normalization is merely the modified survival probability.

Thus, for the emission density FIESK one may define the normalization for the state transition kernel as follows:

$$\int K(s \to t)dt = \begin{cases} \bar{c}(\vec{r}', E') & \text{if multiplying media} \\ \overline{P}_{NA}(\vec{r}', E') & \text{otherwise.} \end{cases} \tag{3.37}$$

Collision Density State Transition Kernel

One may proceed in much the same manner for the collision density FIESK state transition kernel. To begin, equations 3.33 and 3.34 are substituted into Equation 3.31 and the resulting expression is integrated over all possible final states $t \in \Gamma$ to

yield:

$$\begin{aligned}\int L(s \to t)dt &= \int\int\int T(\vec{r}' \to \vec{r}, E, \hat{\Omega})C(\vec{r}', E' \to E, \hat{\Omega}' \to \hat{\Omega})dVdEd\hat{\Omega} \\ &= \int\int \left(\int T(\vec{r}' \to \vec{r}, E, \hat{\Omega})C(\vec{r}', E' \to E, \hat{\Omega}' \to \hat{\Omega})dV\right) dEd\hat{\Omega} \\ &= \int\int C(\vec{r}', E' \to E, \hat{\Omega}' \to \hat{\Omega})dEd\hat{\Omega} \\ &= c(\vec{r}', E'). \end{aligned} \tag{3.38}$$

For the collision density state transition kernel one recovers the average number of particles emitted per collision at point $\vec{r}'$ and energy E'. The case of no multiplication produces the expected result where the double integral over the collision kernel reduces to the survival probability. For the collision density FIESK one may define the normalization for the state transition kernel as follows:

$$\int L(s \to t)dt = \begin{cases} c(\vec{r}', E') & \text{if multiplying media} \\ P_{NA}(\vec{r}', E') & \text{otherwise.} \end{cases} \tag{3.39}$$

Survival Probability

In order to conduct the Monte Carlo random walk process, the PDFs for production, transition, and termination had various requirements detailed in Equation 2.9. One important requirement was the need for the survival probability to be equal to unity minus the probability of termination. This can be seen more clearly if one rearranges the equation to state that the sum of the probability of any transition and termination must be unity,

$$\int_\Gamma p(s \to t)dt + p(s) = 1. \tag{3.40}$$

When multiplying media is not present this property is observed. For example, in the case where there is no multiplication and one wishes to utilize the collision

density FIESK, the following terms could be defined:

$$\begin{aligned}\int_{\Gamma} p(s \to t)dt = \int L(s \to t)dt = P_{NA}(\vec{r}', E') = \frac{\Sigma_S(\vec{r}', E')}{\Sigma_T(\vec{r}', E')} \\ p(s) = \frac{\Sigma_A(\vec{r}', E')}{\Sigma_T(\vec{r}', E')} \\ \Sigma_T(\vec{r}', E') = \Sigma_A(\vec{r}', E') + \Sigma_S(\vec{r}', E') \\ \frac{\Sigma_S(\vec{r}', E')}{\Sigma_T(\vec{r}', E')} + \frac{\Sigma_A(\vec{r}', E')}{\Sigma_T(\vec{r}', E')} = 1. \end{aligned} \tag{3.41}$$

However, in the presence of multiplying media this behavior will no longer be preserved. This can be seen readily by the fact that $c(\vec{r}', E')$ and $\bar{c}(\vec{r}', E')$ are not bounded above by unity. Therefore, in the case of multiplication both the emission density and collision density state transition kernels will need to be multiplied by the ratio of the normalization constant with multiplication to the normalization constant without multiplication to maintain the necessary properties for the Monte Carlo random walk PDFs. That is to say, the emission density state transition kernel must be multiplied by

$$w_{em} = \frac{\overline{P}_{NA}(\vec{r}', E')}{\bar{c}(\vec{r}', E')}, \tag{3.42}$$

while the collision density state transition kernel must be multiplied by

$$w_{col} = \frac{P_{NA}(\vec{r}', E')}{c(\vec{r}', E')} \tag{3.43}$$

in order to maintain the required properties for the Monte Carlo random walk process.

In the next section it will be shown that the need to constantly modify weights for the treatment of multiplication is unnecessary if one treats the production of particles explicitly, generating and transporting each child particle as if it were a random walk.

3.4 Collision Kernel Expansion

In order to understand how sampling is handled internally, as well as to introduce the notion of explicit multiplication, the collision kernel will be expanded into its constituent components. Recall from Equation 3.24 that the collision kernel is the ratio of the double differential total macroscopic cross section to the total

macroscopic cross section as follows:

$$C(\vec{r}, E^{'} \rightarrow E, \hat{\Omega}^{'} \rightarrow \hat{\Omega}) = \frac{\Sigma_T(\vec{r}, E^{'} \rightarrow E, \hat{\Omega}^{'} \rightarrow \hat{\Omega})}{\Sigma_T(\vec{r}, E^{'})}.$$

To begin the expansion, the double differential total macroscopic cross section can be broken into the sum of the the individual double differential macroscopic cross sections. Here it is of use to recall our previous notation that one can write the double differential cross section as follows:

$$\Sigma(\vec{r}, E^{'} \rightarrow E, \hat{\Omega}^{'} \rightarrow \hat{\Omega}) = \Sigma(\vec{r}, E^{'}) f(\vec{r}, E^{'} \rightarrow E, \hat{\Omega}^{'} \rightarrow \hat{\Omega}) c(\vec{r}, E^{'}). \tag{3.44}$$

Where $\Sigma(\vec{r}, E^{'})$ is the cross section at point $\vec{r}$ and energy E', $f(\vec{r}, E^{'} \rightarrow E, \hat{\Omega}^{'} \rightarrow \hat{\Omega})$ is the probability that a particle at point $\vec{r}$ with energy E' and angle $\hat{\Omega}^{'}$ will transfer to an energy E and angle $\hat{\Omega}$, and $c(\vec{r}, E^{'})$ is the average number of particles produced at point $\vec{r}$ and energy E' for the reaction. Using equations 3.44 and 3.24 one can begin the expansion of the collision kernel as

$$C(\vec{r}, E^{'} \rightarrow E, \hat{\Omega}^{'} \rightarrow \hat{\Omega}) = \sum_i \frac{\Sigma_i(\vec{r}, E^{'}) f_i(\vec{r}, E^{'} \rightarrow E, \hat{\Omega}^{'} \rightarrow \hat{\Omega}) c_i(\vec{r}, E^{'})}{\Sigma_T(\vec{r}, E^{'})}, \tag{3.45}$$

where i denotes a specific reaction.

While this is advantageous in separating the various reactions out of the total reaction, it is not yet in a form that matches the underlying data. Cross section data is provided on a per isotope basis, allowing users to construct any material which is an amalgamation of supported isotopes. The next step in the expansion is then to separate out each isotope. This can be done by noting that the likelihood of any individual isotope being selected for a reaction is the total isotopic cross section divided by the total material cross section. That is to say, the probability of sampling a reaction from isotope j in a material can be written as

$$P(j) = \frac{\Sigma_{T,j}}{\Sigma_T}. \tag{3.46}$$

Due to the cross section behavior one must first delineate by isotope and then by reaction as follows:

$$C(\vec{r}, E^{'} \rightarrow E, \hat{\Omega}^{'} \rightarrow \hat{\Omega}) = \sum_j \frac{\Sigma_{j,T}(\vec{r}, E^{'})}{\Sigma_T(\vec{r}, E^{'})} \sum_i \frac{\sigma_{j,i}(E^{'})}{\sigma_{j,T}(E^{'})} c_{j,i}(E^{'}) p_{j,i}(E^{'} \rightarrow E, \hat{\Omega}^{'} \rightarrow \hat{\Omega}). \tag{3.47}$$

At this point the sampling methodology elegantly emerges from the mathematics. The collision kernel first selects an isotope j from the set of all possible isotopes J at point $\vec{r}$ and energy E'. Once the isotope is selected, a specific reaction i is selected from the set of all possible reactions for isotope j at energy E'. At this point, the average number of particles for reaction i of isotope j at energy E' is calculated, as is the transfer probability $p_{j,i}(E' \rightarrow E, \hat{\Omega}' \rightarrow \hat{\Omega})$ which captures the probability that a particle at energy E' and direction $\hat{\Omega}'$ undergoes a reaction i with isotope j and is transferred to energy E and direction $\hat{\Omega}$.

The only outstanding issue at this point is the sampling of the transition probability and the average number of emitted particles. For explicit treatment, only an integer number of particles can be emitted from any reaction, as particles must undergo a random walk. Due to this behavior, the transition probability and average number of emitted particles must also be expanded. For a given isotope j and reaction i one must correctly reproduce the average number of emitted particles for a large number of samples, but each individual sample must produce an integer number of particles. The following probabilities allow only integer sampling but preserve the average number of emitted particles $c_{j,i}(E')$:

$$\sum_{k=1}^{2} p_{j,i,k}(E') \sum_{l=1}^{x_k} p_{j,i,l}(E' \rightarrow E, \hat{\Omega}' \rightarrow \hat{\Omega}). \tag{3.48}$$

The first probability $p_{j,i,k}(E')$ captures the frequency with which the floor or ceiling of $c_{j,i}(E')$ is sampled as

$$p_{j,i,1} = \begin{cases} \lceil c_{j,i}(E') \rceil - c_{j,i}(E') & \text{if } c_{j,i}(E') \text{ non-integer value} \\ 1 & \text{otherwise} \end{cases} \tag{3.49}$$

$$p_{j,i,2} = 1 - p_{i,j,1}. \tag{3.50}$$

To go along with this, the upper limit x_k on the internal summation represents the sampled number of emitted particles. It can be described as follows:

$$x_1 = \begin{cases} \lfloor c_{j,i}(E') \rfloor & \text{if } c_{j,i}(E') \text{ non-integer value} \\ c_{j,i}(E') & \text{otherwise} \end{cases} \tag{3.51}$$

$$x_2 = \lceil c_{j,i}(E') \rceil. \tag{3.52}$$

At this point it is possible to verify that $c_{j,i}(E')$ is preserved using these expressions

assuming $c_{j,i}(E')$ is not an integer as that case can be confirmed by inspection. The following proof shows that the value c is recovered using the probabilities defined in equations 3.50 and 3.48:

$$\begin{aligned} p_{j,i,1}x_1 + p_{j,i,2}x_2 &= (\lceil c \rceil - c)\lfloor c \rfloor + (1 + c - \lceil c \rceil)\lceil c \rceil \\ &= \lceil c \rceil (1 + c - \lceil c \rceil + \lfloor c \rfloor) - c\lfloor c \rfloor \\ &= c\lceil c \rceil - c\lfloor c \rfloor \\ &= c(\lceil c \rceil - \lfloor c \rfloor) \\ &= c. \end{aligned} \tag{3.53}$$

The second probability $p_{j,i,l}(E' \to E, \hat{\Omega}' \to \hat{\Omega})$ captures the explicit production of x_k particles from the known transfer probabilities for reaction i with isotope j at energy E' and angle $\hat{\Omega}'$. The fully expanded collision kernel can be seen in Equation 3.54:

$$\begin{aligned} C(\vec{r}, E' \to E, \hat{\Omega}' \to \hat{\Omega}) = \sum_j \frac{\Sigma_{j,T}(\vec{r}, E')}{\Sigma_T(\vec{r}, E')} \sum_i \frac{\sigma_{j,i}(E')}{\sigma_{j,T}(E')} \sum_{k=1}^{2} p_{j,i,k}(E') \cdot \\ \sum_{l=1}^{x_k} p_{j,i,l}(E' \to E, \hat{\Omega}' \to \hat{\Omega}). \end{aligned} \tag{3.54}$$

Sampling Routine

The expansion of the collision kernel intrinsically provides the procedure for explicitly sampling particles in the Monte Carlo random walk process.

1. The first variable sampled is the isotope or nuclide with which the particle interacts, the probability of which is the ratio of the nuclide total cross section to the material total cross section. This provides the following PDF for nuclide sampling:
$$p(j|\, \vec{r}, E') = \sum_j \frac{\Sigma_{j,T}(\vec{r}, E')}{\Sigma_T(\vec{r}, E')}. \tag{3.55}$$

2. Once the isotope has been selected, the reaction must be selected from all possible reactions with isotope j at energy E'. The probability of this event is the ratio of the cross section for reaction i of isotope j to the total cross section

for isotope j. The following PDF is utilized for reaction sampling:

$$p(i|\, j, E') = \sum_i \frac{\sigma_{j,i}(E')}{\sigma_{j,T}(E')}. \tag{3.56}$$

3. At this point the number of emitted particles is sampled using the previously defined probabilities in Equation 3.50. A PDF can be constructed from these probabilities as follows:

$$p(x_k|\, j, i, E') = \sum_k p_{j,i,k}(E'). \tag{3.57}$$

4. Finally, for each emitted particle the outgoing particle state $(E, \hat{\Omega})$ is sampled from the transfer probabilities $p_{j,i,l}(E' \rightarrow E, \hat{\Omega}' \rightarrow \hat{\Omega})$.

In this way both the generation of child particles and the termination of particles is handled explicitly. There is no need for an additional termination PDF, as an absorption event will produce no emitted particles and thus the termination probability is already considered. Further, child particles will be treated explicitly and will have to be tracked as random walks as well.

3.5 Estimation of Quantities of Interest

As was stated in Chapter 2, the end goal of the Monte Carlo process is to construct an estimate of a response I which is the inner product of the unknown solution to the FIESK and some known response function. While this was treated very generally in the previous chapter, it will now be handled more specifically in relation to the estimation of nuclear quantities of interest.

The most natural assumption of which unknown quantity to use in the inner product would be the angular flux, as this is a physical quantity that is often convolved with cross sectional data to give estimations of reaction rates, heating, energy deposition, etc. Yet the previous derivation of the angular flux FIESK suggests that it is difficult and inefficient to attempt to sample the flux directly. For this reason it is important to find a method for approximating a response I using either the emission density or collision density, but which is still equivalent to the expected

response using the angular flux. Mathematically this equivalence may be stated as:

$$I = \int\int\int a(\vec{r}, E, \hat{\Omega})\varphi(\vec{r}, E, \hat{\Omega})dVdEd\hat{\Omega} \tag{3.58}$$

$$= \int\int\int b(\vec{r}, E, \hat{\Omega})\chi(\vec{r}, E, \hat{\Omega})dVdEd\hat{\Omega} \tag{3.59}$$

$$= \int\int\int c(\vec{r}, E, \hat{\Omega})\psi(\vec{r}, E, \hat{\Omega})dVdEd\hat{\Omega}. \tag{3.60}$$

Here $a(\vec{r}, E, \hat{\Omega})$, $b(\vec{r}, E, \hat{\Omega})$, and $c(\vec{r}, E, \hat{\Omega})$ are known functions. Typically $a(\vec{r}, E, \hat{\Omega})$ is selected by the user to estimate a specific quantity of interest. For example, if the flux is desired the value is unity, and if one wishes for an estimation of the reaction rate the value will be the energy dependent macroscopic cross section. The values for $b(\vec{r}, E, \hat{\Omega})$ and $c(\vec{r}, E, \hat{\Omega})$ can be determined through the previously defined relationships in equations 3.17 and 3.28 respectively.

For the emission density relation in Equation 3.17 the value of $b(\vec{r}, E, \hat{\Omega})$ is found to be:

$$b(\vec{r}, E, \hat{\Omega}) = \int \frac{a(\vec{r}', E, \hat{\Omega})}{\Sigma_T(\vec{r}', E)} T(\vec{r} \to \vec{r}', E, \Omega)dV'. \tag{3.61}$$

Similarly for the collision density relation in Equation 3.28 the value of $c(\vec{r}, E, \hat{\Omega})$ is found to be:

$$c(\vec{r}, E, \hat{\Omega}) = \frac{a(\vec{r}, E, \hat{\Omega})}{\Sigma_T(\vec{r}, E)}. \tag{3.62}$$

By inspection it is significantly easier to conduct the quotient in Equation 3.62 as opposed to the general integral of a potentially complicated function in Equation 3.61. For this reason the collision density is advantageous. Not only is it capable of being readily sampled using the Monte Carlo random walk process without variance issues like the angular flux, it also is capable of estimating flux-like responses with a very simple conversion that does not require numerical integration.

The Track-Length Estimator

One of the most ubiquitous estimators is the track-length flux estimator. The track-length estimator is beneficial as any time a particle interacts with the region of interest Γ_h, the estimator is able to acquire information. A full derivation of the track-length estimator can be found in the text by Spanier and Gelbard, but a brief explanation of its origins will be provided below [8].

For simplicity this explanation will handle the notion of scalar flux, but it should

be noted that the derivation is extensible to other quantities of interest. The quantity of interest will be an estimation of the average scalar flux ϕ in some volume V. one may write the expression for the average scalar flux as follows:

$$\overline{\phi}_V = \frac{1}{V}\int\int\int \phi(\bar{r}, E, t)\,dE\,dt\,dV. \tag{3.63}$$

Recalling that the scalar flux may also be written as the product of the particle velocity and number density Equation 3.63 can be converted to:

$$\overline{\phi}_V = \frac{1}{V}\int\int\int \nu \cdot N(\bar{r}, E, t)\,dE\,dt\,dV. \tag{3.64}$$

As the neutron velocity ν is known, the time dependence can be converted to track-length dependence as $dt = (1/\nu)ds$ where s is the track-length or the distance traveled along the direction of transport. Thus the updated form in terms of track-length may be written as:

$$\overline{\phi}_V = \frac{1}{V}\int\int\int N(\bar{r}, E, s)\,dE\,ds\,dV. \tag{3.65}$$

It should be noted that this modifies the meaning of $N(\bar{r}, E, s)$ from being the particle density to being the track-length density.

In the context of a Monte Carlo simulation with a finite number of random walks, this integral will be approximated by a series of sums. Track-length density can also be approximated for each particle as the total track-length contributed by that particle divided by the volume V. Then the total track-length density is the sum of all particle track-length densities divided by the total number of particles. It must be assumed that an individual particle track-length is calculated as a sum of all sub-tracks which pass through the volume V as

$$x_i = \sum_t T_{i,t} w_{i,t}, \tag{3.66}$$

where $T_{i,t}$ is the sub-track track-length for sub-track t and particle i and $w_{i,t}$ is the associated particle weight for the aforementioned sub-track. Figure 3.1 depicts a single particle track-length which consists of a series of sub-tracks which interact with the volume V.

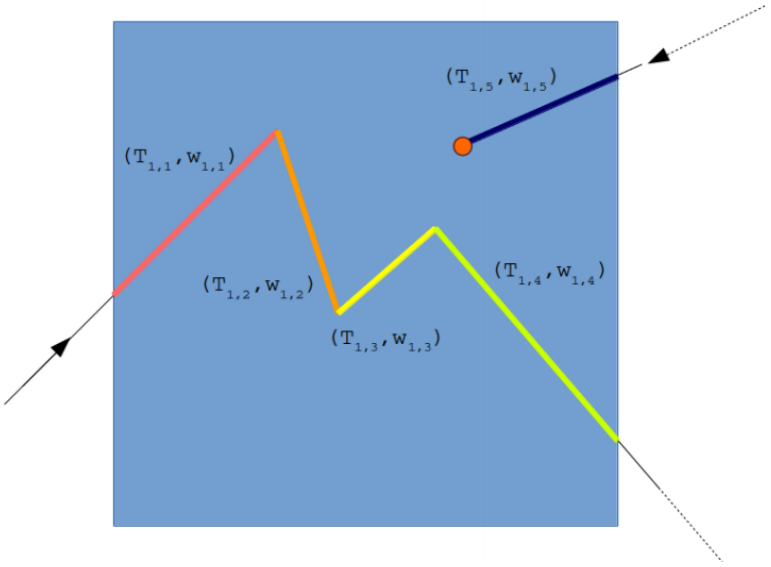

Figure 3.1: **Track-length flux estimator contribution.** *The contribution of an individual particle to the estimation of the track-length scalar flux in volume V is the sum of the individual sub-track contributions, each of which is the product of the track-length of the sub-track contained within V and the particle weight during that sub-track.*

Once the sub-tracks are combined to give a score for the particle, the particle scores x_i may be combined to provide an estimate for the scalar flux in the volume V as

$$\begin{aligned}\overline{\phi}_V &= \frac{1}{N}\sum_i \frac{x_i}{V} \\ &= \frac{1}{NV}\sum_i x_i \\ &= \frac{1}{NV}\sum_i \sum_j T_{i,j} w_{i,j}.\end{aligned} \tag{3.67}$$

At this point an estimation of ϕ in the volume of interest V has been obtained.

Another useful quantity along with the estimate of ϕ is the uncertainty in the estimate. As the estimate of the flux is calculated as the mean of the individual particle contributions, the relative error of the mean is defined as the standard error

of the mean normalized to the mean. Thus the relative error may be written as

$$\begin{aligned} R^2 &= \left(\frac{S_{\overline{x}}}{\overline{x}}\right)^2 \\ &= \frac{1}{N}\left(\frac{S_x}{\overline{x}}\right)^2 \\ &= \frac{1}{N}\left(\frac{\overline{x^2} - \overline{x}^2}{\overline{x}^2}\right) \\ &= \frac{\sum_{i=1}^{N} x_i^2}{\left(\sum_{i=1}^{N} x_i\right)^2} - \frac{1}{N} \\ \therefore \quad R &= \sqrt{\frac{\sum_{i=1}^{N} x_i^2}{\left(\sum_{i=1}^{N} x_i\right)^2} - \frac{1}{N}}. \end{aligned} \tag{3.68}$$

While this is a derivation of a specific case of the track-length estimator, it should provide a general understanding for how the track-length estimator interacts with the region of interest and is able to add information at each interaction. The derivation provided by Spanier and Gelbard is much more in depth and is worth following for any reader who wishes for a more fundamental understanding of how the track-length estimator is derived and is related to the event estimator [8].

3.6 Chapter Summary

This chapter covered a great deal of information and as such a brief overview will be of assistance before proceeding to the following discussions.

- While the integro-differential transport equation is the most common form, for the application of the Monte Carlo random walk process it must be transformed into an integral equation which can be modified into a FIESK depending on the chosen variable.
- The FIESK for the angular flux is easy to conceptually grasp, but it is sub-optimal in terms of the calculational work associated with source sampling as well as the possibility for unchecked growth in particle weights during transport which yields increased estimator variance.
- Two other FIESKS were proposed for the collision density and emission density respectively. Each of these has been deconstructed into a transport kernel

which handles particle transport at a given energy and direction, and a collision kernel which handles the energy and angular transfer at a given location.

- Deconstruction of the collision kernel yields the ability to explicitly model particles produced during transport, as well as informs the general schema for sampling reactions and updating particle states throughout the random walk.
- Estimations of responses can be calculated utilizing the emission density and collision density. Further, relations were found to allow for a response function on the flux to be converted to a response function on the emission and collision densities. It was found that the collision density conversion is significantly more straightforward and is thus the preferred variable for random walks.
- The track-length estimator is a ubiquitous estimator which allows for information to be collected each time an entity interacts with the region of interest.

Chapter 4

Adjoint Radiation Transport Theory

In Chapter 2 a discussion of the dual of the fiesk was introduced in an event to handle the situation where the region of interest over which the response function exists shrinks to a point. The goal of this chapter is to familiarize the reader with the salient features of adjoint transport in relation to forward radiation transport. The end result of this discussion will be an understanding of how the cross section and transfer probabilities for adjoint transport are related to those for forward transport. For this one must analyze the transport and collision kernels for the various FIESKs.

4.1 The Adjoint

The adjoint of any linear operator may be defined generally, but for the discussion herein one should refer to the following definition:

$$\int v(t) \int k(t' \to t) w(t') dt' dt = \int w(t) \int k^{\dagger}(t' \to t) v(t') dt' dt, \tag{4.1}$$

where $v(t)$ and $w(t)$ are arbitrary functions with $k(t' \to t)$ defined as a state transition kernel. If this is the case, then the expression $k^{\dagger}(t' \to t)$ is defined as the adjoint of the state transition kernel $k(t' \to t)$ [23]. If one proceeds to interchange the variables of integration on either the LHS or the RHS, one can find the following relationship between the kernel and its adjoint:

$$k^{\dagger}(t' \to t) = k(t \to t'). \tag{4.2}$$

This provides a physical intuition into the behavior of the adjoint state transition kernel which is merely the forward state transition kernel operating from final state to initial state.

While this expression is useful for the general definition of the adjoint, it will be of use to define the adjoint of a more helpful property. Recall the definition of the emission density FIESK provided in Equation 3.27. One may modify this equation

to define a linear operator H which satisfies the following equation:

$$H\cdot\chi(\vec{r},E,\hat{\Omega}) = \chi(\vec{r},E,\hat{\Omega}) - \iiint C(\vec{r},E^{'}\rightarrow E,\hat{\Omega}^{'}\rightarrow\hat{\Omega})T(\vec{r}^{'}\rightarrow\vec{r},E^{'},\hat{\Omega}^{'})\chi(\vec{r}^{'},E^{'},\hat{\Omega}^{'})dV^{'}dE^{'}d\hat{\Omega}^{'}, \tag{4.3}$$

and thus

$$H\cdot\chi(\vec{r},E,\hat{\Omega}) = S(\vec{r},E,\hat{\Omega}). \tag{4.4}$$

At this point one may define the adjoint of the operator H by maintaining the following equality:

$$\iiint \left(\chi^{\dagger}H\cdot\chi\right) dVdEd\hat{\Omega} = \iiint \left(\chi H^{\dagger}\cdot\chi^{\dagger}\right) dVdEd\hat{\Omega}. \tag{4.5}$$

For the time being the unknown expression on the LHS, $\chi^{\dagger}$, will be defined as the adjoint of the emission density. Yet there is still no physical interpretation of the adjoint operator $H^{\dagger}$ or the interaction between the adjoint operator and the adjoint of the emission density.

By expanding the LHS of Equation 4.5 one obtains the following expression:

$$\begin{aligned}\iiint \left(\chi^{\dagger}H\cdot\chi\right) dVdEd\hat{\Omega} &= \iiint \chi^{\dagger}(\vec{r},E,\hat{\Omega})\chi(\vec{r},E,\hat{\Omega})dVdEd\hat{\Omega} \\ &- \iiint\iiint \chi^{\dagger}(\vec{r}',E',\hat{\Omega}'')\chi(\vec{r}',E',\hat{\Omega}'')C(\vec{r},E^{'}\rightarrow E,\hat{\Omega}^{'}\rightarrow\hat{\Omega}) \\ &T(\vec{r}^{'}\rightarrow\vec{r},E^{'},\hat{\Omega}^{'})dV^{'}dE^{'}d\hat{\Omega}^{'}dVdEd\hat{\Omega}.\end{aligned} \tag{4.6}$$

It can be observed that the order of χ and $\chi^{\dagger}$ may be interchanged in the previous equation and thus one could rewrite the equation as:

$$\iiint \left(\chi^{\dagger}H\cdot\chi\right) dVdEd\hat{\Omega} = \iiint \chi(\vec{r},E,\hat{\Omega}) \left[\chi^{\dagger}(\vec{r},E,\hat{\Omega})dVdEd\hat{\Omega} - \iiint \chi^{\dagger}(\vec{r}',E',\hat{\Omega}')C(\vec{r}',E\rightarrow E',\hat{\Omega}\rightarrow\hat{\Omega}')T(\vec{r}\rightarrow\vec{r}',E,\hat{\Omega})dV'dE^{'}d\hat{\Omega}^{'}\right] dVdEd\hat{\Omega}. \tag{4.7}$$

It should be noted that in order to extract χ from the second term, a change in variables from primed to unprimed was required. From this expression the natural

definition for the adjoint operator $H^\dagger$ takes the form:

$$H^\dagger \cdot \chi^\dagger(\vec{r}, E, \hat{\Omega}) = \chi^\dagger(\vec{r}, E, \hat{\Omega}) - \int\int\int \chi^\dagger(\vec{r}', E', \hat{\Omega}') C(\vec{r}', E \to E', \hat{\Omega} \to \hat{\Omega}') T(\vec{r} \to \vec{r}', E, \hat{\Omega}) dV' dE' d\hat{\Omega}'. \quad (4.8)$$

At this point one may proceed with a derivation in line with what was done previously for the forward case in Chapter 3. First one makes an assumption regarding the behavior of the adjoint operator $H^\dagger$ operating on the adjoint of the emission density $\chi^\dagger$, which must be equal to $c(\vec{r}, E)$ from Equation 3.61. At this point one again uses the method of characteristics to convert the problem to a first order ODE and continue with integration [23]. The final result is the dual emission density FIESK of the form:

$$\chi^\dagger(\vec{r}, E, \hat{\Omega}) = c(\vec{r}, E, \hat{\Omega}) + \int\int\int \Sigma_T(\vec{r}', E \to E', \hat{\Omega} \to \hat{\Omega}') \tau(\vec{r}', \vec{r}, E, -\hat{\Omega}) dV' dE' d\hat{\Omega}' \quad (4.9)$$

Note that the same general procedure may be followed for the collision density and a very similar expression will be found.

What is of interest in these expressions is the behavior of the FIESK. Comparing Equation 4.9 to Equation 3.18 one sees a striking number of similarities. Primarily, the issue of allowing interactions to occur in vacuum regions appears again. For these reasons Hoogenboom describes the adjoint of the emission density as a "flux-like" quantity, and thus the sampling of the adjoint of the emission density is not ideal. The same arguments apply for the adjoint of the collision density. In order to truly sample adjoint transport, one must derive the adjoint emission density and adjoint collision density from the adjoint transport equation [23].

4.2 The Adjoint Transport Equation

The adjoint integro-differential and integral transport equations are described briefly herein.

The Adjoint Integro-Differential Transport Equation

Using the same logic as before, one may define an operator G which captures the behavior of the integro-differential transport behavior from Equation 3.1 that obeys

the following expression:

$$G \cdot \varphi(\vec{r}, E, \hat{\Omega}) = S(\vec{r}, E, \hat{\Omega}). \tag{4.10}$$

Applying the definition of the adjoint from Equation 4.5 one may write the analogous statement

$$\begin{aligned} &\int\int\int \varphi^{\dagger}(\vec{r}, E, \hat{\Omega}) G(\vec{r}, E, \hat{\Omega}) \varphi(\vec{r}, E, \hat{\Omega}) dV dE d\hat{\Omega} = \\ &\qquad \int\int\int \varphi(\vec{r}, E, \hat{\Omega}) G^{\dagger}(\vec{r}, E, \hat{\Omega}) \varphi^{\dagger}(\vec{r}, E, \hat{\Omega}) dV dE d\hat{\Omega}, \end{aligned} \tag{4.11}$$

where $\varphi^{\dagger}$ is defined as the adjoint angular flux, or simply the adjoint flux. A full derivation of the adjoint transport equation can be found in various resources, but the discussion in *Computational Methods of Neutron Transport* is both clear and concise and is suggested by this author [5].

Similar to what was done for the adjoint of the emission density, the adjoint operator acting on the adjoint flux will be set equal to the response function $a(\vec{r}, E, \hat{\Omega})$ from Equation 3.58 in order to maintain the following property when calculating the quantity of interest, I:

$$\begin{aligned} I &= \int\int\int \varphi^{\dagger}(\vec{r}, E, \hat{\Omega}) G(\vec{r}, E, \hat{\Omega}) \varphi(\vec{r}, E, \hat{\Omega}) dV dE d\hat{\Omega} \\ &= \int\int\int \varphi^{\dagger}(\vec{r}, E, \hat{\Omega}) S(\vec{r}, E, \hat{\Omega}) dV dE d\hat{\Omega} \\ &= \int\int\int \varphi(\vec{r}, E, \hat{\Omega}) G^{\dagger}(\vec{r}, E, \hat{\Omega}) \varphi^{\dagger}(\vec{r}, E, \hat{\Omega}) dV dE d\hat{\Omega} \\ &= \int\int\int \varphi(\vec{r}, E, \hat{\Omega}) a(\vec{r}, E, \hat{\Omega}) dV dE d\hat{\Omega}. \end{aligned} \tag{4.12}$$

Physically this requires that the inner product of the angular flux and the response function is equivalent to the inner product of the adjoint angular flux and the source function. The end result of the derivation is the adjoint integro-differential transport equation as follows [5]:

$$\begin{aligned} &-\hat{\Omega} \cdot \vec{\bigtriangledown} \varphi^{\dagger}(\vec{r}, E, \hat{\Omega}) + \Sigma_T(\vec{r}, E) \varphi^{\dagger}(\vec{r}, E, \hat{\Omega}) = \\ &\qquad a(\vec{r}, E, \hat{\Omega}) + \int\int \Sigma_T(\vec{r}, E \rightarrow E', \hat{\Omega} \rightarrow \hat{\Omega}') \varphi^{\dagger}(\vec{r}, E', \hat{\Omega}') dE' d\hat{\Omega}'. \end{aligned} \tag{4.13}$$

The adjoint integro-differential transport equation may also be converted to an integral form such that FIESKs may be developed for newly defined variables like

the adjoint emission density and the adjoint collision density. In an analogy to the forward case, the RHS of Equation 4.13 will be defined as the **adjoint emission density**:

$$\theta^{\dagger}(\vec{r}, E, \hat{\Omega}) = a(\vec{r}, E, \hat{\Omega}) + \int\int \Sigma_T(\vec{r}, E \to E', \hat{\Omega} \to \hat{\Omega}')\varphi^{\dagger}(\vec{r}, E', \hat{\Omega}')dE'd\hat{\Omega}'. \quad (4.14)$$

The Adjoint Integral Transport Equation

At this point the derivation proceeds in the same way as the forward case, with the application of the method of characteristics and solution of the resulting first order ODE with an integrating factor [23]. The end result is that one finds the simplified integral adjoint transport equation of the form:

$$\varphi^{\dagger}(\vec{r}, E, \hat{\Omega}) = \int \theta^{\dagger}(\vec{r}', E, \hat{\Omega})\tau^{\dagger}(\vec{r}', \vec{r}, E, \hat{\Omega})dV'. \quad (4.15)$$

where

$$\tau^{\dagger}(\vec{r}', \vec{r}, E, \hat{\Omega}) = \tau(\vec{r}', \vec{r}, E, -\hat{\Omega}). \quad (4.16)$$

4.3 Definition of the Transport FIESKs

In an analogy to the forward case, one can now define FIESKs for the adjoint emission density and the adjoint collision density. The goal of this exercise is to find an expression for the adjoint collision kernel which can be expanded as was done in the forward case. This will yield important information relating adjoint transport properties to forward transport properties which are known.

The Adjoint Emission Density FIESK

The adjoint emission density FIESK is obtained by substituting Equation 4.15 into Equation 4.14.

$$\begin{aligned}\theta^{\dagger}(\vec{r}, E, \hat{\Omega}) = a(\vec{r}, E, \hat{\Omega}) \\ + \int\int \Sigma_T(\vec{r}, E \to E', \hat{\Omega} \to \hat{\Omega}') \int \theta^{\dagger}(\vec{r}', E', \hat{\Omega}')\tau^{\dagger}(\vec{r}', \vec{r}, E', \hat{\Omega}')dV'dE'd\hat{\Omega}'\end{aligned} \quad (4.17)$$

In order to determine a transport and collision kernel, the integrand must be manipulated by multiplying and dividing by the ratio:

$$W^{\dagger}(\vec{r}, E') = \frac{\int\int \Sigma_T(\vec{r}, E \to E', \hat{\Omega} \to \hat{\Omega}')dEd\hat{\Omega}}{\Sigma_T(\vec{r}, E')} = \frac{\Sigma^{\dagger}(\vec{r}, E')}{\Sigma_T(\vec{r}, E')}, \tag{4.18}$$

where $\Sigma^{\dagger}(\vec{r}, E')$ is referred to as the total adjoint cross section. The expression $W^{\dagger}$ is referred to as the adjoint weight factor, and it is in general not equal to unity [23].

At this point one may define the transport and collision kernels as was done for the forward case to obtain the following expressions:

$$T^{\dagger}(\vec{r}' \to \vec{r}, E, \hat{\Omega}) = \Sigma_T(\vec{r}, E) \exp\left[-\int_0^{|\vec{r}'-\vec{r}|} \Sigma_T(\vec{r} + R'\hat{\Omega}, E)dR'\right] \frac{\delta\left(\hat{\Omega} - \left[\frac{\vec{r}'-\vec{r}}{|\vec{r}'-\vec{r}|}\right]\right)}{|\vec{r}' - \vec{r}|^2}, \tag{4.19}$$

and

$$C^{\dagger}(\vec{r}, E' \to E, \hat{\Omega}' \to \hat{\Omega}) = \frac{\Sigma_T(\vec{r}, E \to E', \hat{\Omega} \to \hat{\Omega}')}{\Sigma^{\dagger}(\vec{r}, E')} \tag{4.20}$$

for the transport and collision kernels respectively [18]. Thus, the FIESK for the adjoint emission density may be written as:

$$\theta^{\dagger}(\vec{r}, E, \hat{\Omega}) = a(\vec{r}, E, \hat{\Omega}) + \int\int W^{\dagger}(\vec{r}, E')C^{\dagger}(\vec{r}, E' \to E' \hat{\Omega}' \to \hat{\Omega}) T^{\dagger}(\vec{r}' \to \vec{r}, E', \hat{\Omega}')dV'dE'd\hat{\Omega}'. \tag{4.21}$$

The Adjoint Collision Density FIESK

Utilizing the same definitions as from the adjoint emission density FIESK as well as the procedures from the derivation of the forward collision density FIESK, the adjoint collision density FIESK may be readily derived. For the sake of brevity this derivation has been intentionally left out but can be produced upon request.

4.4 Adjoint Collision Kernel Expansion

While it is of importance to understand the mathematics behind the adjoint physics at play in radiation transport, the point of this chapter is to determine the relationship

between the adjoint transport properties and the forward transport properties. If one can tie the adjoint transport properties to known forward properties, then the adjoint cross sections and transfer probabilities can be readily constructed. The expansion of the adjoint collision kernel will provide the necessary relationships for calculating the adjoint cross section and transfer probabilities.

From equations 4.18 and 4.20 one may expand the adjoint collision kernel. As was done in the forward case, the adjoint collision kernel will be expanded first by nuclide, then by reaction, and finally by outgoing particle state.

$$\begin{aligned} C^{\dagger}(\vec{r}, E^{'} \rightarrow E, \hat{\Omega}^{'} \rightarrow \hat{\Omega}) &= \frac{\Sigma_T(\vec{r}, E \rightarrow E^{'}, \hat{\Omega} \rightarrow \hat{\Omega}^{'})}{\Sigma^{\dagger}(\vec{r}, E^{'})} \\ &= \sum_j \frac{\Sigma_j^{\dagger}(\vec{r}, E^{'})}{\Sigma^{\dagger}(\vec{r}, E^{'})} \sum_i \frac{\sigma_{j,i}^{\dagger}(E^{'})}{\sigma_{j,T}^{\dagger}(E^{'})} \left(\frac{\sigma_{j,i}(E) c_{j,i}(E) p_{j,i}(E \rightarrow E', \hat{\Omega} \rightarrow \hat{\Omega}')}{\sigma_{j,i}^{\dagger}(E')} \right) \end{aligned} \tag{4.22}$$

This now allows one to define the probabilities of various events occurring. For example, one may define the probability of sampling isotope j from the set of isotopes at location $\vec{r}$ and energy E' as:

$$p_j^{\dagger}(\vec{r}, E') = \frac{\Sigma_j^{\dagger}(\vec{r}, E')}{\Sigma^{\dagger}(\vec{r}, E')}. \tag{4.23}$$

Once the isotope has been selected, one may describe the likelihood of selecting reaction i from the set of all possible reactions for isotope j at location $\vec{r}$ and energy E' as:

$$p_{j,i}^{\dagger}(E' \mid \vec{r}, j) = \frac{\sigma_{j,i}^{\dagger}(E')}{\sigma_{j,T}^{\dagger}(E')}. \tag{4.24}$$

Finally, the probability that the particle exiting an adjoint collision at some energy E and direction $\hat{\Omega}$ may be written as:

$$p_{j,i}^{\dagger}(E \rightarrow E', \hat{\Omega} \rightarrow \hat{\Omega}' \mid \vec{r}, j, i) = \frac{\sigma_{j,i}(E) c_{j,i}(E) p_{j,i}(E \rightarrow E', \hat{\Omega} \rightarrow \hat{\Omega}')}{\sigma_{j,i}^{\dagger}(E')}. \tag{4.25}$$

One can further define the denominator of Equation 4.25 to be as follows:

$$\sigma_{j,i}^{\dagger}(E') = \int\int \sigma_{j,i}(E) c_{j,i}(E) p_{j,i}(E \rightarrow E', \hat{\Omega} \rightarrow \hat{\Omega}') dE d\hat{\Omega}, \tag{4.26}$$

such that the transfer probability is normalized to unity.

The results from equations 4.25 and 4.26 are invaluable, as they provide a functional relationship between the unknown adjoint cross sections and transfer probabilities, and the known forward cross sections and transfer probabilities. Thus, the adjoint data can be calculated from known forward data. This will be incredibly important in developing the adjoint data for elastic and inelastic level scattering, as well as the free gas and $S(\alpha, \beta)$ adjoint methods. However, Chapter 7 will discuss how these physics change in the presence of mobile background media.

4.5 Chapter Summary

While this chapter was significantly shorter than the previous chapter, it accomplished a few key goals as shown below:

- Taking the dual of the emission density or collision density FIESKs from the forward transport model produces a "flux-like" result which suffers from difficult source sampling and the sampling of reactions in voided areas. Thus it is not suggested that this method be employed.
- An adjoint form of the integro-differential and integral transport equation can be derived and utilized to generate adjoint fiesks for new quantities.
- FIESKs can be derived for the newly defined adjoint emission density and adjoint collision density. Further, the transport and collision kernels may also be found and are related to expressions found in the forward case.
- Expanding the adjoint collision kernel suggests a manner of sampling and transporting particles in the same manner as the forward case. Further, the expansion provides equations 4.25 and 4.26 which allow one to determine the unknown adjoint cross sections and transfer probabilities from existing forward data.

Chapter 5

Neutron Transport and Sampling Techniques

To this point in the report, the discussion has been focussed on the generalized processes for applying the Monte Carlo random walk process to radiation transport. In this chapter, application to specific neutron transport mechanisms will be explored. The ENDF manual is of utmost importance in understanding the mechanisms of neutron transport, their mathematical modeling, and the sampling routines that correctly reproduce the expected physical behavior.

5.1 Forward Elastic and Inelastic Level Scattering

When attempting to address neutron transport, the simplest reactions to begin with are the forward elastic and inelastic level scattering. In elastic scattering the neutron interacts with the nucleus, and the internal state of the nucleus remains unchanged. This produces what is often referred to as *billiard ball* scattering, where two particles scatter in the very straight-forward kinematic sense. In inelastic level scattering the target nucleus exits the reaction with an excited internal state E^*. Thus, some portion of the incoming kinetic energy will be stored in the excited state of the target nucleus. It can be seen that the case of elastic scattering is actually a specialization of inelastic level scattering wherein the target nucleus emerges in the ground state and with an excitation energy E^* is zero. As it is very difficult, both theoretically and computationally, to model the interactions between a neutron and a nucleus with regards to inelastic level scattering, the tabulated data from ENDF (specifically the B-VII.1 library) are utilized [15]. These tables provide the user with a set of outgoing neutron states for a large range of incoming neutron energies.

From the ENDF/B-VII.1 manual, the angular distribution for elastic and inelastic level neutron scattering can be expressed as normalized PDFs:

$$p(\mu, E') = \frac{2\pi}{\sigma(E')}\sigma(\mu, E'), \tag{5.1}$$

where

$$\int_{-1}^{1} p(\mu, E')d\mu = 1. \tag{5.2}$$

Typically the angular distribution will be provided in a tabular form, but it may also be given as a series of Legendre polynomials of the form

$$p(\mu, E') = \sum_{l=0}^{N} \frac{2l+1}{2} a_l(E') P_l(\mu). \tag{5.3}$$

Another complication is that the outgoing angle cosine (μ) over which the data is tabulated can be given in the laboratory frame or the center of mass (CM) frame. This is expected to be the CM frame, but it must be accounted for internally that both reference frames are distinct possibilities and one must be able to accurately transpose between them. The actual method of sampling the outgoing neutron angle is the 2-D tabular selection method from the MCNP team [26]. The goal of this method is to determine the upper and lower bin boundaries for the incoming neutron energy, and then to randomly sample the calculated CDF to determine outgoing angle at each of these and interpolate between them based on the interpolation fraction. Note that the ENDF/B-VII.1 manual does discuss what interpolation schemes are valid for interpolating the two dimensional datasets [15].

Once the outgoing angle cosine has been sampled, it is important to be able to calculate the lab frame angle cosine. This can be done using simple kinematics as shown in appendix B. The outgoing lab frame angle cosine can thus be written as [23]

$$\mu_L = \frac{A\sqrt{1 - \left(\frac{A+1}{A}\right)\frac{E^*}{E'}}\mu_{CM} + 1}{\sqrt{A^2\left[1 - \left(\frac{A+1}{A}\right)\frac{E^*}{E'}\right] + 2A\mu_{CM}\sqrt{1 - \left(\frac{A+1}{A}\right)\frac{E^*}{E'}} + 1}}, \tag{5.4}$$

where

$$A = \frac{M}{m_n}$$

is the nuclear mass ratio.

It should also be noted that for two-body kinematics there is a one-to-one correspondence between outgoing energy and angle in forward reactions. That is to say, once the outgoing angle is determined, the outgoing energy is fixed to satisfy the energetics of the reaction. The derivation in appendix B contains an expression for

the outgoing lab energy in terms of the incoming lab energy and the CM scattering angle cosine μ_{CM}. The expression is as follows:

$$E = E' \left[\frac{A^2 \left(1 - \left(\frac{A+1}{A}\right)\frac{E^*}{E'}\right) + 2A\mu_{CM}\left(1 - \left(\frac{A+1}{A}\right)\frac{E^*}{E'}\right)^{1/2} + 1}{(A+1)^2} \right]. \quad (5.5)$$

Note that the minimum and maximum allowable outgoing energies are found when the center of mass scattering angle cosine μ_{CM} achieves the minimum and maximum values of -1 and 1 respectively. Thus the outgoing neutron energy for inelastic level scattering is bounded as:

$$\left(\frac{A\sqrt{1 - \left(\frac{A+1}{A}\right)\frac{E^*}{E}} - 1}{A+1}\right)^2 E' \leqslant E \leqslant \left(\frac{A\sqrt{1 - \left(\frac{A+1}{A}\right)\frac{E^*}{E}} + 1}{A+1}\right)^2 E'. \quad (5.6)$$

5.2 Forward Absorption Reactions

In forward absorption reactions, a neutron enters a reaction with a nucleus and is absorbed into that nucleus. This results in the production of a metastable state for the target nuclei which eventually emits another particle via a relaxation process. Common outgoing particle types in neutron simulations are photons, protons, alpha particles, and other atomic nuclei. In these reactions the outgoing state of the newly produced particle is sampled according to the known outgoing energy and angular distributions associated with the incoming neutron energy E'. If these reactions and their outgoing PDFs are present in the ENDF/ACE tables, they can be modeled and handled in FRENSIE. Absorption reactions can also produce neutrons, such as from multiplication reactions, or even neutrons alongside other particles, such as fission or complex multiplication reactions. These will be discussed presently while the discussion of photon generation will be discussed in more detail in the following chapter.

5.3 Forward Multiplication and Exotic Reactions

There exist far more exotic reactions than the simple two-body elastic and inelastic kinematics discussed above. In the case of two-body kinematics one may state that

energy and momentum were conserved in every reaction, and thus the sampling of the outgoing energy and angle were directly coupled. However, as multi-body reactions come into play the coupling of outgoing energy and angle between many particles becomes much more difficult to calculate. Thus, the manner in which the ENDF data files handle this is to decouple the outgoing energy and angle for any given particle sampled.

For example, with the (n,2n) reaction, the outgoing energy and angle of the two neutrons should be coupled. Yet the data is presented such that each neutron is sampled independently, and their angles and energies are also sampled independently. This will lead to the situation in which the conservation of energy and momentum are not satisfied in general. However, the outgoing probability distributions are constructed in such a way that the average behavior of the total population tends to the correct physical representation. This stochastic approach to physics, while producing non-physical individual results, is applied ubiquitously throughout Monte Carlo radiation transport and is a key feature for efficient sampling routines. It should be noted that if the nuclear data were present for the coupled sampling of these variables it would provide the ability to observe physical cascades in Monte Carlo simulations. This could be of use to the nuclear community and thus it is suggested that research be conducted to begin the generation of coupled generation data sets.

It can be shown that while the particle-by-particle behavior is non-physical, the behavior of the entire population still follows the expected physical behavior. The transfer probability from any energy E' to E and direction $\hat{\Omega}'$ to $\hat{\Omega}$ can be written as follows:

$$\begin{aligned} f(E' \to E, \hat{\Omega}' \to \hat{\Omega}) &= p(E' \to E)p(\hat{\Omega}' \to \hat{\Omega}|E') \\ &= p(E' \to E)p(\mu, E'), \end{aligned} \tag{5.7}$$

where μ is the cosine of the center of mass scattering angle θ_{CM}. Thus the transfer probability may be written as the product of the probability of transferring in energy from E' to E and the probability at the given energy E' of transferring through some scattering angle cosine μ. Referencing the ENDF/B-VII.1 manual again, one must note that equations 5.1 and 5.2 are also applicable in this situation [15]. This states that the angular distributions are normalized to unity, and it may further be noted that the angular distributions are again represented as either tabular data or in legendre polynomial expansions.

The energy distributions for sampling produced particles are also represented in the ENDF/B-VII.1 tables as normalized PDFs of the form:

$$p(E' \to E) = \frac{1}{c\sigma(E')} \frac{d\sigma(E' \to E)}{dE}, \tag{5.8}$$

where c represents the number of emitted particles from the interaction as before [15]. As stated, these PDFs are also normalized to unity, thus

$$\int_0^\infty p(E' \to E) dE = 1. \tag{5.9}$$

It is of note that the nuclear data exists to a maximum energy, and thus the upper limit of the integral in Equation 5.27 will be practically defined as the problem maximum energy E_0, as the probability of a particle transitioning above E_0 will be zero on the range $(E_0, \infty]$.

While the angular distributions are provided as tabular data or legendre polynomial expansions, the energy data is instead represented as either tabular data or given by one of two analytical forms [15]. The analytical forms possible in the ENDF data are the general evaporative spectrum and the evaporation spectrum, both of which are common spectra used to describe multi-particle emissions.

The General Evaporative Spectrum

The first analytical form discussed in the ENDF/B-VII.1 manual is the general evaporative spectrum which has the following functional form:

$$p(E' \to E) = g\left(\frac{E}{\theta(E')}\right). \tag{5.10}$$

The two unknown functions in this probability are $\theta(E')$ and $g(s)$. Both of these are provided as tabular data based on their independent value. Thus, $\theta(E')$ is tabulated for a series of incoming energies E', and $g(s)$ is tabulated for a series of independent variables of the form $s = E/\theta(E')$. Sampling from this distribution requires the construction of a CDF for $g(s)$. Once an appropriate CDF has been calculated, one may sample the CDF with a random number η to arrive at a sampled value s_η. Once s_η is calculated, one may use the functional form for s to determine the outgoing energy using the formula:

$$E = s_\eta \theta(E'), \tag{5.11}$$

where $\theta(E')$ has been interpolated for the incoming energy E'. At this point one may independently sample the energy from the general evaporative spectrum as well as the scattering angle cosine (lab or CM) and update the particle state accordingly.

The Evaporation Spectrum

The alternate analytical form discussed in the ENDF/B-VII.1 manual is the evaporation spectrum which has the following functional form [15]:

$$p(E' \to E) = \frac{E}{I} \exp\left(\frac{-E}{\theta(E')}\right), \tag{5.12}$$

where

$$I = (\theta(E'))^2 \left(1 - \exp\left(-\frac{E' - U}{\theta(E')}\right)\left[1 + \frac{E' - U}{\theta(E')}\right]\right). \tag{5.13}$$

Here again $\theta(E')$ is represented as tabular data for incoming energies E'. U is defined as the upper limit for the final particle energy, or the practical upper energy limit for particles produced from the evaporation spectrum of the selected reaction. The sampling procedure utilized in the evaporation spectrum is notably more complicated than that of the general evaporative spectrum. To better understand the sampling procedure, a simplified procedure will be developed where the evaporation spectrum is not truncated at $(E' - U)$, but is instead taken to infinity. In this approximation the exponential in I will vanish, and the expression will be reduced to:

$$I_\infty = (\theta(E'))^2, \tag{5.14}$$

and thus the expression for the transfer probability will reduce to:

$$p_\infty(E' \to E) = \frac{E}{(\theta(E'))^2} \exp\left(\frac{-E}{\theta(E')}\right). \tag{5.15}$$

At this point one must assume that the final energy E may be represented by the sum of two other energies E_1 and E_2, such that $E = E_1 + E_2$. Further, one must define the probability distribution functions for transferring from some energy E' to E_1 and E_2 as:

$$p_{\infty,1}(E' \to E_1) = \frac{1}{\theta(E')} \exp\left(\frac{-E_1}{\theta(E')}\right), \tag{5.16}$$

and

$$p_{\infty,2}(E' \to E_2) = \frac{1}{\theta(E')} \exp\left(\frac{-E_2}{\theta(E')}\right) \tag{5.17}$$

respectively. At this point one may define the probability distribution for the outgoing energy E as follows [27]:

$$p_\infty(E' \to E) = \int_0^E p_{\infty,1}(E' \to E_1) p_{\infty,2}(E' \to E_2) dE_{1,2}. \tag{5.18}$$

Recalling the definition for E in terms of E_1 and E_2, one may quickly show that this definition recovers the original expression for the transfer probability of E as shown below:

$$\begin{aligned}
p_\infty(E' \to E) &= \int_0^E p_{\infty,1}(E' \to E_1) p_{\infty,2}(E' \to E_2) dE_{1,2} \\
&= \int_0^E p_{\infty,1}(E' \to E_1) p_{\infty,2}(E' \to E - E_1) dE_1 \\
&= \int_0^E \left[\frac{1}{\theta(E')} \exp\left(\frac{-E_1}{\theta(E')}\right)\right] \left[\frac{1}{\theta(E')} \exp\left(\frac{-(E-E_1)}{\theta(E')}\right)\right] dE_1 \\
&= \int_0^E \frac{1}{(\theta(E'))^2} \exp\left(\frac{-(E_1)}{\theta(E')}\right) \exp\left(\frac{-(E-E_1)}{\theta(E')}\right) dE_1 \\
&= \frac{1}{(\theta(E'))^2} \exp\left(\frac{-E}{\theta(E')}\right) \int_0^E dE_1 \\
&= \frac{E}{(\theta(E'))^2} \exp\left(\frac{-E}{\theta(E')}\right).
\end{aligned} \tag{5.19}$$

Thus the expected behavior of sampling the outgoing energy E is recovered if one utilizes the proposed PDFs for E_1, E_2, and E provided in the ENDF/B-VII.1 manual [15, 27].

At this point one may follow the inverse CDF method for sampling E_1 and E_2. The inverse sampling method seeks to solve the following problem. Assume that one has a normalized CDF for some variable, $C(s)$. The inverse sampling method then generates a value for s from the CDF $C(s)$ by solving for $s(C)$, and then noting that C must be a random number on the interval $[0, 1]$. If one first normalizes the PDFs in equations 5.16 and 5.17 and then integrates, the sample CDF for either of these would have the form:

$$P(x) = 1 - \exp\left(-\frac{x}{\theta}\right). \tag{5.20}$$

Solving this for $E(P)$ yields the following expression:

$$x = -\theta \ln(1 - P). \tag{5.21}$$

Noting that $P(x)$ is normalized, the value must always exist in the interval $[0, 1]$, and thus it can be represented as a random number η on the same interval. Further, since η will be a uniformly distributed random number on the interval $[0, 1]$, the expression $(1 - \eta)$ will also be uniformly distributed on the same interval and the equation may be simplified to the form:

$$x = -\theta \ln(\eta). \tag{5.22}$$

Thus x can be sampled randomly from the inverse CDF. Applying this to E_1 and E_2 one finds the values to be

$$E_1 = -\theta \ln(\eta_1), \tag{5.23}$$

and

$$E_2 = -\theta \ln(\eta_2). \tag{5.24}$$

Recall that the outgoing energy E is the sum of E_1 and E_2, and thus can be written as:

$$E = -\theta \ln(\eta_1 \eta_2). \tag{5.25}$$

One correction must be made is to due to the original approximation which stated that the evaporation spectrum continued to infinity. As this is incorrect, one must use a rejection sampling technique wherein if E is sampled to be higher than the evaporation spectrum maximum energy $(E' - U)$, it is rejected and must be resampled. This corrects for the approximation made in generating the PDFs and CDFs for sampling the outgoing energy state from the evaporation spectrum.

5.4 Forward Neutron Induced Fission

In the realm of neutron transport, fission is one of the most important reactions. One might assume that fission is only of importance with respect to modeling nuclear reactors. However, nuclear fission is also used commonly as an investigative tool to understand the presence of fissile and fissionable isotopes in a given sample. For example, nuclear fuel rods must be scanned and verified prior to use via neutron irradiation to ensure that the isotopic fractions of U-235 and U-238 (and less commonly U-232, U-234, and U236) are within acceptable limits for safe operation. Another example of fission outside of reactors is in irradiating shipping containers to search for fissile and fissionable isotopes. In this case one might look for the delayed neutron signal from fission products decaying in order to identify and quantify

the presence of fissile materials in the container. Thus, there are many situations outside of reactors where neutron fission is the reaction of interest.

In FRENSIE, the ability to model critical systems is unavailable and currently unplanned. While there is infrastructure in place to handle such calculations (referred to as K-Code calculations), the restrictions coinciding with offering an open-source and non-export controlled code have caused the development team to postpone this feature for the forseeable future. At some point this issue may be revisited, but it should be noted by the reader that fission in FRENSIE is only allowable in strictly subcritical systems. That said, the previous discussion of the importance of nuclear fission in subcritical assemblies is the driving force behind the implementation of fission in FRENSIE.

Similar to the discussion on multiplication reactions, fission is also handled in a strictly decoupled sense, both between particles produced and within a particle for the energy/angle relationship. This is again in accordance with the format of the data in the ENDF/B-VII.1 libraries [15]. The energy distributions for fission have the same form as those for multiplication, where the only key difference is the number of emitted particles is now referred to as $\nu(E')$, as is the custom with the average number of particles emitted per fission event. The PDFs and normalization are as follows:

The energy distributions for sampling produced particles are also represented in the ENDF/B-VII.1 tables as normalized PDFs of the form:

$$p(E' \rightarrow E) = \frac{1}{\nu(E')\sigma(E')} \frac{d\sigma(E' \rightarrow E)}{dE}, \tag{5.26}$$

and

$$\int_0^\infty p(E' \rightarrow E) dE = 1. \tag{5.27}$$

Again the upper limit of the integral will be defined as the problem maximum energy E_0, but is in general ∞.

As was done for the multiplication reactions, the outgoing energy distributions are provided in either a tabular form or one of two analytical forms. The analytical forms in this case are the Maxwellian fission spectrum and the Watt spectrum [15].

Maxwellian Fission Spectrum

The Maxwellian fission spectrum is as follows:

$$p(E' \to E) = \frac{\sqrt{E}}{I} \exp\left(\frac{-E}{\theta(E')}\right), \tag{5.28}$$

where

$$I = \left(\theta(E')\right)^{3/2} \left[\frac{\sqrt{\pi}}{2} \mathrm{erf}\left(\sqrt{\frac{(E'-U)}{\theta(E')}}\right) - \sqrt{\frac{(E'-U)}{\theta(E')}} \exp\left[\frac{-(E'-U)}{\theta(E')}\right]\right]. \tag{5.29}$$

Here $\theta(E')$ is again a tabulated function of the incoming energy E', and U is defined as the proper upper limit for the final particle energy. Since fission reactions typically produce neutrons on the order of 1 MeV, and the fission cross section is highest for thermal neutrons, the outgoing neutron energy is often many orders of magnitude higher than the incoming neutron energy. Thus, U will often be a very large negative number for fission reactions.

In the case of sampling the Maxwellian fission spectrum, there are multiple methods that can be used. Each method has positives and negatives based on simplicity and efficiency. The methods consist of the direct sampling method, Johnk's algorithm, and Mohamed's algorithm.

Direct Sampling

The simplest method is to directly sample the value of the outgoing energy using three random variables on the interval $[0, 1]$. The value of E is sampled from the following equation:

$$E = \theta(E')\left(-\ln(\eta_1) - \ln(\eta_2)\cos^2\left(\frac{\eta_3\pi}{2}\right)\right). \tag{5.30}$$

As this method is directly sampling the value for E, the efficiency is 100%, however it requires the generation of three random variables and must calculate two natural logarithms and a cosine function. For this reason, the direct sampling method is computationally inefficient [28].

Johnk's Algorithm

The sampling method utilized in the MCNP code is that of Johnk's algorithm. It is also discussed as sampling method C64 in the Monte Carlo sampling report

from LANL [29]. In this method one first generates two random numbers η_1 and η_2. If the sum of the squares of the random numbers is greater than 1, the sample is rejected. Otherwise a value for E is calculated based on the sampling of two additional random variables η_3 and η_4 as follows:

$$E = -\theta(E')\left(\frac{\eta_{1,2}^2 \ln(\eta_3)}{\eta_1^2 + \eta_2^2} + \ln(\eta_4)\right). \tag{5.31}$$

The flow diagram in Figure 5.1 depicts the general sampling routine for Johnk's algorithm.

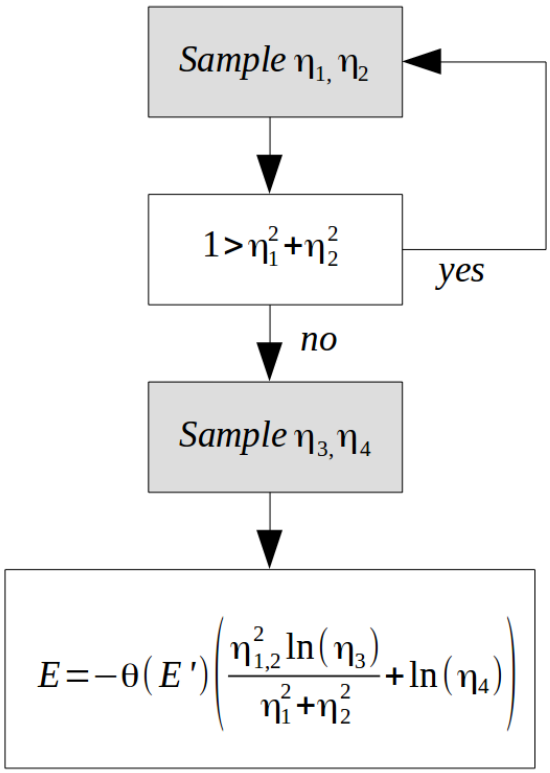

Figure 5.1: **Johnk's Algorithm**. *This sampling procedure, often referred to as Johnk's algorithm is the sampling procedure for the Maxwellian fission spectrum utilized by MCNP [28].*

Johnk's algorithm is slightly more efficient than the direct algorithm. It requires 4.56 random numbers on average per sample, but only requires two logarithms rather than two logarithms and a cosine as was required in the direct sampling

method. The acceptance efficiency of the sampling routine is 78%, and the overall increase in efficiency over the direct method roughly 10% per unit time [28].

Mohamed's Algorithm

Nader Mohamed proposed an updated algorithm in 2011 for sampling from the Maxwellian fission spectrum. Mohamed's algorithm, while less efficient on a rejection basis than Johnk's algorithm, turns out to be more efficient per unit calculation time. The full derivation of Mohamed's rejection sampling method can be found in [28]. Figure 5.2 depicts the flow diagram for Mohamed's proposed sampling routine.

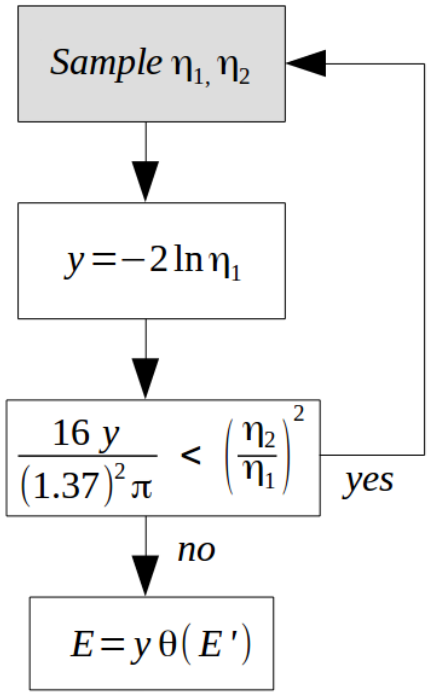

Figure 5.2: **Mohamed's Algorithm**. *Mohamed's proposed sampling procedure has a lower acceptance efficiency than Johnk's algorithm, but has the added benefit of being more computationally efficient per unit calculation time [28].*

Mohamed's sampling routine, while having a lower acceptance efficiency of 73% is more computationally efficient in producing a valid sample. Table 5.1 compares the various methods and their efficiency in rejection sampling as well as their computational efficiency to generate an outgoing energy sample. It can be seen that Mohamed's proposed algorithm for sampling outgoing energy states from the

Maxwellian fission spectrum is significantly more computationally efficient, and is thus the preferred method for sampling.

Table 5.1: **Comparison of Maxwellian Fission Spectrum Sampling** *Mohamed's sampling routine is the most efficient at generating outgoing Energy samples, even though it has a slightly lower acceptance efficiency than Johnk's algorithm. Note that both modified algorithms are superior to the direct sampling method [modified from [28]].*

	Direct	Jonhk's	Mohamed
Acceptance Efficiency	100%	78%	73%
Random Numbers per Sample	3	4.56	2.74
Expensive Calculations	2 ln, cos	2 ln	ln
Relative Computational Time per Sample	1	0.91	0.625

Watt Fission Spectrum

The alternative analytical form that the outgoing neutron energy data may be sampled from is the Watt fission spectrum. The Watt fission spectrum has the following functional form:

$$p(E' \to E) = \frac{1}{I} \exp\left(-\frac{E}{a(E')}\right) \sinh\left(\sqrt{Eb(E')}\right), \tag{5.32}$$

where

$$\begin{aligned} I(E') = &\left(\frac{\pi a(E')^3 b(E')}{16}\right)^{1/2} \exp\left(\frac{a(E')b(E')}{4}\right) \left[\operatorname{erf}\left(\sqrt{\frac{E'-U}{a(E')}} - \sqrt{\frac{a(E')b(E')}{4}}\right)\right. \\ &\left. \operatorname{erf}\left(\sqrt{\frac{E'-U}{a(E')}} + \sqrt{\frac{a(E')b(E')}{4}}\right)\right] \\ &- a(E') \exp\left(-\frac{E'-U}{a(E')}\right) \sinh\sqrt{b(E'-U)}. \end{aligned} \tag{5.33}$$

As with $\theta(E')$ before, $a(E')$ and $b(E')$ are functions which are tabulated as a function of the incoming neutron energy. Once more, U retains the same definition as the proper upper limit for the final particle energy. As with the Maxwellian fission spectrum, there are multiple sampling methods. The methods are referred to as Kalos's algorithm and a modified direct sampling routine again by Mohamed.

Kalos's Algorithm

Kalos's algorithm is of interest because it is the manner by which MCNP samples the Watt fission spectrum. The sampling methodology for Kalos's argument may be seen in Figure 5.3. The acceptance efficiency of this method is 67%.

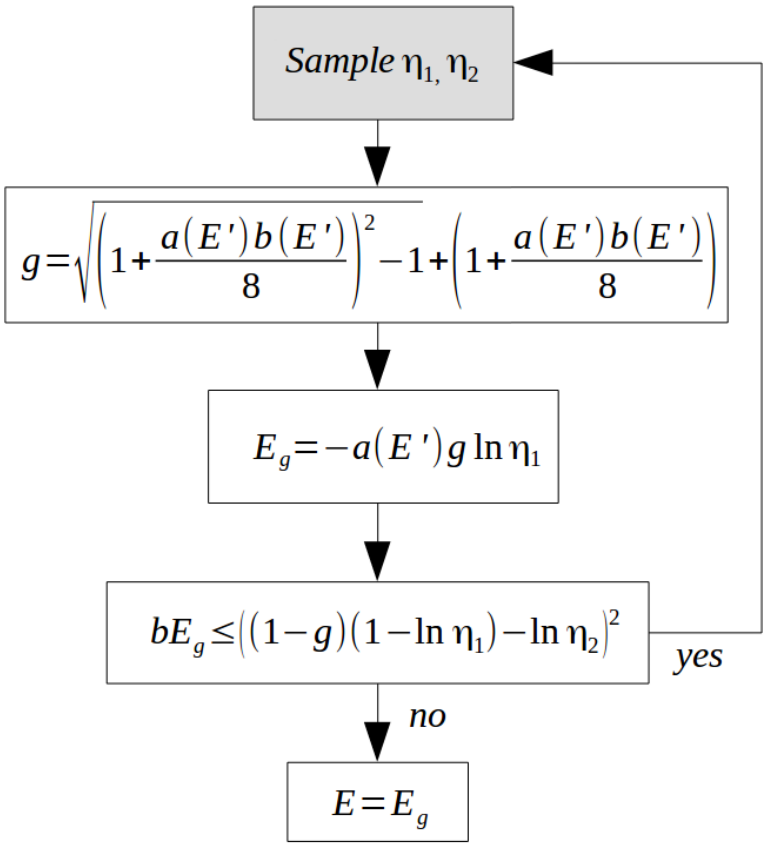

Figure 5.3: **Kalos's Algorithm**. *Kalos's algorithm is used to sample outgoing neutron energies from the Watt fission spectrum. This algorithm is in use in the MCNP5/6 code [28].*

Mohamed's Watt Algorithm

Mohamed's approach to sampling the Watt fission spectrum is a direct sampling method. In Mohamed's Watt algorithm, one begins by first generating a random variable y using Mohamed's proposed Maxwellian sampling method. Thus, one would sample the variable y from the Maxwellian sampling method by making the substitution that $\theta(E') = a(E')$. After y has been sampled, the outgoing energy E

can be directly calculated using the following equation:

$$E = y + \frac{a(E')^2 b(E')}{4} + (2\eta_1 - 1)\sqrt{a(E')^2 b(E') y} \tag{5.34}$$

Mohamed's Watt algorithm is approximately 10% more efficient at generating outgoing energy samples per unit computational time, and is thus the preferred method for handling the ENDF Watt spectrum data.

5.5 Forward Thermal Scattering

In a previous section elastic and inelastic level scattering was discussed with respect to the existing cross section and transfer probability data in the ENDF/B-VII.1 library. However, this discussion was predicated on the assumption that the average neutron kinetic energy was much larger than the kinetic energy of the target nucleus. This is the same as stating that the target nucleus is at rest. The previous discussion and the derivations in appendix B all assume a target at rest.

While this is a good assumption for the majority of the neutron energy space, as the kinetic energy of the neutron approaches the thermal kinetic energy of the medium in which it resides, this assumption becomes invalid. There is no hard cut-off for when thermal motion can be neglected, but an accepted value is that for neutron energies below roughly 4 eV, thermal motion will begin to play a significant role and a more accurate model of the two-body physics must be considered with respect to the stochastic movement of the target media.

The simplest possible model for dealing with thermal neutrons is to treat them as a homogenous group of neutrons at an average thermal temperature and with an appropriately averaged scattering cross section. In this model, any neutron which enters the thermal region is assumed to remain at the same energy through all elastic scattering collisions. The particle may be absorbed, but scattering collisions do not allow a particle to scatter out of the thermal group. While this model may produce a rough sketch of thermal neutron behavior in a system, the assumption that the thermal cross section can be accurately averaged is largely erroneous and will lead to poor results. It is for this reason that the one-thermal-group treatment of adjoint neutrons in MCBEND is undesirable, and an alternative method is presented in this work.

A slightly more complicated model for dealing with thermal neutrons would be to model all interactions as interactions with a free gas nucleus. That is to say, the

target atom is not atomically bound to any other atoms, and there are no external forces on the target. In this model, the target velocity is randomly sampled based on the Maxwell-Boltzmann distribution for the velocity of free gas particles in a system of temperature T. The key assumptions built into this model are that the scattering cross sections are independent of the relative speed of the two bodies, and that the absorption cross sections are well known [25].

A final and more complex model for thermal neutron treatment is often referred to as the $S(\alpha, \beta)$ model which captures behaviors arising from atoms bound in molecules and in crystalline solids such as molecular binding energy and phonon scattering. While more data is being added with each iteration of the ENDF library, there are only a handful of materials which currently have $S(\alpha, \beta)$ data associated with them [15]. Furthermore, one must handle the $S(\alpha, \beta)$ data with slightly more care, as it must be used only for the specific molecules it describes and must be used for each nuclide in said materials [30]. If this is not done, one will often find a less accurate result than if the model was not used at all.

The primary focus of this work as discussed in Chapter 7 is the development of a forward and adjoint free gas thermal neutron transport model. One goal of this development is to improve the treatment of thermal neutrons in forward calculations where $S(\alpha, \beta)$ data is unavailable but existing cross section and angular transfer probabilities are known. Another goal is to allow for the energy dependent modeling of thermal neutrons in adjoint calculations, as well as to construct self-adjoint thermal neutron transport problems. Having these capabilities in an open source code will promote the utilization of adjoint transport while also furthering the theoretical development neutron transport and modeling.

5.6 Adjoint Elastic and Inelastic Level Scattering

Section 5.1 discussed the sampling mechanisms for handling forward elastic and inelastic level neutron scattering. This section will discuss the modifications that must be made to the forward sampling routines to allow for adjoint elastic and inelastic level scattering to be modeled. Just as with forward transport, in order to model adjoint transport one must first derive the cross section and the transfer probabilities.

In order to model adjoint elastic and inelastic level scattering, one must first obtain the cross section and transfer probabilities. Recalling the discussion of the adjoint collision kernel expansion from Chapter 4, the adjoint cross sections and

transfer probabilities can be calculated from the known forward data. For the elastic and inelastic level scattering, the transfer probability can be represented as [23]:

$$p(E' \rightarrow E, \mu_{CM}) = p(E', \mu_{CM})\delta(E - E_\delta), \tag{5.35}$$

where E_δ is the outgoing energy from the scattering event as found in Equation 5.5,

$$E_\delta = E' \left[\frac{A^2 \left(1 - \left(\frac{A+1}{A}\right)\frac{E^*}{E'}\right) + 2A\mu_{CM}\left(1 - \left(\frac{A+1}{A}\right)\frac{E^*}{E'}\right)^{1/2} + 1}{(A+1)^2} \right]. \tag{5.36}$$

The presence of the delta function is due to the fact that there is a one-to-one correspondence in the outgoing energy and direction from elastic and inelastic level scattering reactions.

In order to arrive at the energy transfer probability one must integrate over the center of mass scattering angle cosine μ_{CM}:

$$p(E' \rightarrow E) = \int_{-1}^{1} p(E' \rightarrow E, \mu_{CM}) d\mu_{CM}. \tag{5.37}$$

Integration in the presence of a delta function is quite easy to evaluate. Thus, it would be beneficial to convert the integral in angle space in Equation 5.37 to one over energy space. This can be done by referencing the relationship between the scattering angle cosine and the incoming and outgoing energies found in appendix B. Taking the derivative of Equation 5.5 with respect to energy and center of mass scattering angle cosine yields the following differential relationship:

$$dE = \left[\frac{2AE'\left(1 - \left(\frac{A+1}{A}\right)\frac{E^*}{E'}\right)^{1/2}}{(A+1)^2} \right] d\mu_{CM}. \tag{5.38}$$

Thus, the energy transfer probability may be written in terms of energy as:

$$p(E' \rightarrow E) = \int_{E_{min}}^{E_{max}} p(\mu_{CM}, E')\delta(E - E_\delta) \left[\frac{(A+1)^2}{2AE'\left(1 - \left(\frac{A+1}{A}\right)\frac{E^*}{E'}\right)^{1/2}} \right] dE. \tag{5.39}$$

Therefore,

$$p(E' \rightarrow E) = p(\mu_{CM}(E', E_\delta), E') \left(\frac{(A+1)^2}{2AE' \left(1 - \left(\frac{A+1}{A}\right)\frac{E^*}{E'}\right)^{1/2}} \right). \tag{5.40}$$

At this point one may now define the adjoint elastic and inelastic level scattering cross section in terms of previously defined quantities as follows:

$$\sigma^\dagger(E') = \int_{E_{min}}^{E_{max}} \sigma(E) p(E \rightarrow E') dE. \tag{5.41}$$

The only remaining unknowns left in specifying the adjoint cross section are the limits of integration, E_{min} and E_{max}. One might assume that they can be directly observed from Equation 5.5. However, upon further analysis one will find that this expression can not be solved directly for E' in general. This is due to the fact that the outgoing energy E is now fixed and one wishes to determine the incoming energy E' and the center of mass scattering angle cosine μ_{CM}. If one plots Equation 5.5 as outgoing energy vs. incoming energy for various values of μ_{CM}, it becomes apparent that there is a limit below which the one-to-one energy-to-angle correspondence breaks down in the adjoint case. This can be seen in Figure 5.4. For center of mass scattering angle cosine values $\mu_{CM} < 0$, the one-to-one correspondence between incoming energy and scattering angle for a specified outgoing angle is lost.

While this can be seen from analyzing the outgoing energy as a function of incoming energy for specific scattering angle cosines, another way to observe this behavior is to look at the relationship between the scattering angle cosine in the laboratory and center of mass reference frames for different incoming energies E'. One may take the partial derivative of μ_L with respect to μ_{CM} in equation 5.4 to yield:

$$\frac{\partial \mu_L}{\partial \mu_{CM}} = \frac{A^2 \left(1 - \left(\frac{A+1}{A}\right)\frac{E^*}{E'}\right) \left(A\sqrt{1 - \left(\frac{A+1}{A}\right)\frac{E^*}{E'}} + \mu_{CM}\right)}{\left[A^2 \left(1 - \left(\frac{A+1}{A}\right)\frac{E^*}{E'}\right) + 2A\mu_{CM}\sqrt{1 - \left(\frac{A+1}{A}\right)\frac{E^*}{E'}} + 1\right]^{3/2}} \tag{5.42}$$

It can be seen that there are values for which the derivative of this expression will

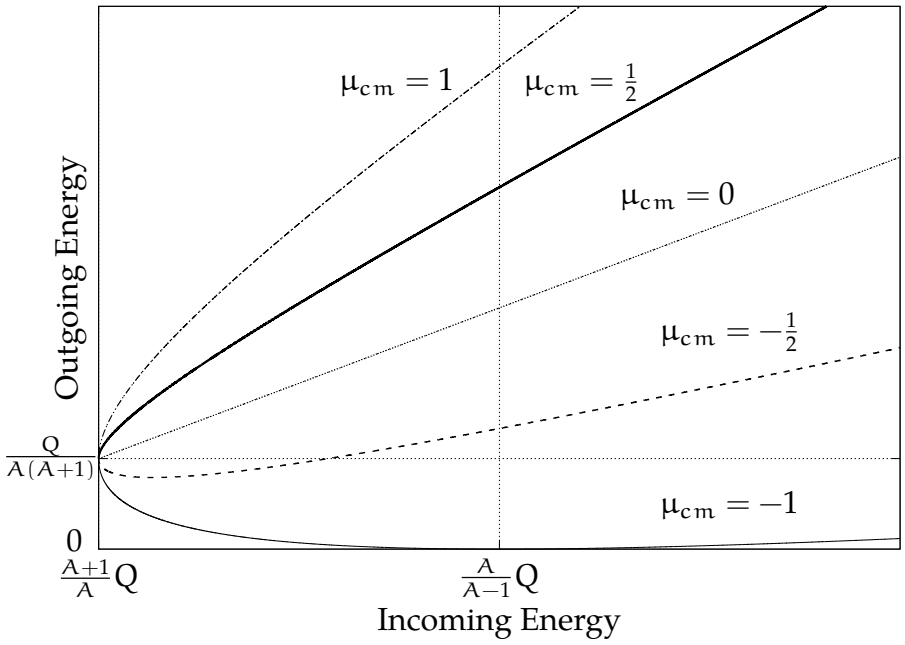

Figure 5.4: **Outgoing energy versus incoming energy of inelastic level scattering for specific CM scattering angle cosines**. *When the outgoing energy is fixed, as in the case of adjoint scattering, the one-to-one correspondence between incoming energy and center of mass scattering angle cosine is lost for negative cosine values [Modified from [23]].*

be zero. Namely when

$$\mu_{CM} = -A\sqrt{1 - \left(\frac{A+1}{A}\right)\frac{E^*}{E'}}, \quad \mu \in [-1, 1] \tag{5.43}$$

the derivative of the expression will be zero, and thus the function $\mu_L(\mu_{CM})$ is no longer guaranteed to be single valued. This behavior can be seen in Figure 5.5.

To remedy this issue one must reformulate the previous expression in equation 5.5 which relates the incoming energy, outgoing energy, and center of mass scattering angle cosine to be in terms of the laboratory angle cosine. Recall that an expression was found to relate the scattering angle cosine in the laboratory and center of mass reference frames in Equation 5.4. Solving Equation 5.5 for μ_{CM} and substituting

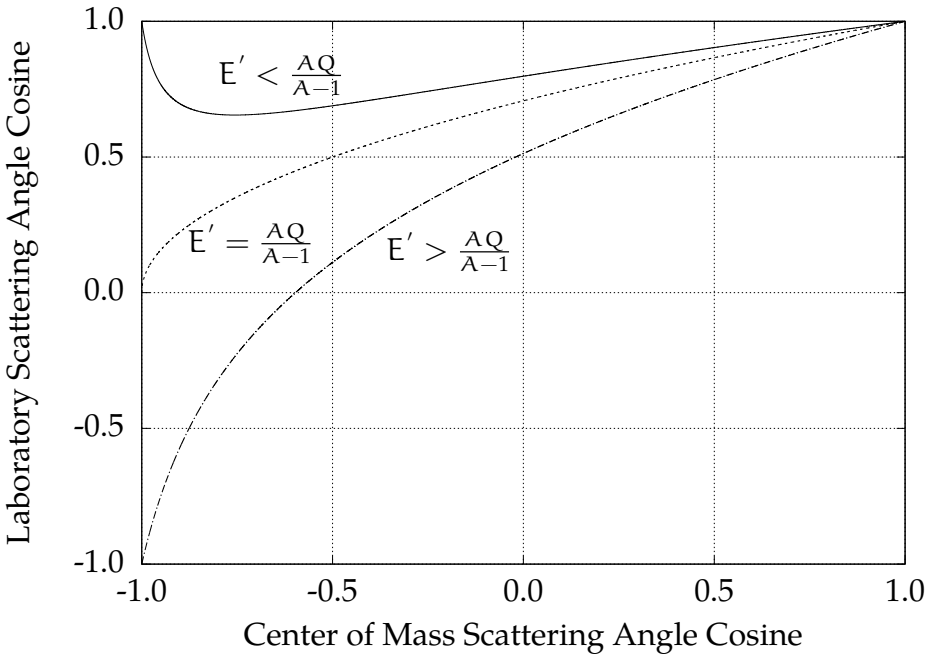

Figure 5.5: **CM versus laboratory scattering angle cosine for adjoint inelastic level scattering**. *When the incoming energy is below a threshold, one will observe the behavior that center of mass scattering angle cosine is multivalued for a given laboratory scattering angle cosine [Modified from [23]].*

into Equation 5.4 produces the following expression:

$$E' = E\left(\frac{A^2-1+2\mu_L^2+A(A-1)\frac{E^*}{E}-2\mu_L\left(A^2-1+\mu_L^2+A(A-1)\frac{E^*}{E}\right)^{1/2}}{(A-1)^2}\right). \tag{5.44}$$

It should be noted that Equation 5.44 is now describing the incoming neutron energy in terms of the outgoing energy and laboratory frame scattering angle cosine. In this case the one-to-one correspondence exists between any specific outgoing energy and laboratory scattering angle cosine. Thus if one samples the outgoing energy and knows the incoming energy (as is the case in adjoint scattering), the laboratory scattering angle cosine can be calculated therefrom. Figure 5.6 plots Equation 5.44 as outgoing energy versus incoming energy for a series of laboratory scattering angle cosines.

At this point one is able to calculate the upper and lower energy limits for the problem by inputting the maximum and minimum values for $\mu_L = -1$ and 1. The

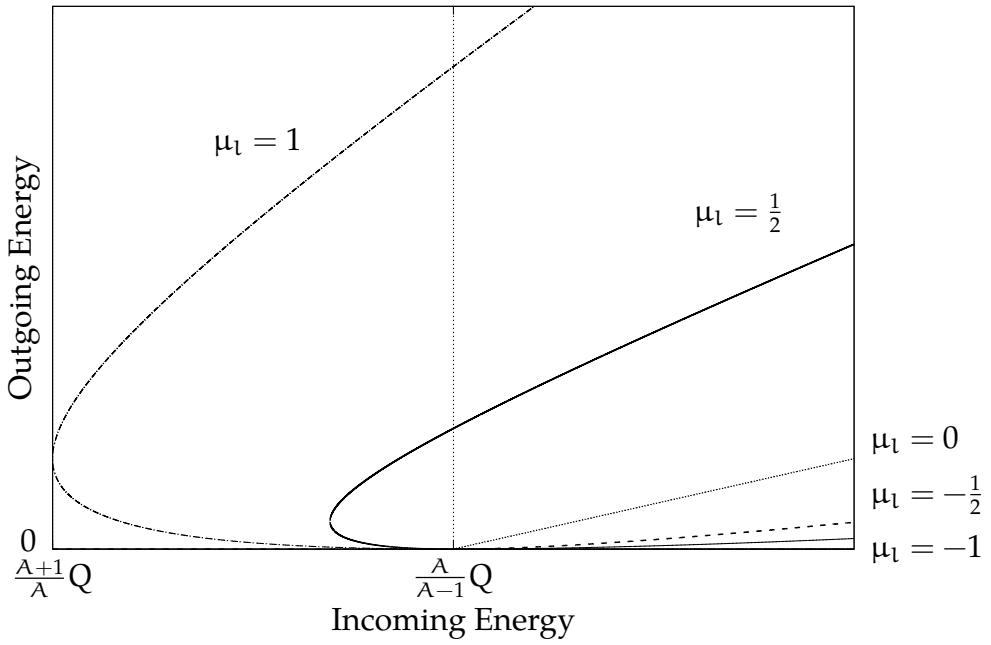

Figure 5.6: **Outgoing energy versus incoming energy of inelastic level scattering for specific laboratory scattering angle cosines**. *When the outgoing energy is fixed, as in the case of adjoint scattering, the one-to-one correspondence between the incoming energy and the laboratory frame scattering angle cosine is retained [Modified from [23]].*

energy limits are as follows:

$$\left(\frac{A\sqrt{1-\left(\frac{A+1}{A}\right)\frac{E^*}{E}}-1}{A-1}\right)^2 E \leqslant E' \leqslant \left(\frac{A\sqrt{1-\left(\frac{A+1}{A}\right)\frac{E^*}{E}}+1}{A-1}\right)^2 E \quad (5.45)$$

Now one may calculate the adjoint cross section by conducting the integration in Equation 5.41. This then allows for the calculation of the transfer probability for the adjoint scattering event. Note that the elastic scattering case is again a sub-case of the inelastic case wherein the excitation energy $E^* = 0$. The final form of the adjoint energy transfer probability for elastic and inelastic level scattering is as follows [23]:

$$p^\dagger(E' \to E) = \frac{\sigma(E)}{\sigma^\dagger(E')} p(E \to E'). \quad (5.46)$$

In order to be able to sample this transfer probability efficiently, tables will be

generated for each isotope. While this is computationally expensive in the short term, the long term computational efficiency of table look-up rather than on-the-fly calculation suggests that it is the best option.

Finally, once the incoming energy has been sampled the laboratory frame scattering angle cosine may be back-calculated using the following expression:

$$\mu_L = -\left[\frac{\left(\frac{E'}{E}\right)(A-1)^2 - A^2\left(1-\left(\frac{A+1}{A}\right)\frac{E^*}{E}\right)+1}{2\left(\frac{E'}{E}\right)^{1/2}(A-1)}\right]. \tag{5.47}$$

5.7 Chapter Summary

This chapter dealt primarily with the handling of neutron transport in the forward and adjoint cases for existing cross sections. Some of the key takeaways from this chapter are:

- The ENDF libraries contain cross section and transfer probabilities for neutron reactions, as well as suggested methods for interpreting the data. For neutrons reactions consist of scattering, absorption, multiplication, particle production, and fission reactions.
- For modeling the fission spectrum there are currently more efficient ways to sample the existing data sets. Mohamed's proposed algorithms are roughly 45% more efficient for sampling the Maxwellian fission spectrum and 10% more efficient for sampling the Watt fission spectrum.
- Thermal neutron scattering is of great interest as it is the energy region in which the neutrons are closest in kinetic energy to the target nucleus. Thus, it is important to develop methods for accurately modeling the stochastic nature of target movement due to thermal motion.
- The adjoint elastic and inelastic level scattering cross sections and energy transfer probabilities were derived. These utilize the known forward cross sections and transfer probabilities and will need to be calculated and tabulated for each isotope.

Chapter 6

ACE Forward Neutron and $S(\alpha, \beta)$ Implementation and Validation

Throughout the course of study a large amount of theoretical and practical work has been conducted in relation to the specific research of neutron transport and methods development. Other projects and publications have been completed on FRENSIE and the Monte Carlo code FACEMC within FRENSIE to allow them to move forward as software packages that are not directly relevant to this work.

6.1 Implementation of Forward Neutron Reactions

Before developing the theoretical backing or technical implementation for adjoint neutronics, it was key to fully develop forward neutronics in FRENSIE. Currently FRENSIE is capable of modeling all forward neutron reactions present in MCNP5/6 which do not result in the production of charged particles. This includes the following reactions:

- Elastic scattering
- Inelastic level scattering
- Inelastic continuum scattering
- Absorption
- Multiplication
- Fission

While the previous chapter discussed the ENDF data files, all neutron reactions except for the newly developed free gas $S(\alpha, \beta)$ reaction utilize the ACE (A Compact ENDF) file type from Los Alamos in order to allow benchmarking with the gold standard MCNP5/6/X codes. Thus, the implementation of these reactions requires the ability to parse ACE data files appropriately based on the reaction type and the format of the specific data. This information is stored in ACE laws which can

Table 6.1: **Set of ACE Forward Neutron Validation Studies.** *A set of validation runs were conducted to ensure that FRENSIE achieved the same results as MCNP5/6 when utilizing the ACE data files [modified from [32]].*

Test	Material	Temperature (K)	Radius (cm)	Density	E_s (MeV)
1	^{1}H	293.6	1.0	1 at/b·cm	1
2	^{1}H	2500	1.0	1 at/b·cm	1
3	^{16}O	293.6	3.0	1 at/b·cm	9
4	^{16}O	293.6	3.0	1 at/b·cm	19
5	H_2O	293.6	3.0	1.0 g/cm^3	19
6	^{235}U	293.6	1.0	19.1 g/cm^3	10
7	^{238}U	293.6	1.0	19.1 g/cm^3	10

be found in the second manual for MCNP [31]. All ACE laws are implemented in FRENSIE which allows for the appropriate transfer probability sampling for any neutron reaction from the ACE tables, and thus any neutron reaction present in MCNP5/6/X.

Validation of Forward Physics

In terms of testing, large scale validation has yet to be completed in the form of every isotope and reaction present in ACE. However, significant testing has been done to ensure that FRENSIE accurately reproduces the neutron transport present in the ACE data files. A sample of seven tests is included herein to capture the reactions listed above. Table 6.1 lists the sample of validation tests [32].

All tests in Table 6.1 consist of an isotropic neutron point source at energy E_s at the center of a sphere. The energy as well as the geometric and material constraints vary between tests and are described in the table. Tests 1 and 2 are designed to evaluate elastic scattering and absorption, with tests 3 and 4 adding inelastic scattering to and higher energy transport. Test 5 is designed to combine all of these physics into a single test by combining hydrogen and oxygen with a high energy source. Tests 6 and 7 are designed to add fission and multiplication to the reaction with ^{235}U as the medium.

In all of these tests the measured quantity is the surface current on the boundary of the sphere of material. Outside of the sphere of material is a void region followed by the particle graveyard. Three of the results will be plotted explicitly with the remaining results and an additional first collided source investigation plotted in Appendix D. The results for test 1 may be seen in Figure 6.1. Test 1 is dominated by

Table 6.2: **Set of ACE Forward Neutron Validation Studies.** *A set of validation runs were conducted to ensure that FRENSIE achieved the same results as MCNP5/6 when utilizing the ACE data files [modified from [32]].*

Fraction of C/E Ratio in Standard Deviations								
	Test Number							
σ	1	2	3	4	5	6	7	**Expected**
1	0.680	0.692	0.691	0.610	0.709	0.667	0.667	**0.6827**
2	0.940	0.967	0.935	0.943	0.961	0.959	0.935	**0.9645**
3	0.990	1.000	0.100	1.000	1.000	1.000	1.000	**0.9973**

the elastic scattering and absorption reactions present for hydrogen, with the added caveat that the free gas cross section card in MCNP6 is flagged (i.e. the TMP card). This is why the neutrons in the thermal region form an equilibrium distribution. It can be seen from the ratio of the calculated (FRENSIE) and experimental (MCNP6) results that there is good agreement between the two codes. Table 6.1 depicts the three-sigma ratios for all tests. Assuming both codes are unbiased and are randomly sampling from the same normal distribution of scores, one expects the variance in the C/E ratio to likewise be represented by a normal distribution. Thus, roughly 68% of the events should lie within one standard deviation, 95% within two standard deviations, and 99.7% within three standard deviations.

The results for test 5 may be seen in Figure 6.2. Test 5 is designed to include the elastic and absorption reactions from hydrogen while adding the same reactions in oxygen alongside inelastic scattering. It can be seen that the agreement between MCNP6 and FRENSIE is again very good across the entire energy spectrum, with the C/E ratio for the energy bins of the surface current detector agreeing with the expected values on the three-sigma rule.

The results for test 6 may be seen in Figure 6.3. Test 6 is designed to take the reactions from the previous tests and combine it with the added complexity of fission and multiplication reactions. Chapter 5 discusses the sampling routines for multiplication and fission reactions which have been implemented in FRENSIE. Once again FRENSIE and MCNP6 show good agreement across the entire energy spectrum and have the expected values for the three-sigma rule. Table 6.1 depicts the three-sigma values for the C/E ratios on all tests, and it can be seen that there are no validation tests which exhibit statistically significant deviations for the implementation of the forward ACE cross sections in FRENSIE.

While these tests provide a foundation for the neutron validation efforts in

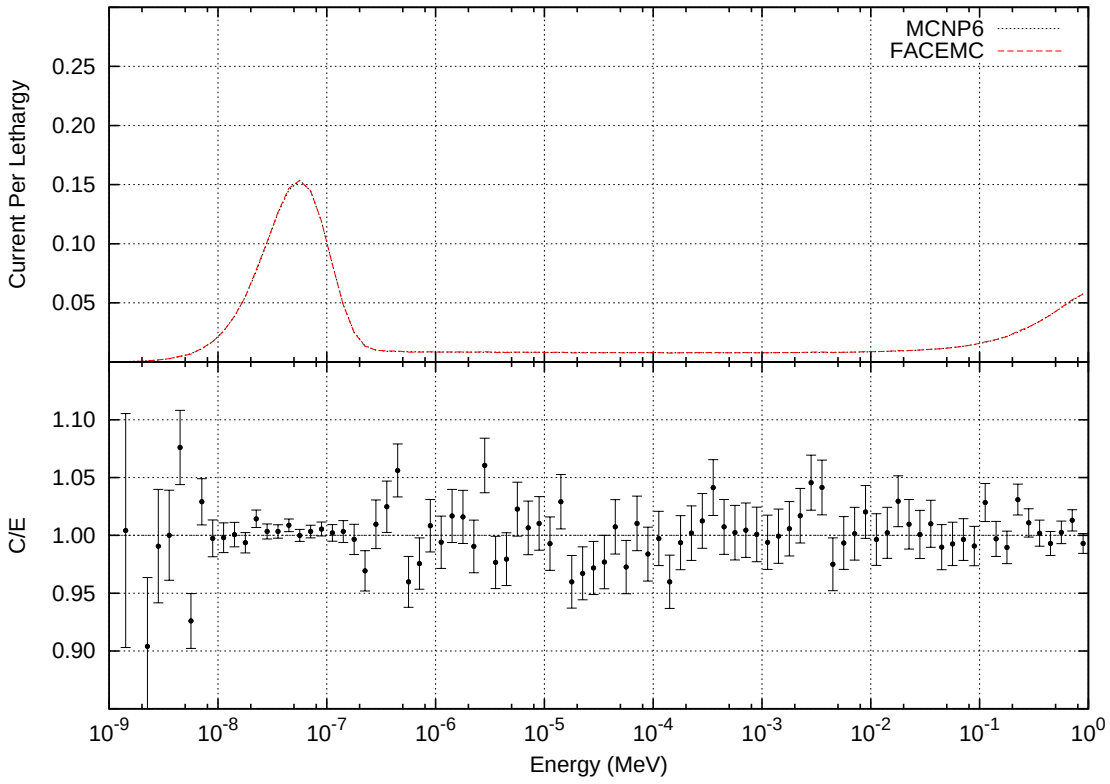

Figure 6.1: **Comparison of FRENSIE vs. MCNP for Test 1.** *It can be seen that for scattering on hydrogen at 1 at/b·cm and 293.6K with a neutron birth energy of 1 MeV, FRENSIE accurately reproduces the behavior of MCNP6 when using the ACE data. This test also utilizes the TMP free gas cross section card in MCNP* [32].

FRENSIE, it is desired to eventually run full SINBAD simulations as is done in the MCNP6 test suite. Such complicated and highly studied simulations will allow for higher levels of confidence in FRENSIE as a production level radiation transport code.

6.2 Photon Generation from Neutron Reactions

Radiative capture is a common absorption reaction in nuclear physics. For example, a parasitic capture mechanism in nuclear reactors is the $^{238}U(n,\gamma)^{239}U$ radiative capture reaction which tends to absorb thermal neutrons, preventing them from causing fission in ^{235}U. Beyond this, radiative capture can be used to detect the presence and concentration of specific isotopes found in explosives and contraband by examining the energy spectrum of the resulting characteristic gamma radiation.

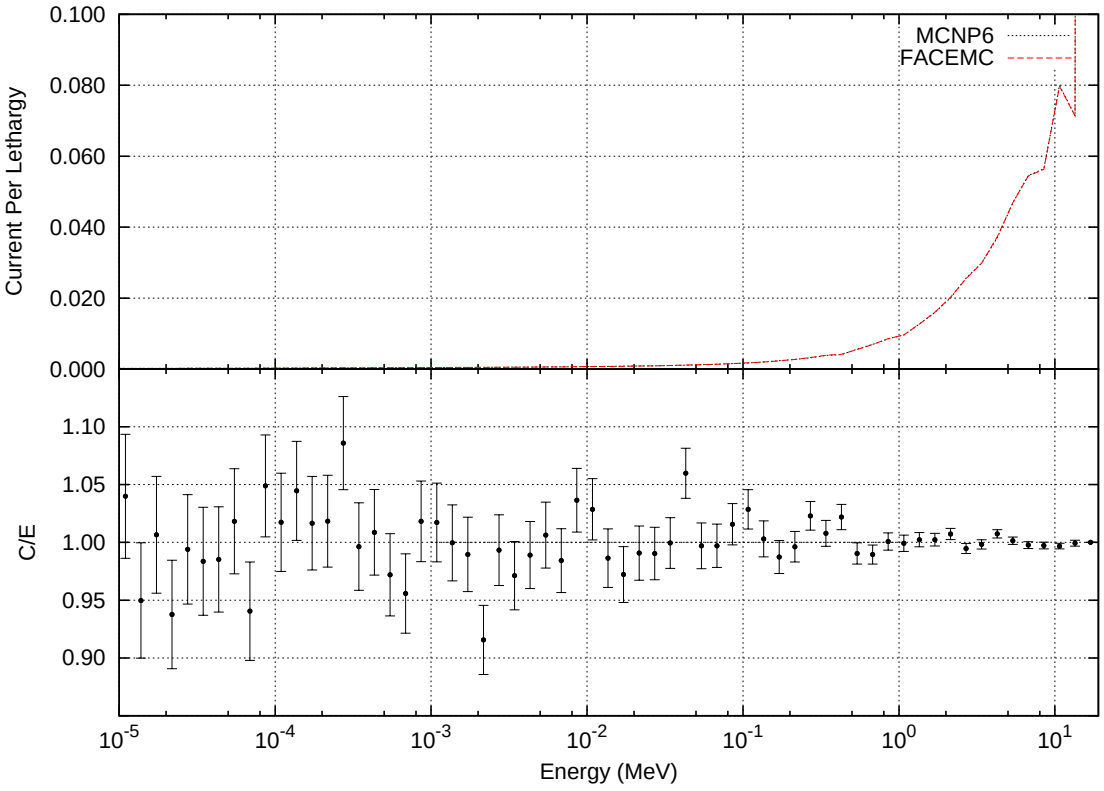

Figure 6.2: **Comparison of FRENSIE vs. MCNP for Test 6.** *It can be seen that for scattering on water H_2O at 1 g/cm^3 and 293.6K with a neutron birth energy of 19 MeV, FRENSIE accurately reproduces the behavior of MCNP6 when using the ACE data* [32].

As many isotopes have known high-yield characteristic gamma reactions, neutrons can be used as a non-destructive tool for isotopic investigation. This can be used for detecting nuclear materials, illicit drugs, and even improvised explosive devices (IED) in warzones. For these reasons it was imperative that photon generation from neutron reactions be implemented in FRENSIE.

The photon production cross sections and transfer probabilities utilized in FRENSIE can again be found in the ACE data files packaged with the MCNP5/6/X releases. Photon production in ACE is handled in a stochastic manner and is sampled at every neutron interaction. That is to say, the generation of a photon from a specific reaction does not require the accompanying neutron reaction to have occurred at that collision site. At each neutron collision, if the nuclide of interaction has photon production cross sections then photons will be produced. In order to account for the fact that photons should not be produced from every reaction, the photons produced

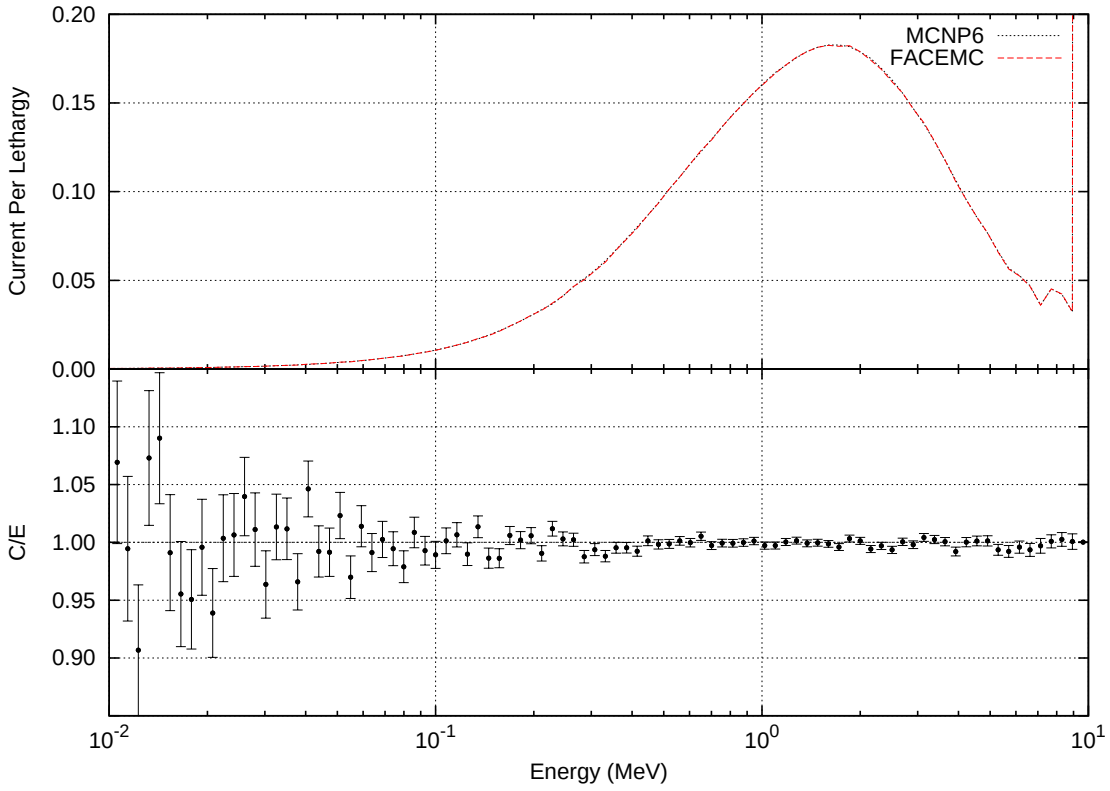

Figure 6.3: **Comparison of FRENSIE vs. MCNP for Test 5.** *It can be seen that for scattering on water ^{235}U at 1 g/cm^3 and 293.6K with a neutron birth energy of 19 MeV, FRENSIE accurately reproduces the behavior of MCNP6 when using the ACE data* [32].

will have weights adjusted by the following ratio:

$$w_\gamma = w_n \frac{\sigma_{pp}}{\sigma_T}, \tag{6.1}$$

where σ_T is the total neutron cross section for the nuclide and σ_{pp} is the total photon production neutron cross section for the nuclide. For example, if there is an isotope wherein only reaction i produces photons, then the ratio would be σ_i/σ_T. Physically, the weight represents the likelihood that any given reaction with isotope i will produce a photon. One of the downsides of this approach is that cascades cannot be observed, as there is no connection between a neutron reaction which produces a photon and a photon being sampled from that specific reaction. For this reason, these methods are referred to as the *decoupled photon production* methods within FRENSIE. Once the additional classes have been written to handle the production of these photons from their various ACE formats, application of the pre-existing

ACE laws allows them to be sampled and transported.

As these capabilities are of interest to Professor Henderson's research outside of methods development, it is important that the results are validated with MCNP. Two tests were conducted to ensure that photons were being generated appropriately. The first test is referred to as a broomstick test. The geometry of the test consists of a 500 cm long thin cylinder of radius 0.01 cm filled with low density ^{7}Li at 1 g/cm^{3}. The neutron source impinges on the end of the cylinder and is monodirectional along the axis of the cylinder and monoenergetic with energy $E = 0.5463$ MeV. The point of the broomstick test is to have particles interact a single time before being scattered out through the surface of the cylinder. Similarly, the goal is to have photons generated via the single neutron interaction and subsequently transported to the surface of the cylinder without undergoing any interactions. This was ensured by having a collision index bin on the results, as some small fraction of the photons will have an interaction with the low density medium. Figure 6.4 depicts the results for both MCNP6 and FRENSIE in this simulation. It can be seen that FRENSIE and MCNP6 achieve the same result to within the statistical uncertainty of the models.

The second test was designed to ensure that photons could be accurately generated and transported through energy space. The second model consists of a 1 MeV monoenergetic isotropic neutron point source at the center of a 25 cm radius sphere of hydrogen at density 1 at/b·cm and temperature 2500K. The energy-dependent photon track-length flux spectrum was tallied on the sphere and compared with MCNP6. Figure 6.5 displays the results of the test. Again it can be seen that FRENSIE and MCNP6 match very well and agree to within the statistical uncertainty of the models.

Forward photon generation from neutron reactions has been implemented and tested in FRENSIE. Results have been benchmarked against MCNP6 and have been found to be statistically sound. As was done for the previous validation studies, Table 6.2 depicts the three-sigma C/E statistics for the second photon validation test. It can be seen that there is no indication of statistically significant deviation between FRENSIE and MCNP6.

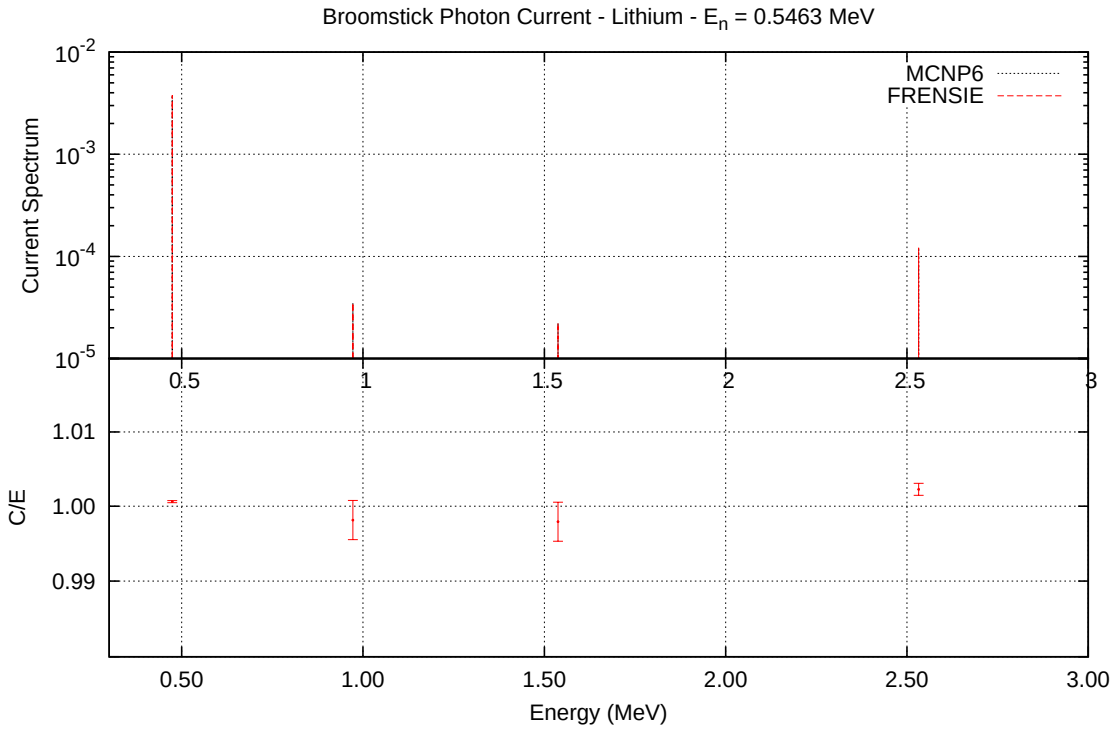

Figure 6.4: **Lithium broomstick problem for photon generation from neutron reactions.** *In this broomstick problem, neutrons are born at the end of a very long, thin cylinder of lithium. Photons are generated from neutron reactions using the ACE tables and the photon current is binned on the surface of the cylinder for photons which have not undergone any reactions.*

Table 6.3: **ACE Forward Neutron Decoupled Photon Production Validation Study.** *Decoupled photon production in FRENSIE has been implemented to allow for photon production from neutron reactions. Photons are produced in a hydrogen medium from the* (n, γ) *capture reaction and are then transported through the random walk process, with a track-length flux tally over the sphere. The C/E ratios comparing MCNP6 and FRENSIE are listed herein for the energy bins of the the tally.*

σ	C/E Fraction	**Expected**
1	0.6625	**0.6827**
2	0.9625	**0.9645**
3	1.0000	**0.9973**

6.3 ACE S(α, β) Continuous and Discrete Energy Implementations

As previously mentioned in Chapter 5, the ACE $S(\alpha, \beta)$ scattering data seeks to perform more accurate modeling of the transport of thermal neutrons in the presence

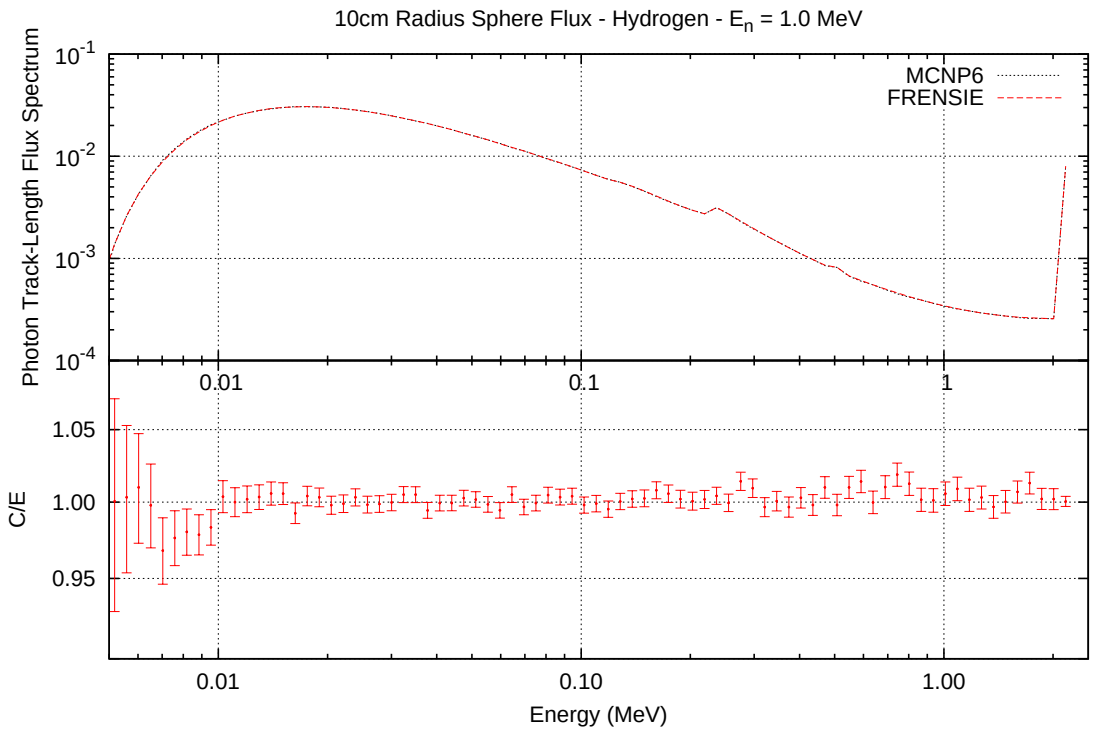

Figure 6.5: **Hydrogen sphere problem for photon generation from neutron reactions.** *In this problem, a monoenergetic 1 MeV isotropic neutron source is located at the center of a hydrogen sphere of density 1 at/b-cm and temperature 2500K. Photons are generated and are transported through the medium and tallied via an energy-dependent track-length flux tally.*

of molecules and crystalline solids. The $S(\alpha, \beta)$ thermal scattering cross section in the ENDF and ACE files can be broken up into primary three components: coherent scattering, incoherent scattering, and inelastic scattering [17].

Coherent and incoherent scattering arise from the interaction of a neutron with a system of N particles. The primary difference between coherent and incoherent elastic scattering is that coherent depends on the interaction of generated waves, while incoherent is a simple sum of noninterfering waves. For example, coherent elastic scattering involves the scattering of the neutron off of an entire lattice which can be described as an infinitely massive target. In this way, coherent elastic scattering is incredibly important for materials which have crystalline lattice structures, such as graphite and beryllium. As incoherent elastic scattering is a sum of non-interfering waves, it is best used to describe the interactions of neutrons with systems which

do not have a firm crystalline structure. For this reason, incoherent elastic scattering will be the dominant form of scattering in hydrogenous materials such as polyethylene and water [17].

Inelastic scattering, as the name implies, refers to the scattering event in which kinetic energy is lost through an interaction. This occurs when a neutron excites the target. Rather than the typical form of excitation, in thermal neutronics the excitation is typically in the form of phonon production in crystalline structures and vibrations and rotations for liquids or gases. The functional form of the inelastic scattering cross section used in ENDF and ACE is as follows [17]:

$$\sigma_{in}(E' \rightarrow E, \hat{\Omega}' \rightarrow \hat{\Omega}, T) = \frac{\sigma_b}{2kT}\sqrt{\frac{E}{E'}}e^{-\beta/2}S(\alpha, \beta \mid T). \tag{6.2}$$

Here again α and β retain their previous definitions as the momentum and energy transfer terms respectively. They are stated again for clarity as follows:

$$\alpha(E', E, \mu) = \frac{E' + E - 2\mu\sqrt{E'E}}{AkT}, \tag{6.3}$$

and

$$\beta(E', E) = \frac{E - E'}{kT}. \tag{6.4}$$

In these equations E' and E are the incident and resultant energies respectively, μ is the scattering angle cosine, A is the atomic mass ratio, and kT is the ambient temperature of the target medium. The functional form and derivation of the $S(\alpha, \beta)$ function which captures the coherent and incoherent elastic scattering physics is presented in [17].

One goal of this work is to implement and utilize the existing $S(\alpha, \beta)$ data in the forward case to complete the forward neutron physics in FRENSIE. To do so, the ability to parse and model ACE version of the $S(\alpha, \beta)$ transport has been implemented. In order to achieve this in FRENSIE the following tasks were completed:

- Parse and construct the cross sections and energy/angle transfer probabilities associated with the elastic (coherent and incoherent) and inelastic (coherent and incoherent) data present in the ACE tables.
- Construct reaction classes to handle the new sampling mechanics as well as modify existing cross sections in the thermal region of interest.
- Construct nuclide classes which contain the modified reactions.

- Refactor the collision handler to allow for the generation of duplicate nuclides which differ in the thermal scattering cross section.

All of these tasks have been completed and for a more in depth look at how the structure of FRENSIE changed due to the addition of these changes see appendix C which contains comparison flow charts. Further, appendix C discusses how these changes allow for the investigation of specific reactions and mechanics going forward to better test and benchmark FRENSIE.

A benchmark test was run to compare the FRENSIE implementation of the ACE $S(\alpha, \beta)$ data against the MCNP6 implementation. The test problem consists of a 20 cm radius sphere of hydrogen (modeled as H in H_2O) at a density of 1 g/cm^3 and ambient temperature of 293.6K. Neutrons were produced from an isotropic distribution at the center of the sphere with an energy of 1 eV. The results are shown in Figure 6.6.

It can be seen that for energies below roughly $1e{-}8$ MeV, the results are in good agreement and the three sigma rule indicates that there are no significant differences between the two models. However, above this region there is statistically significant deviation, well outside of the range of three standard deviations. For this reason, significant internal testing in FRENSIE was undergone to ensure that the sampling procedures for the ACE $S(\alpha, \beta)$ reactions were implemented properly. Thorough unit testing ensured that the sampling procedures were in fact correct and were producing the expected results when sampling and interpolating on the data.

After verification of the internal sampling routines in FRENSIE, investigation into the ACE data itself was initiated. It was found that there exist several severe numerical inaccuracies in the continuous energy $S(\alpha, \beta)$ data sets published in 2012. For example, while parsing through the data one is able to find a handful of instances wherein the cosine scattering distributions are not bounded on the region [-1,1], but exceed these bounds by up to 20%. This is, of course, non-physical behavior as scattering angle cosine must be bounded on the region [-1,1]. Dr. Jeremy Conlin is one of the primary authors of the 2012 continuous energy $S(\alpha, \beta)$ ACE data and has been helpful through personal communication in highlighting and understanding these errors. Through communication Dr. Conlin expressed that these errors were previously unknown, that there is little significant error checking and correction (as is done in FRENSIE for these data sets), and that there is no specific timeline for the correction of the data [33].

As one more layer of investigation work was undertaken to utilize the older discrete $S(\alpha, \beta)$ tables which sample discrete outgoing energies and angles. One of

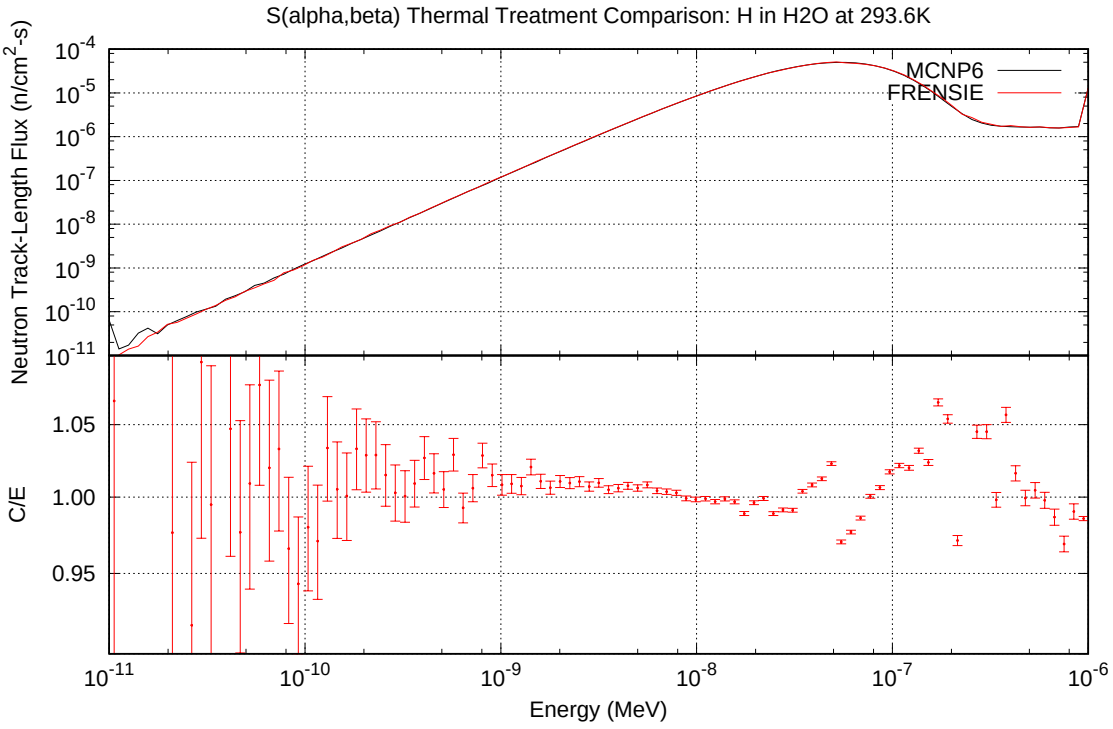

Figure 6.6: **Comparison of S(α, β) treatment in MCNP6 and FRENSIE.** *In this problem 1 eV neutrons are produced isotropically at the center of a sphere of hydrogen using the S(α, β) cross section. While there is good agreement over the lower energy range* (1e−11, 1e−8) *MeV, the high energy region of the thermal spectrum shows significant deviations.*

the primary reasons this data is no longer in use is due to the fact that distributions of only roughly 64 outgoing energies and 20 angles per outgoing energy for each incoming energy produces ray effects (spatially and energetically) in low density and voided regions. However, there still existed concern that FRENSIE was incapable of sampling the provided data appropriately. Thus, the discrete $S(\alpha, \beta)$ tables were implemented in FRENSIE and significant work was undertaken to ensure that the underlying sampling routines correctly reproduced the 64 discrete outgoing energies and 20 discrete outgoing angles per energy. It was found that FRENSIE appropriately samples the outgoing energy and angle states from the discrete ACE $S(\alpha, \beta)$ tables.

One final error was found in the discrete tables which is also present in the continuous tables and appears to be an error in MCNP5/6 and not in the underlying

data itself. MCNP adopts a right-sided approach to matching the elastic cross section to the thermal scattering $S(\alpha, \beta)$ cross section. As these two distributions do not exist on the same energy grid, the elastic scattering cross section and transfer probabilities are extended down to the maximum energy E_m in the $S(\alpha, \beta)$ tables. However, at the interface between these two distributions the edge case is not handled. One can show with a broomstick problem that as one approaches E_m from above, the expected elastic scattering behavior is observed. Further, if one approaches E_m from below, the expected $S(\alpha, \beta)$ behavior is observed. However, as one becomes arbitrarily close to the energy $E = E_m$, neither model matches (or even approximates) the observed result. The average energy is found to drop by roughly 1.5 orders of magnitude, a value far below what would be expected for any form of elastic scattering. It is suspected that MCNP5/6 do not handle the edge case transition well between these two distributions, and thus scattering through the energy E_m may also induce error when using the $S(\alpha, \beta)$ treatment in MCNP5/6. Figure 6.7, 6.8, and 6.9 depict the outgoing energy behavior of neutrons when approaching above, below and at the transition energy E_m and utilizing the discrete $S(\alpha, \beta)$ reaction data for a hydrogen broomstick problem. It can be clearly seen that when the incident energy is exactly the energy E_m, the outgoing energy physics do not match either the elastic scattering model or the discrete $S(\alpha, \beta)$ model, nor is it a convolution of the two methods.

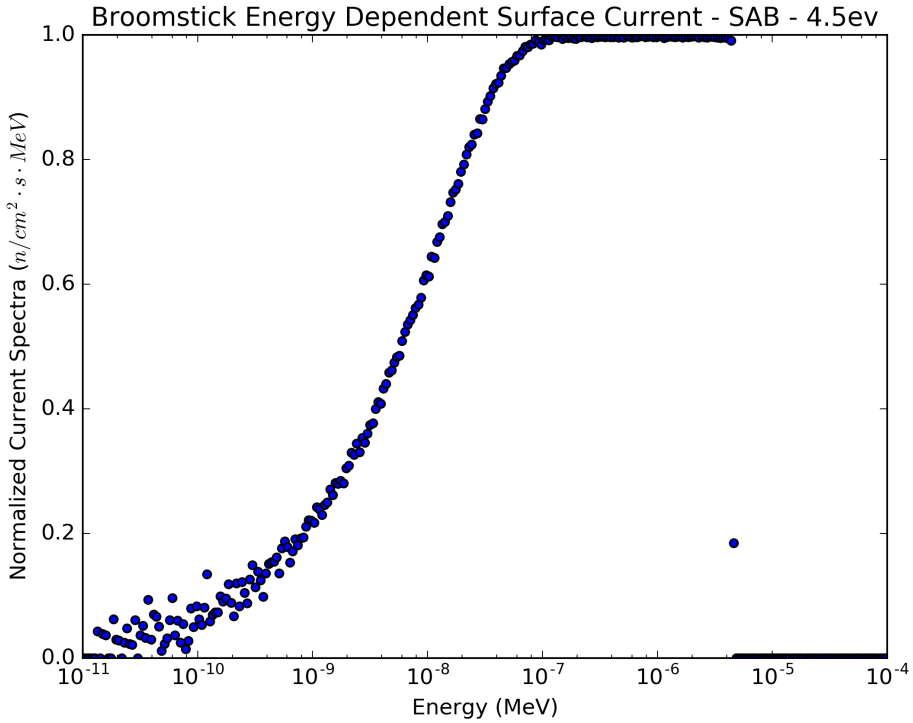

Figure 6.7: **Normalized broomstick neutron surface current just above S(α, β) region.** *When the incident neutron energy is just above the* S(α, beta) *region, the expected elastic scattering behavior is observed in MCNP5/6.*

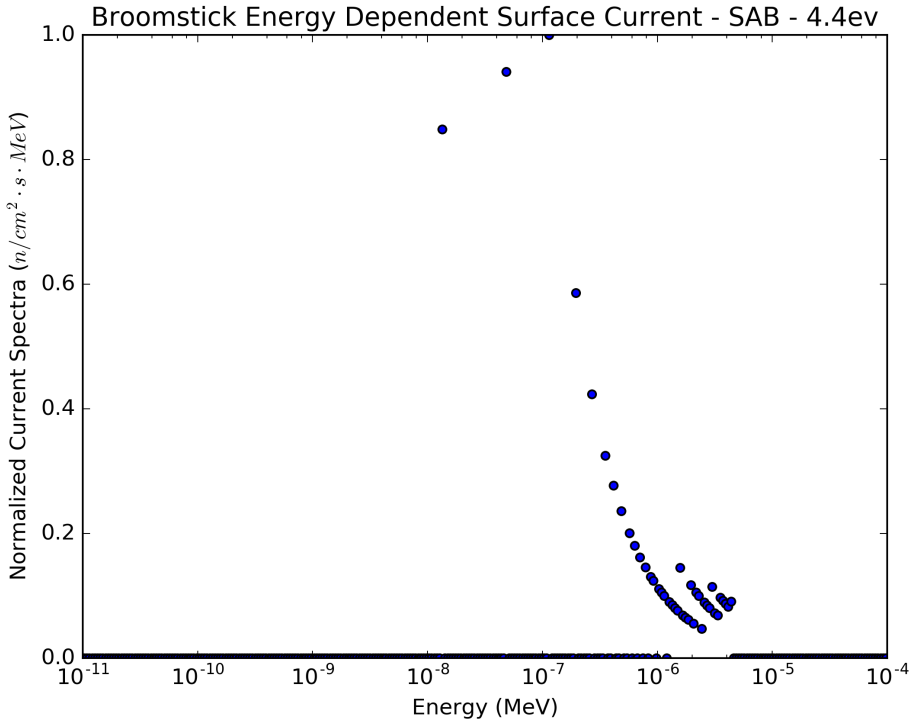

Figure 6.8: **Normalized broomstick neutron surface current just below S(α, β) region.** *When the incident neutron energy is just above the* S(α, beta) *region, the expected elastic scattering behavior is observed in MCNP5/6, with the population of 64 discrete energy bins.*

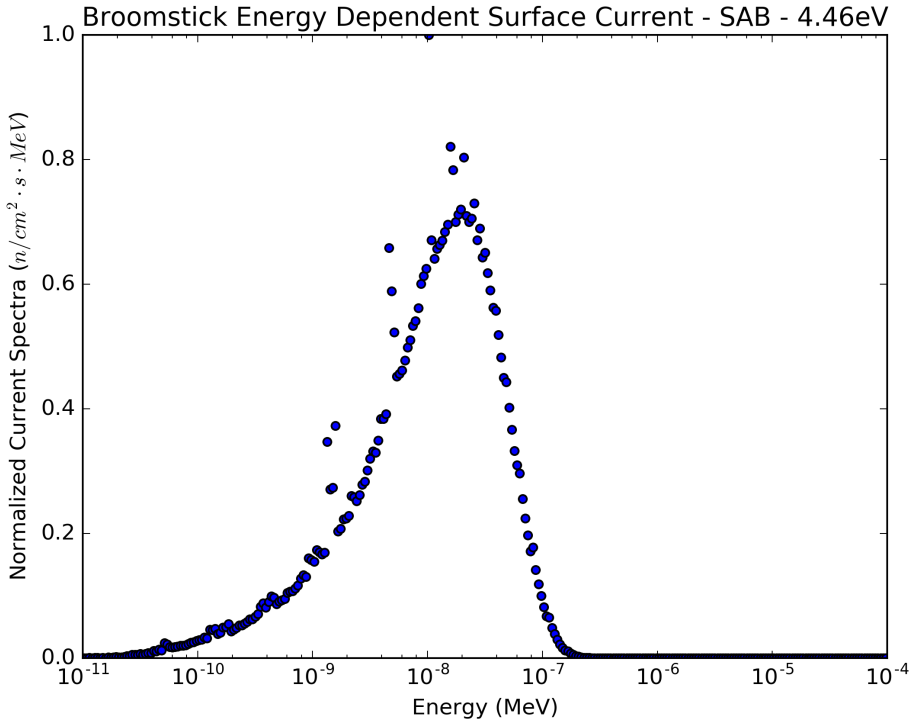

Figure 6.9: **Normalized broomstick neutron surface current at S(α, β) cutoff energy.** *When the incident neutron energy is exactly the S(α, β) cutoff energy, erroneous behavior is observed in the outgoing neutron energy sampling in MCNP5/6.*

6.4 Chapter Summary

This chapter dealt with the implementation and validation of forward neutron physics in FRENSIE. Some of the key takeaways from this chapter are:

- All forward neutron physics present in the ACE data files used by MCNP have been implemented in FRENSIE.
- Several validation test cases have been run to ensure that all ACE laws are implemented and all reactions contained in the ACE tables may be sampled and modeled appropriately. Test results show good agreement between FRENSIE and MCNP.
- Decoupled photon production from neutron reactions has been implemented in FRENSIE and shows good agreement with MCNP.

- The 2012 ACE interpretation of the ENDF $S(\alpha, \beta)$ data has been implemented in FRENSIE. In the process of implementation errors were found in the underlying data which consisted primarily of non-physical bounds on cosine bins for the outgoing angular states.
- Further investigation was undertaken via the implementation of the multi-group ACE $S(\alpha, \beta)$ data and additional non-physical behavior was found in the sampling routines in MCNP5/6 regarding the transition from the standard elastic scattering cross section to the $S(\alpha, \beta)$ cross section.
- Dr. Jeremy Conlin, the primary author on the ACE $S(\alpha, \beta)$ data at Los Alamos has been made aware of these previously unknown issues with the underlying data and sampling routines.

Chapter 7

Forward and Adjoint Free Gas S(α, β) Derivation

Chapters 5 and 6 touched on thermal neutron scattering and the importance of accurate models. This chapter will discuss the derivation of a novel free gas thermal neutron scattering method which is applicable both in the forward and adjoint cases. This will not only provide the ability for more accurate transport for thermal particles in existing simulations, but will allow for high fidelity continuous-energy adjoint thermal neutron problems to be constructed.

7.1 Motivation for a New Thermal Neutron Treatment

It may appear at first unimportant to develop a new model for thermal neutron transport when cross sections in the thermal region currently exist, and there have been various methods developed for free gas scattering [16]. Yet there exist two key reasons which have driven the development of this method.

The first reason for developing a new free gas thermal scattering method is to be able to handle nuclear data without approximation. Typically approximations are made to simplify the integration of the cross section that arises from the derivation of free gas scattering. This is often either a legendre polynomial expansion of the cross section, or a simplified functional form, or sum of functional forms [16]. The issue with these methods is that they do not utilize the wealth of information that is currently available in the tabular cross section data. Another key approximation made in many of these derivations is that the transfer probability for the scattering angle cosine is isotropic in the center of mass. However, as the particle increases in energy this approximation becomes less accurate. There exists the scattering angle transfer probabilities tabulated in the ENDF/ACE data which may be used directly. For these reasons it is imperative that a free gas scattering model be derived with the ability to utilize the existing tabular data for cross sections and scattering angle transfer probabilities. While the differences in the forward simulation will be small due to the need to use existing zero-temperature cross sections and angular data, the ability to have a model which can utilize any form of the zero-temperature

cross section and angular transfer probability opens up the door to higher fidelity modeling in the future.

The second and primary reason for developing this method is to have a high-fidelity continuous-energy treatment of adjoint thermal scattering. Currently the only modern Monte Carlo radiation transport code which has implemented adjoint neutronics methods is MCBEND. However, one of the outstanding issues with the implementation is the treatment of the thermal neutron group using the one-group approximation [19]. This states that all neutrons within the thermal group are at a single energy and utilize a thermally averaged cross section. As was discussed in Chapter 5 a one-group method does not accurately capture the behavior of the thermal neutrons. Further, one cannot resolve behavior within the thermal energy range which is quite often the energy range of interest. As the cross section rapidly changes in the thermal region, and the applications for thermal neutronics require high degrees of accuracy, the inability to resolve the behavior of neutrons within the thermal energy group greatly diminishes the efficacy of the adjoint implementation in MCBEND. For these reasons it is important to have a method which can be applied in the adjoint which will allow for the treatment of thermal neutrons. Note that the adjoint elastic and inelastic scattering cross sections derived in 5 could be of some use, however the additional physics regarding the temperature of the background media included in the free gas model makes it the preferred model for low energy neutron modeling. The remainder of this chapter will discuss the derivation of this method as well as the sampling routines developed for it. The numerical results associated with this work may be found in Chapter 8 and a fleshed out derivation may be found in Appendix A.

7.2 Derivation Overview

The derivation of this method is inspired by a historical derivation conducted by Blackshaw and Murray [16]. In their derivation two key assumptions were made which must be unmade in this work. The first assumption was that the scattering transfer probability is isotropic in the center of mass (CM) frame. Instead one will assume that there is polar isotropy, but the azimuthal angle which represents the scattering angle will have a generalized form $p(\mu_{cm} \mid E)$. The data associated with this may be generated by the user or can be taken directly from the ACE/ENDF data files. The second key assumption was the application of various expansions and functional forms of the cross section which will be replaced by the utilization

of a generalized form of the zero-temperature scattering cross section, $\sigma_b(E)$.

To begin, one assumes that the physics at play are elastic scattering events between neutrons and nuclei in a monatomic gas as reference temperature T. Further, the monatomic gas is assumed to have velocities in line with an isotropic Maxwellian velocity distribution for temperature T. Thus, the relative velocity between a neutron and target nucleus is of utmost importance in determining the outgoing particle states. This forces the derivation to be handled primarily in velocity space. Once a result has been obtained it will be transformed to energy and angle space, and eventually to α and β space for easier evaluation in the forward and adjoint.

To begin, one will define a scattering kernel $K(\bar{v}, \bar{v}')$ as

$$K(\bar{v}, \bar{v}') = \int_{\bar{V}} \nu_r \sigma_s(\nu_r) M(\bar{V}) P(\bar{v}, \bar{v}') d\bar{V}, \tag{7.1}$$

where

$\bar{v}$ is the incident neutron velocity in the lab frame,
$\bar{v}'$ is the outgoing neutron velocity in the lab frame,
$\bar{V}$ is the target nucleus velocity in the lab frame,
ν_r is the relative speed between the nucleus and the neutron,
$M(\bar{V})$ is the Maxwellian velocity distribution for nuclei,
and $P(\bar{v}, \bar{v}')$ is the probability that a neutron at $\bar{v}$ will scatter to $\bar{v}'$.

The meaning of $K(\bar{v}, \bar{v}')$ can be interpreted as the probability per unit time that a neutron at initial velocity $\bar{v}$ will interact with a medium which has velocities prescribed by Maxwellian distribution $M(\bar{V})$ and will be scattered into velocity $\bar{v}'$. Thus it is often referred to as the velocity scattering kernel, as it handles the state transition for a particle in state $\bar{v}$ to state $\bar{v}'$. It can be seen that $K(\bar{v}, \bar{v}')$ consists of three main components: the relative velocity and scattering cross section, the Maxwellian distribution for target nuclei velocities, and the probability of scattering from some velocity $\bar{v}$ to $\bar{v}'$. Each of these components will be handled individually.

Maxwellian Velocity Distribution

Perhaps the simplest component to handle is the Maxwellian velocity distribution for the target nuclei. The Maxwellian distribution for velocities in a monatomic gas of temperature T is a well known functional form. The assumption herein is

that there is no preferred direction for particles in the media, meaning simply that there must be a uniform concentration of particles of the nuclei throughout the media. Since materials are defined as uniformly mixed in Monte Carlo simulations, this approximation is upheld and thus the functional form of the Maxwellian is as follows:

$$M(\bar{V}) = \frac{M(V)}{4\pi} = \frac{B^3}{\pi^{3/2}} V^2 \exp\left(-B^2 V^2\right), \tag{7.2}$$

where

$$B^2 = \frac{M}{2kT}. \tag{7.3}$$

Here V is the speed of the monatomic gas nucleus which exists on the range $[0, \infty]$, M is the mass of the nucleus, k is the Boltzmann constant, and T is the temperature of the monatomic gas. This expression may be substituted into Equation 7.1. It should be noted that the integration over the target velocity $\bar{V}$ is actually an integration over the target speed V and angles ϕ and θ (or μ).

Scattering Probability $P(\bar{v}, \bar{v}')$

The scattering probability derivation is rather involved and thus an overview of it will be provided in this section. For more clarity in the derivation of the scattering probability see appendix A. Similar to the treatment for the transport kernels in Chapters 3 and 4, $P(\bar{v}, \bar{v}')$ may be broken up into the probability of changing speeds and the probability of changing directions. Thus, one will search for a form of $P(\bar{v}, \bar{v}')$ by first finding $P(v, v')$ and $P(\hat{\Omega}, \hat{\Omega}')$.

The first step in the derivation is to convert from the lab frame to the CM frame. Figure 7.1 depicts a vector diagram for the velocities in the lab and CM frames. From this one may define the following useful quantities:

$$\bar{v}_c = \left(\frac{1}{A+1}\right)\bar{v} + \left(\frac{A}{A+1}\right)\bar{V} \tag{7.4}$$

$$v_c^2 = \frac{v^2 + A^2V^2 + 2Avv\mu}{(A+1)^2} \tag{7.5}$$

$$v_r^2 = v^2 + V^2 - 2vV\mu \tag{7.6}$$

$$v_{cm} = \frac{Av_r}{A+1} = v'_{cm} \tag{7.7}$$

$$(v')^2 = (v'_{cm})^2 + v_c^2 + 2v_c v'_{cm}\mu_{cm} \tag{7.8}$$

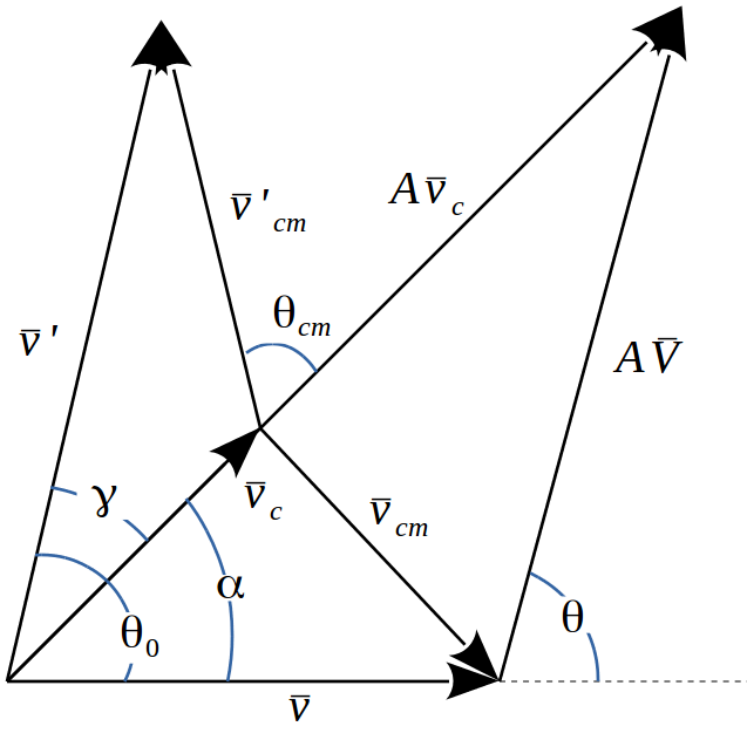

Figure 7.1: **Vector diagram for neutron and nucleus velocities in the lab and CM frames.** *In order to calculate the velocity transfer probability* $P(\bar{v}, \bar{v}')$*, one must make a transformation to the CM frame. The quantities defined in this diagram allow one to connect the CM velocities to lab velocities [16].*

$$\cos(\alpha) = \frac{v + AV\mu}{v_c(A+1)} \tag{7.9}$$

Here $\bar{v}_c$ represents the velocity of the CM frame, v_c is the speed of the CM frame, v_r is the relative speed between the neutron and the nucleus, v_{cm} is the CM neutron speed which is the same before and after elastic scattering collisions in the CM, v' is the outgoing neutron speed in the lab frame, α is the angle between the incoming lab neutron velocity and the CM velocity, and $mu_0 = \cos(\theta_0)$ is the lab frame scattering angle cosine.

At this point one has the tools to convert from the lab frame to the CM frame for the scattering probability $P(\bar{v}, \bar{v}')$. First, one must define the expression $P(\bar{v}, \bar{v}')dv'd\mu_0 d\phi_0$ as the probability that a neutron of velocity $\bar{v}$ will scatter into a velocity $d\bar{v}'$ about $\bar{v}'$. This could also be stated as the probability that a neutron of velocity $\bar{v}$ will scatter into a speed dv' about v', polar angle cosine of $d\mu_0$ about μ_0, and azimuthal angle

$d\phi_0$ about ϕ_0. Similarly, one could define the same quantity for the case in the CM frame, $P(\bar{v}_{cm}, \bar{v}'_{cm})dv'_{cm}d\mu_{cm}d\phi_{cm}$.

One may also note that both probabilities defined above refer to a neutron being scattered to the same point in the velocity phase space. Thus, the probabilities cannot be dependent upon the selected frame of reference and one may state the equality of these two probabilities as:

$$P(\bar{v}, \bar{v}')dv'd\mu_0 d\phi_0 = P(\bar{v}_{cm}, \bar{v}'_{cm})dv'_{cm}d\mu_{cm}d\phi_{cm}. \tag{7.10}$$

This expression can be simplified further if one recalls the Jacobian of transformation between the CM frame and the laboratory frame for two-body elastic kinematics as:

$$\frac{dv'_{cm}d\mu_{cm}d\phi_{cm}}{dv'd\mu_0 d\phi_0} = \frac{(v')^2}{(v'_{cm})^2}, \tag{7.11}$$

thus

$$P(\bar{v}, \bar{v}') = P(\bar{v}_{cm}, \bar{v}'_{cm})\frac{(v')^2}{(v'_{cm})^2}. \tag{7.12}$$

Now one may expand the CM scattering probability as the product of the angular transfer probability and the speed transfer probability as

$$P(\bar{v}_{cm}, \bar{v}'_{cm}) = P(v_{cm}, v'_{cm})P(\hat{\Omega}_{cm}, \hat{\Omega}'_{cm}). \tag{7.13}$$

For the angular scattering probability, one will assume that the system is isotropic in the azimuthal angle. This is due to the fact that in two-body reactions, the angle of interest is the change in angle from incoming direction, and thus the azimuthal angle becomes unimportant as the direction can be incoming direction is arbitrarily oriented in space. However, this derivation will not assume isotropic behavior in the scattering angle cosine, and thus the angular scattering probability may be written as:

$$P(\hat{\Omega}_{cm}, \hat{\Omega}'_{cm}) = \frac{1}{2\pi}p(\mu_{cm}), \tag{7.14}$$

where $p(\mu_{cm})$ is assumed to be a known probability function for sampling the scattering angle cosine.

The speed scattering probability may be observed directly from Equation 7.7. It is known that the incoming and outgoing velocities for elastic scattering in the CM frame will be identical, and thus the probability of changing speed is zero. Therefore

the speed scattering probability will be represented as the dirac delta function:

$$P(\nu_{cm}, \nu'_{cm}) = \delta(\nu'_{cm} - \nu_{cm}). \tag{7.15}$$

At this point one has a functional form for the initial velocity scattering probability $P(\bar{\nu}, \bar{\nu}')$ as

$$P(\bar{\nu}, \bar{\nu}') = \frac{(\nu')^2}{(\nu'_{cm})^2} \left(\frac{\delta(\nu'_{cm} - \nu_{cm})}{2\pi} \right) p(\mu_{cm}). \tag{7.16}$$

To continue with the derivation, one must convert the scattering probability $P(\bar{\nu}, \bar{\nu}')$ into a form which will allow for the evaluation of the total scattering kernel $K(\bar{\nu}, \bar{\nu}')$. While this is a very important component in the derivation, it is lengthy and rather involved. Thus the final result of this portion of the derivation will be presented herein to allow the reader to proceed. The contents of this portion of the derivation are located in appendix A for those interested. The final result is the expression

$$P(\bar{\nu}, \bar{\nu}') = \left[\frac{\nu' \nu_{cm} \delta\left(\phi(\nu'_{cm}) - \phi(\nu_{cm})\right)}{\pi (\nu'_{cm})^2 \nu_c \left(k_2^2 - (s - k_1)^2\right)^{1/2}} \right] p(\mu_{cm}), \tag{7.17}$$

where ϕ is the azimuthal angle of $\bar{\nu}_c$ and $\bar{V}$ about $\bar{\nu}$ as defined in appendix A. The remaining unknowns are defined as follows:

$$k_1 = \mu_0 \cos(\alpha), \tag{7.18}$$

$$k_2 = \sqrt{1 - \mu_0^2} \sin(\alpha), \tag{7.19}$$

and

$$s = \frac{(\nu')^2 - \nu_{cm}^2 + \nu_c^2}{2\nu' \nu_c}. \tag{7.20}$$

Again note that α is the angle between the CM and lab frames.

Scattering Kernel $K(\bar{\nu}, \bar{\nu}')$

Substituting equations 7.2 and 7.16 into Equation 7.1 one finds the following expression:

$$K(\bar{\nu}, \bar{\nu}') = \int\int\int \left[\nu_r \sigma_s(\nu_r) P(\mu_{cm})\right] \left[\frac{\nu' \nu_{cm} \delta\left(\phi(\nu'_{cm}) - \phi(\nu_{cm})\right)}{\pi (\nu'_{cm})^2 \nu_c \left(k_2^2 - (s - k_1)^2\right)^{1/2}} \right] \left[\frac{B^3}{\pi^{3/2}} V^2 \exp\left(-B^2 V^2\right) \right] dV d\mu d\phi. \tag{7.21}$$

One may immediately integrate over the azimuthal angle ϕ as it appears only in the delta function and $\nu_{cm} = \nu'_{cm}$. Simplifying the expression slightly leads to:

$$K(\bar{\nu}, \bar{\nu}') = \int\int [\nu_r \sigma_s(\nu_r) P(\mu_{cm})] \left[\frac{\nu'}{\pi \nu_{cm} \nu_c \left(k_2^2 - (s - k_1)^2\right)^{1/2}} \right] \left[\frac{B^3}{\pi^{3/2}} V^2 \exp\left(-B^2 V^2\right) \right] dV d\mu. \tag{7.22}$$

The expression can be simplified further by noting the relationship between ν_r and ν_{cm} found in Equation 7.7:

$$K(\bar{\nu}, \bar{\nu}') = \int\int \left(\frac{A+1}{A} \right) \frac{\nu' \sigma_s(\nu_r) P(\mu_{cm})}{\pi \nu_c \left(k_2^2 - (s - k_1)^2\right)^{1/2}} \left[\frac{B^3}{\pi^{3/2}} V^2 \exp\left(-B^2 V^2\right) \right] dV d\mu. \tag{7.23}$$

At this point one must step back and assess the current state of the equation. There currently exist four possible variables for integration: V, μ, ν_c, and ν_r. To remove ν_c from the equation, one must replace it with the expression from Equation 7.5 which will replace it with V and μ. To eliminate μ, one must rewrite μ and its integration as a function of V and ν_r, at which point the problem will be left in terms of two variables V and ν_r. Utilizing Equation 7.6 one may take the derivative of each side to find:

$$d\mu = -\frac{\nu_r}{\nu V} d\nu_r. \tag{7.24}$$

Combined with Equation 7.6 one may now remove μ from the equation and the integration. Thus the simplified expression becomes:

$$K(\bar{\nu}, \bar{\nu}') = -\frac{2B^3}{\pi^{3/2}} \left[\frac{(A+1)^2 (\nu')^2}{A \pi \nu} \right] \int_{\nu_r} \nu_r \sigma_s(\nu_r) p(\mu_{cm}) \cdot \left[\int_{V(\nu_r)} \frac{V \exp(-B^2 \nu^2)}{\sqrt{a' V^4 + b' V^2 + c'}} dV \right] d\nu_r \tag{7.25}$$

where the definitions for a', b', and c' are as follows:

$$a' = -\frac{A^2 (\nu^2 + (\nu')^2 - 2\nu\nu'\mu_0)}{\nu^2}, \tag{7.26}$$

$$b' = 2A\left(-\nu^2 - \left(2\mu_0^2(A+1)+1\right)(\nu')^2 + A\nu_r^2 + \frac{A(\nu_r\nu')^2}{\nu^2} + (A+3)\nu\nu'\mu_0 + \frac{(A+1)(\nu')^3\mu_0}{\nu} - \frac{2A\nu'\nu_r^2\mu_0}{\nu}\right) \tag{7.27}$$

$$\begin{aligned} c' = &-\nu^4 - (A+1)^2(\nu')^4 - \frac{A^2}{\nu^2}\left(\nu^2 + (\nu')^2 - 2\nu\nu'\mu_0\right)\nu_r^4 \\ &- \left[(A+1)^2 + a + 4\mu_0^2(A+1)\right](\nu\nu')^2 + 2A(\nu\nu_r)^2 \\ &+2A(2A+1+2\mu_0^2)(\nu')^3\nu_r^2 + 2(A+1)(A+2)\nu(\nu')^3\mu_0 + 2(A+2)\nu^3\nu'\mu_0 \\ &-2A(A+3)\nu\nu'\nu_r^2\mu_0 - 2A(A+1)\frac{(\nu')^3\nu_r\mu_0}{\nu} \end{aligned} \tag{7.28}$$

Now one must handle the interior integral over the target speed V. To do this a change of variables is suggested. If one allows $y = V^2B^2$, the interior integration over V may be rewritten as:

$$\frac{1}{2}\int_y \frac{\exp(y)}{\sqrt{ay^2+by+c}}, \tag{7.29}$$

where

$$\begin{aligned} a &= a' \\ b &= B^2 b' \\ c &= B^4 c'. \end{aligned}$$

Another change of variables is suggested to allow for the analytical evaluation of the integral and its limits. Take the following expression for y:

$$y = \frac{-\sqrt{-b^2-4ac}\cos(\lambda)}{2a} - \frac{b}{2a}. \tag{7.30}$$

This definition leads to the limits of integration $[y_1, y_2]$ transforming to the new limits of integration $[\lambda_1, \lambda_2]$ which take on the values of $[0, \pi]$ respectively. Thus the integral in Equation 7.29 may be written as

$$\frac{1}{2\sqrt{-a}}\exp\left(\frac{b}{2a}\right)\int_0^\pi \exp\left(\frac{-\sqrt{-b^2-4ac}\cos(\lambda)}{2a}\right)d\lambda. \tag{7.31}$$

The equation now can be related to a known integral solution of the following form

[16]:

$$\int_0^{\pi} \exp\left(\pm\rho\cos r\right) dr = \pi I_0(\rho), \tag{7.32}$$

where I_0 is the zero-order modified Bessel function of the first kind. Thus, one may apply the general solution to find the the simplified expression for the scattering kernel as:

$$\begin{aligned} K(\bar{v},\bar{v}') = &\frac{4B^3}{\pi^{3/2}}\left(\frac{A+1}{A}\right)^2 \frac{v'^2}{\sqrt{v^2+v'^2-2vv'\mu}} \cdot \exp\left\{\left(\frac{-B^2}{A}\right)\left[(A+1)vv'\mu - v^2\right]\right\} \\ &\int_{v_{r1}}^{v_{r2}} v_r\ \sigma_s(v_r)\ p(\mu_{cm}|E)\ \exp(-B^2v_r^2) \\ &\cdot I_o\left(2B^2vv'\left\{(1-\mu^2)\left[\frac{v_r^2}{(v^2+v'^2-2vv'\mu)} - \left(\frac{A+1}{2A}\right)^2\right]\right\}^{1/2}\right) dv_r. \end{aligned} \tag{7.33}$$

Conversion to Energy and Angle Space

While the expression in Equation 7.33 is certainly of use, there is no tabular cross section data in terms of the relative speed between a neutron and a target. Further, it is common to think of neutron reactions in terms of energy, rather than speed, and thus the expression must be modified to be in terms of energy and angle rather than relative velocity. In order to do this one must revisit the kinematic discussion to relate the relative speed v_r and the CM scattering angle cosine μ_{cm}. Osborn provides an incredibly detailed schematic for thermal neutron kinematics in his paper *Some Characteristics of the Thermal Neutron Scattering Probability* [34]. For more visually minded readers, it is suggested to view the schematic in the referenced work. The feature of interest from Osborn's discussion is the relationship between the relative velocity and the center of mass scattering angle:

$$\bar{v}_r = \frac{\bar{v}-\bar{v}'}{2\cos((\pi-\theta_{cm})/2)}\left(\frac{A+1}{A}\right). \tag{7.34}$$

To simplify the cosine expression one must recall the following trigonometric identity:

$$\begin{aligned}\cos((\pi-\theta_{cm})/2) &= \sqrt{\frac{1+\cos(\pi-\theta)}{2}} \\ &= \sqrt{\frac{1+(\cos\pi\cos\theta-\sin\pi\sin\theta)}{2}} \\ &= \sqrt{\frac{1-\cos\theta}{2}} \\ &= \sqrt{\frac{1-\mu_{cm}}{2}}. \end{aligned} \tag{7.35}$$

This can be substituted into Equation 7.34 to arrive at the expression:

$$v_r = \frac{|\bar{v}-\bar{v}'|}{2\sqrt{\frac{1-\mu_{cm}}{2}}}\left(\frac{A+1}{A}\right). \tag{7.36}$$

One may also define a new term p which captures magnitude of the the change in velocity:

$$\begin{aligned} p^2 &= (|\bar{v}-\bar{v'}|)^2 \\ &= (\bar{v}-\bar{v'})\cdot(\bar{v}-\bar{v'}) \\ &= v^2+v'^2-2vv'\mu. \end{aligned} \tag{7.37}$$

Thus Equation 7.36 may be written even more simply as:

$$v_r^2 = \frac{p^2}{2(1-\mu_{cm})}\left(\frac{A+1}{A}\right)^2. \tag{7.38}$$

Taking the derivative of both sides with respect to v_r and μ_{cm} respectively yields the differential relationship:

$$v_r dv_r = p^2\left(\frac{A+1}{A}\right)^2\left(\frac{1}{4(1-\mu_{cm})^2}\right)d\mu_{cm} \tag{7.39}$$

At this point one may convert the integral in Equation 7.33 over the relative velocity to an integral over the CM scattering angle cosine:

$$\begin{aligned}
&\int_{\nu_{r1}}^{\nu_{r2}} \nu_r\ \sigma_s(\nu_r)\exp(-B^2\nu_r^2)\cdot I_o\left(2B^2\nu\nu'\left\{(1-\mu^2)\left[\frac{\nu_r^2}{p^2}-\left(\frac{A+1}{2A}\right)^2\right]\right\}^{1/2}\right)d\nu_r \\
&\quad=\int_{\mu_{cm1}}^{\mu_{cm2}}\frac{p^2}{(1-\mu_{cm})^2}\cdot\left(\frac{A+1}{A}\right)^2\ \sigma_s(\mu_{cm})\ p(\mu_{cm}|E)\ \exp\left(-\frac{B^2p^2}{2(1-\mu_{cm})}\cdot\left(\frac{A+1}{A}\right)^2\right)\cdot \\
&\qquad I_o\left(2B^2\nu\nu'\left\{(1-\mu^2)\left[\frac{1}{2(1-\mu_{cm})}\cdot\left(\frac{A+1}{A}\right)^2-\left(\frac{A+1}{2A}\right)^2\right]\right\}^{1/2}\right)d\mu_{cm} \\
&\quad=\left(\frac{A+1}{A}\right)^2 p^2\int_{\mu_{cm1}}^{\mu_{cm2}}\frac{\sigma_s(\mu_{cm})\ p(\mu_{cm}|E)}{(1-\mu_{cm})^2}\ \exp\left(-\frac{B^2p^2}{2(1-\mu_{cm})}\cdot\left(\frac{A+1}{A}\right)^2\right)\cdot \\
&\qquad I_o\left(2B^2\nu\nu'\left(\frac{A+1}{2A}\right)\left\{(1-\mu^2)\left[\frac{2}{1-\mu_{cm}}-1\right]\right\}^{1/2}\right)d\mu_{cm}. \qquad (7.40)
\end{aligned}$$

One may now rewrite all of Equation 7.33 in terms of energy and angle if one notes the kinetic energy relationship:

$$E=\frac{m\nu^2}{2}. \qquad (7.41)$$

Thus the simplified expression in Equation 7.33 after algebraic manipulation becomes:

$$\begin{aligned}
K(\bar{v},\bar{v}') =&\frac{2B^3p}{\pi^{3/2}}\left(\frac{A+1}{A}\right)^4\left(\frac{E'}{m}\right)\cdot\exp\left(\frac{E}{kT}\right)\exp\left(-\frac{(A+1)\sqrt{EE'}\mu}{kT}\right)\cdot \\
&\int_{\mu_{cm1}}^{\mu_{cm2}}\frac{\sigma_s(\mu_{cm})\ p(\mu_{cm}|E)}{(1-\mu_{cm})^2}\ \exp\left(-\frac{B^2p^2}{2(1-\mu_{cm})}\left(\frac{A+1}{A}\right)^2\right)\cdot \\
&I_o\left(\left(\frac{A+1}{kT}\right)\sqrt{EE'(1-\mu^2)\left[\frac{1+\mu_{cm}}{1-\mu_{cm}}\right]}\right)d\mu_{cm}. \qquad (7.42)
\end{aligned}$$

All that is left to do now is to convert the limits of integration from relative velocity to CM scattering angle cosine. It can be shown from Equation 7.6 that the maximum and minimum relative velocities are:

$$\nu_{r,min}=p\left(\frac{A+1}{2A}\right)\quad,\quad\nu_{r,max}=\infty. \qquad (7.43)$$

One may then relate these relative velocities to μ_{cm} via Equation 7.36 to find the cosine limits as:

$$\mu_{min} = -1 \ , \quad \mu_{max} = 1. \tag{7.44}$$

Thus the final expression for the scattering kernel in terms of energy and angle is as follows:

$$\begin{aligned} K(E \to E', \mu) = &\frac{2B^3 p}{\pi^{3/2}} \left(\frac{A+1}{A}\right)^4 \left(\frac{E'}{m}\right) \cdot \exp\left(\frac{E}{kT}\right) \exp\left(-\frac{(A+1)\sqrt{EE'}\mu}{kT}\right) \cdot \\ &\int_{-1}^{1} \frac{\sigma_s(\mu_{cm})\ p(\mu_{cm}|E)}{(1-\mu_{cm})^2}\ \exp\left(-\frac{B^2 p^2}{2(1-\mu_{cm})}\left(\frac{A+1}{A}\right)^2\right) \cdot \\ &I_o\left(\left(\frac{A+1}{kT}\right)\sqrt{EE'(1-\mu^2)\left[\frac{1+\mu_{cm}}{1-\mu_{cm}}\right]}\right) d\mu_{cm}. \end{aligned} \tag{7.45}$$

Now one may write a generalized function which captures the impact of thermal motion on the elastic scattering cross section as [34]:

$$\nu\sigma_s(E \to E', \mu) dE' d\mu = \int \nu_r \sigma(\nu_r) P(\bar{\nu}, \bar{\nu}') M(\bar{V}) d\bar{V} d\bar{\nu}' d\mu. \tag{7.46}$$

Rearranging this equation yields an expression for the double differential elastic scattering cross section in terms of the previously derived scattering kernel K from Equation 7.45:

$$\begin{aligned} \sigma_s(E \to E', \mu) &= \left(\frac{1}{\nu}\right) \frac{d\nu'}{dE'} \int \nu_r \sigma(\nu_r) P(\bar{\nu}, \bar{\nu}') M(\bar{V}) d\bar{V} \\ &= \frac{K(E \to E', \mu)}{m_n \nu \nu'}. \end{aligned} \tag{7.47}$$

For the sake of clarity, the final form of the forward double differential elastic scattering cross section in energy and angle space is:

$$\begin{aligned} \sigma(E \to E', \mu) = &\frac{B^3 p}{m\pi^{3/2}} \left(\frac{A+1}{A}\right)^4 \sqrt{\frac{E'}{E}} \cdot \exp\left(\frac{E}{kT}\right) \exp\left(-\frac{(A+1)\sqrt{EE'}\mu}{kT}\right) \cdot \\ &\int_{-1}^{1} \frac{\sigma_s(\mu_{cm})\ p(\mu_{cm}|E)}{(1-\mu_{cm})^2}\ \exp\left(-\frac{B^2 p^2}{2(1-\mu_{cm})} \cdot \left(\frac{A+1}{A}\right)^2\right) \cdot \\ &I_o\left(\left(\frac{A+1}{kT}\right)\sqrt{EE'(1-\mu^2)\left[\frac{1+\mu_{cm}}{1-\mu_{cm}}\right]}\right) d\mu_{cm}. \end{aligned} \tag{7.48}$$

Conversion from (E, E', μ) to (α, β)

Although difficult to observe a priori, generation and sampling of the adjoint double differential cross section in terms of (E, E', μ) will prove cumbersome and computationally inefficient. For this reason, both the forward and adjoint cases will be converted to (α, β) space. One other benefit of this choice, outside of computational difficulty, is the reduction in data storage required. Rather than requiring tables which link $(E \to E' \to \mu)$ one need only link $(\beta \to \alpha)$, greatly reducing the quantity of data stored for each isotope.

The terms α and β describe the momentum and energy change of a particle in an interaction respectively. They are defined as follows:

$$\alpha = \frac{E + E' - 2\mu\sqrt{EE'}}{AkT}, \tag{7.49}$$

and

$$\beta = \frac{E' - E}{kT}, \tag{7.50}$$

where now E and E' represent the incoming and outgoing energies respectively. The valid range for each of these quantities is:

$$\beta \in \left[-\frac{E}{kT}, \infty\right], \tag{7.51}$$

and

$$\alpha \in \left[\frac{\left(\sqrt{E} - \sqrt{E - kT\beta^\dagger}\right)^2}{AkT}, \frac{\left(\sqrt{E} + \sqrt{E - kT\beta^\dagger}\right)^2}{AkT}\right]. \tag{7.52}$$

To implement this change of variables, one must calculate the Jacobian of transformation from (E', μ) to (α, β). It will be easiest to take the Jacobian of transformation from (α, β) to (E', μ) and then to invert the expression. The Jacobian may be calculated by taking the determinant of the mixed partial differential matrix. Thus the resulting expression is:

$$\begin{aligned}\sigma_s(\alpha, \beta) &= \frac{\sigma_s(E \to E', \mu)}{J_{\alpha,\beta}(E', \mu)} \\ &= \frac{A(kT)^2}{2\sqrt{EE'}}\sigma_s(E \to E', \mu)\end{aligned} \tag{7.53}$$

At this point one must substitute in the known expression for the double differential

cross section from Equation 7.48 and perform algebraic manipulations to convert from expressions of (E, E', μ) to (α, β). As the change of variables is key to the derivation of the method the conversion of each term will be shown below such that the final expression is left in terms of the incoming energy E, and the energy and momentum transfer terms β and α.

The leading terms ahead of the integration in Equation 7.48 after application of the Jacobian have the form

$$LT = \left(\frac{A(kT)^2}{2\sqrt{EE'}}\right) \frac{B^3 p}{m\pi^{3/2}} \left(\frac{A+1}{A}\right)^4 \sqrt{\frac{E'}{E}}. \tag{7.54}$$

Recalling the definitions for B and p provided earlier, this expression may be written in (α, β) space as

$$\begin{aligned}
&\left(\frac{A(kT)^2}{2\sqrt{EE'}}\right) \frac{(M/2kT)^{3/2}\left(\nu^2 + \nu'^2 - 2\nu\nu'\mu\right)^{1/2}}{m\pi^{3/2}} \left(\frac{A+1}{A}\right)^4 \sqrt{\frac{E'}{E}} \\
&= \left(\frac{A(kT)^2}{2E}\right) \left(\frac{A+1}{A}\right)^4 \left(\frac{M}{m}\right)^{3/2} \left(\frac{1}{2(\pi kT)^{3/2}}\right) \cdot \sqrt{E + E' - 2\sqrt{EE'}\mu} \\
&= \left(\frac{A(kT)^2}{2E}\right) \left(\frac{A+1}{A}\right)^4 \left(\frac{M}{m}\right)^{3/2} \left(\frac{1}{2(\pi kT)^{3/2}}\right) \sqrt{AkT}\sqrt{\alpha} \\
&= \frac{(A+1)^4}{4A\pi^{3/2}} \left(\frac{kT}{E}\right) \sqrt{\alpha}.
\end{aligned} \tag{7.55}$$

The leading exponential terms ahead of the integration in 7.48 may be converted to (α, β) space as

$$\begin{aligned}
&\exp\left(\frac{E}{kT}\right) \exp\left(-\frac{(A+1)\sqrt{EE'}\mu}{kT}\right) \\
&= \exp\left(\frac{E}{kT}\right) \exp\left(\frac{(A+1)A}{2}\left[\frac{-2\sqrt{EE'}\mu}{AkT}\right]\right) \\
&= \exp\left(\frac{E}{kT}\right) \exp\left(\frac{(A+1)A}{2}\left[\alpha - \frac{E}{AkT} - \frac{E'}{AkT}\right]\right) \\
&= \exp\left(\frac{E}{kT}\right) \exp\left(\frac{(A+1)A\alpha}{2}\right) \exp\left(-(A+1)\left[\frac{E}{2kT} + \frac{E'}{2kT}\right]\right) \\
&= \exp\left(-\frac{\beta}{2}\right) \exp\left(\frac{(A+1)A\alpha}{2}\right) \exp\left(-\frac{A\beta}{2}\right) \exp\left(-\frac{AE}{kT}\right) \\
&= \exp\left(-\frac{\beta}{2}\right) \exp\left(\frac{A}{2}\left[(A+1)\alpha - \beta\right]\right) \exp\left(-\frac{AE}{kT}\right).
\end{aligned} \tag{7.56}$$

The exponential within the integral in 7.48 may be converted to (α, β) space as

$$\begin{aligned}
&\exp\left[-\frac{(A+1)^2 p^2 B^2}{2A^2(1-\mu_{cm})}\right] \\
=&\exp\left[-\frac{(A+1)^2\left(\frac{2}{m}\right)(E+E'-2\sqrt{EE'}\mu)\left(\frac{M}{2kT}\right)}{2A^2(1-\mu_{cm})}\right] \\
=&\exp\left[-\frac{(A+1)^2\alpha}{2(1-\mu_{cm})}\right]. \qquad (7.57)
\end{aligned}$$

Finally, the modified Bessel function within the integral in 7.48 may be converted to (α, β) space as

$$\begin{aligned}
&I_o\left(\left(\frac{A+1}{kT}\right)\sqrt{EE'(1-\mu^2)\left[\frac{1+\mu_{cm}}{1-\mu_{cm}}\right]}\right) \\
=&I_o\left(\left(\frac{A+1}{kT}\right)\sqrt{EE'-EE'\mu^2\left[\frac{1+\mu_{cm}}{1-\mu_{cm}}\right]}\right) \\
=&I_o\left(\left(\frac{A+1}{kT}\right)\sqrt{(E^2+EE'-2\sqrt{EE'}\mu-E^2-EE'\mu^2+2\sqrt{EE'}\mu)\left[\frac{1+\mu_{cm}}{1-\mu_{cm}}\right]}\right) \\
=&I_o\left(\left(\frac{A+1}{kT}\right)\sqrt{\left[(AkTE)\alpha-(\sqrt{EE'}\mu-E)^2\right]\left[\frac{1+\mu_{cm}}{1-\mu_{cm}}\right]}\right) \\
=&I_o\left(\left(\frac{A+1}{kT}\right)\sqrt{\left[(AkTE)\alpha-(\beta-A\alpha)^2\frac{(kT)^2}{4}\right]\left[\frac{1+\mu_{cm}}{1-\mu_{cm}}\right]}\right) \\
=&I_o\left(\left(\frac{A+1}{2}\right)\sqrt{\left[\frac{4AE}{kT}\alpha-(\beta-A\alpha)^2\right]\left[\frac{1+\mu_{cm}}{1-\mu_{cm}}\right]}\right) \qquad (7.58)
\end{aligned}$$

Substituting in equations 7.55, 7.56, 7.57, and 7.58 into 7.48, the final expression for the neutron forward free-gas double differential elastic scattering cross section in (α, β) space is as follows:

$$\sigma_s(\alpha,\beta) = \frac{(A+1)^4}{4A\pi^{3/2}}\left(\frac{kT}{E}\right)\exp\left(-\frac{\beta}{2}\right)S(\alpha,\beta), \qquad (7.59)$$

where

$$S(\alpha,\beta) = \alpha^{1/2}\exp\left(\frac{A}{2}((A+1)\alpha-\beta)\right)I(\alpha,\beta), \qquad (7.60)$$

and

$$I(\alpha,\beta) = \int_{-1}^{1} \frac{\sigma_s(\mu_{cm})p(\mu_{cm} \mid E)}{(1-\mu_{cm}^2)} \exp\left(-\frac{(A+1)^2\alpha}{2(1-\mu_{cm})}\right) \cdot \exp\left(-\frac{AE}{kT}\right) I_0\left[\frac{A+1}{2}\sqrt{\left(\frac{4AE\alpha}{kT} - (\beta - A\alpha)^2\right)\left(\frac{1+\mu_{cm}}{1-\mu_{cm}}\right)}\right] d\mu_{cm}. \quad (7.61)$$

Now one has a fully defined expression for the double differential scattering cross section for free gas thermal scattering in terms of (α, β) and the known incoming energy E. All that is left is to generate the probability distributions governing α and β and develop sampling routines.

Notes on the Derivation of the Adjoint

The derivation of the adjoint free gas scattering model follows the same structure as the forward case. The primary difference is in definition the adjoint double differential scattering cross section. For elastic scattering with stationary scattering centers the adjoint elastic cross section is related to the forward cross section as [23]:

$$\sigma_s^\dagger(E \to E') = \sigma_s(E' \to E). \quad (7.62)$$

However, when the scattering centers are assumed to be in motion with a distribution of speeds from a Maxwellian velocity distribution about temperature T, one must use the principle of detailed balance to determine the relationship, as the one-to-one correlation between energy states is no longer preserved for the neutron kinetic energy as the relative speed of the nucleus plays a role in the kinematics. The principle of detailed balance may be stated as [6]:

$$\nu\, M(E)\, \Sigma_s^\dagger(E \to E') = \nu'\, M(E')\, \Sigma_s(E' \to E), \quad (7.63)$$

where

$$M(E) \equiv \frac{2\pi}{(\pi kT)^{3/2}} \sqrt{E} \exp\left(-\frac{E}{kT}\right). \quad (7.64)$$

It may also be assumed that the number density, N, is constant with respect to energy and thus drops out of both sides of Equation 7.63. This yields an expression in energy space for the principle of detailed balance as

$$E \exp\left(\frac{E}{kT}\right) \sigma_s^\dagger(E \to E') = E' \exp\left(\frac{E'}{kT}\right) \sigma_s(E' \to E), \quad (7.65)$$

thus

$$\sigma_s^\dagger(E \to E') = \frac{E'}{E} \exp\left(-\frac{E'-E}{kT}\right) \sigma_s(E' \to E). \tag{7.66}$$

Thus, the full form of the adjoint double differential free gas neutron scattering cross section in (E, E', μ) space as

$$\begin{aligned}\sigma^\dagger(E \to E', \mu) =& \frac{B^3 p}{m\pi^{3/2}} \left(\frac{A+1}{A}\right)^4 \sqrt{\frac{E'}{E}} \cdot \exp\left(\frac{E}{kT}\right) \exp\left(-\frac{(A+1)\sqrt{EE'}\mu}{kT}\right) \cdot \\ & \int_{-1}^{1} \frac{\sigma_s(\mu_{cm})\, p(\mu_{cm}|E')}{(1-\mu_{cm})^2} \exp\left(-\frac{B^2p^2}{2(1-\mu_{cm})} \cdot \left(\frac{A+1}{A}\right)^2\right) \cdot \\ & I_o\left(\left(\frac{A+1}{kT}\right)\sqrt{EE'(1-\mu^2)\left[\frac{1+\mu_{cm}}{1-\mu_{cm}}\right]}\right) d\mu_{cm}. \end{aligned} \tag{7.67}$$

where E is now the incoming adjoint energy and E' is the outgoing adjoint energy, with σ and $p(\mu_{cm})$ still reference the forward zero-temperature cross section and angular transfer probability respectively.

Another important distinction is in the definition of the adjoint $\alpha^\dagger$ and adjoint $\beta^\dagger$ as follows:

$$\alpha^\dagger = \frac{E + E' - 2\mu\sqrt{EE'}}{AkT} = \alpha, \tag{7.68}$$

and

$$\beta^\dagger = \frac{E - E'}{kT} = -\beta. \tag{7.69}$$

Note that there is no change in the momentum transfer term between the forward and the adjoint, but the adjoint energy transfer term $\beta^\dagger$ is the negative of the forward energy transfer term β. Along with the redefinition of $\alpha^\dagger$ and $\beta^\dagger$ one must recalculate the ranges over which these quantities exist for the limits of integration on the marginal probability density function (PDF) and cumulative distribution functions (CDF) used in sampling. The quantities $\alpha^\dagger$ and $\beta^\dagger$ exist over the ranges

$$\alpha^\dagger \in \left[\frac{\left(\sqrt{E} - \sqrt{E - kT\beta^\dagger}\right)^2}{AkT}, \frac{\left(\sqrt{E} + \sqrt{E - kT\beta^\dagger}\right)^2}{AkT}\right], \tag{7.70}$$

and

$$\beta^\dagger \in \left(-\infty, \frac{E}{kT}\right]. \tag{7.71}$$

At this point one may perform the conversion from (E, E', μ) space to $(\alpha^\dagger, \beta^\dagger)$

space. Utilizing the arguments in the forward conversion, one may directly infer that the adjoint double differential cross section in $(\alpha^\dagger, \beta^\dagger)$ space is as follows:

$$\sigma_s^\dagger(\alpha^\dagger, \beta^\dagger) = \frac{(A+1)^4}{4A\pi^{3/2}} \left(\frac{kT}{E}\right) \exp\left(\frac{\beta^\dagger}{2}\right) S(\alpha, \beta), \tag{7.72}$$

where

$$S(\alpha^\dagger, \beta^\dagger) = \left(\alpha^\dagger\right)^{1/2} \exp\left(\frac{A}{2}((A+1)\alpha^\dagger + \beta^\dagger)\right) I(\alpha^\dagger, \beta^\dagger), \tag{7.73}$$

and

$$I(\alpha^\dagger, \beta^\dagger) = \int_{-1}^{1} \frac{\sigma_s(\mu_{cm}) p(\mu_{cm} \mid E - kT\beta^\dagger)}{(1-\mu_{cm}^2)} \exp\left(-\frac{(A+1)^2\alpha^\dagger}{2(1-\mu_{cm})}\right) \cdot \exp\left(-\frac{AE}{kT}\right) I_0\left[\frac{A+1}{2}\sqrt{\left(\frac{4AE\alpha^\dagger}{kT} - (\beta^\dagger + A\alpha^\dagger)^2\right)\left(\frac{1+\mu_{cm}}{1-\mu_{cm}}\right)}\right] d\mu_{cm}. \tag{7.74}$$

One very interesting property of this formulation is that the adjoint cross section may be analytically calculated without the forward cross section equivalent. That is to say, the forward free gas cross section is not needed, merely the forward zero-temperature cross section and angular transfer probability.

The generation and evaluation of the associated PDFs and CDFs for $\alpha^\dagger$, $\beta^\dagger$, and $S(\alpha^\dagger, \beta^\dagger)$ follow the same procedure provided in for the forward case in the following section.

7.3 Sampling Techniques

The previous section handled the derivation of a free gas thermal scattering cross section for neutron elastic scattering. While the theoretical development of the model is a key portion of the work, it is also important to recognize the fact that methods must be developed in order to sample α and β and calculate the double differential cross section using the scattering function $S(\alpha, \beta)$. This section discusses the generation of the PDFs and CDFs associated with sampling α and β as well as the general schema for sampling from the free gas thermal scattering reaction.

β Sampling

One begins by constructing the marginal PDF and CDF for sampling β. This is defined as expected as the ratio of the double differential cross section integrated over α to the double differential cross section integrated over both α and β:

$$f(\beta \mid E, T) = \frac{\int_{\alpha_{min}}^{\alpha_{max}} \sigma_s(\alpha, \beta \mid E, T) d\alpha}{\int_{\beta_{min}}^{\beta_{max}} \int_{\alpha_{min}}^{\alpha_{max}} \sigma_s(\alpha, \beta \mid E, T) d\alpha d\beta}. \tag{7.75}$$

This expression can be simplified somewhat by cancelling the constants from both the numerator and denominator to yield:

$$f(\beta \mid E, T) = \frac{\int_{\alpha_{min}}^{\alpha_{max}} \exp(\beta/2) S(\alpha, \beta \mid E, T) d\alpha}{\int_{\beta_{min}}^{\beta_{max}} \int_{\alpha_{min}}^{\alpha_{max}} \exp(\beta/2) S(\alpha, \beta \mid E, T) d\alpha d\beta}. \tag{7.76}$$

Thus, the marginal CDF can be constructed by integrating the marginal PDF over the β bounds as:

$$F(\beta \mid E, T) = \int_{\beta_{min}}^{\beta_{max}} f(\alpha, \beta \mid E, T) d\beta. \tag{7.77}$$

α Sampling

As α is dependent upon β, one may proceed to generate the marginal PDF for α as:

$$g(\alpha \mid \beta, E, T) = \frac{\sigma_s(\alpha, \beta \mid E, T)}{\int_{\alpha_{min}}^{\alpha_{max}} \sigma_s(\alpha, \beta \mid E, T) d\alpha}. \tag{7.78}$$

Once again constants may be eliminated to end up at the following expression:

$$g(\alpha \mid \beta, E, T) = \frac{S(\alpha, \beta \mid E, T)}{\int_{\alpha_{min}}^{\alpha_{max}} S(\alpha, \beta \mid E, T) d\alpha}. \tag{7.79}$$

The marginal CDF for sampling α may be constructed by integrating the marginal PDF over the α bounds as:

$$G(\alpha \mid \beta, E, T) = \int_{\alpha_{min}}^{\alpha_{max}} g(\alpha, \beta \mid E, T) d\alpha. \tag{7.80}$$

Sampling Procedure

The sampling procedure for the free gas thermal neutron scattering model is as follows:

1. Given the incoming energy E and temperature T, the bounds for β are calculated and a β grid is constructed.
2. For each point in the β grid, the associated limits for α are calculated.
3. Using the inverse CDF method β is sampled as:

$$\beta = F^{-1}(\eta_1 \mid E, T). \tag{7.81}$$

4. Using the inverse CDF method α is sampled as:

$$\alpha = G^{-1}(\eta_2 \mid \beta(\eta_1), E, T). \tag{7.82}$$

5. Calculate the outgoing neutron energy and scattering angle cosine from α and β as follows:

$$E' = E + kT\beta, \tag{7.83}$$

and

$$\mu = \frac{E + E' - AkT\alpha}{2\sqrt{EE'}}. \tag{7.84}$$

7.4 Testing: Constant Cross Section and Isotropic Model

In order to be able to test that the software implementation for the $S(\alpha, \beta)$ method was working appropriately it became apparent that a simplified analytical method would need to be derived that could be compared against. This was done by returning to the derivation presented earlier in this chapter with the assumptions of isotropic scattering in the CM frame and a constant cross section. For simplicity the constant cross section will be taken as unity.

One will start with the expression provided in Equation 7.33 with the modification of isotropic CM scattering angle and a constant unity cross section. These

modifications result in the following equation:

$$K(\bar{\nu},\bar{\nu}') = \frac{2B^3}{\pi^{3/2}}\left(\frac{A+1}{A}\right)^2\frac{\nu'^2}{p}\cdot\exp\left\{\left(\frac{-B^2}{A}\right)[(A+1)\nu\nu'\mu-\nu^2]\right\}$$
$$\int_{\nu_{r1}}^{\nu_{r2}}\nu_r\exp(-B^2\nu_r^2)\cdot I_o\left(2B^2\nu\nu'\left\{(1-\mu^2)\left[\frac{\nu_r^2}{p^2}-\left(\frac{A+1}{2A}\right)^2\right]\right\}^{1/2}\right)d\nu_r \tag{7.85}$$

By introducing the following change of variable [16]

$$w = B^2\left(\nu_r^2-\left(\frac{A+1}{2A}\right)^2p^2\right), \tag{7.86}$$

one may rewrite Equation 7.85 as

$$K(\bar{\nu},\bar{\nu}') = \frac{B}{\pi^{3/2}}\left(\frac{A+1}{2A}\right)^2\frac{(\nu')^2}{p}\exp\left(-\frac{B^2}{A}\left[(A+1)\nu\nu'\mu_0-\nu^2+A\left(\frac{A+1}{2A}\right)^2p^2\right]\right)\cdot$$
$$\int_0^\infty\exp(-w)I_0\left(\frac{2B\nu\nu'}{p}\sqrt{(1-\mu_0^2)w}\right)dw. \tag{7.87}$$

At this point one must introduce a new transformation defined by the following set of equations:

$$x = \frac{w}{\tau_n}, \tau_n = \frac{B^2}{B^2+\rho_n}, \text{ and } \lambda_n = 1+A(1-\tau_n^2).$$

This transforms the integral in the equation into one of the form:

$$\int_0^\infty exp(-x)\cdot I_0\left(2\sqrt{\kappa x}\right)dx = \exp(\kappa). \tag{7.88}$$

Utilizing the general solution provided by Davison one may rewrite equation 7.87 as [35]:

$$K(\bar{\nu},\bar{\nu}') = \frac{B}{\pi^{3/2}}\left(\frac{A+1}{2A}\right)^2\frac{(\nu')^2}{p}\cdot$$
$$\left[\sum_{n=0}^{N}\sigma_n\tau_n^2\exp\left(-\left(\rho_n\tau_n^2\nu^2+\frac{B^2+\rho_n}{4p^2}\left[\tau_n^2((\nu')^2-\nu^2)+\frac{p^2\lambda_n}{A}\right]^2\right)\right)\right]. \tag{7.89}$$

Since the goal of this derivation is to determine the case for a constant unity cross section, it can be noted that $\rho_n \to 0$ and thus $\tau_n \to 1$ and $\lambda_n \to 1$. Thus, the simplified expression can be written as:

$$K(\bar{\nu}, \bar{\nu}') = \frac{B}{\pi^{3/2}} \left(\frac{A+1}{2A} \right)^2 \frac{(\nu')^2}{p} \exp\left(-\frac{B^2}{4p^2} \left[(\nu')^2 - \nu^2 + \frac{p^2}{A} \right]^2 \right). \tag{7.90}$$

Transforming this to energy and angle space can be done by substituting in the expressions for ν, ν', and p, resulting in the expression:

$$K(E \to E', \mu) = \frac{B}{p\pi^{3/2}} \left(\frac{A+1}{2A} \right)^2 \frac{2E'}{m_n} \exp\left(-\frac{B^2}{4p^2} \left[\frac{2E'}{m_n} - \frac{2E}{m_n} + \frac{p^2}{A} \right]^2 \right). \tag{7.91}$$

One may then substitute this in to find an expression for the double differential transfer cross section in the presence of a unity cross section and isotropic scattering as follows:

$$\sigma_s(E \to E', \mu) = \frac{B}{m_n p\pi^{3/2}} \left(\frac{A+1}{2A} \right)^2 \sqrt{\frac{E'}{E}} \exp\left(-\frac{B^2}{4p^2} \left[\frac{2E'}{m_n} - \frac{2E}{m_n} + \frac{p^2}{A} \right]^2 \right). \tag{7.92}$$

Finally, this expression may be converted from (E, E', μ) to (α, β) using the previously defined expressions for α and β. The resultant expression is the simplified analytical model which can be used for testing the implementation of the free gas thermal scattering model derived herein:

$$\sigma_{s,approx}(\alpha, \beta) = \frac{(A+1)^2 kT}{16\pi^{3/2} AE\sqrt{\alpha}} \exp\left(-\frac{(\alpha+\beta)^2}{4\alpha} \right). \tag{7.93}$$

7.5 Chapter Summary

This chapter discussed the development of a high-fidelity free gas scattering method for forward and adjoint thermal neutron transport. Some of the key takeaways from this chapter are summarized herein:

- Currently existing models for free gas scattering often contain approximations regarding the behavior of the cross section as either a functional form or a legendre polynomial expansion.

- Further, existing models are based on the assumption that scattering is always isotropic in the CM for cases where the thermal motion of a particle produces a non-negligible effect on transport.
- A new method has been developed from first principles which allows for arbitrary forms for the forward zero-temperature scattering cross section and angular transfer probability to be utilized.
- Further, this new method has been developed for both the forward and adjoint cases, extending the current adjoint neutron capabilities to allow for continuous energy thermal neutron transport. The adjoint free gas cross section does not require the forward free gas cross section to be computed.
- Probability distributions for sampling α, β, and thus calculating $S(\alpha, \beta)$ have been developed for the forward and adjoint cases.
- Finally, a simplified model with constant cross section and isotropic scattering has been derived to allow for validation of the free gas model discussed in this chapter.

Chapter 8

Forward and Adjoint Free Gas S(α, β) Results

Chapter 7 handled the derivation of a novel free gas thermal neutron elastic scattering method in the forward and adjoint. This chapter will extend the aforementioned derivation by discussing numerical results from the implementation of this method in FRENSIE and comparison to theory and MCNP.

8.1 Forward Energy Differential Scattering Cross Section

In understanding the forward physics of elastic scattering it is of use to study the energy differential scattering cross section. One may recall from the derivations presented in Chapters 3 and 4 that the transfer kernel was often broken into the transport and collision kernels. The transport kernel handled the physics of transporting a particle from an initial position to a final position, while the collision kernel handled physics associated with the change in phase space which occurs at a collision site (i.e. change in energy and angle). In order to validate the method derived herein, a simple model which assumes isotropic scattering on free gas particles in the CM frame and a constant zero-temperature elastic scattering cross section will be utilized for comparison of the energy transfer function. This model, referred to as the Wigner-Wilkins model, provides a theoretical underpinning for how the physics should behave in the presence of simplifying assumptions.

Wigner-Wilkins Model

Bell and Glasstone provide a derivation for the energy transfer function for elastic neutron scattering on a monatomic gas in motion in their text *Nuclear Reactor Theory* [25]. An abridged derivation is provided herein, as this model will be used throughout the chapter as a means of validation of the newly derived method from Chapter 7. One must begin with the expression for the probability of collision per unit time of a neutron on a monatomic gas:

$$\text{Probability of Collision per Unit Time} = \nu_r \sigma_{s,zt} P(\overline{V}) d\overline{V}, \tag{8.1}$$

where $\sigma_{s,zt}$ is the zero-temperature elastic scattering cross section, ν_r is the relative velocity between the neutron and target nucleus, and $P(\overline{V})d\overline{V}$ is the probability that a target nucleus has velocity in $d\overline{V}$ about $\overline{V}$. The total scattering rate for a neutron of velocity $\overline{v}$ is then found by integrating Equation 8.1 over all velocities $\overline{V}$ of the target nuclei as

$$\sigma_s(\nu) = \frac{\sigma_{s,zt}}{\nu} = \int_{\overline{V}} \nu_r P(\overline{V}) d\overline{V}. \tag{8.2}$$

One may now recall that the isotropic Maxwellian distribution may be used to describe the distribution of nuclear velocities of a free gas in thermal equilibrium at temperature T. Thus, one may write

$$P(\overline{V})d\overline{V} = \left(\frac{M}{2mkT}\right)^{3/2} V^2 \exp\left(-\frac{MV^2}{2kT}\right) d\phi d\mu dV. \tag{8.3}$$

At this point one must seek to determine the probability that a neutron of incident speed ν will interact with the background monatomic gas and will exit the collision with a resultant speed in $d\nu'$ about ν'. To do this it is convenient to transfer analysis from the laboratory frame to the CM frame. Recalling the expressions for the velocity of the CM frame ($\overline{V}_c$) and the neutron speed in the CM frame (ν_c) from kinematics, one may write the outgoing neutron speed in the laboratory frame ν' as:

$$\nu = \left[V_c^2 + \left(\frac{A\nu_r}{A+1}\right)^2 + 2V_c\left(\frac{A\nu_r}{A+1}\right)\cos\theta\right]^{1/2}, \tag{8.4}$$

where θ is the angle between $\overline{V}_c$ and $\overline{\nu}_c$. Inspection of Equation 8.4 shows that once the target velocity is fixed (i.e. V and μ), the CM speed and relative speed are also fixed. Thus, from Equation 8.4 one may infer

$$\nu \, d\nu = V_c \left(\frac{A\nu_r}{A+1}\right) d\cos\theta. \tag{8.5}$$

As this derivation assumes that there is isotropic scattering in the CM, one may also note that the probability of a neutron exiting a collision with direction $\cos\theta$ is proportional to $d\cos\theta$. Thus, the probability of having a speed in the interval $d\nu$

about v is simply proportional to $v\ dv$, which yields

$$g(v \rightarrow v') \propto v, \tag{8.6}$$

where $g(v \rightarrow v')$ is the probability that a neutron of incident speed v exits a scattering event with resultant speed v'. One can then determine the speed transfer cross section for a neutron interacting with a monatomic background gas as

$$\sigma_s(v) f_s(v \rightarrow v') = \frac{\sigma_{s,zt}}{v} \int_0^\infty \int_{-1}^1 v_r g(v \rightarrow v') 2\pi P(V) d\mu dV. \tag{8.7}$$

Carrying out integration over the bounds in Equation 8.7 and converting from speed to energy phase space yields the Wigner-Wilkins generalized expression for the energy transfer term of a neutron interacting with a monatomic gas as

$$\begin{aligned} \sigma_s(E) f_s(E \rightarrow E') = \frac{\sigma_{s,zt}\eta^2}{2E} \Bigg[\exp\left(\frac{E-E'}{kT}\right) \Bigg(\operatorname{erf}\left[\eta\sqrt{\frac{E}{kT}} - \rho\sqrt{\frac{E'}{kT}}\right] \\ \pm \operatorname{erf}\left[\eta\sqrt{\frac{E}{kT}} + \rho\sqrt{\frac{E'}{kT}}\right]\Bigg) + \operatorname{erf}\left(\eta\sqrt{\frac{E'}{kT}} - \rho\sqrt{\frac{E}{kT}}\right) \\ \mp \operatorname{erf}\left(\eta\sqrt{\frac{E}{kT}} + \rho\sqrt{\frac{E'}{kT}}\right)\Bigg], \end{aligned} \tag{8.8}$$

where

$$\eta \equiv \frac{A+1}{2\sqrt{A}}, \tag{8.9}$$

and

$$\rho \equiv \frac{A-1}{2\sqrt{A}}. \tag{8.10}$$

The upper signs in Equation 8.8 are to be utilized in the case of upscattering (i.e. $E \leqslant E'$) and the lower signs are to be used in the case of downscattering (i.e. $E > E'$) [25]. Equation 8.8 will be used throughout this chapter as a means of validation for model derived in Chapter 7 and implemented in FRENSIE. While the Wigner-Wilkins model does not allow for additional physics through the use of an arbitrary zero-temperature cross section and angular scattering distribution, it can be used to verify that FRENSIE reduces to the theoretical solution under the same set of simplifying assumptions.

Numerical Results

As discussed in Chapter 7, before calculating the full cross section the energy differential cross section must be calculated. This is done by calculating the normalization constant for the β integration at a given incoming energy, E. Further, recall that the generation of the β normalization constant requires the integration of α over the entire α space, a phase space which is dependent upon the selected β. The data presented in this section is then the treatment of the energy transfer probabilities extracted from the β probability density and cumulative distribution functions after integration over the α domain.

For an initial validation study FRENSIE was supplied with a constant zero-temperature cross section and isotropic scattering distribution. The goal of this test was to validate the energy transfer probabilities computed in FRENSIE versus those from the theoretical Wigner-Wilkins model. Figure 8.1 depicts the comparison of the energy transfer function for neutron scattering on a monatomic hydrogen gas at 293.6K and in thermal equilibrium.

Inspection of Figure 8.1 shows good agreement between the FRENSIE model using simplifying assumptions and the Wigner-Wilkins model. There appear to be no statistically significant deviations between the two models, and this is as expected. The only slight variations between the two models (on the order of 1×10^{-5} relative) come about from the numerical integration. The numerical integration and optimizations made to the integrator will be discussed later in this chapter. It should also be noted that the full FRENSIE calculation is being computed in this case, with the only change being that the zero-temperature cross section and scattering distribution are constructed to be constant and isotropic respectively. There are no other simplifications and the full calculation is performed as derived in Section 7.2, not the simplified FRENSIE model derived in Section 7.4 which is used internally for unit-testing of the $S(\alpha, \beta)$ calculation.

As the energy transfer probability has been shown to match theory with simplified inputs, it is now worthwhile to calculate the expected outgoing energy probability density and cumulative distribution functions for the general case of the zero-temperature cross section and angular transfer probabilities extracted from the ACE tables in MCNP. The angular transfer probability for the thermal region in the ACE tables is assumed to be isotropic in the CM frame, and as such this does not result in a change in the angular treatment going forward. A later section will discuss how the zero-temperature cross section is extracted from MCNP and implemented

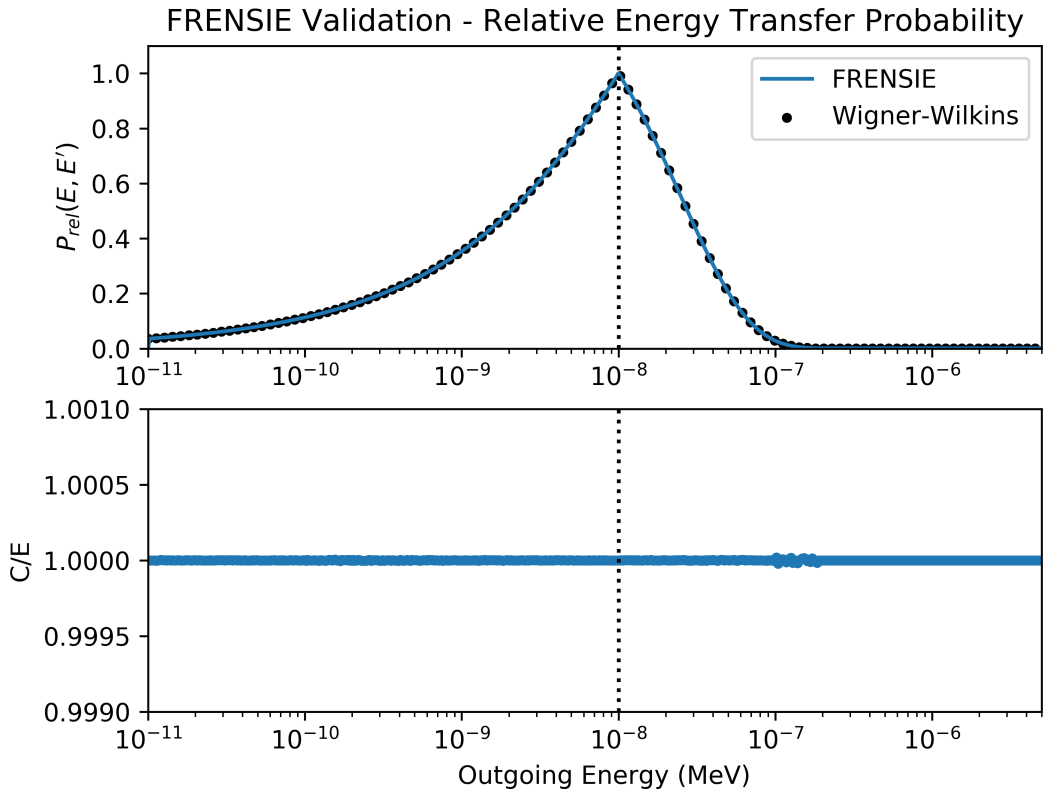

Figure 8.1: **Comparison of FRENSIE and Wigner-Wilkins Energy Transfer Functions.** *FRENSIE was supplied with a constant zero-temperature cross section and an isotropic scattering distribution to allow for direct comparison with the theoretical Wigner-Wilkins monatomic gas scattering model for monatomic hydrogen. Results show that the energy transfer probability from FRENSIE exactly matches theory. Slight variations in the C/E ratio are due to the numerical integrator and are discussed later in this chapter.*

in FRENSIE. Figures 8.2 and 8.3 depict the forward free gas probability density and cumulative distribution functions respectively at various incident neutron energies throughout the thermal region and for a temperature of 293.6K utilizing the ACE zero-temperature cross section data.

Figures 8.2 and 8.3 display a non-physical behavior at the low energy region which must be addressed. For FRENSIE a minimum problem energy of $\mathrm{E}_{min} = 1 \times 10^{-11}$ MeV is in place for neutrons, and thus the tabulation of the neutron transfer properties is stopped at this minimum energy. While this introduces an error where the PDF discontinuously drops to zero, the portion of the CDF which is cutoff is less than 1×10^{-6} for $\mathrm{E} = \mathrm{E}_{min}$, and thus the impact on the total neutron population

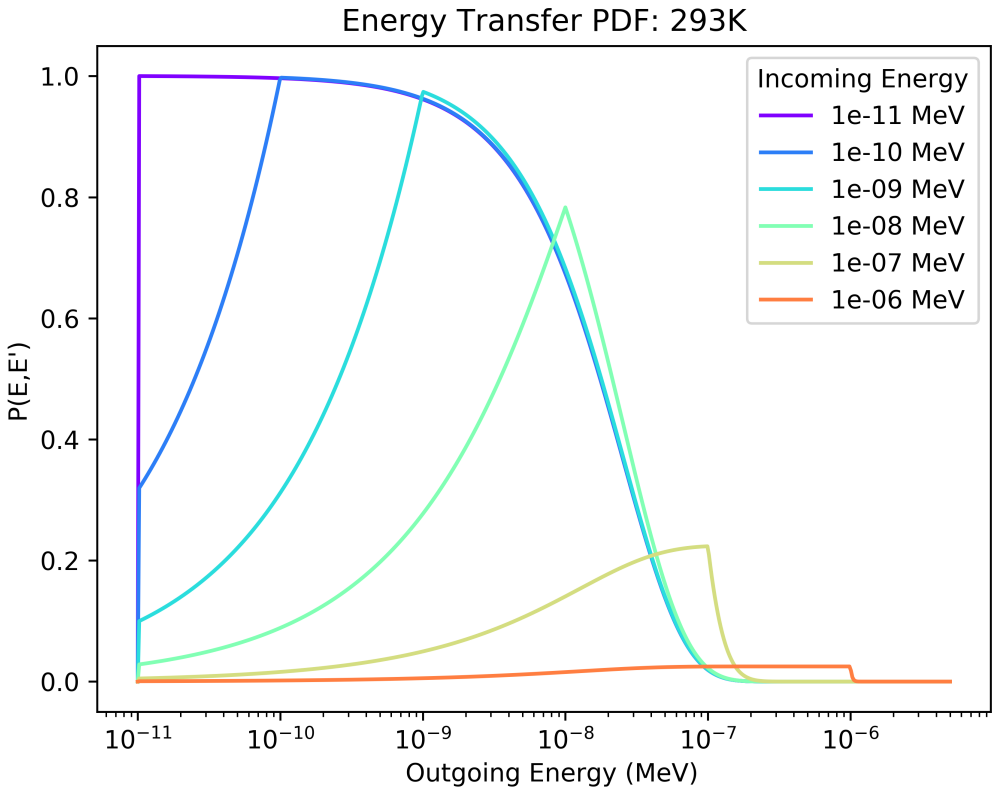

Figure 8.2: **FRENSIE Free Gas Energy Transfer PDF at 293K.** *The free gas energy transfer PDF is plotted for various incoming neutron energies incident on a monatomic hydrogen gas a temperature of 293.6K. It should be noted that there is a minimum problem energy of* 1×10^{-11} *MeV, and all distributions are forced to zero at that energy. One may observe that as the incoming energy increases beyond the background temperature, downscattering becomes the primary form of scattering.*

is negligible. The minimum cutoff energy exists in MCNP currently at the same energy of 1×10^{-11} MeV for neutrons. It is possible in FRENSIE to extend the cutoff energy below this value, but the change in the cross section is minimal and the computational time required to converge by the numerical integration grows rapidly. Many cases were found where below $\mathrm{E}_{\mathrm{min}} = 1 \times 10^{-12}$ MeV the integrator was incapable of converging with the available computational memory resources.

It may also be seen in these Figures 8.2 and 8.3 that the probability of upscattering, or a neutron gaining energy from an elastic scattering interaction, is reduced as the incident neutron energy exceeds the background temperature of the distribution. This is as expected, as at the maximum energy in the free gas approximation one

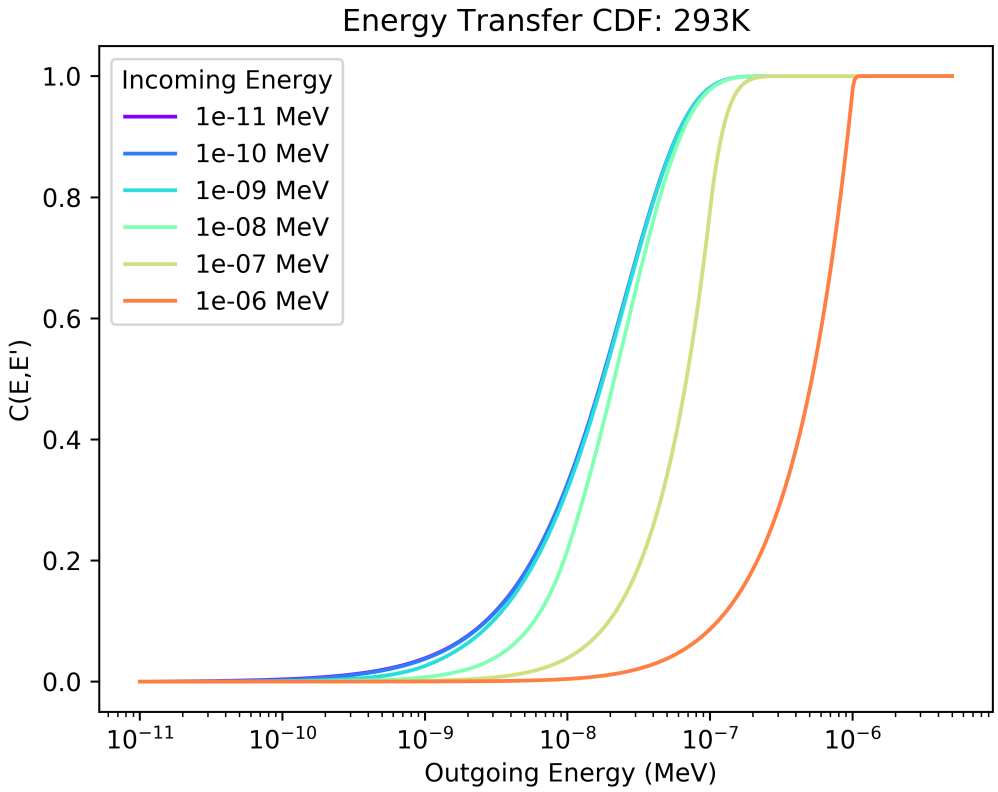

Figure 8.3: **FRENSIE Free Gas Energy Transfer CDF at 293K.** *The free gas energy transfer CDF is plotted for various incoming neutron energies incident on a monatomic hydrogen gas a temperature of 293.6K. It should be noted that there is a minimum problem energy of* 1×10^{-11} *MeV, and all distributions are forced to zero at that energy. One may observe that as the incoming energy increases beyond the background temperature, downscattering becomes the primary form of scattering. At* $\mathrm{E} = 1$ *eV less than 1% of all scattering events are upscattering.*

must transition back to the standard forward elastic scattering treatment in which the scattering center is assumed stationary and there is zero probability of upscattering. The maximum problem energy was chosen as 5 eV to be in line with what is done historically in MCNP [31]. This value was chosen such that that the perturbation in the free gas cross section just above the maximum thermal energy would less than 0.1% of the standard elastic scattering cross section for hydrogen [6]. The maximum energy for thermal free gas treatment is currently a function of the atomic weight ratio, but should be updated to also be a function of the background temperature as suggested by Duderstadt [6]. Overall, all results converge well over the energy

region of interest and match the theoretical calculations.

For the sake of brevity the results for other temperatures will not be shown in this chapter but are contained in Appendix E. In order to have parity with the common tabulated temperatures in MCNP [31], all forward and adjoint free gas data has been generated for temperatures $T = [293,\ 600,\ 900,\ 1200,\ 2500]K$.

8.2 Forward Free Gas Scattering Cross Section

The previous section discussed the generation of the forward free gas energy differential scattering cross section. This section will deal with the total free gas scattering cross section over all incoming energies. In order to calculate the total scattering cross section, one must take the energy differential cross section in (α, β) space and integrate over β for all incoming energies, E.

Comparison of Scattering Cross Section

In order to validate the free gas scattering method derived herein, the total free gas scattering cross section has been calculated and compared against MCNP6.2. The base zero-temperature elastic scattering cross section, $\sigma_{s,zt}$ utilized herein is derived from MCNP. Figure 8.4 depicts the comparison of the free gas elastic scattering cross section for a monatomic hydrogen gas at temperature 293.6K.

It may be seen in Figure 8.4 that FRENSIE and MCNP calculate nearly equivalent cross sections given the same underlying zero-temperature cross section. There are slight deviations across the thermal energy regions but these are on the order of 2×10^{-4} and are not strictly one-sided. Figure 8.5 depicts the comparison between the two cross sections at 2500K.

At 2500K one may begin to observe more pronounced deviations but still within the error envelope of 2×10^{-4}. This is due to the numerical integration which is required both for the α and β domains in the construction of the marginal PDF and CDF, and eventually in the construction of the $S(\alpha, \beta)$ function. While this error is very small, it warrants a discussion as the reduction of error to the current order was an area that required a great deal of effort. For the sake of completeness the comparisons between FRENSIE and MCNP at all five temperatures are shown in Appendix G, along with a plot comparing the cross sections for FRENSIE at all five temperatures alongside one another.

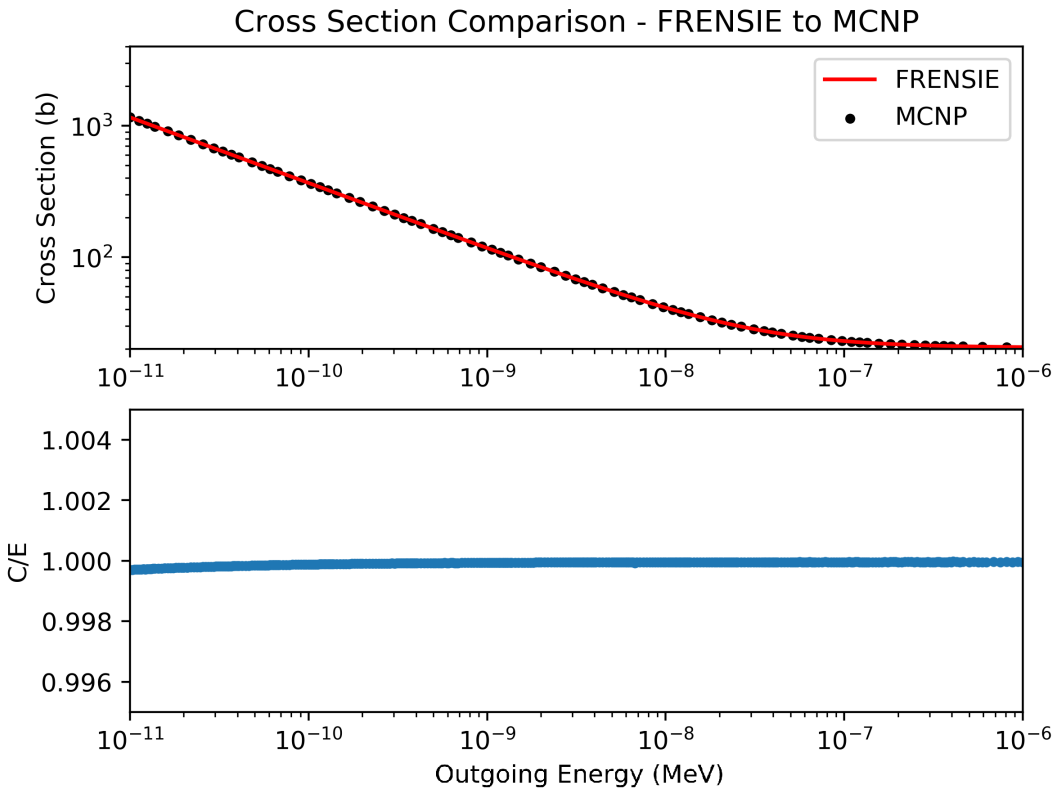

Figure 8.4: **Comparison of FRENSIE and MCNP Free Gas Cross Section at 293K.** *The free gas cross section for neutrons incident on monatomic hydrogen at 293.6K is plotted for FRENSIE and MCNP. Both models agree very well, with deviations on the order of* 2×10^{-4} *relative. Note that the numerical error on the integrator is bounded at* 1×10^{-4} *and thus this result shows good agreement.*

Numerical Integration

The free gas cross section routines in FRENSIE rely upon an adaptive integrator which utilizes the Gauss-Kronrod quadrature formula. The power of the Guass-Kronrod integrator comes in its ability to estimate the error of the integral calculation in situ. This is done by first calculating an approximation for the integral utilizing only the Gauss quadrature. The calculated function values are then used with the Kronrod nodes to produce a higher order approximation. The difference between the two calculations provides an indication for how accurately the scheme is capturing the behavior of the integral, and thus may be used to estimate the error of the integration. This error is then utilized as a stopping criteria for the adaptive iteration loop [36].

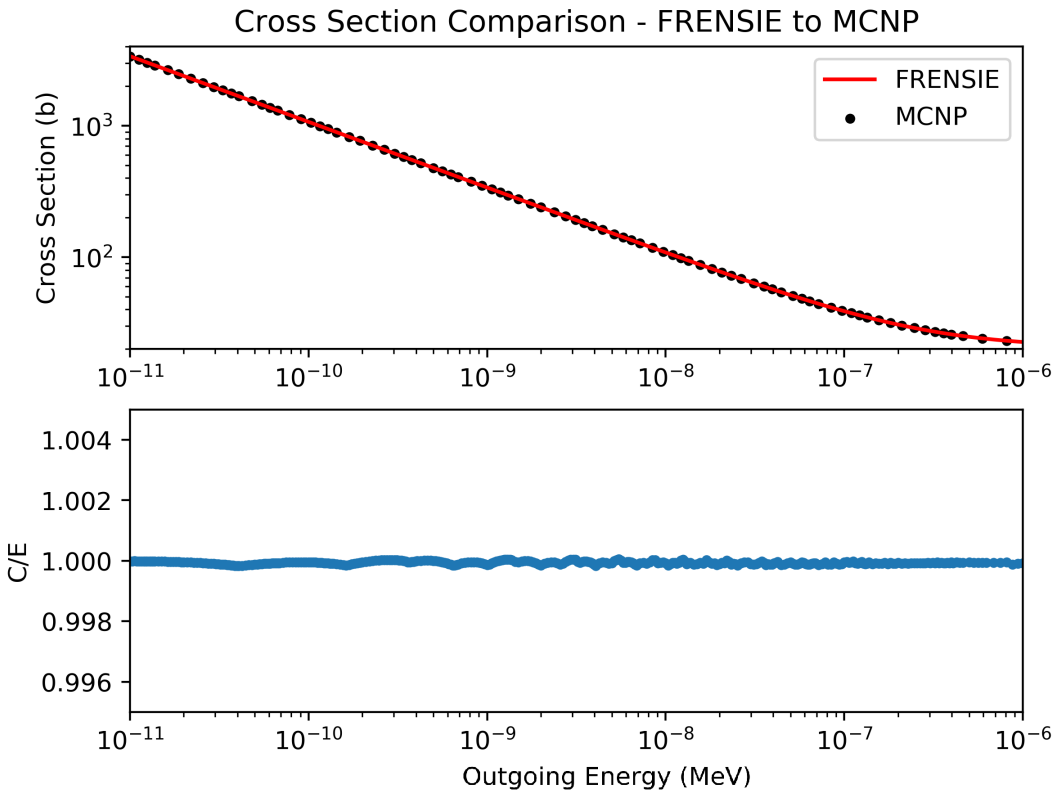

Figure 8.5: **Comparison of FRENSIE and MCNP Free Gas Cross Section at 2500K.** *The free gas cross section for neutrons incident on monatomic hydrogen at 2500K is plotted for FRENSIE and MCNP. Both models agree very well, with deviations on the order of* 2×10^{-4} *relative, but the error from the numerical integration is now more apparent and varied over the thermal energy region.*

The initial version of the adaptive Guass-Kronrod integrator in FRENSIE was implemented by Luke Kersting. However, early calculations of the free gas scattering cross section were hampered by two key issues in the method. First, in order for an accurate calculation of the total cross section, the energy differential cross section in β space must be integrated over the full β range. One may recall the form of β as

$$\beta = \frac{E' - E}{kT}.$$

As the incoming energy E increases relative to kT the region of integration in β

space grows, as one may recall that β is bounded as

$$-\frac{E}{kT} \leqslant \beta \leqslant \infty.$$

Due to this, the β region over which the integral takes place grows by orders of magnitude over the course of the calculation of the elastic scattering cross section. Gradually this calculation requested more memory until the system ran out of available random access memory (RAM) at 128 GB for the high energy ($E > 1$ eV) calculations. To remedy this issue the integrator has been refactored to allow for one to remap the function of interest to exist on the range $[0, 1]$. By doing so one now starts from the same β grid at each integration and the grid is adaptively refined therefrom. This avoids the issue of having the grid over-refined in regions of low importance as the range of integration grows.

The second issue with the initial implementation was the inability to handle grids with arbitrary spacing. As the stencil is incapable of knowing in general how the spacing exists at neighboring points, integration over regions with varying spacing led to large numerical errors on the order of $\pm 2\%$. This has been remedied by searching over the independent variable grid and grouping sections with the same spacing. The integration is then carried out over each section individually and the results are combined. If there exist no neighboring spaces of the same width, the integration is then carried out between each set of neighboring points and summed. While this is more computationally expensive, it was found to reduce the maximum error in the total cross section by roughly two orders of magnitude from 2% to 0.02% relative. The combination of these two corrections reduced the computational time of a full free gas cross section calculation by factor of 15.7, from over twelve hours to roughly 46 minutes for the case of hydrogen at 293.6K while also reducing the error as discussed above.

8.3 Forward Free Gas Transport

The previous sections have discussed the generation of the free gas energy transfer function and free gas scattering cross section, and results have shown good agreement between FRENSIE, MCNP, and theory. It is also important to recall that in all of these comparisons FRENSIE has been supplied with the simplified inputs to match these models (i.e. isotropic scattering and the MCNP constant zero-temperature cross section in the thermal region). However, FRENSIE is not restricted by these

inputs and can accept arbitrary forms of the zero-temperature cross section and angular scattering probability, and thus is capable of producing more accurate results provided more accurate input data is available. This section builds upon the previous sections by providing a validation study performed to test the full forward transport of particles for the FRENSIE free gas method.

Single Scattering Study

The simplest test for determining if forward free gas physics are implemented properly is a single scattering test. The single scattering test allows neutrons to interact with a background gas and scatter a single time before having their energy recorded. Practically, this is often simulated via a broomstick problem. A broomstick problem consists of a semi-infinite cylinder of infinitesimal radius with monodirectional neutrons incident on the end of the cylinder and in line with the axis. Due to the geometry of the problem, neutrons are ejected through the cylindrical surface after a single reaction, and the surface current of exiting neutrons is tallied. For greater assurance the collision bin is also collected to ensure that neutrons only have a single event within the cylinder.

The single scattering study herein was conducted in a similar fashion but with a very small sphere and an isotropic neutron source at the center of the sphere. Neutrons were emitted from the source, and only those which had a single collision before passing through the sphere surface were collected in the surface current tally. This test consisted of a 0.1 mm radius hydrogen sphere at 293.6K and 1.0 at/b·cm. Neutrons were born at 2.5301×10^{-8} MeV, which is equivalent with the background temperature of 293.6K.

Upon further inspection of the problem, one will recognize that due to the monoenergetic nature of the source and the fact that particles are only allowed to collide once, the total scattering cross section utilized has no impact on the outgoing neutron states. Thus, one is directly sampling the outgoing neutron distribution which results from a single incoming energy. Due to this behavior the Wigner-Wilkins method was also constructed and the outgoing neutron states were sampled for a single collision with a hydrogen gas at 293.6K and incident neutron energy of 2.5301×10^{-8} MeV. Figure 8.6 depicts MCNP6.2, FRENSIE, and the Wigner-Wilkins method outgoing neutron energy distribution for a single scatter of a neutron incident energy of 2.5301×10^{-8} MeV on monatomic hydrogen at 293.6K.

Figure 8.6 shows that FRENSIE matches the Wigner-Wilkins theoretical model

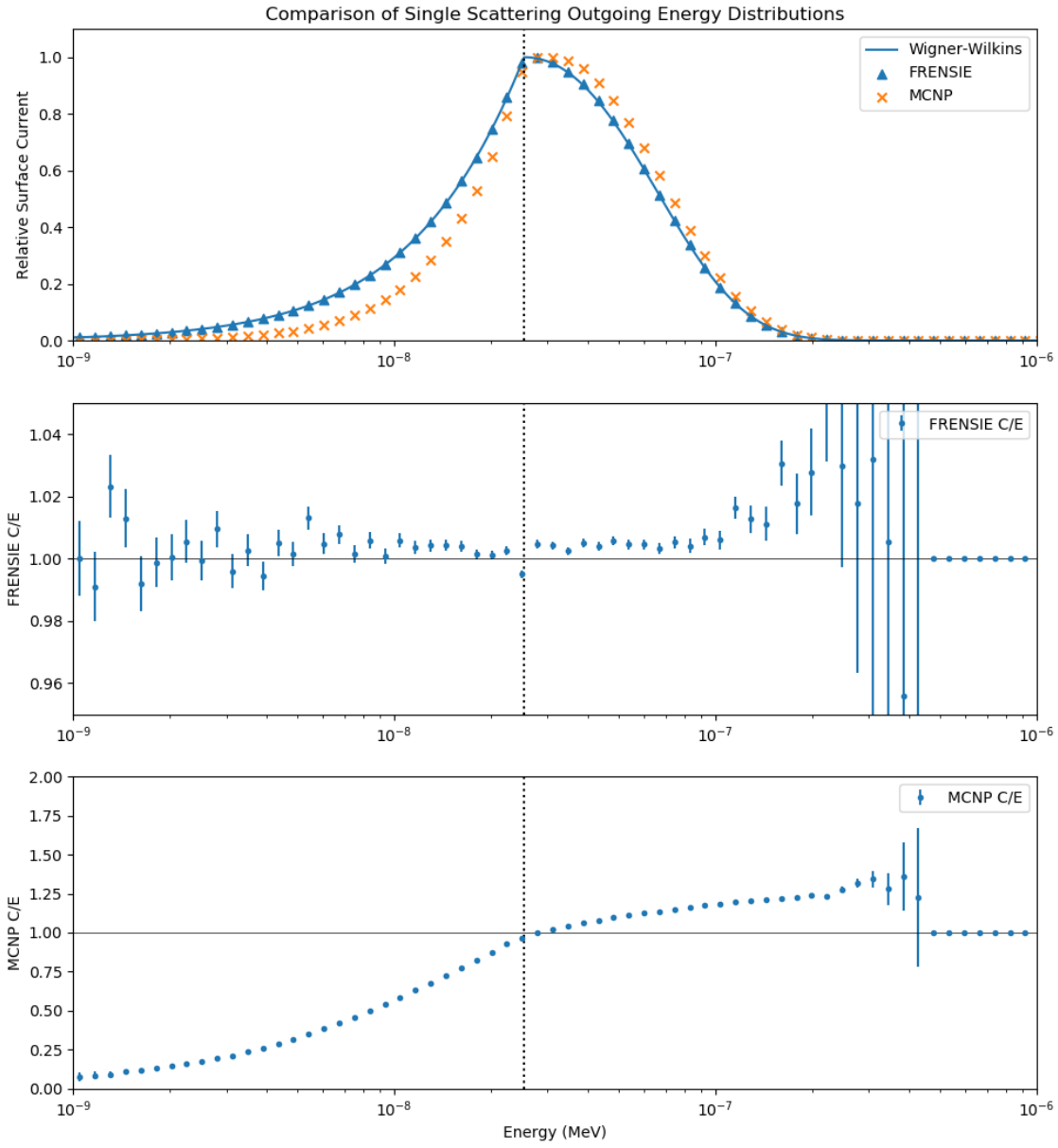

Figure 8.6: **Comparison of FRENSIE, MCNP, and the Wigner-Wilkins Model for Free Gas Single Scattering.** *The outgoing neutron energy distribution for an incident neutron of energy* 2.5301×10^{-8} *MeV experiencing a single scattering event on monatomic hydrogen at 293.6K has been recorded for FRENSIE, MCNP, and the Wigner-Wilkins theoretical model. Results show that FRENSIE matches theory well, but MCNP underestimates the downscattering and overestimates the upscattering, predicting a higher average energy than FRENSIE and theoretical models.*

for the outgoing neutron energy distribution quite well. For clarity it should be stated that the Wigner-Wilkins model was produced in Python (ver. 3.6.7) using the `UnivariateSpline` sub-module from the `scipy.integrate` module, and thus it is expected to have larger numerical error from the integration when compared to the adaptive Guass-Kronrod scheme utilized in FRENSIE. With this in mind one may deduce that FRENSIE is capable of accurately predicting the outgoing neutron energy states for a single elastic scattering event of a neutron incident on a background gas at thermal equilibrium. However, MCNP does not appear to match the theoretical prediction for the outgoing energy states. In fact, it dramatically underpredicts the downscattering of neutrons and overpredicts the upscattering of neutrons. Thus, it is clear that MCNP tends to move particles higher in energy than FRENSIE and Wigner-Wilkins. Due to this unexpected behavior in MCNP it became necessary to investigate further.

MCNP: Free Gas Investigation

The lack of agreement between MCNP and the Wigner-Wilkins model is concerning. The MCNP Manual Volume I provides the theoretical approach for free gas scattering utilized in MCNP [26]. The general overview is that MCNP breaks the treatment up into three discrete calculations. The first calculation is to apply a transform function to the zero-temperature cross section to obtain the energy dependent free gas scattering cross section for a specified temperature. The form of this equation is

$$F(E, A, T) = (1 + 0.5/a^2)\,\mathrm{erf}(a) + \exp(-a^2)/(a\sqrt{\pi}), \tag{8.11}$$

where $a = \sqrt{AE/kT}$, A is the atomic weight ratio, E is the neutron energy, and T is the temperature of the free gas distribution. Thus the free gas thermal scattering cross section is calculated as:

$$\sigma_s(E) = \sigma_{ZT}(E) \cdot F(E, A, T), \tag{8.12}$$

where $\sigma_{ZT}(E)$ is the zero-temperature elastic scattering cross section. The zero-temperature cross section used in FRENSIE for the previous comparisons is extracted from MCNP utilizing the inverse of this function on the cross section in the 293.6K ACE data file.

The second calculation in computing the free gas transport in MCNP is the sampling of the target velocity. The target speed and angle cosine between the target

velocity and neutron velocity are returned from this sampling technique. The theory behind this derivation is contained in the first volume of the MCNP5 manual [26]. The sampling routine will be detailed herein to allow for testing. The sampling routine is as follows [26]:

1. Sample random variable α, and calculate upscattering and downscattering sampling efficiencies ϵ_1 and ϵ_2 as:

$$\epsilon_1 = \left(1 + \left(\sqrt{\pi}\beta\frac{v_n}{2}\right)\right)^{-1}, \tag{8.13}$$

and

$$\epsilon_2 = 1 - \epsilon_1. \tag{8.14}$$

2. With probability ϵ_1, sample the distribution $P_1(y) = y\exp(-y)$ and convert the sampled y to V as $V = \sqrt{y}/\beta$.

3. With probability ϵ_2, sample the distribution $P_2(y) = (4/\sqrt{\pi})y^2\exp(-y^2)$ and convert the sampled y to V as $V = y/\beta$.

4. Uniformly sample a random number on the range $[-1, 1]$ for the cosine of the angle between the target velocity and neutron velocity, μ_t.

5. Check for rejection utilizing the rejection function:

$$R(V, \mu_t) = \frac{\sqrt{v_n^2 + V^2 - 2Vv_n\mu_t}}{v_n + V} \leqslant 1. \tag{8.15}$$

Once the target speed and angle cosine have been returned, the final calculation which consists of the two-body kinematics is carried out to determine the outgoing neutron particle state. In theory this should produce the same result as the integral approach, wherein the elastic scattering cross section and energy transfer functions are calculated by including the Maxwellian in the derivation of the cross section.

The first two steps have been implemented independently to ensure that they are being done correctly, while the third step is still being investigated in the MCNP source files. For step one, it has been shown that for all energies at which the MCNP ACE files are tabulated, the inverse function $F^{-1}(E, A, T)$ calculates the same zero-temperature cross section. The second step has also been implemented via a Python script to determine if the MCNP target velocity sampling routine is correct. The results for the second step show that the equilibrium Maxwellian distribution of

target velocities is correctly computed. However, it appears that there is additional work being done in the third step that is not as expected. One would expect in the absence of absorption that the neutron population at any given collision number would be in thermal equilibrium with the background monatomic gas. While the flux shape should be shifted up in energy due to the $1/v$ shape of the scattering cross section, the collision-by-collision population distribution for an infinite medium problem should approach the thermal equilibrium distribution of the background gas. Even without an infinite medium, examining the neutron energy distribution on a collision basis provides a result that is independent of the total scattering cross section.

To better study these issues a model was constructed in which neutrons were born at $E = kT = 293.6K$ in the center of a monatomic hydrogen sphere. The surface current was collected at increasing collision numbers until an equilibrium was reached wherein increasing collision number had no statistically significant impact on the surface current energy distribution. Figure 8.7 shows the calculated target energy distribution using the MCNP sampling technique plotted alongside the MCNP equilibrium neutron energy distribution. For this test the absorption cross section was also removed from the ACE cross section file, with the total cross section being appropriately adjusted.

From Figure 8.7 it can be seen that for the 50^{th} collided surface current with absorption disabled, the neutron distribution in MCNP does not come in to equilibrium with the background monatomic hydrogen gas. It is unclear what is causing this issue, but further investigation into the calculation of the outgoing neutron energy is currently ongoing.

Multiple Scattering Study

Extending the single scatter analysis, validation of FRENSIE requires that a full transport calculation for the neutron free gas elastic scattering be completed. In the multiple scatter model the goal is to verify that FRENSIE agree with the Wigner-Wilkins method when allowing particles to scatter in to an equilibrium energy distribution. Note that for these tests absorption has been disabled and particles have been transported through 100 collisions to ensure that the distribution reached equilibrium. After the 100^{th} collision the neutron energy distribution was recorded and compared between FRENSIE and Wigner-Wilkins. This of course required a full working model of the Wigner-Wilkins method for multiple scattering which

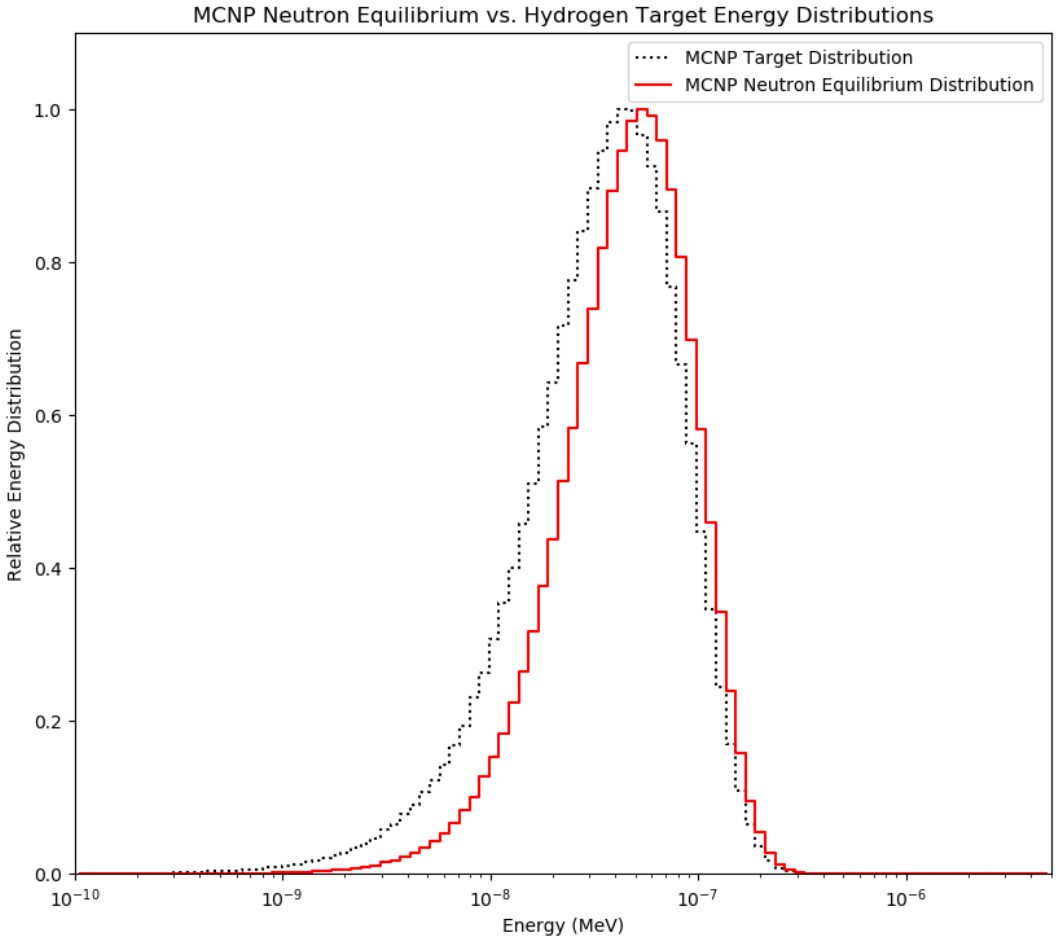

Figure 8.7: **Comparison of MCNP Neutron and Hydrogen Energy Distributions.** *The target ^{1}H energy distribution at thermal equilibrium is plotted alongside the 50^{th} collided neutron surface current with absorption disabled. Note that the neutron distribution does not match the expected behavior of equilibrating with the background media.*

has been implemented in Python.

This test consisted of an infinite hydrogen medium with a uniform neutron source in space. The neutron source produced neutrons at energy $E = kT = 2.53101 \times 10^{-8}$ MeV in an isotropic distribution, and elastic scattering was the only reaction enabled during transport. Figure 8.8 depicts the comparison of FRENSIE and the Wigner-Wilkins theoretical model for this test.

By inspection of Figure 8.8 it may be seen that FRENSIE is in good agreement with the theoretical calculation using the Wigner-Wilkins model. Due to the constraints of running the Wigner-Wilkins model in Python, better statistics could be obtained

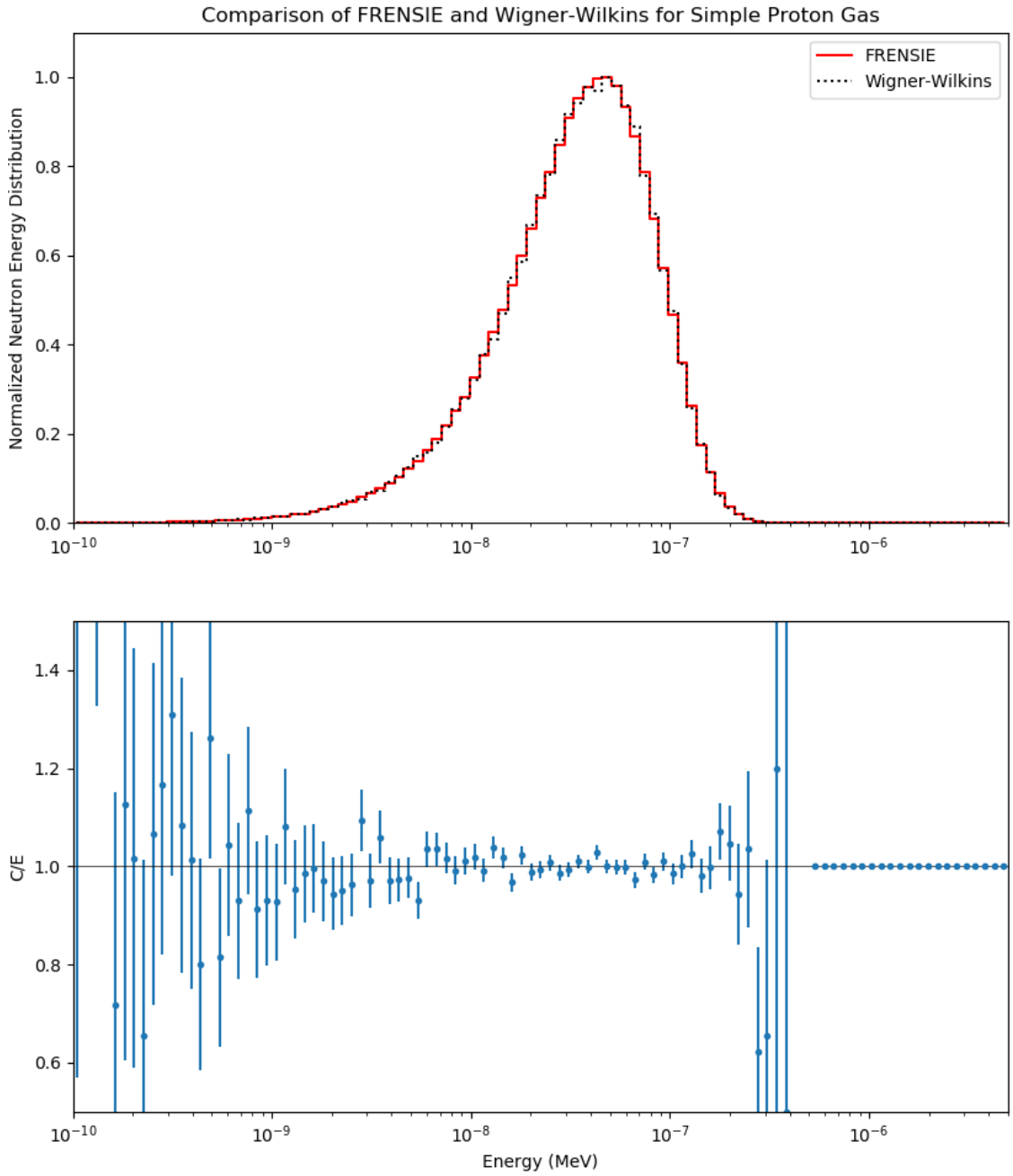

Figure 8.8: **Comparison of FRENSIE and Wigner-Wilkins Equilibrium Neutron Distributions.** *FRENSIE and Wigner-Wilkins method were both tested for the transport of neutrons in a free gas of monatomic ^{1}H without absorption. Results show that both methods generate similar equilibrium neutron energy distributions when utilizing a constant zero-temperature cross section and isotropic scattering distribution.*

Table 8.1: **Comparison of FRENSIE and Wigner-Wilkins Equilibrium Neutron Distributions.** *FRENSIE and Wigner-Wilkins method were both tested for the transport of neutrons in a free gas of monatomic ^1H without absorption. Results show that both methods generate similar equilibrium neutron energy distributions when utilizing a constant zero-temperature cross section and isotropic scattering distribution Results show generally good agreement with the three-sigma rule.*

σ	C/E Fraction	**Expected**
1	0.74	**0.6827**
2	0.98	**0.9645**
3	1.00	**0.9973**

by running longer. It is suggested that future work consist of adding a Wigner-Wilkins routine within FRENSIE for direct unit-testing of short free gas transport problems. Table 8.3 depicts the results of the three-sigma test on this problem and shows good agreement between FRENSIE and the Wigner-Wilkins model. The level of agreement suggests that the FRENSIE model, when supplied with simplifying assumptions, reduces to the purely theoretical model and is capable of performing accurate forward free gas thermal neutron transport.

Forward Self-Adjoint Study

The final numerical result needed for the forward free gas model is a test which can be used to draw a connection between the forward and adjoint models. In many cases it is easy to design self-adjoint problems, however the presence of the thermal equilibrium causes issues. For example, any energy in the thermal region will result in neutrons reaching thermal equilibrium. However, if the same were true in the adjoint, particles would never be able to leave thermal equilibrium. Thus, the behavior of particles in the presence of scattering centers in thermal equilibrium differs in the forward and adjoint case and one must study the difference in the underlying physics.

In order to attempt to find a solution, a problem has been constructed where in the forward particles are birthed at the problem maximum energy. These particles are then tracked as a function of collision number until they are sufficiently close to equilibrium. The equilibrium distribution is then used as the form of the adjoint source term, and particles are transported in the adjoint back to the maximum problem energy. While this is not a directly self-adjoint result, it allows one to draw a connection between the forward and adjoint and verify that they are capturing

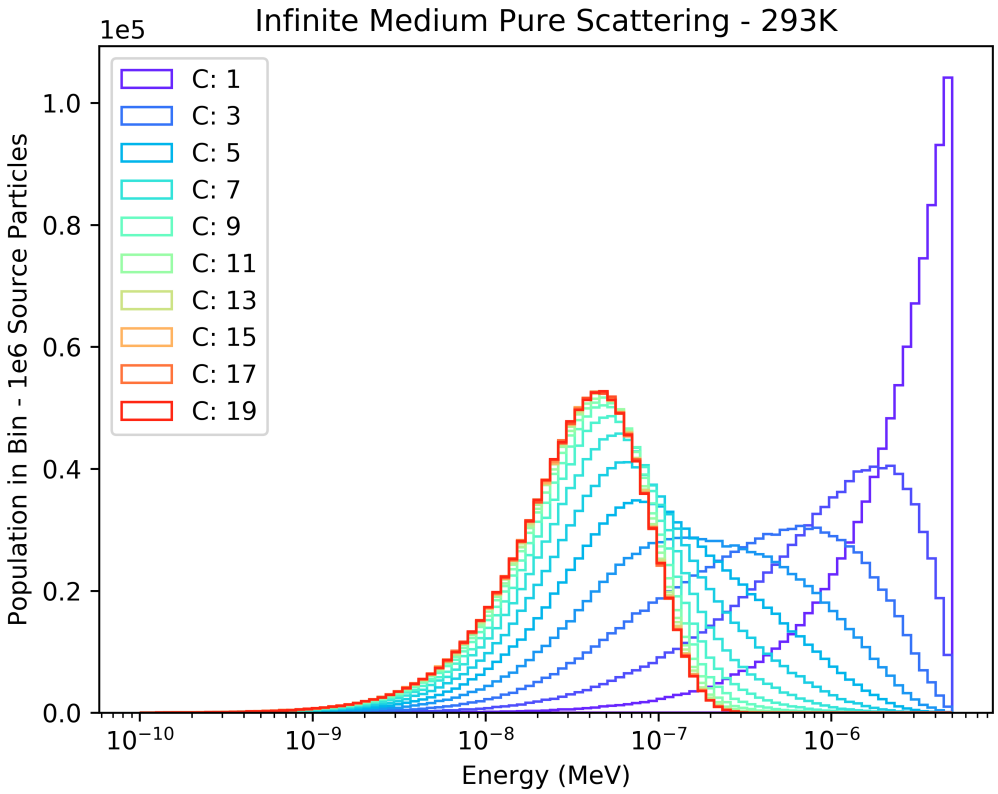

Figure 8.9: **Forward Free Gas Neutron Transport.** *In order to construct a comparative test for the adjoint, a full forward neutron transport model was constructed. Neutrons were born at 5 eV and were scattered through elastic interactions on an infinite medium of monatomic hydrogen gas. The neutrons approached equilibrium after roughly 20 scattering events and the neutron energy distribution at various collision numbers is presented herein.*

the same general order of movement.

This test consisted of pure scattering in an infinite medium of monatomic hydrogen at various temperatures. The result for $kT = 293K$ will be presented in this section, but the remaining results are shown in Appendix H. It should also be noted that the case where absorption is enabled is also shown in Appendix H. Neutrons have been born uniformly in space with an energy of $E = 5$ eV and an isotropic distribution. Figure 8.9 depicts the neutron population energy distribution at various collision numbers.

It may be seen in Figure 8.9 that the neutron scattering distribution starts from the line energy at 5 eV and scatters down to the equilibrium distribution. Further, the equilibrium distribution is approached at roughly ten scattering events in a purely

Table 8.2: **Forward Free Gas Neutron Energy Equilibration.** *The mean neutron energy of the population of neutrons born at 5 eV and scattered in a monatomic hydrogen gas at 293.6K is tabulated as a function of collision number.*

Collision Number	$\overline{E}$ [MeV]	$\overline{E}/\overline{E}_{eq}$
0	5.00E-06	112.9725
1	2.51E-06	56.6338
2	1.31E-06	29.5732
3	6.91E-07	15.6046
4	3.72E-07	8.4062
5	2.09E-07	4.7284
6	1.27E-07	2.8595
7	8.50E-08	1.9208
8	6.43E-08	1.4527
9	5.41E-08	1.2222
10	4.91E-08	1.1083
11	4.66E-08	1.0532
12	4.54E-08	1.0259
13	4.48E-08	1.0126
14	4.46E-08	1.0067
15	4.44E-08	1.0040
16	4.43E-08	1.0021
17	4.43E-08	1.0002
18	4.43E-08	1.0000
19	4.43E-08	1.0000
20	4.43E-08	1.0000

scattering medium, with less than 0.02% change in the neutron energy distribution as a function of collision number by the twentieth collision. Table 8.3 depicts the relative rate at which the average energy of the neutron population approaches equilibrium.

Table 8.3 depicts the change in mean energy of the neutron distribution as a function of collision number. It may be seen that when the incident neutron energy is much greater than the temperature, the average energy outgoing energy is roughly half of the incoming energy. This is expected from standard forward kinematic scattering. However, as the neutron energy approaches the equilibrium energy this breaks down, and generally smaller changes in the mean energy occur until the neutron population asymptotically approaches thermal equilibrium. A similar study has been conducted in the adjoint as a means of displaying the forward-adjoint relationship in the presence of a background scattering media in motion.

8.4 Adjoint Energy Differential Scattering Cross Section

Similar to the discussion laid out in the previous sections, this section handles the numerical results from the implementation of the adjoint free gas scattering method derived in Chapter 7. The goal is to discuss the form of the adjoint differential energy scattering cross section, the adjoint downscattering probability, the total adjoint free gas scattering cross section, and the results of an adjoint Monte Carlo test in which these physics have been implemented.

The first set of results to be discussed is the adjoint energy differential scattering cross section. Recall from Chapter 4 that for standard elastic scattering the form of the energy transfer function in the adjoint is as

$$\sigma_s^\dagger(E \to E', \mu) = \sigma_s(E' \to E, \mu). \tag{8.16}$$

However, due to the presence of scattering centers in motion Chapter 7 depicted an alternate relationship between the forward and adjoint energy transfer functions as

$$\sigma_s^\dagger(E \to E', \mu) = \frac{E'}{E} \exp\left(-\frac{E' - E}{kT}\right) \sigma_s(E' \to E, \mu). \tag{8.17}$$

Therefore, in order to calculate the adjoint energy differential scattering cross section one must utilize the principle of detailed balance to relate the forward and adjoint energy transfer functions. The theory for this calculation has been laid out in Chapter 7. The result is that an expression for the adjoint scattering cross section has been produced without the direct use of the forward scattering cross section. While it appears that the forward cross section is still utilized, the only form of forward data required for the adjoint calculation is that of the zero-temperature elastic scattering cross section and the forward angular transfer probability. The actual calculation of the forward free gas cross section is not required for the calculation of the adjoint, and as such the adjoint cross section is derived from first principles, calculated directly, and is independent of the forward free gas cross section.

While this may appear to be a secondary point, this author stresses that the ability to independently calculate an adjoint cross section is of great importance. The primary benefit is that the numerical error induced in the calculation is not carried over from the forward to the adjoint, compounding the numerical error of the problem. In the same vein, adjoint data has historically been calculated

from tabulated forward data in the energy and angle phase space. This data has interpolation policies associated with it, and the application of multiple interpolation policies again leads to loss of physics through the introduction of systematic error. This is especially true when numerical integration is carried out on data with poorly documented interpolation policy, or energy and angular grids which have not been refined with a specified interpolation accuracy in mind. By developing an independent calculation for the forward and adjoint free gas cross sections both retain their accuracy through direct calculation of the derived expressions.

The calculation of the adjoint free gas energy differential cross section proceeds in the same fashion as the forward cross section. The marginal PDF and CDF for $\alpha^\dagger$ are constructed at each point in $\beta^\dagger$ space. The normalization constant for the integration of $\alpha^\dagger$ yields the probability of sampling $\beta^\dagger$ given an incoming energy E. In energy space it defines the probability of sampling an outgoing energy E' given an incoming energy E. The integration over $\beta^\dagger$ space yields the normalization constant which allows for the construction of the marginal PDF and CDF for $\beta^\dagger$ from which the energy transfer probability is calculated. Figure 8.10 depicts the adjoint energy transfer probability density function for neutrons of various incident neutron energies scattering on monatomic hydrogen at 293.6K.

Figure 8.10 depicts the adjoint probability density function for neutrons scattering on a monatomic gas of hydrogen at 293.6K. From this function one may imagine that the adjoint cross section is performing opposite of expectations, as it appears to be peaking at low energies. However the PDF here is shown in a semi-log configuration in the independent variable and thus upon inspection of the CDF one will observe a behavior which tends to push neutrons up in energy, favoring upscattering in the adjoint. Figure 8.11 depicts the CDF of neutrons of various incident energies scattering on monatomic hydrogen at 293.6K

From Figure 8.11 it can be seen that the gross physics of the adjoint energy transfer CDF matches what one would expect. That is to say, in the vicinity of the background gas temperature neutrons have a chance of both downscattering and upscattering, but the primary component of energy transfer is upscattering. This matches the expected behavior of the adjoint energy transfer function in which neutrons gain energy through adjoint scattering reactions. The primary difference between the work presented here and that of the standard adjoint elastic scattering method is the inclusion of mobile scattering centers which presents the opportunity for adjoint particles to downscatter. For the interested reader figures for adjoint energy transfer PDF and CDF are included in Appendix F for all aforementioned

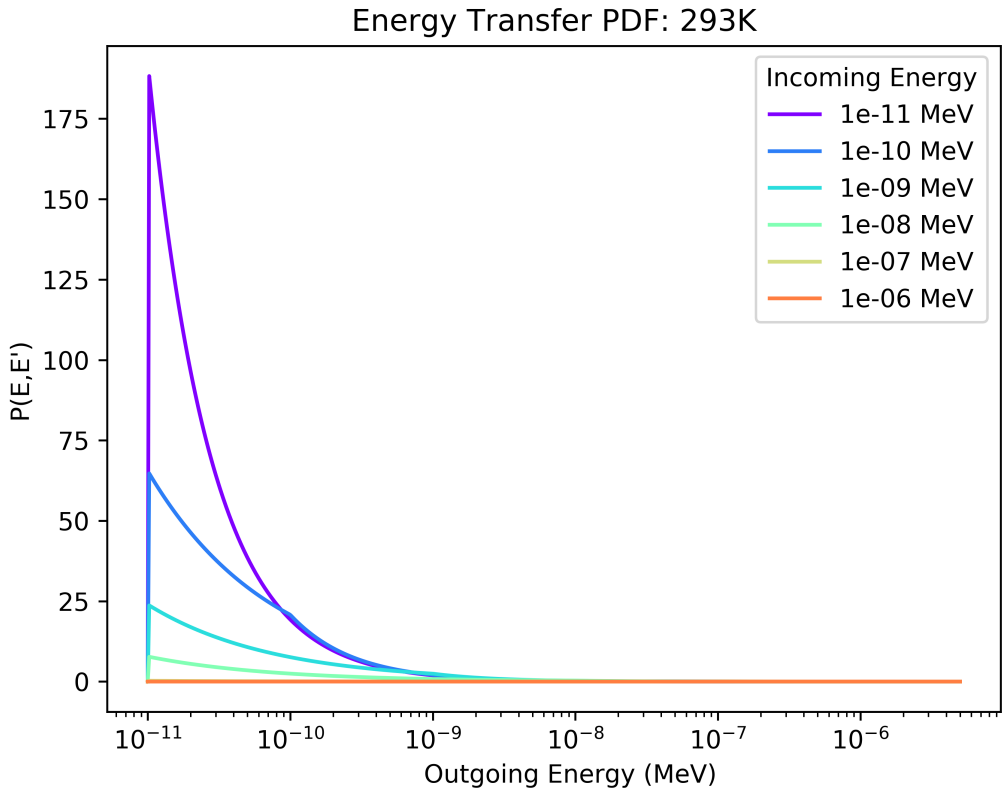

Figure 8.10: **Adjoint Free Gas Energy Transfer PDF.** *The adjoint free gas energy transfer PDF is plotted for various incoming adjoint neutron energies incident on a monatomic hydrogen gas a temperature of 293.6K. It should be noted that there is a minimum problem energy of* 1×10^{-11} *MeV, and all distributions are forced to zero at that energy. One may observe that as the incoming adjoint energy increases beyond the background temperature, upscattering becomes the primary form of scattering.*

temperatures.

Adjoint Energy Transfer Validation

In order to validate the adjoint energy transfer function, an adjoint energy transfer function for the Wigner-Wilkins model has been calculated for the simplified case where the background media consists of a proton gas. The forward expression for

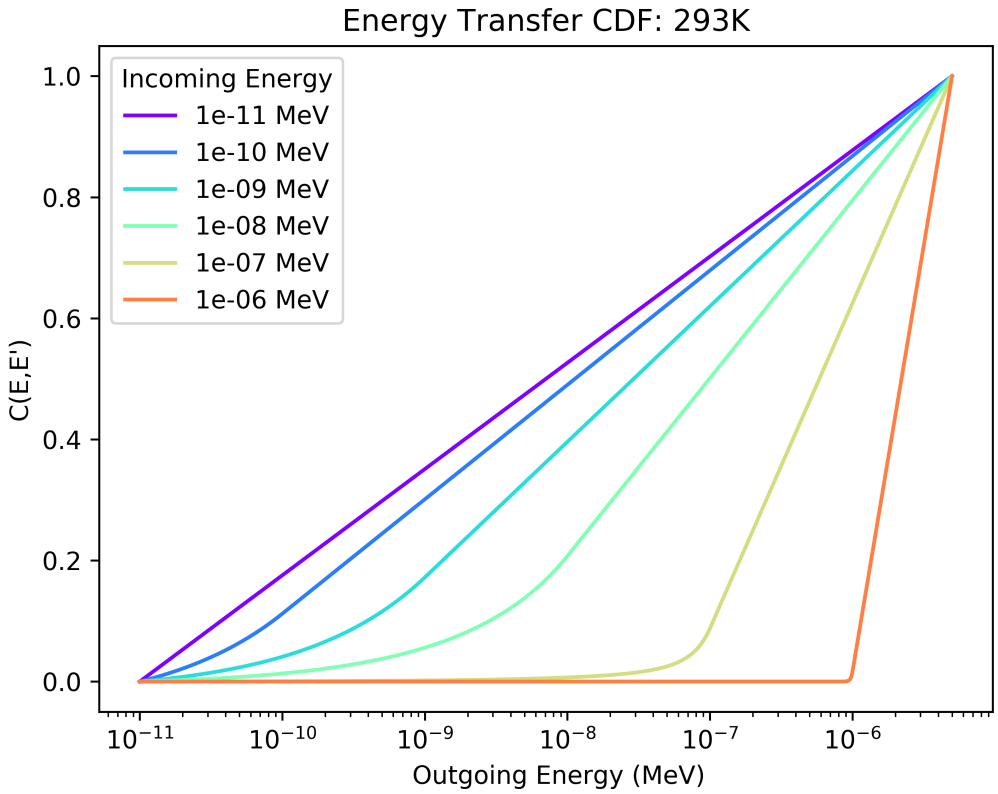

Figure 8.11: **Adjoint Free Gas Energy Transfer CDF.** *The adjoint free gas energy transfer CDF is plotted for various incoming adjoint neutron energies incident on a monatomic hydrogen gas a temperature of 293.6K. One may observe that as the incoming adjoint energy increases beyond the background temperature, upscattering becomes the primary form of scattering. Further, one may note that near the background temperature the fraction of particles experiencing downscattering appears to increase.*

the Wigner-Wilkins energy transfer cross section when $A = 1$ may be written as [25]

$$\sigma_s(E \to E') = \begin{cases} \dfrac{\sigma_{s,zt}}{E} \operatorname{erf}\sqrt{\dfrac{E'}{kT}} & E' < E, \\ \dfrac{\sigma_{s,zt}}{E} \exp\left(\dfrac{E - E'}{kT}\right) \operatorname{erf}\sqrt{\dfrac{E}{kT}} & E' > E. \end{cases} \tag{8.18}$$

This expression may be converted to an adjoint energy transfer function in the same way as the FRENSIE free gas model. That is to say, application of the principle of detailed balance allows for the generation of an adjoint energy transfer function for neutrons scattering on a proton gas at thermal equilibrium. Recall the principle

of detailed balance listed in Equation 7.66 yields an expression for the adjoint cross section in terms of the forward cross section and the Maxwellian distribution of target energies. This calculation was implemented in the Python script utilized for the forward calculation of the Wigner-Wilkins model. At this point one may compare the Wigner-Wilkins adjoint model to the FRENSIE free gas adjoint model when using a constant zero-temperature free gas cross section, isotropic scattering distribution, and proton background gas. Figure 8.12 shows the normalized adjoint energy transfer functions for both models for the case of an incoming energy of 0.01 eV and a monatomic hydrogen background media of temperature 293.6K. It may be seen from Figure 8.12 that the FRENSIE free gas normalized adjoint energy transfer functions matches the theoretical expression from the Wigner-Wilkins adjoint proton gas model.

Adjoint Downscattering Probability

An interesting artifact of the inclusion of background motion is the fact that adjoint neutrons in the thermal energy range are capable of experiencing downscattering from an adjoint elastic scattering event. This is analogous to the fact that neutrons in the forward case may experience upscattering with energies in the vicinity of the background temperature of the scattering centers. As continuous energy adjoint neutron transfer in the thermal region has not been implemented before, it is useful to express how the adjoint downscattering probability behaves over the thermal energy range.

The adjoint downscattering probability is defined as the value of the energy transfer CDF at the incident neutron energy. That is to say, the cumulative probability that the outgoing neutron energy is at or below the incident neutron energy is taken as the adjoint downscattering probability. Mathematically it is represented as

$$P^{\dagger}_{downscatter}(E) = \int_{E_{min}}^{E} P(E \rightarrow E')dE'. \tag{8.19}$$

Figure 8.13 depicts the adjoint downscattering probability over the thermal energy region for neutrons incident on a monatomic hydrogen gas at various temperatures.

Inspection of Figure 8.13 suggests that the distribution of target velocities provides an *attractive* function which tends to slow neutrons down as they pass through the region of energy space over which the target particles are primarily distributed. Further, as the incident energy of the neutron begins to exceed the background

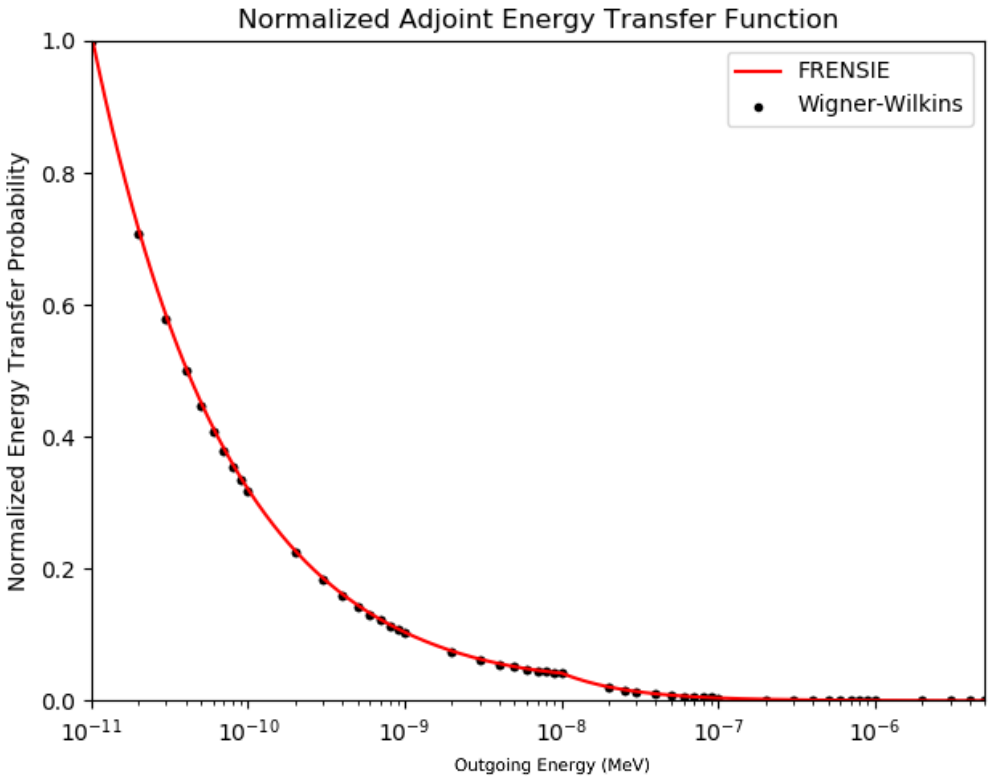

Figure 8.12: **Normalized Adjoint Energy Transfer Functions: FRENSIE vs. Wigner-Wilkins.** *The normalized adjoint free gas energy transfer for both FRENSIE and Wigner-Wilkins have been calculated in order to validate FRENSIE. The two models show good agreement when FRENSIE uses the same simplifying assumptions which form the basis of the Wigner-Wilkins model. This figure depicts the normalized adjoint energy transfer function for neutrons of 0.01 eV interacting with a proton gas in thermal equilibrium about 293.6K.*

temperature the probability of downscattering diminishes. This is an analogy to the probability of upscattering in the forward model. In forward physics the probability of upscattering decreases as $E_{in} >> kT$, and thus in adjoint physics one may observe that the probability of downscattering decreases as $E_{in} >> kT$.

It may also be seen that the location of the peak value of $P^{\dagger}_{downscatter}(E)$ increases with increasing background temperature, and further that the peak value itself increases. The increase with increasing background temperature indicates again that the background gas is slowing the energy gain of adjoint particles as neutrons pass through the energy space associated with the highest density of scattering centers. The fact that the peak value of the downscattering probability increases

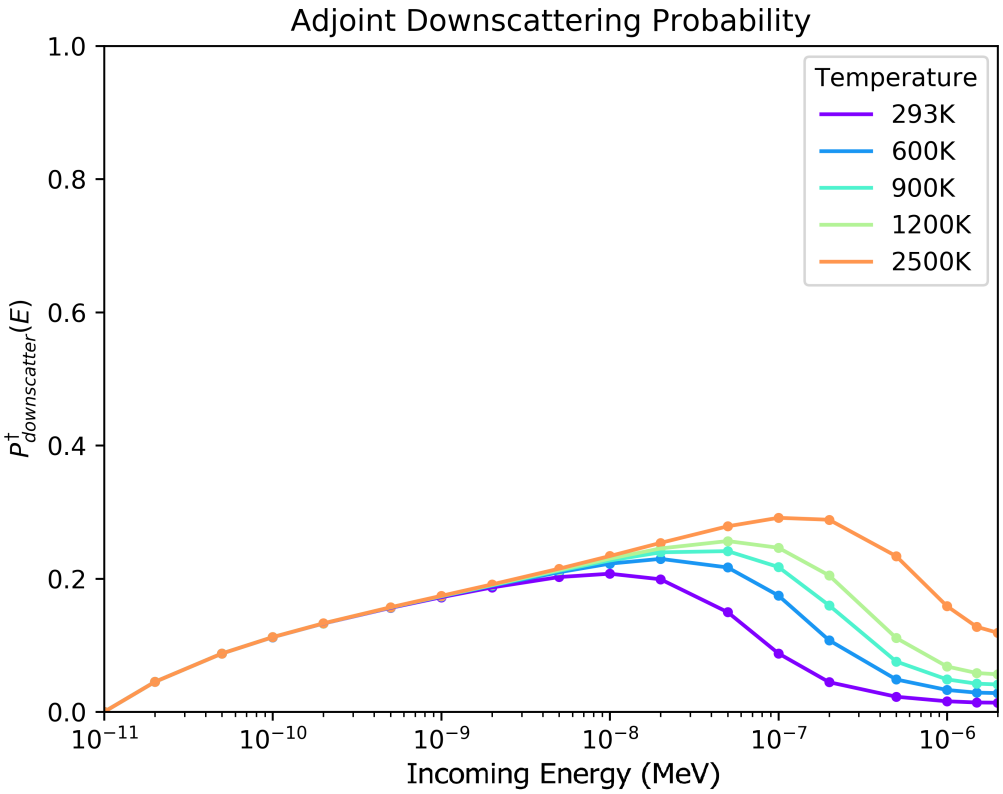

Figure 8.13: **Adjoint Free Gas Probability of Downscatter.** *Inspection of the adjoint free gas CDF yields the adjoint downscatter probability which quantifies the probability that a particle at incident adjoint energy* E *will result in a lower energy* $\mathrm{E}' < \mathrm{E}$ *from the adjoint elastic scattering reaction. As the incident adjoint energy greatly exceeds the background temperature the solution tends towards pure upscattering as in the stationary scattering center case.*

indicates that as the temperature of the background gas increases, the total number of neutrons undergoing downscattering also increases, and thus the number of scattering events required to escape the thermal energy region increases.

For example, at a temperature of 2500K, the maximum value of $\mathrm{P}^{\dagger}_{\mathrm{downscatter}}(\mathrm{E})$ is 29.13% and occurs at an energy of 0.10 eV. In the standard treatment of adjoint elastic neutron scattering, every particle would experience an upscattering event and thus the downscatter probability would be zero. The standard treatment would then incorrectly predict the transport of particles by roughly 29.13%, and particles would escape the thermal energy space in far fewer interactions. This is important because the primary reaction rates of interest for many studies are maximized within

the thermal energy region, and thus appropriately handling the transport and interaction with thermally equilibrated background media is pivotal to achieving accurate results and designing solutions which are capable of filling real-world needs.

8.5 Adjoint Free Gas Scattering Cross Section

As was done in the forward, the adjoint free gas scattering cross section is calculated by integrating the adjoint free gas energy differential cross section over $\beta^\dagger$ space. This is completed utilizing the same adaptive Gauss-Kronrod integration scheme utilized in the calculations of the forward physics and the $\alpha^\dagger$ and $\beta^\dagger$ marginal PDF and CDF. Figure 8.14 depicts the adjoint free gas scattering cross section for neutrons incident on a monatomic hydrogen gas.

From Figure 8.14 one may observe the fact that the peak of the adjoint free gas scattering cross section increases as the background temperature increases. Physically this indicates that neutrons are most likely to undergo an elastic scattering reaction when the energy of the neutron and the target nucleus are similar. It may also be seen that at the maximum problem energy the neutron cross sections instantaneously drop to zero. In order to stop particles from scattering to infinite energies, a maximum problem energy is required for the generation of adjoint cross sections. As FRENSIE currently does not have continuous energy adjoint cross sections for neutrons outside of the thermal region, the maximum problem energy is specified as the maximum energy of the thermal region. Once additional adjoint neutron physics are completed one may increase the maximum problem energy to be the maximum possible neutron energy (i.e. 20 MeV in the ACE data tables) and recalculate the adjoint free gas scattering cross sections. This will require some work in creating a transfer function which hands the physics off appropriately from free gas to non-free gas model, and is listed as future work for this research.

8.6 Adjoint Free Gas Transport

At this point an adjoint transport simulation may be run, as the state transfer probabilities and scattering cross section are calculated for the adjoint case. Similar to the forward model this consists of an infinite medium of free gas hydrogen at the five aforementioned temperatures. In each of these cases the source term for the adjoint transport is uniformly distributed in space, and the energy distribution it is taken

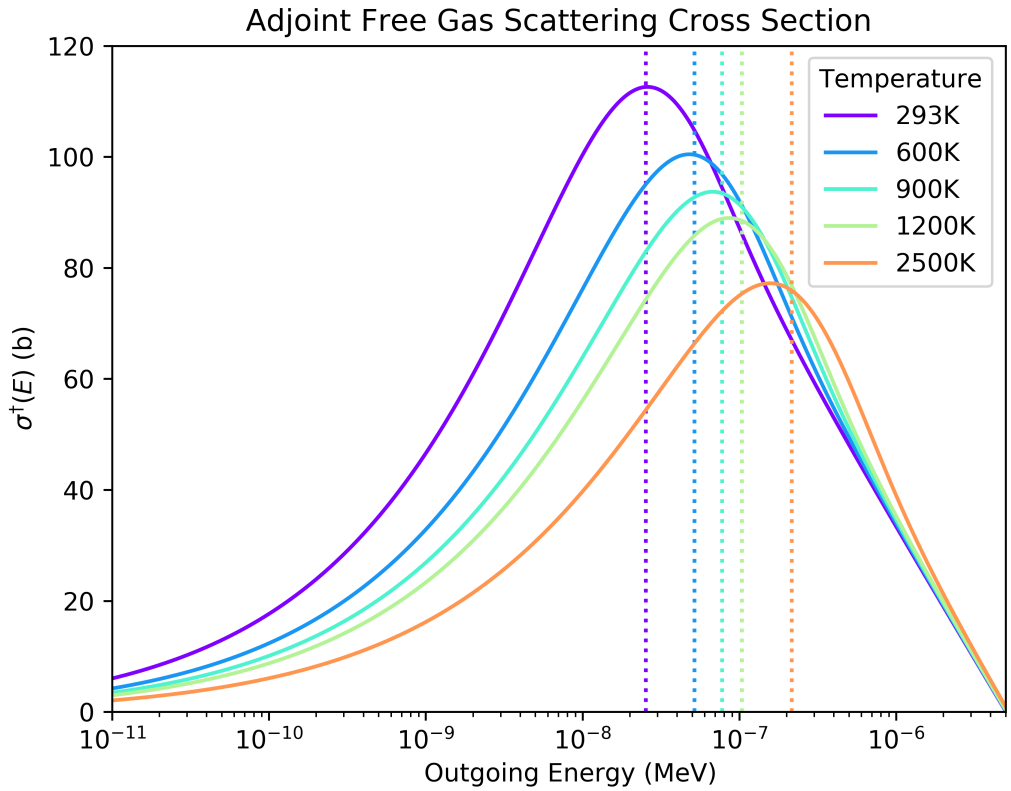

Figure 8.14: **Adjoint Free Gas Scattering Cross Section.** *The adjoint free gas cross section is calculated from the integration of the energy differential cross section over* $\beta^{\dagger}$ *space. The cross sections are dependent upon the maximum problem energy, here set to 5 eV. The dotted lines indicate the background temperature* kT *for the cross section of the associated color. Note that the cross sections peak near the background temperature.*

to be the equilibrium neutron energy distribution from the forward transport case at the same temperature. The goal is to observe the forward and adjoint transport associated with starting at a maximum line energy and reaching equilibrium in the forward, followed by adjoint transport back to the maximum line energy. Figure 8.15 depicts the adjoint neutron energy distribution as a function of collision number.

From Figure 8.15 it may be seen that adjoint neutrons tend to increase in energy, a result which matches the expected behavior from the investigation of the energy transfer probabilities. One may observe that the neutrons quickly begin to scatter up in energy in the adjoint case after starting from the forward equilibrium distribution. Gradually the neutrons approach the maximum problem energy of 5 eV at which point they equilibrate, as there is no cross section defined above the maximum

problem energy. This simulation may be run again but for different temperatures. Figure 8.16 depicts the same test but for a monatomic hydrogen gas at 2500K.

By inspecting Figure 8.16 one may observe that the maximum problem energy of 5 eV is now in a region where the downscattering probability is still over 10%, and thus rather than congregating at the line energy of 5 eV the particles are distributed in the local energy space. For this reason the maximum β for forward calculations and thus minimum $\beta^{\dagger}$ for adjoint calculations should be temperature dependent, and set at $\pm 500A$. This is done to ensure that the free gas physics have sufficiently decreased and the stationary target model is accurate at the transition energy. All other temperatures of the adjoint free gas transport problem may be seen in Appendix I.

As was done in the forward, the rate of convergence and energy transfer in the adjoint is worth investigating. Table 8.6 depicts the mean energy of the neutron distribution after each scattering event. It may be seen that after ten events the neutrons are within 2% of the maximum problem energy. Scattering thereafter causes tighter grouping with the mean of the distribution after twenty collisions only 0.25% less than the theoretical limit of 5 eV and effectively at the converged value.

From Table 8.6 it may be seen that the converged value is not exactly equal to the maximum problem energy of 5 eV and this has to do with the calculation of the CDF at energies very close to the maximum problem energy. The class which stores the data for the outgoing energy state is called `TabularOneDDistribution` and takes the independent variables and associated PDF values as input, along with an interpolation policy for interpolation and calculation of the CDF. However, at some point as one approaches the maximum problem energy nearly the entire CDF is encapsulated between a single pair of datapoints. At this point one continues to sample the same distribution over and over, never fully approaching the problem energy. This may be remedied by either refining the grid to sufficient accuracy in the vicinity of the maximum problem energy, or applying a nudge factor for particles which reach the average sampled energy in the maximum energy bin. One final option would be to generate an additional data ponit above the maximum problem energy and simply terminate particles that scatter into the additional energy range.

Table 8.3: **Adjoint Free Gas Neutron Energy Equilibration.** *The mean neutron energy of the population of adjoint neutrons born at the forward equilibrium distribution and scattered in a monatomic hydrogen gas at 293.6K is tabulated as a function of collision number.*

Collision Number	$\overline{E}$ [MeV]	$\overline{E}/\overline{E}_{eq}$
0	4.44E-08	0.0089
1	8.54E-07	0.1708
2	1.91E-06	0.3811
3	2.86E-06	0.5721
4	3.59E-06	0.7189
5	4.11E-06	0.8213
6	4.44E-06	0.8880
7	4.65E-06	0.9303
8	4.78E-06	0.9566
9	4.86E-06	0.9726
10	4.91E-06	0.9825
11	4.94E-06	0.9885
12	4.96E-06	0.9922
13	4.97E-06	0.9944
14	4.98E-06	0.9958
15	4.98E-06	0.9966
16	4.99E-06	0.9971
17	4.99E-06	0.9973
18	4.99E-06	0.9975
19	4.99E-06	0.9976
20	4.99E-06	0.9976

8.7 Chapter Summary

This chapter has discussed the numerical results of implementing the free gas thermal neutron scattering model derived in Chapter 7. In forward physics the FRENSIE model shows excellent agreement with theory when utilizing the inputs from the theoretical derivation (i.e. constant zero-temperature cross section and isotropic scattering probability). MCNP has been found to produce different results and is currently being investigated.

In the adjoint, FRENSIE has produced a continuous energy free gas thermal neutron scattering cross section. This new cross section not only serves to allow for continuous energy transport in the thermal regime, but to provide additional accuracy by considering the kinematic effects of thermal motion. The energy differential scattering cross sections, total cross sections, and transport problems have been

analyzed in the adjoint for a hydrogen monatomic gas at various temperatures and their behavior has been studied, as these values have not been previously studied in the presence of scattering centers in motion.

It should be noted that the implementation in FRENSIE is not limited to hydrogen, and one may calculate all forward and adjoint quantities for any material which contains an MCNP ACE dataset with an elastic cross section. Further, FRENSIE allows for an arbitrary form of the zero-temperature cross section and angular scattering probability, opening the door to more accurate results when better underlying data is available.

Summary

- The novel forward free gas model has been implemented in FRENSIE and shows good agreement with the Winger-Wilkins theoretical model. This includes the energy transfer cross section, total cross section, single scatter, and multiple scatter data.
- MCNP and FRENSIE have good agreement for the total cross section but the energy transfer functions appear to differ on MCNP. This is currently being investigated and is classified as future work.
- Full forward scattering models have been constructed in FRENSIE which match the theoretical equilibrium distribution and may also be run in the presence of absorption.
- The novel adjoint free gas model has been implemented in FRENSIE. The energy transfer functions show an interesting form of the downscattering probability whereby the background energy distribution acts as an attractive force, slowing down neutron energy gain through that region of phase space.
- The total adjoint free gas scattering cross section is calculated and is shown to peak near the background distribution temperature. Note that the ultimate shape of the adjoint cross section is dependent on the maximum problem energy.
- Full adjoint scattering models have been constructed in FRENSIE which correctly show particles scattering up through energy space toward the maximum problem energy.

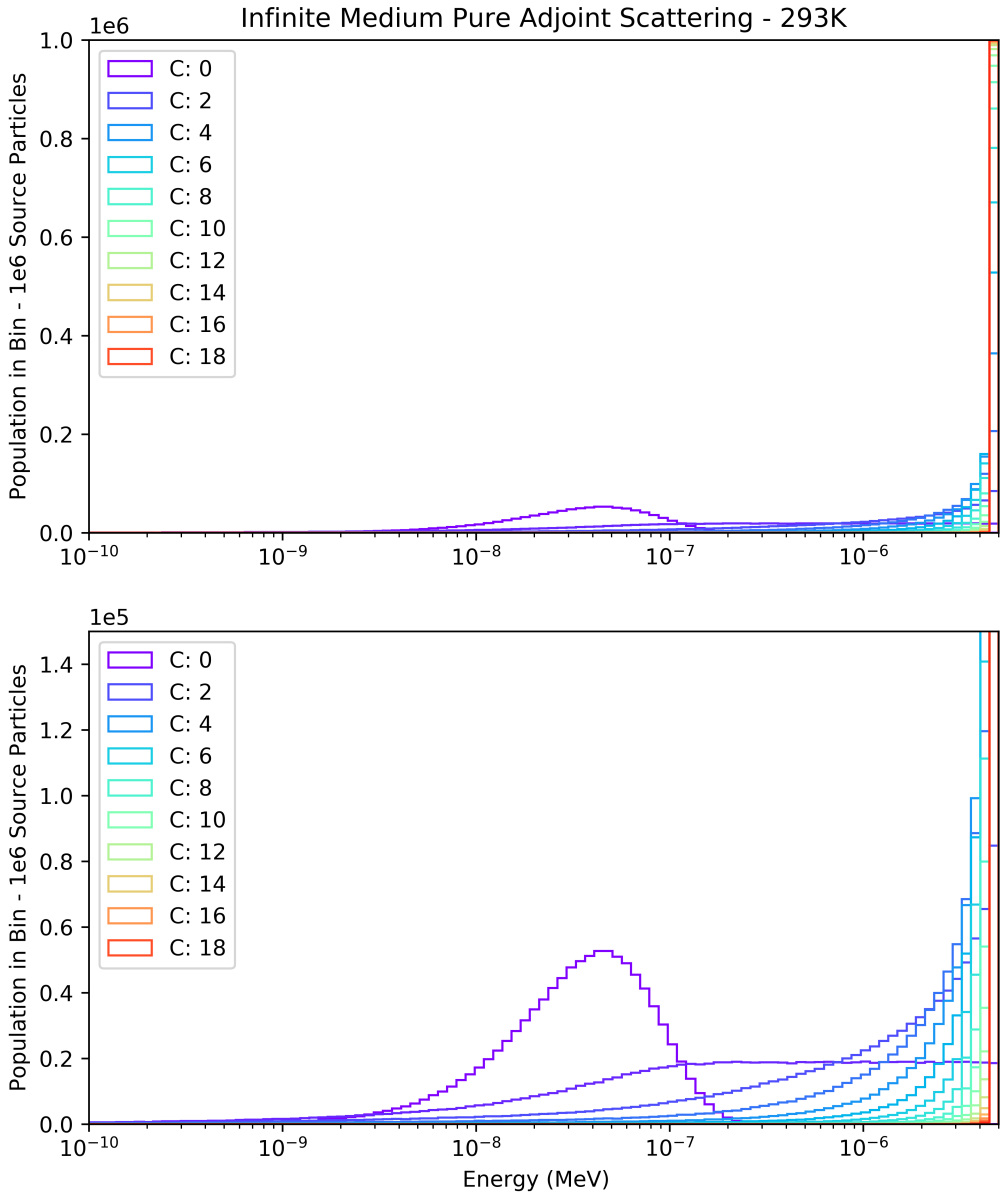

Figure 8.15: **Adjoint Free Gas Neutron Transport at 293K.** *Adjoint neutrons were transported through an infinite medium of monatomic hydrogen gas at 293.6K. The neutron source was uniform in space and the energy profile matched that of the corresponding forward free gas equilibrium neutron distribution. The resultant neutron energy distribution is plotted at various collision numbers to display the progression from the equilibrium forward distribution back toward a line energy at the maximum problem energy.*

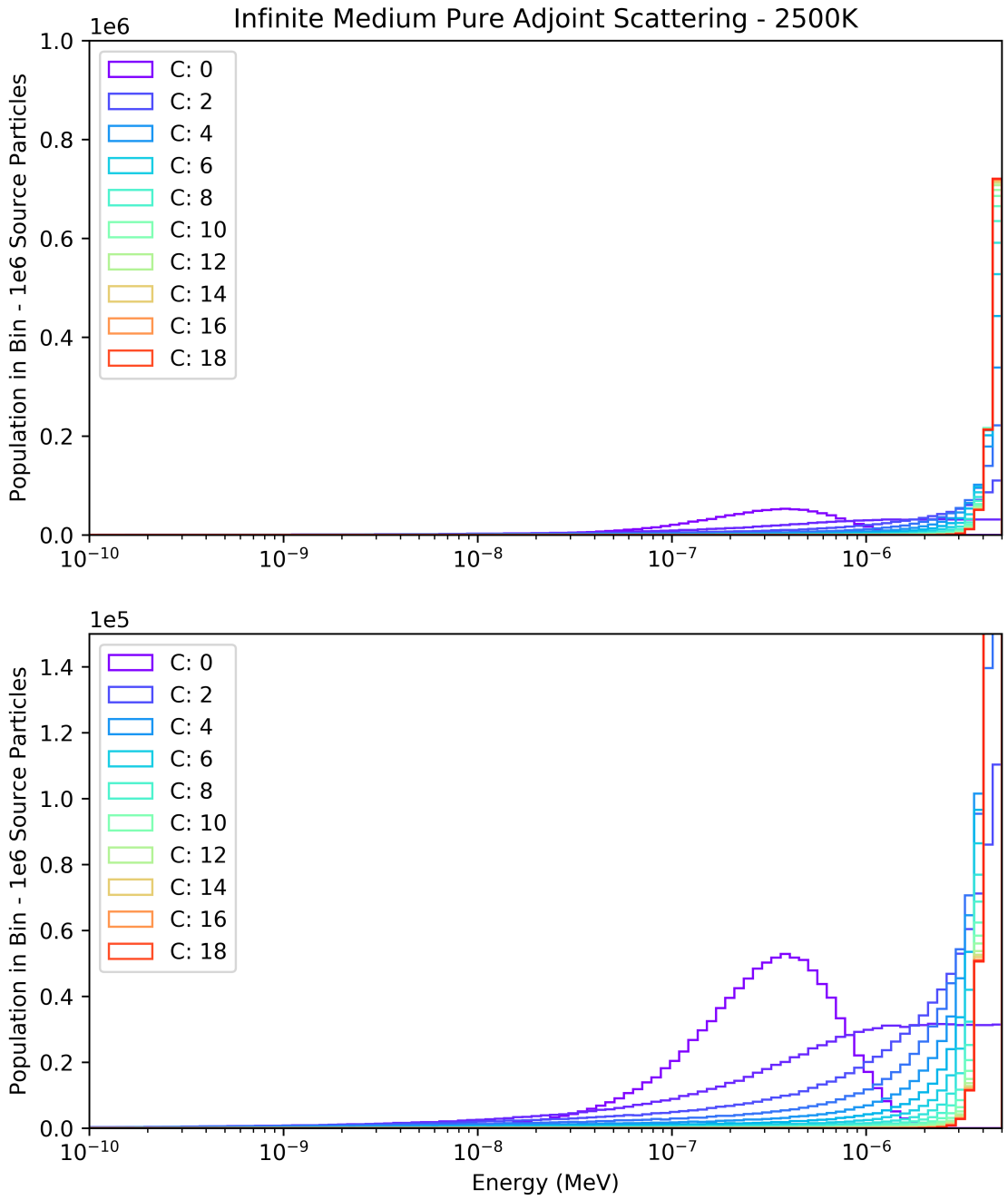

Figure 8.16: **Adjoint Free Gas Neutron Transport at 2500K.** *Adjoint neutrons were transported through an infinite medium of monatomic hydrogen gas at 2500. The neutron source was uniform in space and the energy profile matched that of the corresponding forward free gas equilibrium neutron distribution. The resultant neutron energy distribution is plotted at various collision numbers to display the progression from the equilibrium forward distribution back toward a line energy at the maximum problem energy.*

Chapter 9

Conclusion

The ultimate goal of this report is to present a novel free gas scattering method for forward and adjoint thermal neutron transport, both in a theoretical framework and in a practical radiation transport code. In achieving this primary goal, the structure of this report has been designed to:

- provide a derivation of the Monte Carlo random walk process and prove its applicability in solving FIESKs,
- develop the theory for generalized forward and adjoint radiation transport using the random walk process,
- develop the necessary theory and sampling routines for handling forward neutron physics and adjoint elastic and inelastic level scattering in FRENSIE,
- derive a novel forward and adjoint free gas thermal scattering model,
- and discuss the numerical implementation of the free gas thermal scattering model and its comparison to theory and existing codes.

9.1 Report Summary

Each chapter in this report will be summarized herein to provide the reader with an overview of the material presented.

Monte Carlo Applications to Solving Fredholm Integral Equations

Chapter 2 handled the development and solution of FEISK problems. It was shown that FIESKs may be solved via the method of successive approximations. However, as the number of variables increases the method of successive approximations becomes more difficult to utilize. In this way the Monte Carlo (MC) process is ideal for solving FIESKs with many variables. One can define the MC random walk PDFs which govern the generation, state transition, and termination of any given random walk. Utilizing these PDFs one prove that the MC random walk does in fact solve the original FIESK.

Further, it was shown that there are multiple types of estimators which are derived from the inner product of a known response function and the unknown function of the FIESK. This is useful in estimating quantities of interest from the MC random walk process, and the uncertainty in these estimations may be easily quantified. Finally, the issue of estimating a quantity at a single point was considered. Assuming the response function exists only at a point, one can define the dual of the FIESK and solve the newly defined problem. At this point one finds that the dual of the FIESK is optimal in the case where the response function is defined in a much smaller region than the source, and the original FIESK is optimal in the reverse case.

The primary takeaway from Chapter 2 is that the MC method can be applied to solve FIESKs, and that responses may be estimated using either the FIESK or the dual of the FIESK.

Forward Radiation Transport Theory

Chapter 3 handled the development of the forward transport FIESKs from the forward transport equation. Starting from the integro-differential equation, the forward integral transport equation was derived via the method of characteristics. The first FIESK defined was for the angular flux, as the flux is a very common quantity in nuclear science and engineering. However, it was shown that the flux FIESK is poorly conditioned for sampling, as the source is an integral value and the lack of the total scattering cross section allows for interactions to occur in voided regions.

Thus, the emission density and collision density FIESKs were derived. For each of these the transfer kernel was defined as the product of a collision kernel and transport kernel. The collision kernel handled the change in energy and angle for a particle colliding at a specific point in space, while the transport kernel handled the transport of a particle at some energy and angle between points. By deconstructing the collision kernel one gained the ability to not only explicitly handle production and absorption, but it also provided a general schema for sampling a specific outgoing particle state.

Finally, estimations of responses were considered in respect to the flux. Typically responses such as reaction rates are thought of as being the product of the flux and the cross section. Yet due to the nature of the flux FIESK, it is unlikely that the flux will be solved for using MC transport. This forced the derivation of variables which allow the collision density and emission density to estimate flux-like quantities.

The collision density variable for conversion is very easy to calculate, and thus the collision density FIESK is an ideal candidate for the MC random walk.

Adjoint Radiation Transport Theory

Chapter 4 began by showing that taking the dual of the forward emission density and collision density FIESKs did not provide useful results. In fact, the dual in each case provided a flux-like FIESK which has the properties of an integral source and allowing interactions in voided regions. Thus the development of the adjoint form of the integro-differential and therefrom the integral transport equation was undertaken.

From the adjoint integral transport equation FIESKs for the adjoint emission density and adjoint collision density were derived. Again the transport and collision kernels were defined in an analogous manner to the forward case. The primary focus of Chapter 4 was to expand the adjoint collision kernel to arrive at the following equations:

$$p^{\dagger}_{j,i}(E \to E', \hat{\Omega} \to \hat{\Omega}' \mid \vec{r}, j, i) = \frac{\sigma_{j,i}(E) c_{j,i}(E) p_{j,i}(E \to E', \hat{\Omega} \to \hat{\Omega}')}{\sigma^{\dagger}_{j,i}(E')}, \tag{9.1}$$

and

$$\sigma^{\dagger}_{j,i}(E') = \int\int \sigma_{j,i}(E) c_{j,i}(E) p_{j,i}(E \to E', \hat{\Omega} \to \hat{\Omega}') dE d\hat{\Omega}. \tag{9.2}$$

These two equations provide the necessary relationships between the currently undefined adjoint cross sections and transfer probabilities to the well-known forward cross sections and transfer probabilities for stationary scattering centers. This provided a starting point for developing adjoint physics.

Neutron Transport and Sampling Techniques

Chapter 5 covered the physics and sampling techniques associated with the forward neutron data contained in the ENDF files. The forward reactions considered were:

- elastic scattering,
- inelastic level scattering,
- absorption,
- multiplication,

- and fission.

The adjoint reaction physics and sampling methods derived in Chapter 5 are the adjoint elastic and inelastic level scattering. One important point from the derivation was the fact that the center of mass (CM) scattering angle cosine cannot be used for the adjoint process since it becomes double valued. Thus, the conversion had to be made to the lab frame scattering angle cosine.

ACE Forward Neutron and S(α, β) Implementation and Validation

Chapter 6 covered the implementation of forward neutron physics contained in the ACE data files within FRENSIE. All of the reactions discussed in Chapter 5 except the adjoint scattering have been implemented, and FRENSIE is capable of modeling all ACE reactions. Validation studies have been undertaken to compare FRENSIE and MCNP across a wide variety of tests to ensure that all physics are handled appropriately. Further, photon generation from neutron reactions has also been implemented using the ACE data files. This has been thoroughly tested and has been shown to match MCNP5/6 in discrete and integral test cases. One may find the full set of these tests in Appendix D.

The ACE data files also contain thermal S(α, β) data which captures the elastic and inelastic scattering mechanics of neutrons with molecules and crystalline structures. This method has been implemented in FRENSIE and has been thoroughly tested, however it has been found that there is statistical disagreement between FRENSIE and MCNP. Analysis of the underlying data has found various numerical errors in the ACE S(α, β) data, as well as incorrect handling of edge cases in MCNP. For these reasons contact has been established with LANL and they have been made aware of the issues.

Forward and Adjoint Free Gas S(α, β) Derivation

Chapter 7 handled the development of a high-fidelity free gas thermal scattering method for both forward and adjoint neutron transport. Current models for forward free gas scattering often assume a functional form for the cross section, or isotropic scattering in the CM frame. Further, MCBEND has implemented adjoint neutronics but the adjoint thermal physics are assumed to be a single group with a unified average cross section. This method then provides utility in both the forward and adjoint cases as compared to existing models by providing increased fidelity in the

forward and continuous energy adjoint physics with mobile scattering centers in the adjoint.

The model developed in Chapter 7 is developed from first principles using the generalized forms of the zero-temperature cross section and scattering angle transfer probabilities. The method has been developed for both forward and adjoint thermal neutron transport, and provides an independent method of calculation for forward and adjoint transport. Further, sampling methods for α, $\alpha^\dagger$, β, $\beta^\dagger$ have been developed, as well as a general sampling routine for $S(\alpha,\beta)$ and therefore σ_s. Finally, a simplified model was derived using the isotropic assumption and constant cross section to allow for unit testing of the method.

Forward and Adjoint Free Gas S(α, β) Results

Chapter 8 covered the implementation of the methods derived in Chapter 7 in FRENSIE. In the forward physics implementation FRENSIE displayed excellent agreement with the Wigner-Wilkins theoretical model for neutron elastic scattering on a monatomic gas at thermal equilibrium. Further, FRENSIE was found to correctly reproduce the expected cross section utilized in MCNP, and the full forward transport of FRENSIE and Wigner-Wilkins matched well. There were discrepancies in the transport in MCNP which are currently being investigated.

In the adjoint, the newly developed free gas model in FRENSIE allows for continuous energy thermal neutron adjoint transport which was previously not available in any radiation transport codes. This new cross section not only allows for codes such as MCBEND to expand the continuous energy implementation in the adjoint, but it adds additional accuracy by including the effects of thermal motion on the nuclear scattering center. It is hoped that these developments may be used in the field at large and serve to push adjoint neutron transport forward.

9.2 Impact of the Work

As stated above the goal of this work is two-fold. The primary goal is to develop methods for more accurate treatment of thermal neutrons in both forward and adjoint transport. This will allow problems which rely heavily on the thermal neutron spectrum to more accurately predict results, especially in the cases where materials do not have existing $S(\alpha,\beta)$ tables in the ACE/ENDF libraries. Whether it is improvised explosive device (IED) detection, fissile material inspection, or thermal

neutron radiography, superior accuracy in modeling the physics at play in forward simulations will allow for more confidence in the results obtained. By removing the baseline assumptions built into existing free gas implementations the FRENSIE free gas implementation allows for higher fidelity solutions as more accurate underlying data becomes available, allowing it to be used in simulations going forward. For example, if a more accurate zero-temperature cross section and angular scattering probability become available, FRENSIE is capable of immediately integrating them into the calculation.

With respect to the adjoint, there was previously no continuous energy thermal neutron treatment implemented in a professional radiation transport code. The goal of this method is to not only have adjoint neutron scattering, but to have high-fidelity adjoint neutron scattering which includes the additional accuracy from the free gas derivation. This will also allow for self-adjoint thermal neutron problems to be constructed for validation and benchmarking of future tools and methods. Thus, the derivation and implementation of these methods provide a resource for the nuclear engineering community, extending the current free gas derivations of forward neutrons as well as providing a free gas adjoint model. Beyond simply pushing methods development forward, more accurate forward and adjoint thermal neutron transport serves to produce better results in real world problems in which neutron scattering is the key physics at play.

The secondary goal of this work is to implement these methods in an open-source Monte Carlo software package using a modern software language. Achieving this goal should promote the usage of the FRENSIE code, while also aiding in the adoption of these methods by other transport codes. By providing the methodology alongside a working and freely obtainable implementation the barrier to adopting these new techniques may be substantially lowered. It is the hope of this author that the thermal neutron methods derived and implemented herein will be quickly adopted by larger transport codes such as MCNP, GEANT, and MCBEND thereby increasing the accuracy of radiation transport for the community at large.

9.3 Future Work

While this study has been successful in developing a high-fidelity forward and adjoint free gas thermal neutron scattering treatment, it is certainly not the end of the work. This author believes that future work on this subject may be divided into the following general tasks:

- Further investigation of the discrepancy between the theoretical energy transfer functions and MCNP energy transfer functions. Contact has been made with Los Alamos, and this author intends to continue investigating this issue.
- Generation of data for all ACE isotopes. This report has dealt primarily with hydrogen due to the small set of possible reactions and the readily available theoretical models. However, the software developed works for any ACE data table in general, assuming it contains a specified temperature and an elastic scattering cross section.
- Construction of the non-thermal adjoint elastic and inelastic level scattering as derived in Chapter 5. Along with this a transfer function will need to be studied to hand off from free gas to non-free gas physics in a smoothly varying manner.
- Run full adjoint problems over the entire energy space which allow for true self-adjoint studies and benchmarking.

Appendix A

Salient Features from the Derivation of a Forward and Adjoint Free Gas S(α, β) Scattering Cross Section

The derivation provided in Chapter 7 was relatively thorough except for the derivation of the quantity $P(\bar{\nu}, \bar{\nu}')$. This component of the derivation is included herein for completeness.

A.1 Derivation of $P(\bar{\nu}, \bar{\nu}')$

This derivation will begin from the expression:

$$P(\bar{\nu}, \bar{\nu}') = \frac{(\nu')^2}{(\nu'_{cm})^2} \left(\frac{\delta(\nu'_{cm} - \nu_{cm})}{2\pi} \right) p(\mu_{cm}). \tag{A.1}$$

At this point two orthogonal cartesian coordinate systems will be defined for the CM and laboratory frames respectively. The unprimed directions are taken to represent the laboratory frame with the direction $\hat{x}$ coincident with the incoming neutron velocity $\bar{\nu}$. The primed coordinates correspond to the CM frame with the direction $\hat{x}'$ coincident with the velocity of the center of mass $\bar{\nu}_c$. The following angles are defined in relation to the two coordinate systems and will be necessary for the derivation:

$$\alpha = \text{the angle between the } \hat{x} \text{ and } \hat{x}' \text{ axes,}$$

$$\phi = \text{azimuthal angle of } \bar{\nu}_c \text{ and } \bar{V} \text{ about } \bar{\nu},$$

$$\phi_0 = \text{azimuthal angle of } \bar{\nu}' \text{ about } \bar{\nu}, \text{ and}$$

$$\phi_c = \text{azimuthal angle of } \bar{\nu}'_{cm} \text{ about } \bar{\nu}_c.$$

One can then define an orthonormal matrix $\bar{\bar{A}}$ which allows for the transformation of any vector $\bar{X}$ in the laboratory frame to be related to the velocity vector $\bar{X}'$ in the CM frame as:

$$\bar{X} = \bar{\bar{A}}\bar{X}'. \tag{A.2}$$

The matrix $\bar{\bar{A}}$ can be written as

$$\bar{\bar{A}} = \begin{bmatrix} a_{11} & a_{12} & a_{13} \\ a_{21} & a_{22} & a_{23} \\ a_{31} & a_{32} & a_{33} \end{bmatrix}, \tag{A.3}$$

or

$$\bar{\bar{A}} = \begin{bmatrix} \cos(\hat{x}', \hat{x}) & \cos(\hat{y}', \hat{x}) & \cos(\hat{z}', \hat{x}) \\ \cos(\hat{x}', \hat{y}) & \cos(\hat{y}', \hat{y}) & \cos(\hat{z}', \hat{y}) \\ \cos(\hat{x}', \hat{z}) & \cos(\hat{y}', \hat{z}) & \cos(\hat{z}', \hat{z}) \end{bmatrix}. \tag{A.4}$$

The notation $\cos(\bar{i}, \bar{j})$ indicates the cosine of the angle between vectors $\bar{i}$ and $\bar{j}$. For example, $\cos(\hat{x}', \hat{x}) = \cos(\alpha)$. All of the other terms may be calculated from the angles expressed above.

The most important vector to be able to represent across both the lab frame and the CM frame is the resultant velocity $\bar{v}'$ in the lab frame. Using $\bar{\bar{A}}$ as defined above, the outgoing velocity $\bar{v}'$ may be converted to the CM frame as follows: if

$$\bar{X} = \begin{bmatrix} v'_x \\ v'_y \\ v'_z \end{bmatrix} = \begin{bmatrix} v'\mu_0 \\ v'\sqrt{1-\mu_0^2}\cos(\phi_0) \\ v'\sqrt{1-\mu_0^2}\sin(\phi_0) \end{bmatrix}, \tag{A.5}$$

then

$$\bar{X}' = \begin{bmatrix} v'_{x'} \\ v'_{y'} \\ v'_{z'} \end{bmatrix} = \begin{bmatrix} v'_{cm,x'} + v_{c,x'} \\ v'_{cm,y'} + v'_{c,y'} \\ v'_{cm,z'} + v'_{c,z'} \end{bmatrix}. \tag{A.6}$$

Substituting in the known expressions for $v_c m$ and v_c one finds:

$$\bar{X}' = \begin{bmatrix} v'_{cm}\mu_c + v_c \\ v'_{cm}\sqrt{1-\mu_{cm}^2}\cos(\phi_c) \\ v'_{cm}\sqrt{1-\mu_{cm}^2}\sin(\phi_c) \end{bmatrix}. \tag{A.7}$$

In the same vein, one can state that $\bar{X}'$ can be calculated by utilizing the inverse matrix $\bar{\bar{A}}^{-1}$. Utilizing this to calculate the first term in $\bar{X}'$ yields the expression:

$$\begin{aligned} v'_{cm}\mu_c + v_c = \cos(\alpha)v'\mu_0 + \sin(\alpha)\cos(\phi)v'\sqrt{1-\mu_0^2}\cos(\phi_0) \\ + \sin(\alpha)\sin(\phi)v'\sqrt{1-\mu_0^2}\sin(\phi_0). \end{aligned} \tag{A.8}$$

One can then rewrite this expression as

$$\mu_{cm} = \frac{\nu' F - \nu_c}{\nu'_{cm}}, \tag{A.9}$$

where

$$F = \mu_0 \cos(\alpha) + \sqrt{1-\mu_0^2}\sin(\alpha)\cos(\phi - \phi_0). \tag{A.10}$$

Constants k_1 and k_2 will be introduced to further simplify F as:

$$k_1 = \mu_0 \cos(\alpha), \tag{A.11}$$

and

$$k_2 = \sqrt{1-\mu_0^2}\sin(\alpha). \tag{A.12}$$

Thus

$$F = k_1 + k_2 \cos(\phi - \phi_0). \tag{A.13}$$

Substituting Equation 7.8 into Equation A.9 one finds an alternate expression for F as

$$F = \frac{(\nu')^2 - (\nu'_{cm})^2 + \nu_c^2}{2\nu'\nu_c}. \tag{A.14}$$

Equating the previous two expressions for F and solving for ϕ yields the following expression:

$$\phi = \cos^{-1}\left[\frac{(\nu')^2 - (\nu'_{cm})^2 + \nu_c^2}{2k_2\nu'\nu_c} - \frac{k_1}{k_2}\right] + \phi_0. \tag{A.15}$$

At this point one must evoke the delta-function transformation theorem proposed by Davison [37]:

$$\delta(y(x) - y(x_0)) = \left.\frac{\partial x}{\partial y}\right|_{y=y_0} \cdot \delta(x(y) - x(y_0)). \tag{A.16}$$

In the context of this work it will convert the term $\delta(\nu'_{cm} - \nu_{cm})$ to $\delta(\phi(\nu'_{cm}) - \phi(\nu_{cm}))$. One need only calculate the partial derivative as:

$$\left.\frac{\partial \phi}{\partial \nu'_{cm}}\right|_{\nu'_{cm}=\nu_{cm}} = \frac{\nu_{cm}}{\nu'\nu_c\sqrt{k_2^2 - \left(\frac{(\nu')^2 - (\nu'_{cm})^2 + \nu_c^2}{2\nu'\nu_c} - k_1\right)^2}}, \quad \phi \in [\phi_0, \phi_0 + \pi] \tag{A.17}$$

It must be noted that this only covers half of the azimuthal space. However, it can be observed that F is symmetric for the positive and negative half-spaces of $(\phi - \phi_0)$,

and thus the expression need only be multiplied by 2 to appropriately capture both regions. Substituting this expression into Equation 7.16 one finds the result:

$$P(\bar{\nu}, \bar{\nu}') = \left[\frac{\nu' \nu_{cm} \delta \left(\phi(\nu'_{cm}) - \phi(\nu_{cm}) \right)}{\pi (\nu'_{cm})^2 \nu_c \left(k_2^2 - (s - k_1)^2 \right)^{1/2}} \right] p(\mu_{cm}), \tag{A.18}$$

where

$$s = \frac{(\nu')^2 - \nu_{cm}^2 + \nu_c^2}{2\nu' \nu_c}. \tag{A.19}$$

Appendix B

Neutron Kinematic Derivations

In Chapter 5 the derivation of several kinematic quantities was omitted for brevity. They are included herein for the sake of completeness.

B.1 Inelastic Level Scattering Kinematic Derivation

The kinematics of inelastic level scattering (and therefore elastic scattering when $E^* = 0$) are derived. One must begin by first defining the center of mass (CM) reference frame to be the reference frame in which there is no net momentum. Thus the velocity of the center of mass may be found by determining the velocity of the net mass in the laboratory frame as follows:

$$\begin{aligned} \bar{V}_{CM}(m_n + M) &= (m_n \bar{v}_l + M\bar{V}_l) \\ \bar{V}_{CM} &= \frac{m_n}{m_n + M}\bar{v}_l. \end{aligned} \tag{B.1}$$

Here the assumption was made that the target nucleus is at rest in the laboratory frame. The previous expression can be further simplified by defining the mass ratio $A = M/m$ which yields

$$\bar{V}_{CM} = \frac{1}{1 + A}\bar{v}_l. \tag{B.2}$$

To handle the kinematics in the CM frame, one also needs to determine the velocity of the neutron and the target in that frame. This can be done by taking the relative velocity between their lab frame velocities and the velocity of the CM frame as follows:

$$\begin{aligned} \bar{v}_c &= \bar{v}_L - \bar{V}_{CM} \\ &= \frac{A}{A + 1}\bar{v}_L \end{aligned} \tag{B.3}$$

and

$$\begin{aligned}\bar{V}_c &= \bar{V}_L - \bar{V}_{CM} \\ &= -\bar{V}_{CM} \\ &= -\frac{1}{A+1}\bar{v}_L \end{aligned} \tag{B.4}$$

Before proceeding it is also of use to have an expression relating the scattering angle of the neutron θ in the laboratory frame and the CM frame. This can be done by observing the relationship between the final velocities in the respective frames as follows:

$$\hat{x}: \quad v'_L \cos\theta_L = V_{cm} + v'_c \cos\theta_c, \tag{B.5}$$

and

$$\hat{y}: \quad v'_L \sin\theta_L = v'_c \sin\theta_c. \tag{B.6}$$

Taking the ratio of these two expressions yields the following equation:

$$\tan\theta_L = \frac{\sin\theta_c}{\frac{V_{cm}}{v'_c} + \cos\theta_c}. \tag{B.7}$$

At this point one must consider the relationship between the initial and final energies, utilizing the center of mass scattering angle. Note that one often deals with the center of mass scattering angle, rather than the laboratory scattering angle when sampling from the ENDF/ACE data files. One can find this relationship by squaring and summing equations B.5 and B.6 to find:

$$v'^2_L = V^2_{cm} + 2V_{cm}v'_c\mu_c + v'^2_c, \tag{B.8}$$

where

$$\mu_c = \cos\theta_c. \tag{B.9}$$

Substituting in the known expression for the velocity of the CM reference frame, one finds the following expression:

$$v'^2_L = \left(\frac{1}{A+1}\right)^2 v^2_L + 2\left(\frac{1}{A+1}\right) v_L v'_c \mu_c + v'^2_c \tag{B.10}$$

One can then divide by V_{cm}^2 to yield:

$$(A+1)^2 \frac{v_L'^2}{v_L^2} = 1 + 2(A+1)\frac{v_c'}{v_L}\mu_c + \frac{v_c'^2}{v_L^2} \tag{B.11}$$

By inspection the ratio of the square of the laboratory frames is also the ratio of the laboratory energies. Thus,

$$\frac{E'}{E} = \frac{1}{(A+1)^2}\left(1 + 2(A+1)\frac{v_c'}{v_L}\mu_c + \frac{v_c'^2}{v_L^2}\right) \tag{B.12}$$

The only remaining unknown in this expression is the center of mass final neutron speed. In order to determine this value, one must analyze the kinematics of the inelastic scattering in the CM frame. First, the total energy in the system before and after the scattering event may be written as

$$\frac{1}{2}m_n v_c^2 + \frac{1}{2}MV_c^2 = \frac{1}{2}m_n v_c^2 + \frac{1}{2}MV_c^2 + E^*, \tag{B.13}$$

where E^* denotes the excitation energy of the target nucleus. Recall that if $E^* = 0$ this derivation reduces to the elastic scattering derivation. In order to relate the velocities one must recognize that the definition of the CM frame states that there is no net momentum. Thus, before the collision one would write:

$$m\bar{v}_c = M\bar{V}_c. \tag{B.14}$$

Squaring both sides of this equation and simplifying yields the expression

$$\frac{1}{2}MV_c^2 = \left(\frac{1}{A}\right)\frac{1}{2}mv_c^2. \tag{B.15}$$

The same relationship may be formed for the no-net momentum case post scattering event as well. Substituting these expressions into the conservation of energy simplifies the expression to

$$\frac{1}{2}m_n v_c^2\left(\frac{1+A}{A}\right) = \frac{1}{2}m_n v_c^2\left(\frac{1+A}{A}\right) + E^*, \tag{B.16}$$

The initial velocity in the CM frame is already known in terms of the known velocity in the lab frame. Substituting in this known relationship yields:

$$\frac{1}{2}m_n v_L^2 \left(\frac{A}{1+A}\right) = \frac{1}{2}m_n v_c^2 \left(\frac{1+A}{A}\right) + E^*, \tag{B.17}$$

The right hand side (RHS) can be simplified using the expression for the kinetic energy and the entire equation may be rearranged to solve for the unknown outgoing speed in the CM frame as follows:

$$v_c' = \sqrt{\frac{2}{m}\left(\frac{A}{A+1}\right)\left[\left(\frac{A}{A+1}\right)E + E^*\right]}. \tag{B.18}$$

This can be substituted back into Equation B.12 and the outgoing energy can be found. In a similar fashion the outgoing angle may also be found as there is a one-to-one correspondence between the outgoing energy and angle for two-body kinematics. A simplified expression after algebraic manipulation for the outgoing energy is as follows:

$$E' = E\left[\frac{A^2\left(1-\left(\frac{A+1}{A}\right)\frac{E^*}{E}\right) + 2A\mu_{CM}\left(1-\left(\frac{A+1}{A}\right)\frac{E^*}{E}\right)^{1/2} + 1}{(A+1)^2}\right] \tag{B.19}$$

Appendix C

ACE S(α, β) Data Structure and Code Changes

Appendix C briefly discusses the changes made to allow for the use of the $S(\alpha, \beta)$ data from the ACE tables in FRENSIE. It should first be noted that while it is referred to as a function of α and β, the actual information has been stored in three dimensional tables of (E', E, μ) rather than two dimensional tables of (α, β). This has the marked effect of making the data tables significantly larger than necessary (n^3 rather than n^2). Nonetheless, the actual transfer probability data structure can be seen in Figure C.3. For each incoming energy there exists an associated outgoing energy distribution and for each value in the outgoing energy distribution there exists a uniformly distributed set of outgoing scattering angle cosines.

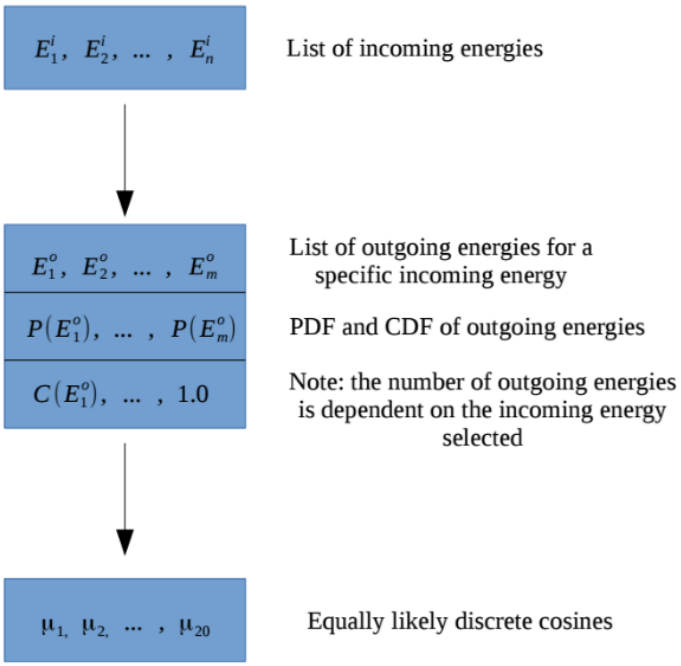

Figure C.1: **Transfer probability data structure of S(α, β) ACE tables.** *While referred to as a function of* (α, β)*, the actual transfer probabilities are stored as a function of* (E', E, μ) *in the ACE data files.*

As was stated in Chapter 6, significant changes needed to be implemented to allow FRENSIE to utilize S(α, β) data. These changes are also relevant to the implementation of the free gas S(α, β) method derived in this work. Namely, the changes required the development of new sampling routines to handle the nested distributions in the ACE S(α, β), as well as new reaction and nuclide classes to handle the data, and finally a refactor of the existing collision handler to allow for the production and utilization of nuclides with the same base data sets but selected differing reactions. Figures X and Y depict the previous and current state of the collision module. The red boxes indicate the production of new classes and refactoring of old classes.

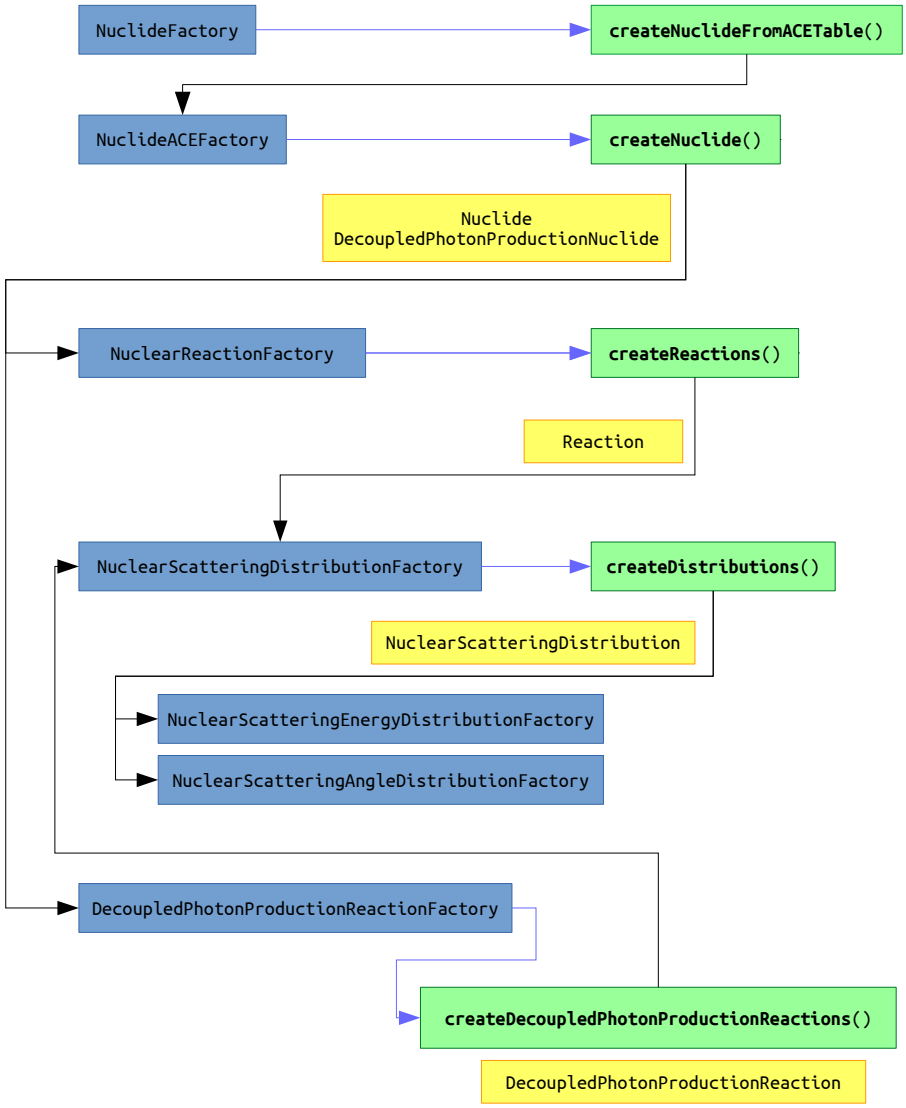

Figure C.2: **Previous structure of the collision module.** *The previous structure of the collision module only allowed for a single form of each nuclide to be constructed. This did not allow for the manipulation of nuclides within specific materials or regions of interest.*

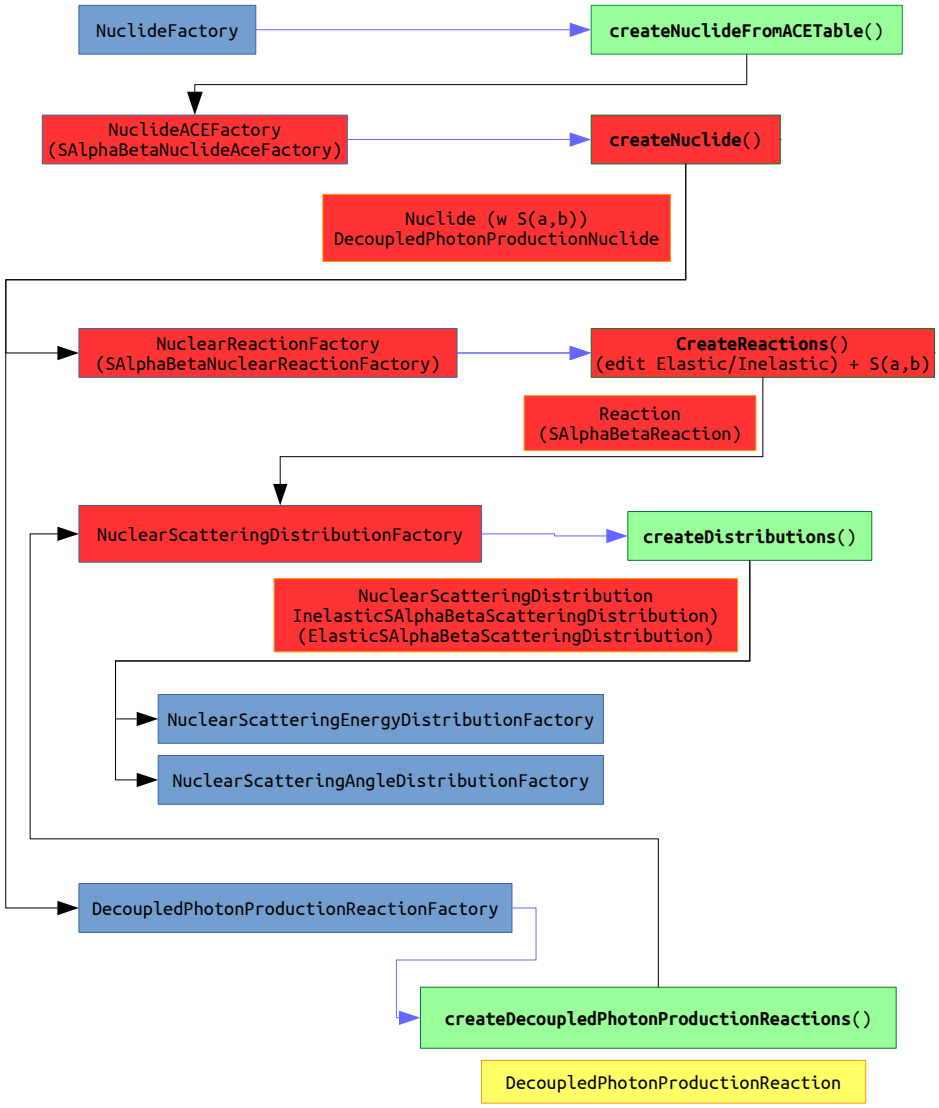

Figure C.3: **Updated structure of the collision module to allow for specialized reactions.** *The updated collision module now allows for multiple versions of any nuclide to be constructed. This allows one to study specific reactions of interest, include previously undefined reactions, or to turn reactions off entirely. This new structure is of importance both for implementing the S(α, β) work, but also for the testing of specific reactions going forward.*

Appendix D

Forward Neutron Validation Graphs

Appendix D includes the graphs of seven forward neutron validation problems for FRENSIE. These problems are described in Table 6.1. One additional validation study is included to validate the first collided source.

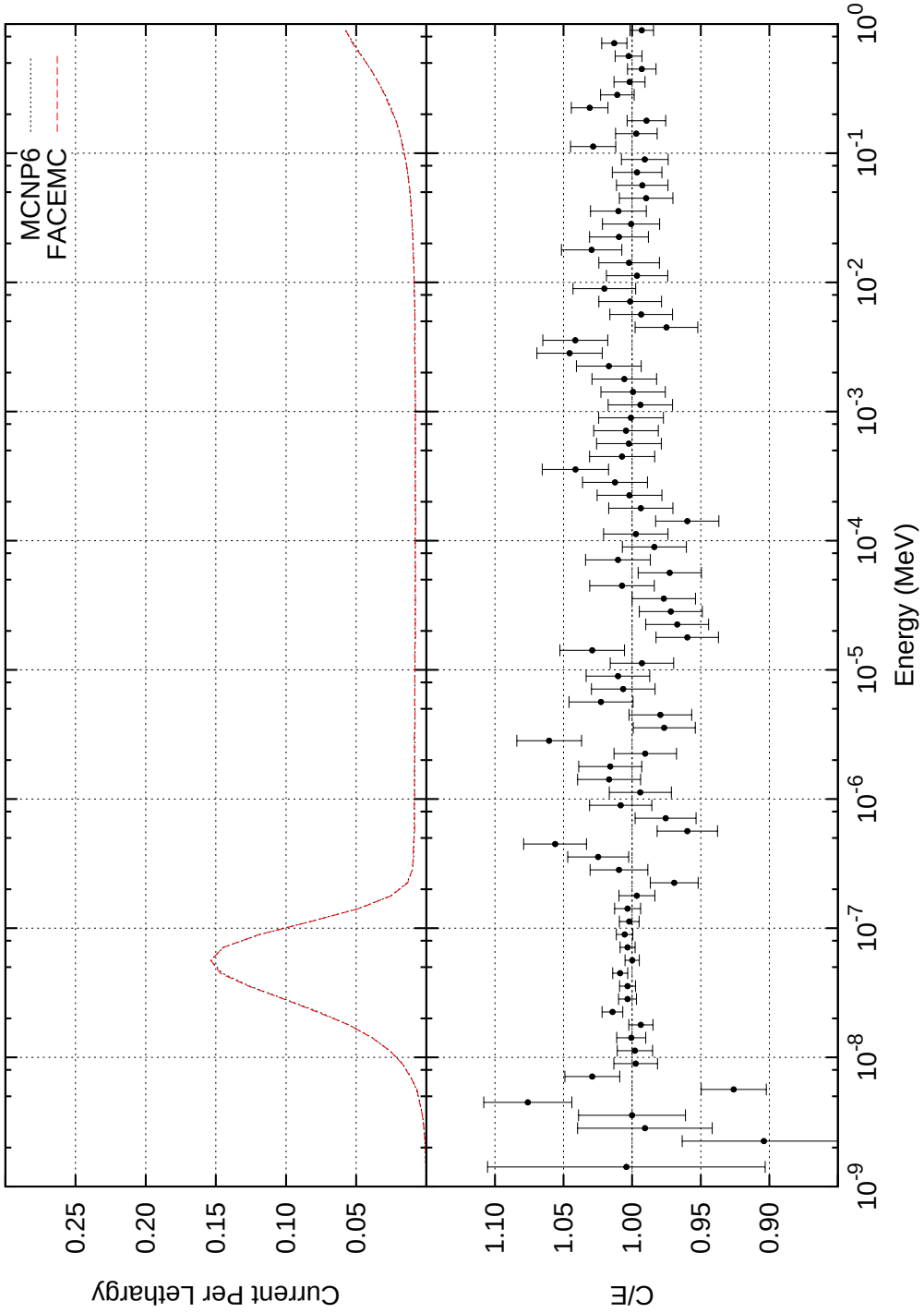

Figure D.1: **Comparison of FRENSIE vs. MCNP for Test 1.** *This problem consists of a 1 cm radius hydrogen sphere at 1 at/b-cm and 293.6K with a point source of neutrons at the origin of 1.0 MeV.*

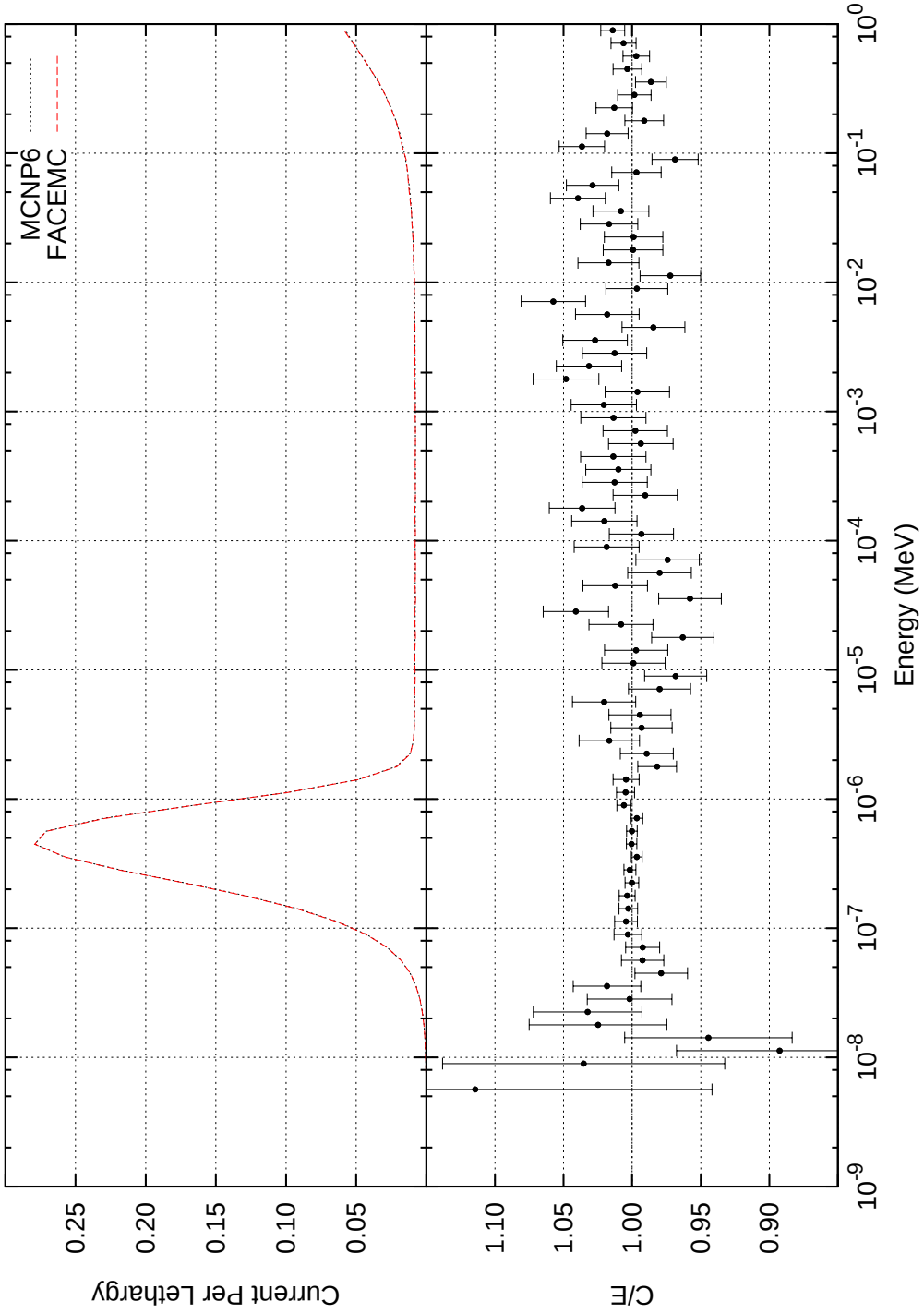

Figure D.2: **Comparison of FRENSIE vs. MCNP for Test 2.** *This problem consists of a 1 cm radius hydrogen sphere at 1 at/b-cm and 2500K with a point source of neutrons at the origin of 1.0 MeV.*

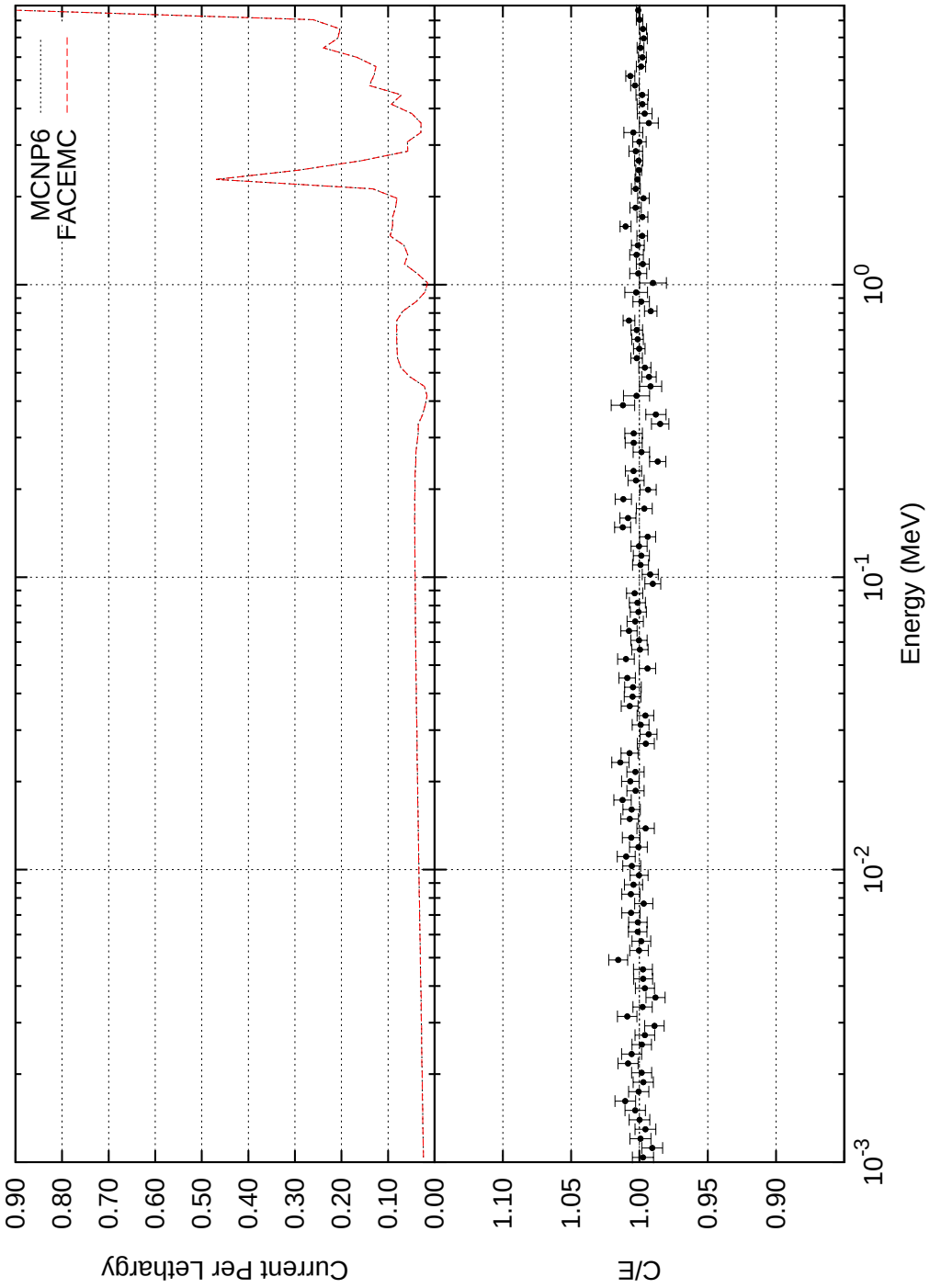

Figure D.3: **Comparison of FRENSIE vs. MCNP for Test 3.** *This problem consists of a 3 cm radius oxygen sphere at 1 at/b-cm and 293.6K with a point source of neutrons at the origin of 9.0 MeV.*

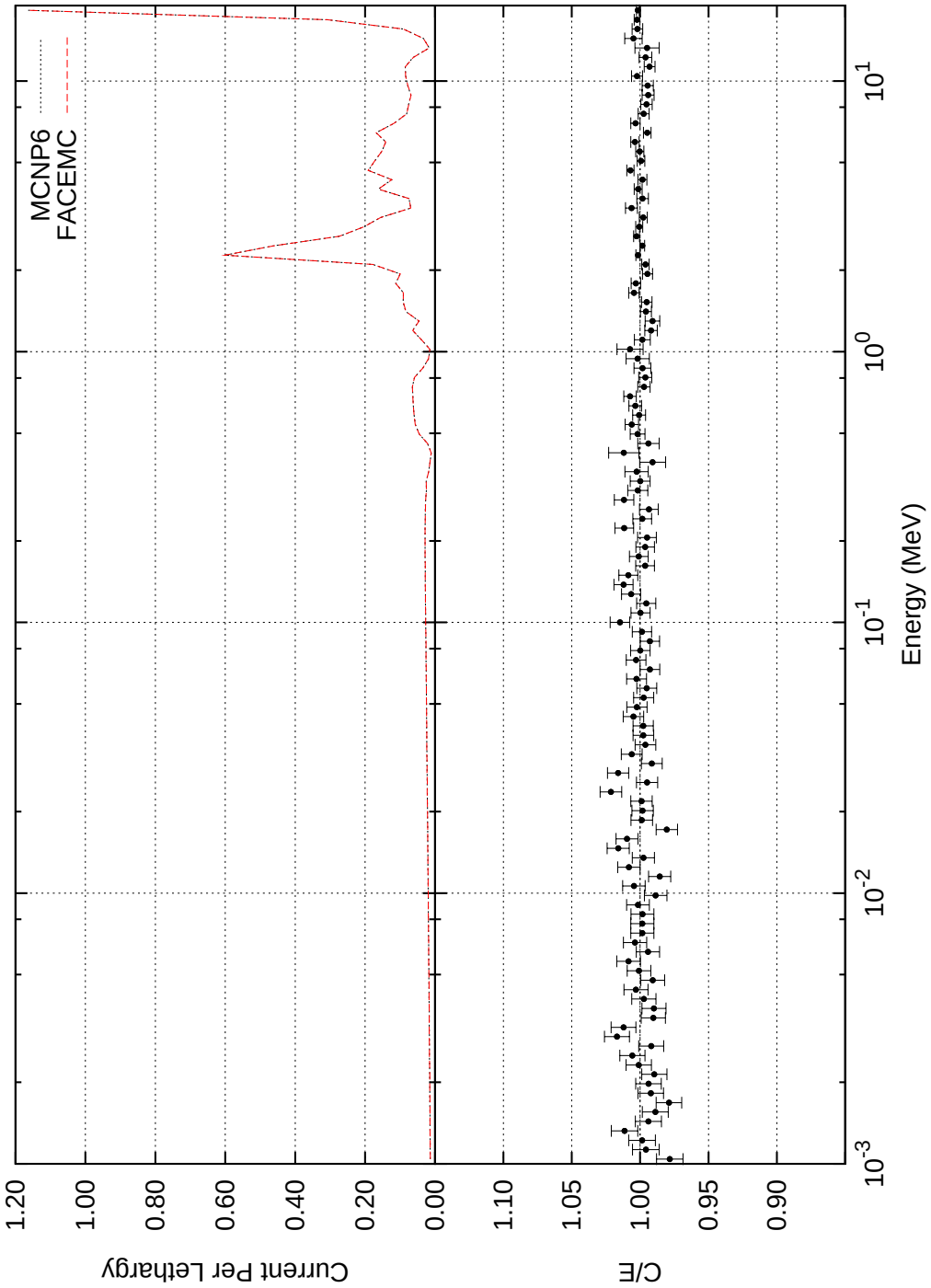

Figure D.4: **Comparison of FRENSIE vs. MCNP for Test 4.** *This problem consists of a 3 cm radius oxygen sphere at 1 at/b-cm and 293.6K with a point source of neutrons at the origin of 19.0 MeV.*

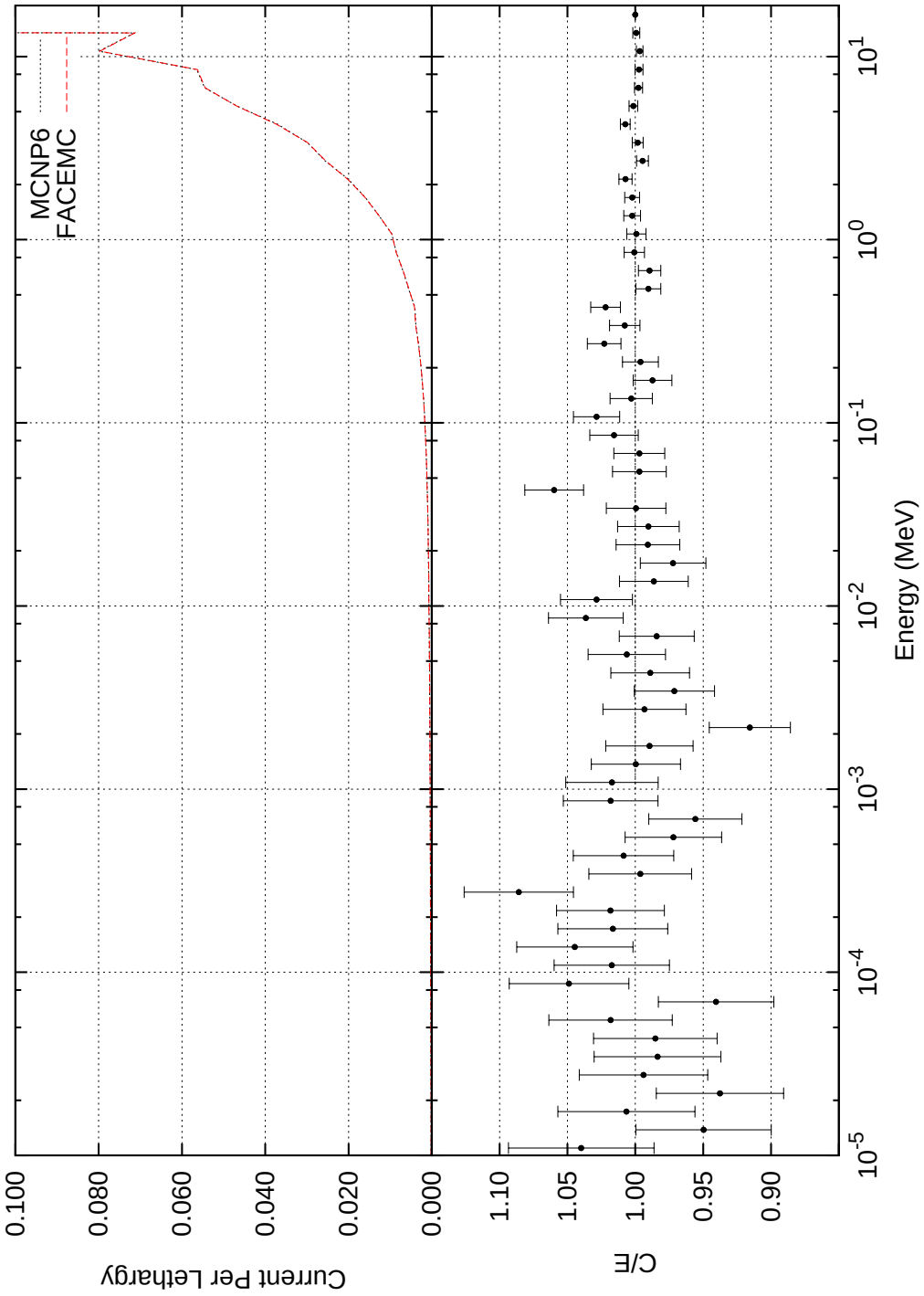

Figure D.5: **Comparison of FRENSIE vs. MCNP for Test 5.** *This problem consists of a 3 cm radius water sphere at 1 at/b-cm and 293.6K with a point source of neutrons at the origin of 19.0 MeV.*

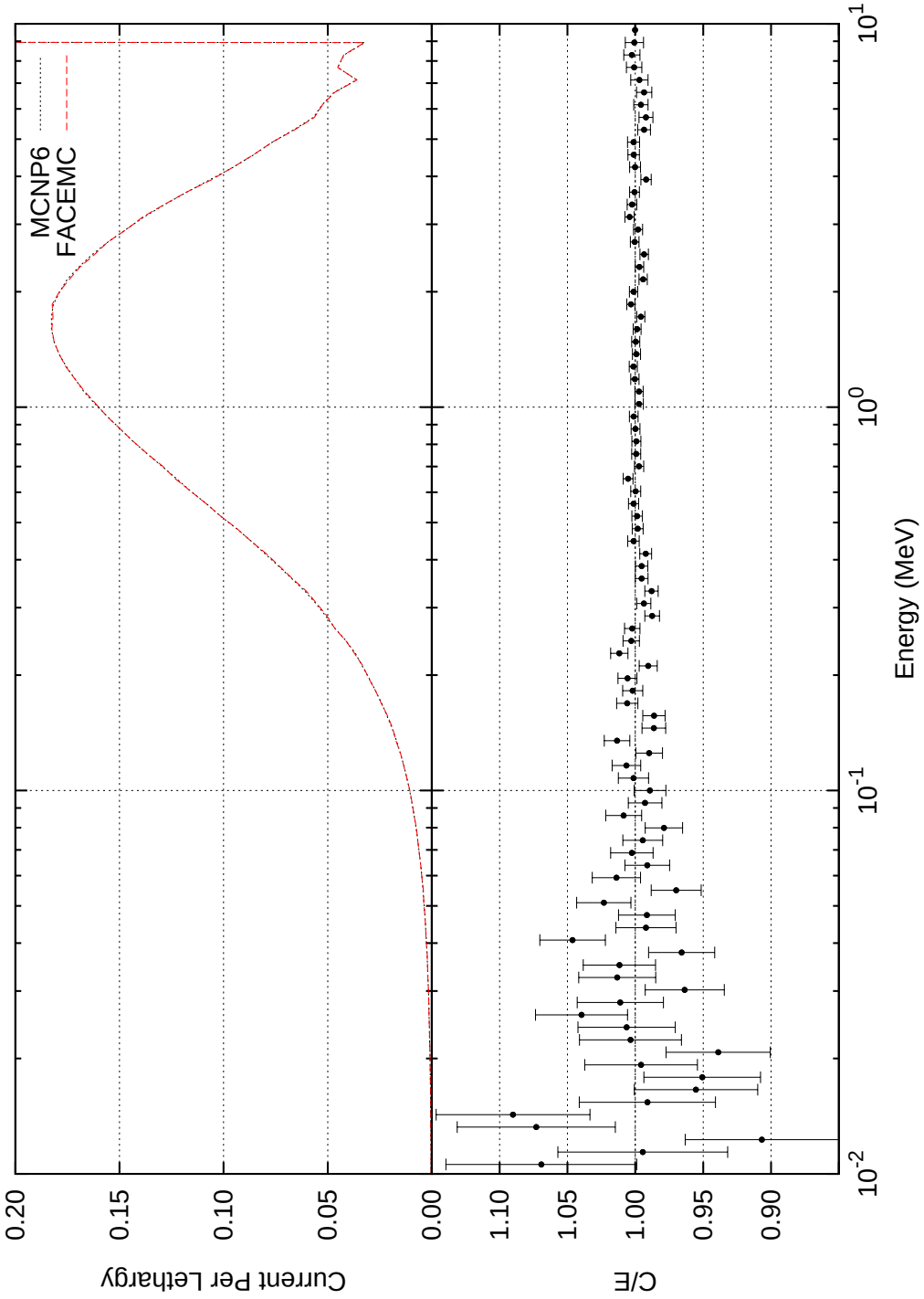

Figure D.6: **Comparison of FRENSIE vs. MCNP for Test 6.** *This problem consists of a 1 cm radius ^{235}U sphere at 1 at/b-cm and 293.6K with a point source of neutrons at the origin of 10.0 MeV.*

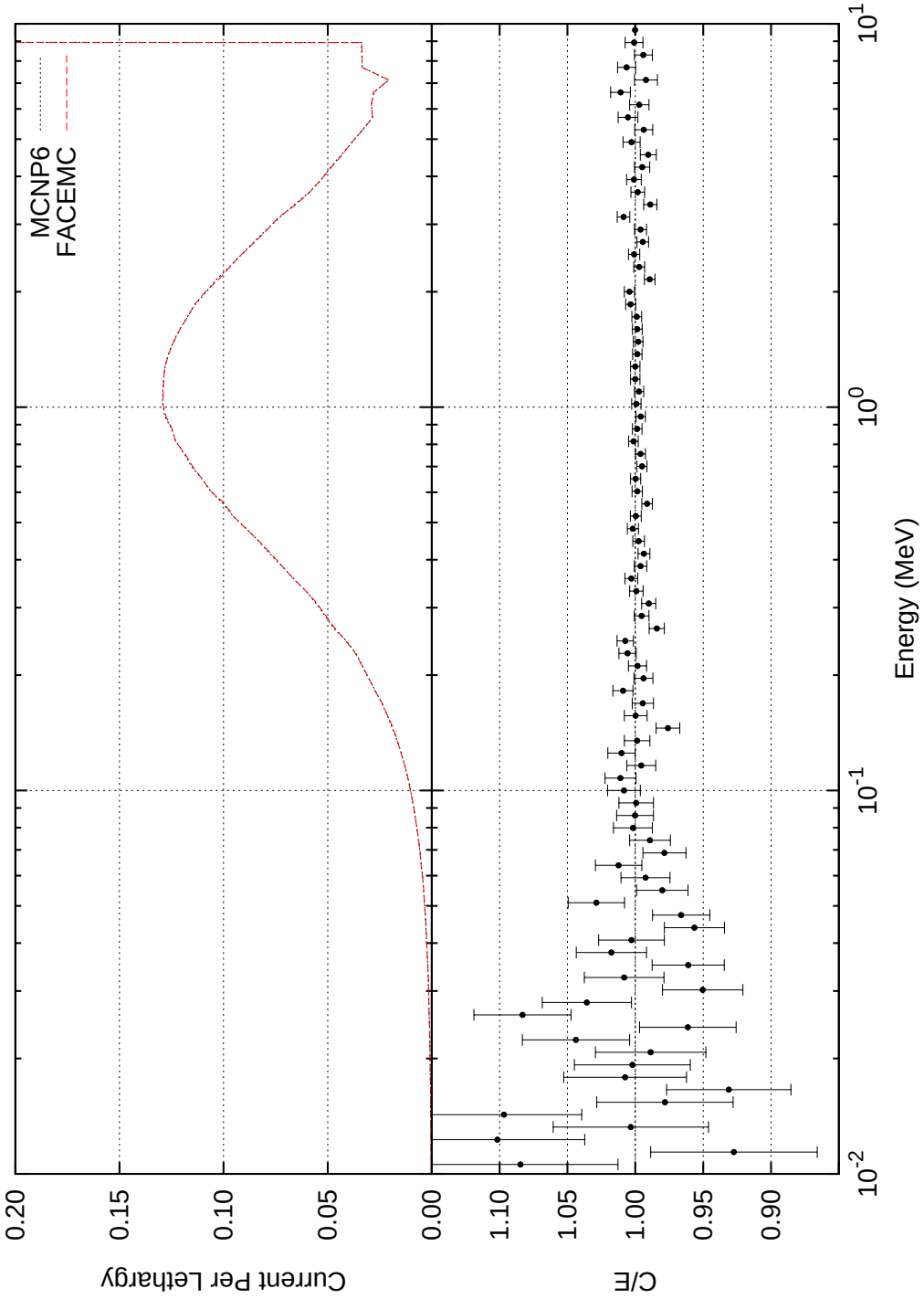

Figure D.7: **Comparison of FRENSIE vs. MCNP for Test 7.** *This problem consists of a 1 cm radius ^{238}U sphere at 1 at/b-cm and 293.6K with a point source of neutrons at the origin of 10.0 MeV.*

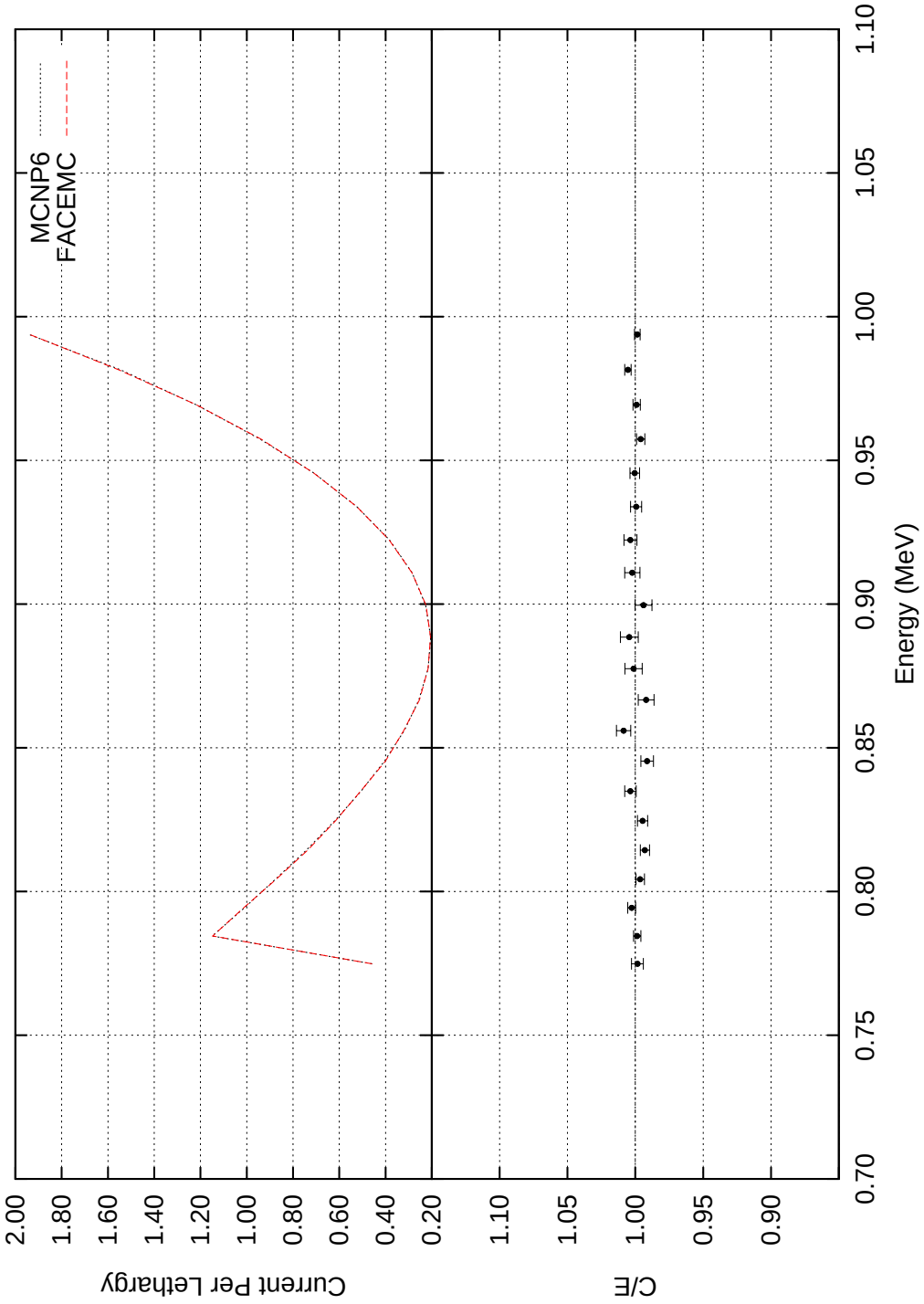

Figure D.8: **Comparison of FRENSIE vs. MCNP for Test 8.** *This problem consists of a 1 cm radius water sphere at 1 at/b-cm and 293.6K with a point source of neutrons at the origin of 1.0 MeV. Only the first collided current is investigated.*

Appendix E

FRENSIE Forward Free Gas Energy Transfer PDF and CDF Plots

Appendix E includes the plots of the FRENSIE forward free gas energy transfer PDF and CDF results.

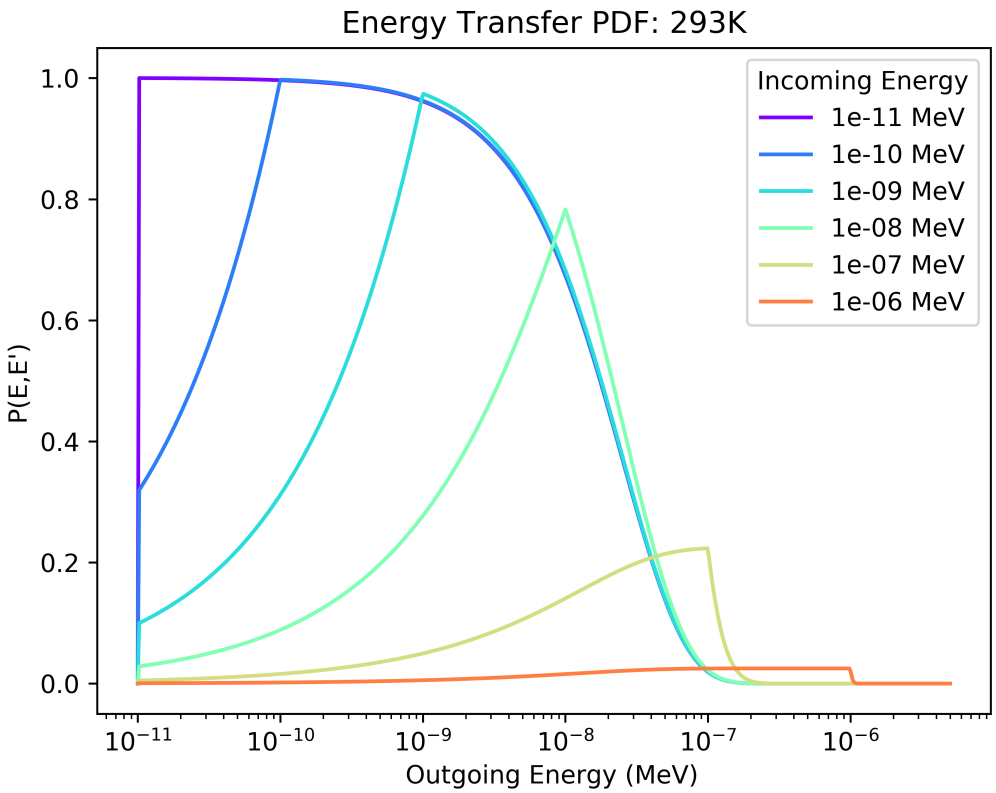

Figure E.1: **FRENSIE Free Gas Energy Transfer PDF at 293K.** *The free gas energy transfer PDF is plotted for various incoming neutron energies incident on a monatomic hydrogen gas a temperature of 293K.*

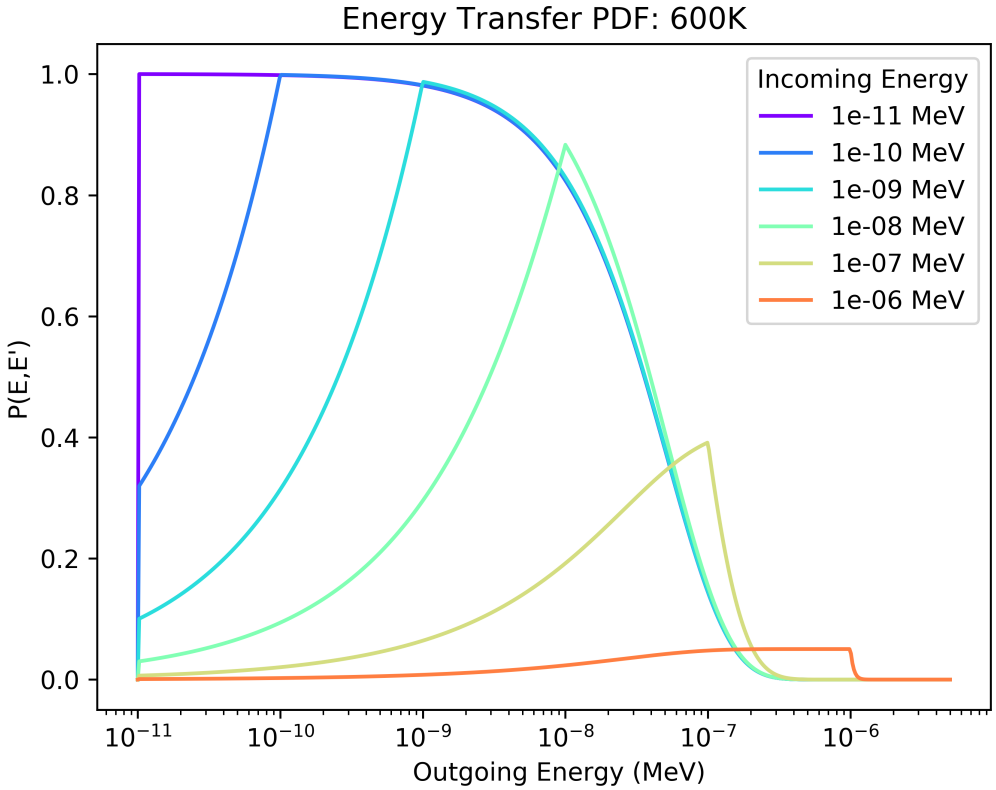

Figure E.2: **FRENSIE Free Gas Energy Transfer PDF at 600K.** *The free gas energy transfer PDF is plotted for various incoming neutron energies incident on a monatomic hydrogen gas a temperature of 600K.*

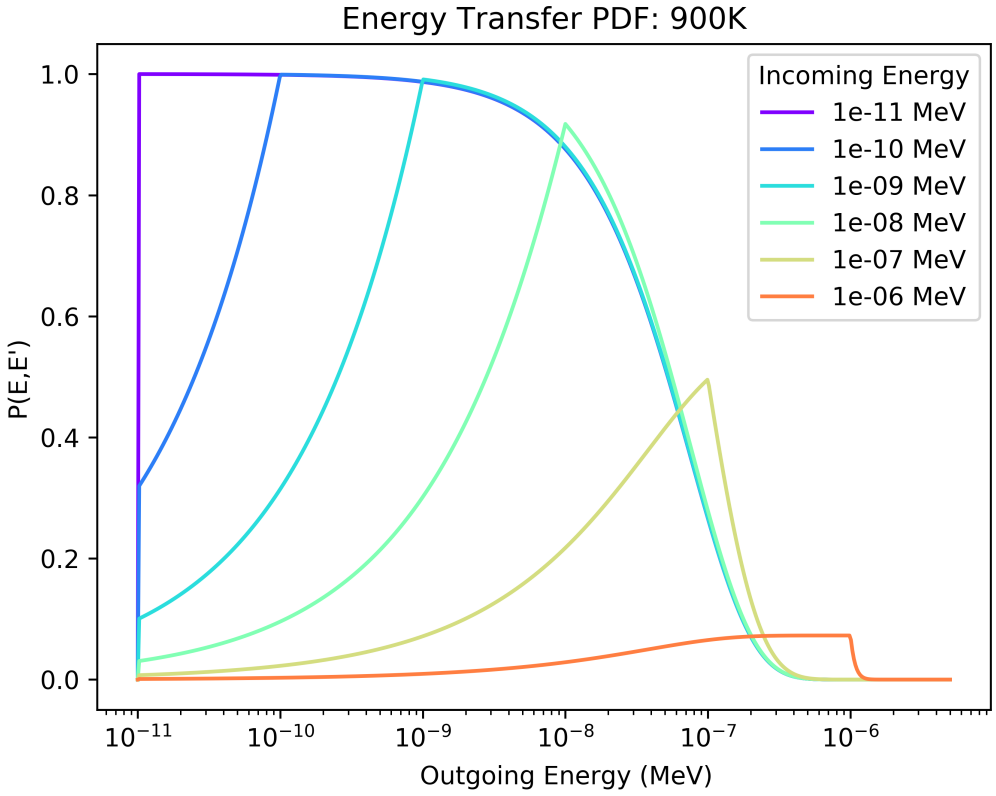

Figure E.3: **FRENSIE Free Gas Energy Transfer PDF at 900K.** *The free gas energy transfer PDF is plotted for various incoming neutron energies incident on a monatomic hydrogen gas a temperature of 900K.*

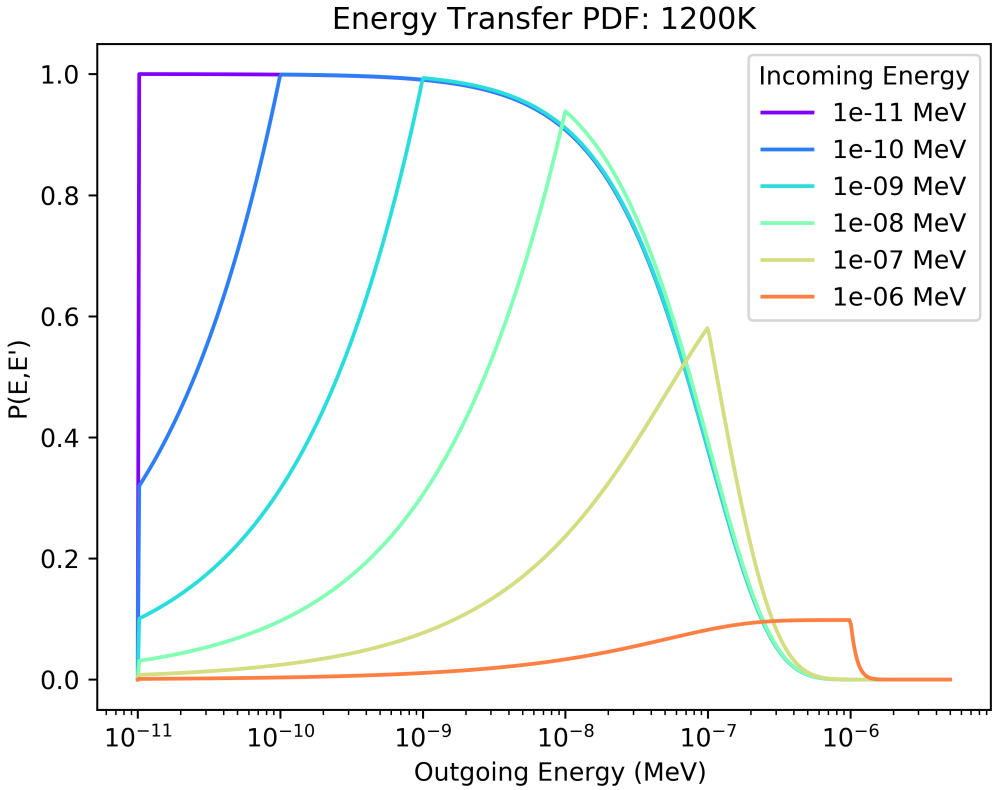

Figure E.4: **FRENSIE Free Gas Energy Transfer PDF at 1200K.** *The free gas energy transfer PDF is plotted for various incoming neutron energies incident on a monatomic hydrogen gas a temperature of 1200K.*

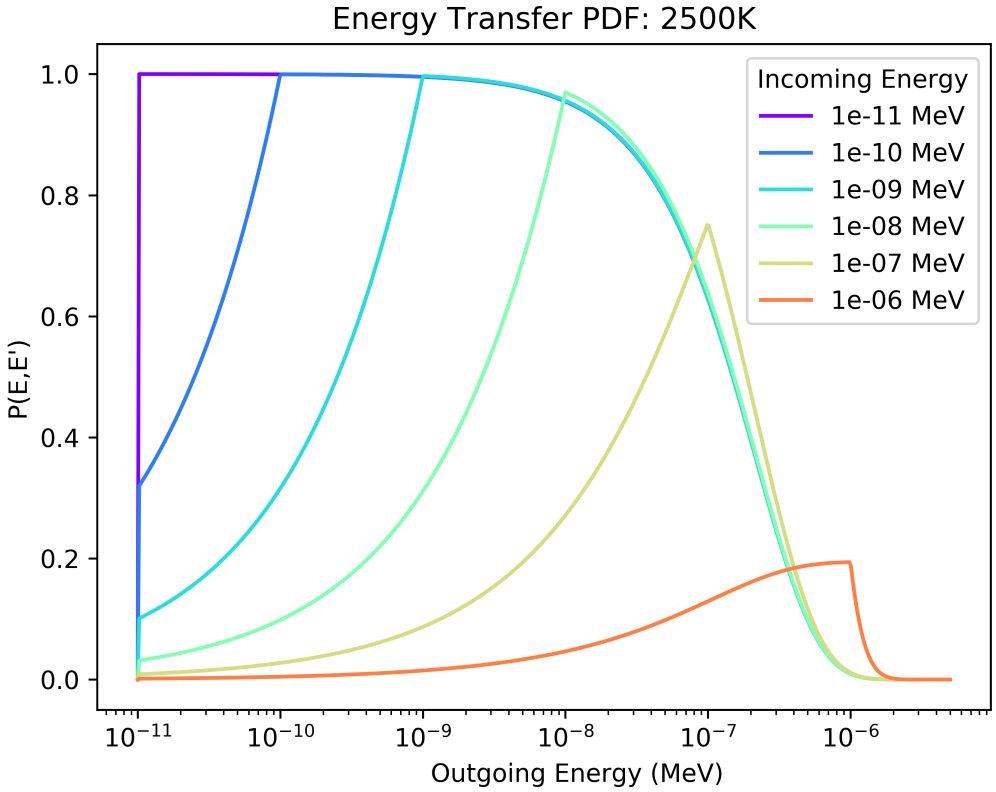

Figure E.5: **FRENSIE Free Gas Energy Transfer PDF at 2500K.** *The free gas energy transfer PDF is plotted for various incoming neutron energies incident on a monatomic hydrogen gas a temperature of 2500K.*

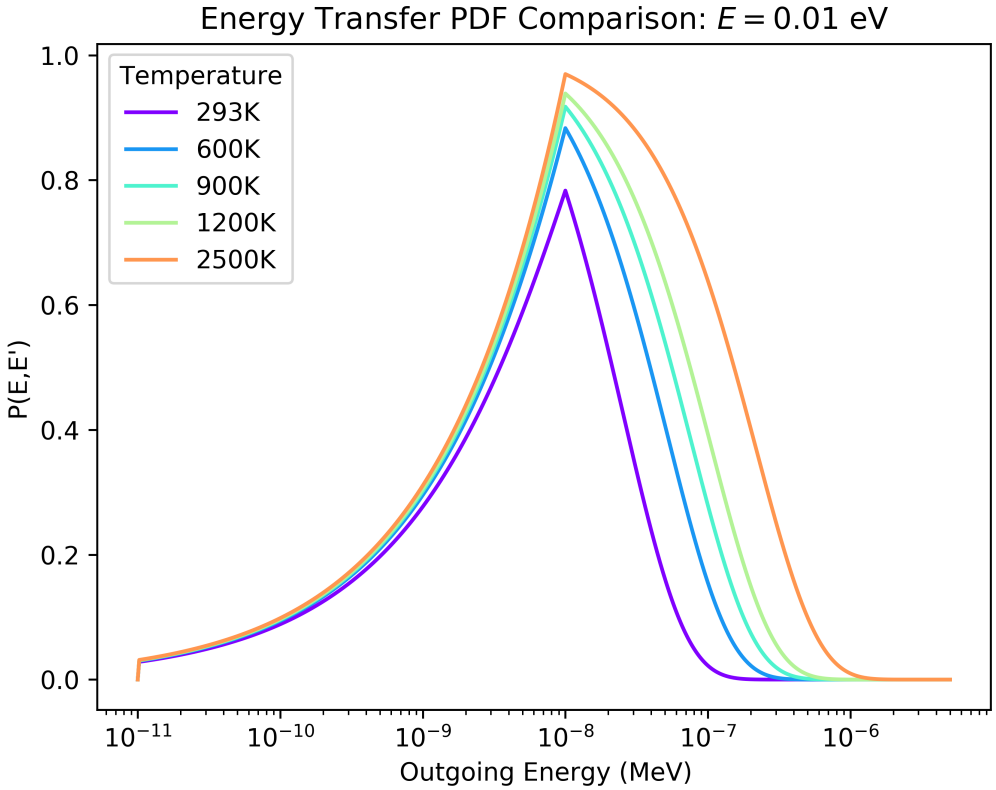

Figure E.6: **FRENSIE Free Gas Energy Transfer PDF at Varying Temperatures for Incident Energy of 0.01 eV.** *The free gas energy transfer PDF is plotted for various temperatures with a fixed incident neutron energy of 0.01 eV.*

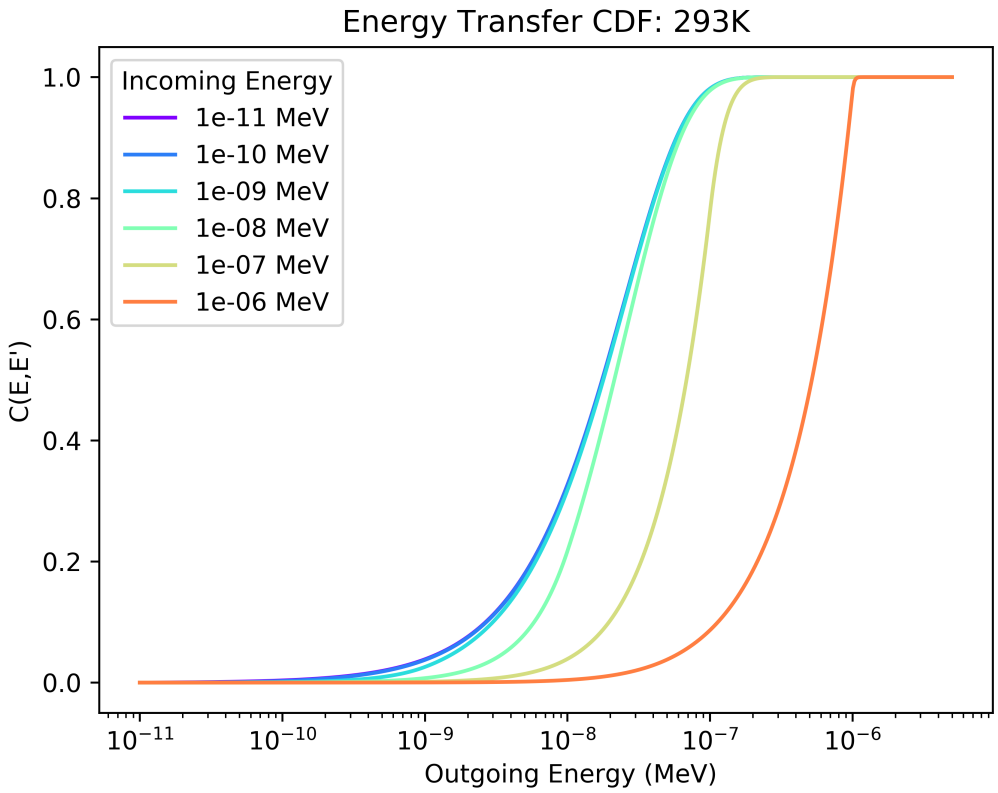

Figure E.7: **FRENSIE Free Gas Energy Transfer CDF at 293K.** *The free gas energy transfer CDF is plotted for various incoming neutron energies incident on a monatomic hydrogen gas a temperature of 293K.*

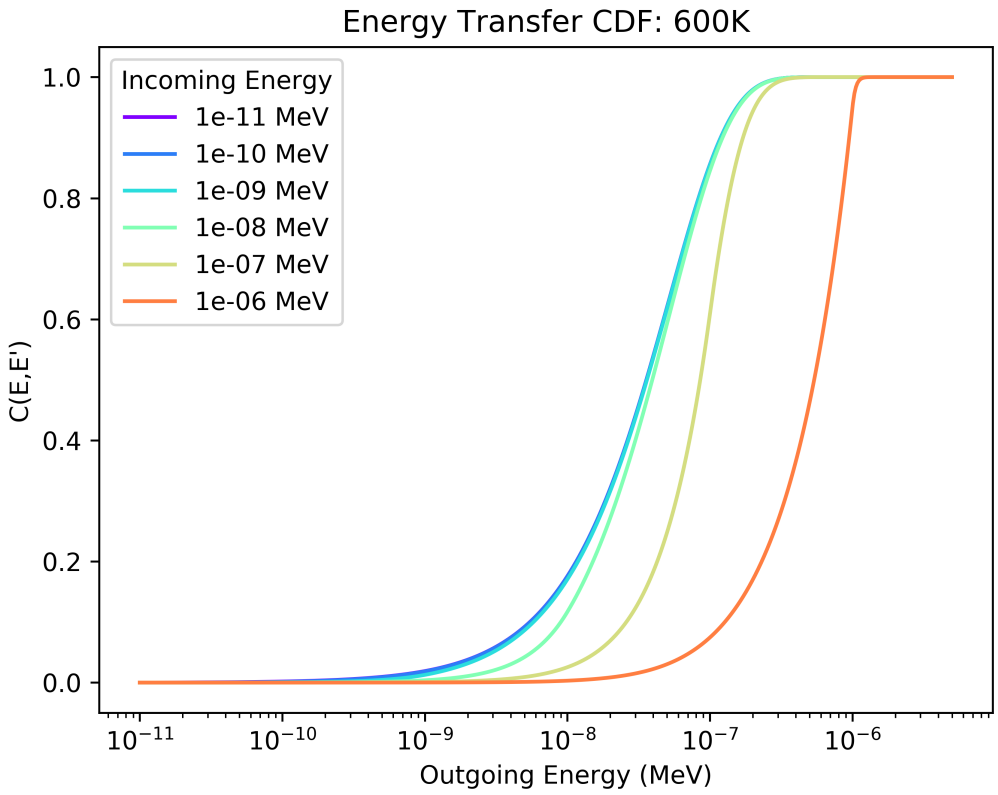

Figure E.8: **FRENSIE Free Gas Energy Transfer CDF at 600K.** *The free gas energy transfer CDF is plotted for various incoming neutron energies incident on a monatomic hydrogen gas a temperature of 600K.*

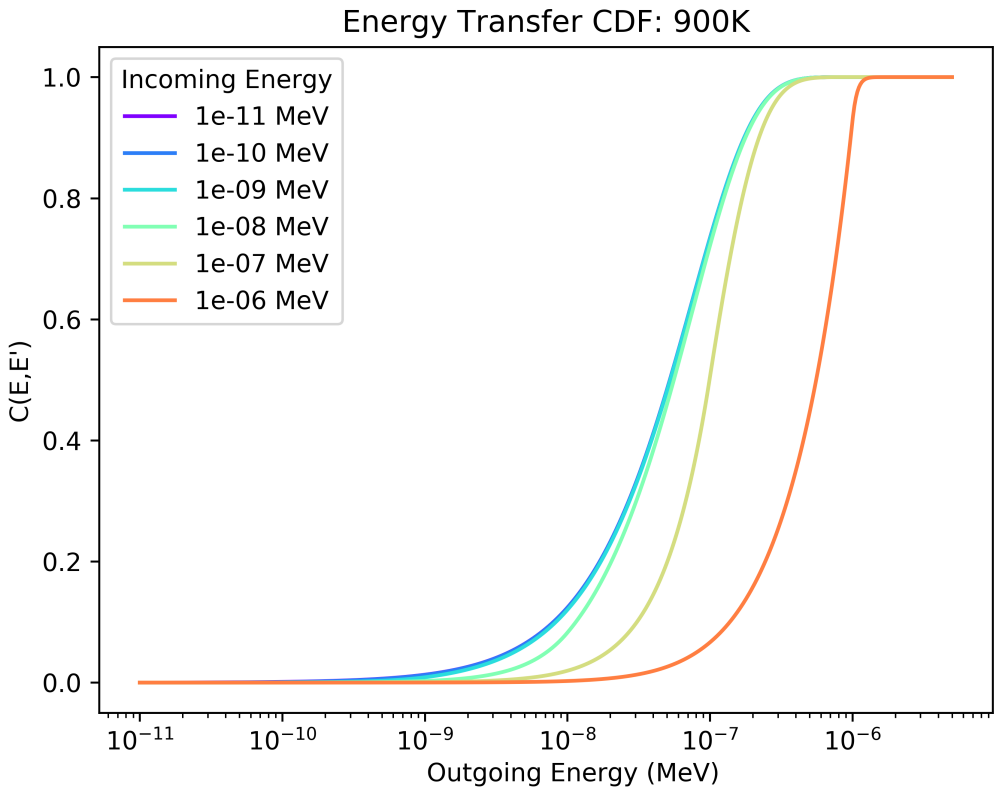

Figure E.9: **FRENSIE Free Gas Energy Transfer CDF at 900K.** *The free gas energy transfer CDF is plotted for various incoming neutron energies incident on a monatomic hydrogen gas a temperature of 900K.*

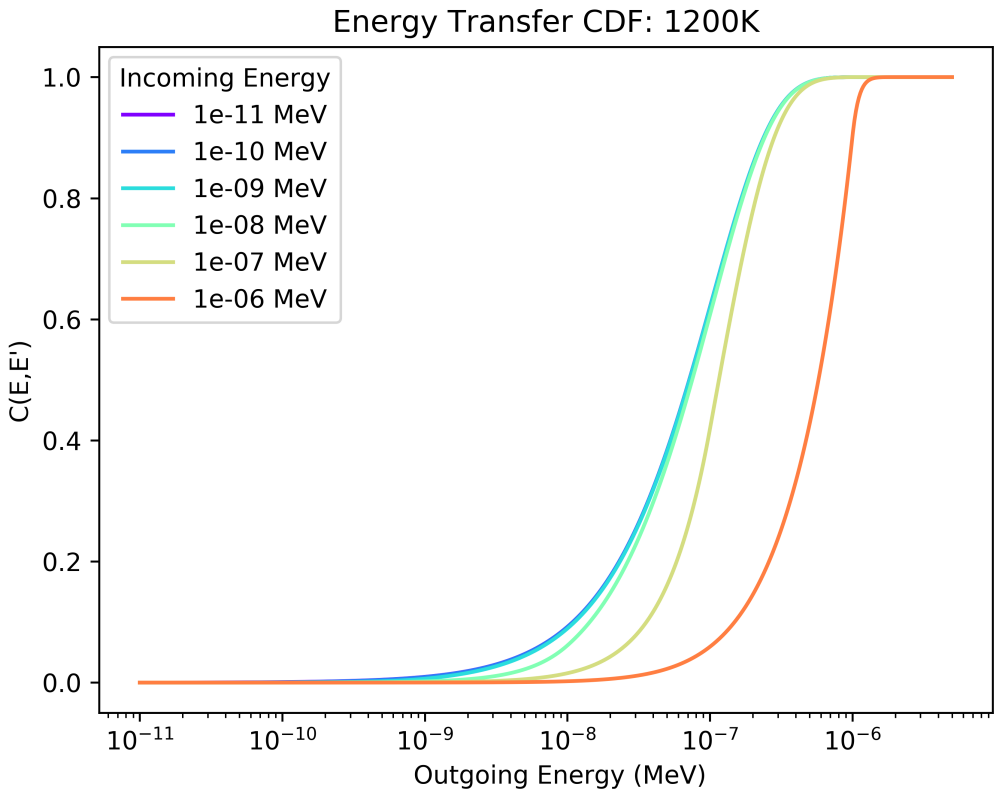

Figure E.10: **FRENSIE Free Gas Energy Transfer CDF at 1200K.** *The free gas energy transfer CDF is plotted for various incoming neutron energies incident on a monatomic hydrogen gas a temperature of 1200K.*

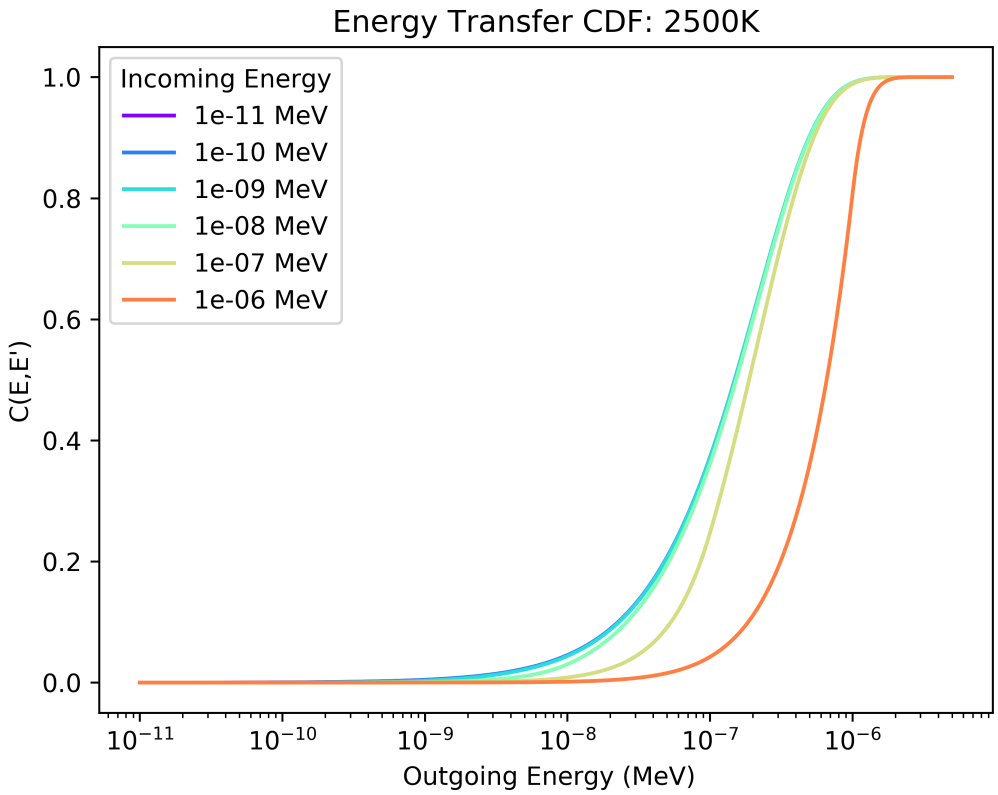

Figure E.11: **FRENSIE Free Gas Energy Transfer CDF at 2500K.** *The free gas energy transfer CDF is plotted for various incoming neutron energies incident on a monatomic hydrogen gas a temperature of 2500K.*

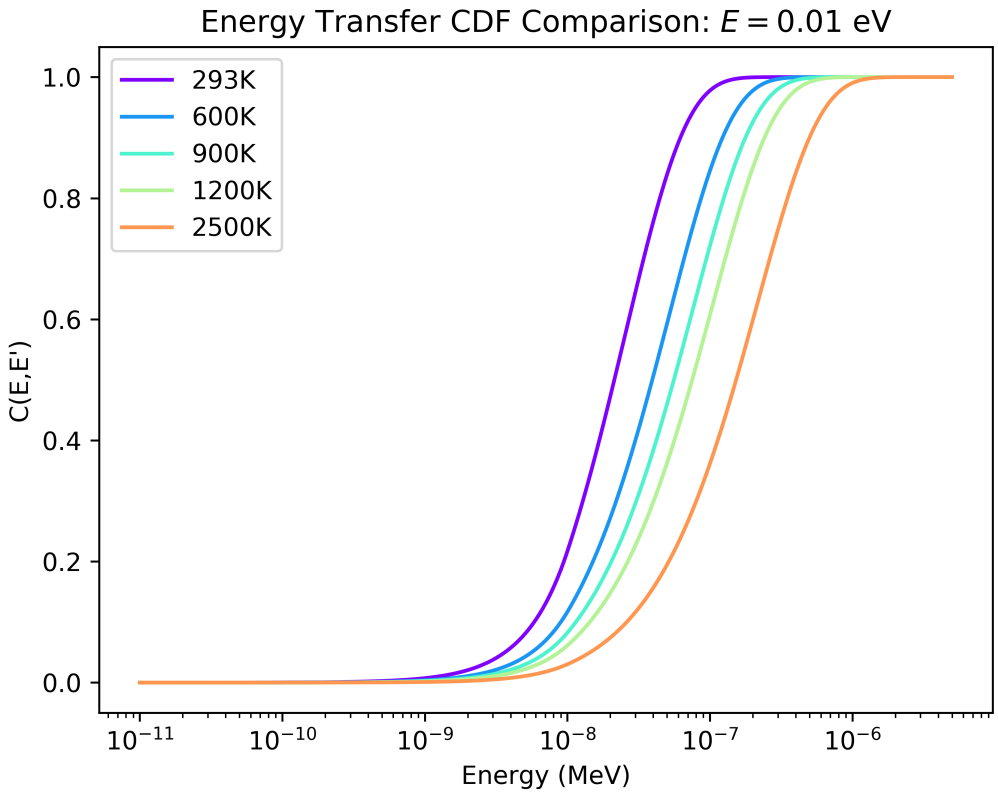

Figure E.12: **FRENSIE Free Gas Energy Transfer CDF at Varying Temperatures for Incident Energy of 0.01 eV.** *The free gas energy transfer CDF is plotted for various temperatures with a fixed incident neutron energy of 0.01 eV.*

Appendix F

FRENSIE Adjoint Free Gas Energy Transfer PDF and CDF Plots

Appendix F includes the plots of the FRENSIE adjoint free gas energy transfer PDF and CDF results.

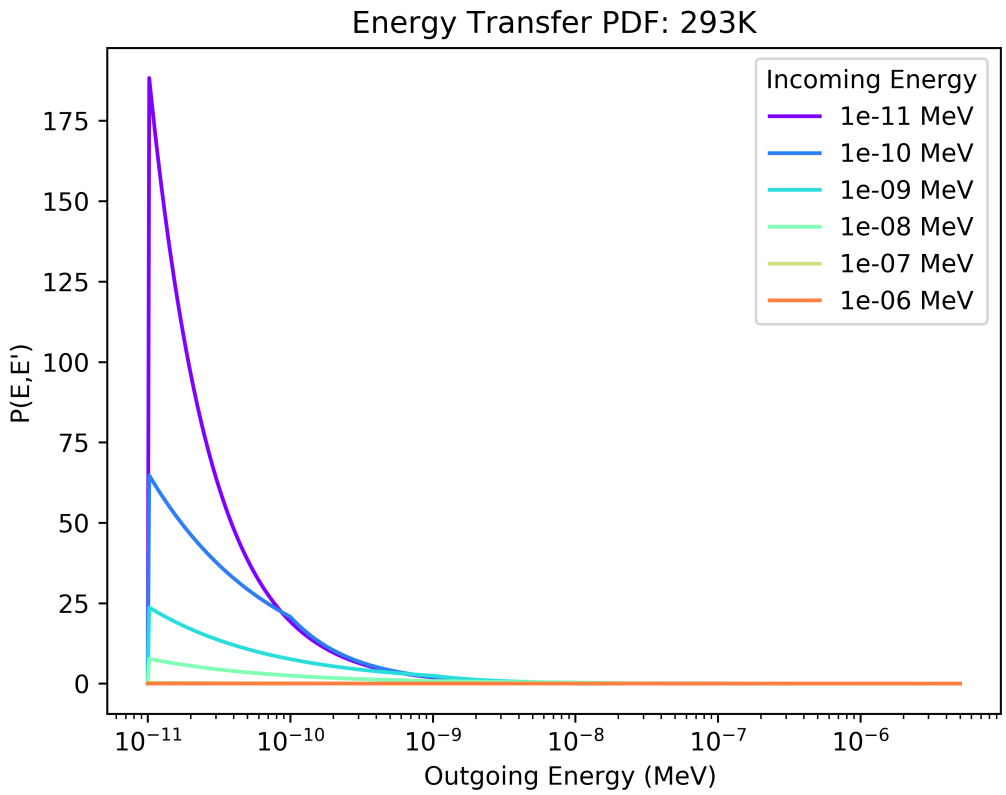

Figure F.1: **FRENSIE Adjoint Free Gas Energy Transfer PDF at 293K.** *The free gas energy transfer PDF is plotted for various incoming neutron energies incident on a monatomic hydrogen gas a temperature of 293K.*

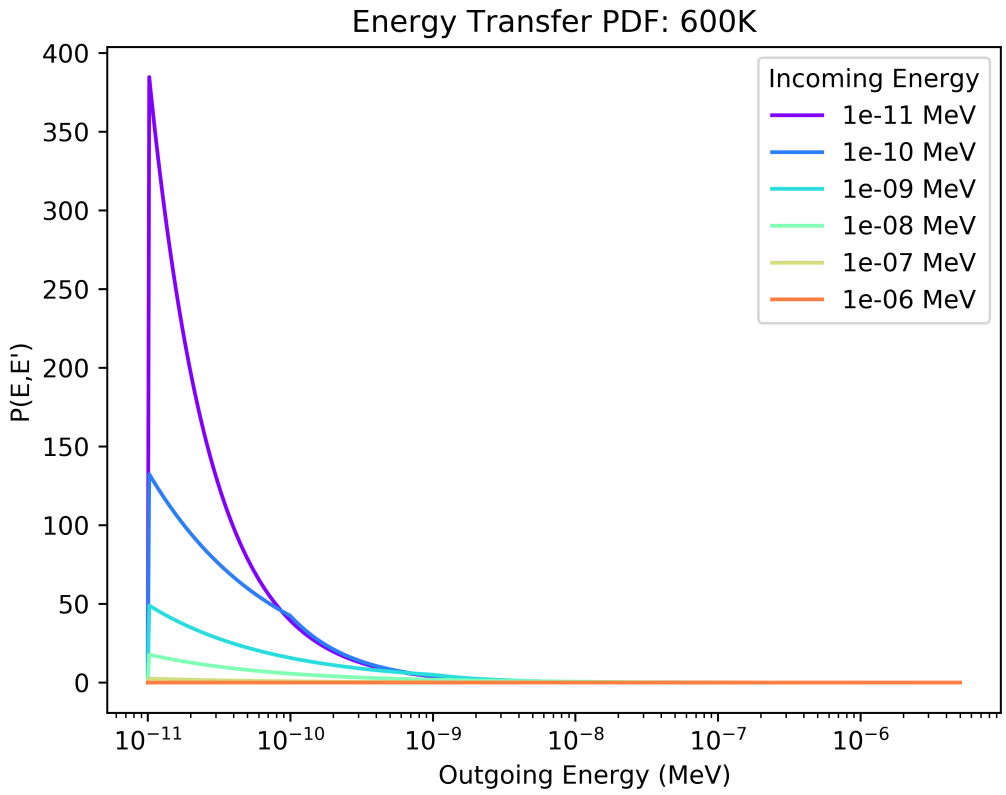

Figure F.2: **FRENSIE Adjoint Free Gas Energy Transfer PDF at 600K.** *The free gas energy transfer PDF is plotted for various incoming neutron energies incident on a monatomic hydrogen gas a temperature of 600K.*

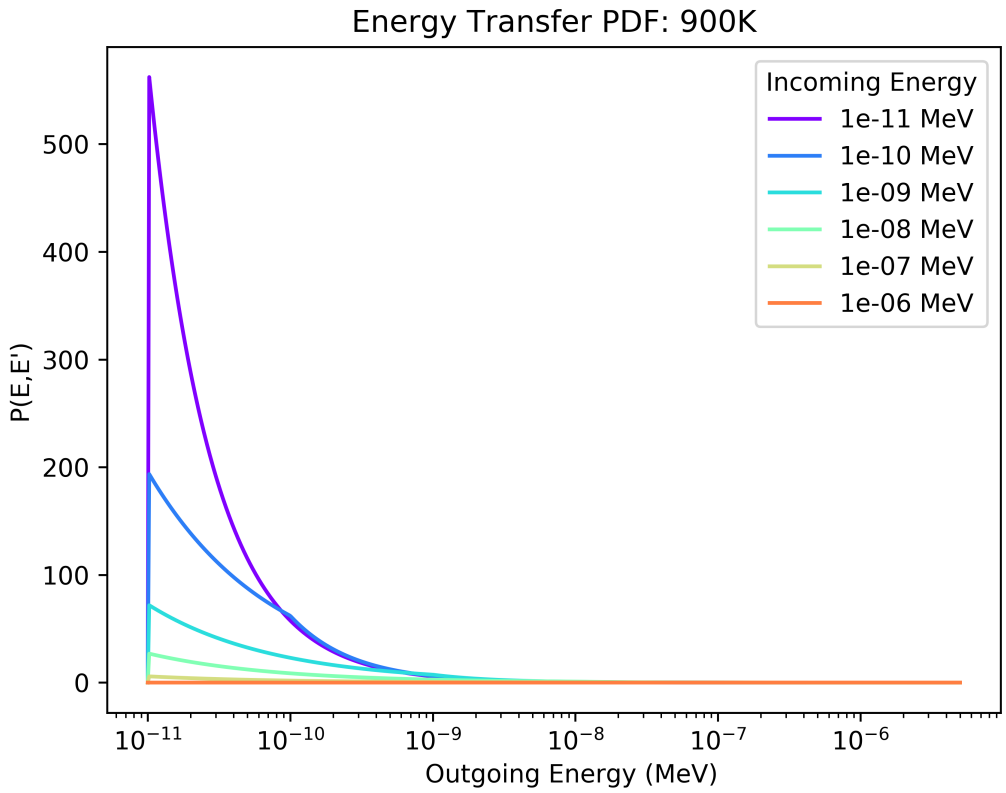

Figure F.3: **FRENSIE Adjoint Free Gas Energy Transfer PDF at 900K.** *The free gas energy transfer PDF is plotted for various incoming neutron energies incident on a monatomic hydrogen gas a temperature of 900K.*

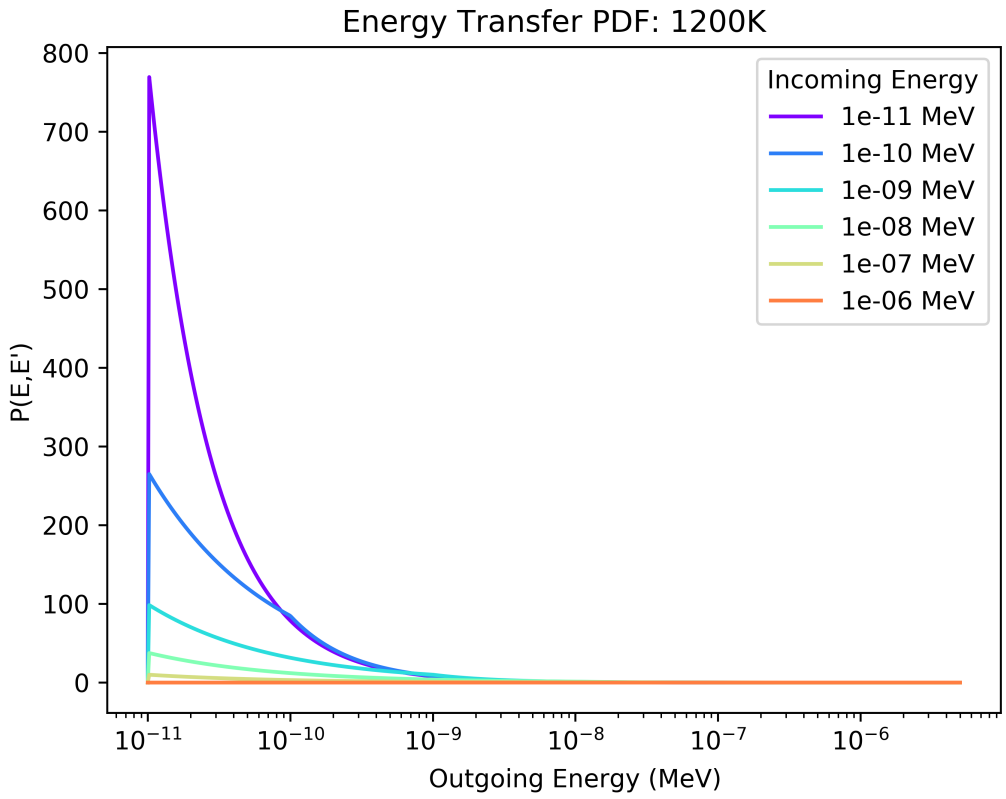

Figure F.4: **FRENSIE Adjoint Free Gas Energy Transfer PDF at 1200K.** *The free gas energy transfer PDF is plotted for various incoming neutron energies incident on a monatomic hydrogen gas a temperature of 1200K.*

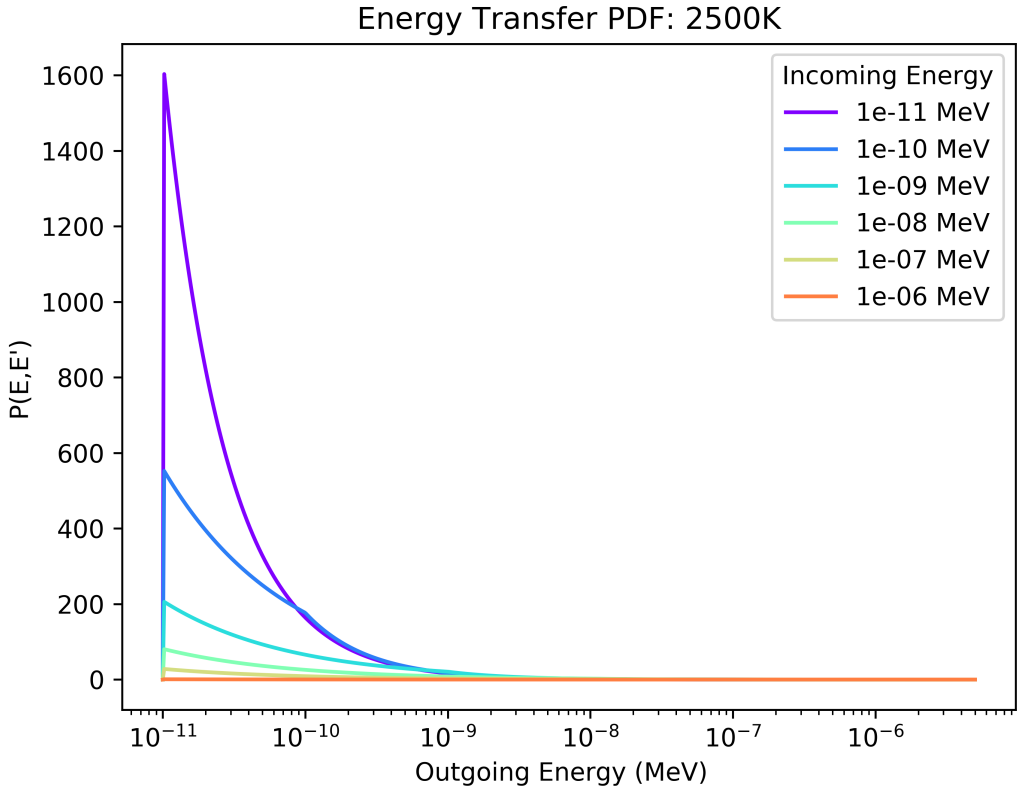

Figure F.5: **FRENSIE Adjoint Free Gas Energy Transfer PDF at 2500K.** *The free gas energy transfer PDF is plotted for various incoming neutron energies incident on a monatomic hydrogen gas a temperature of 2500K.*

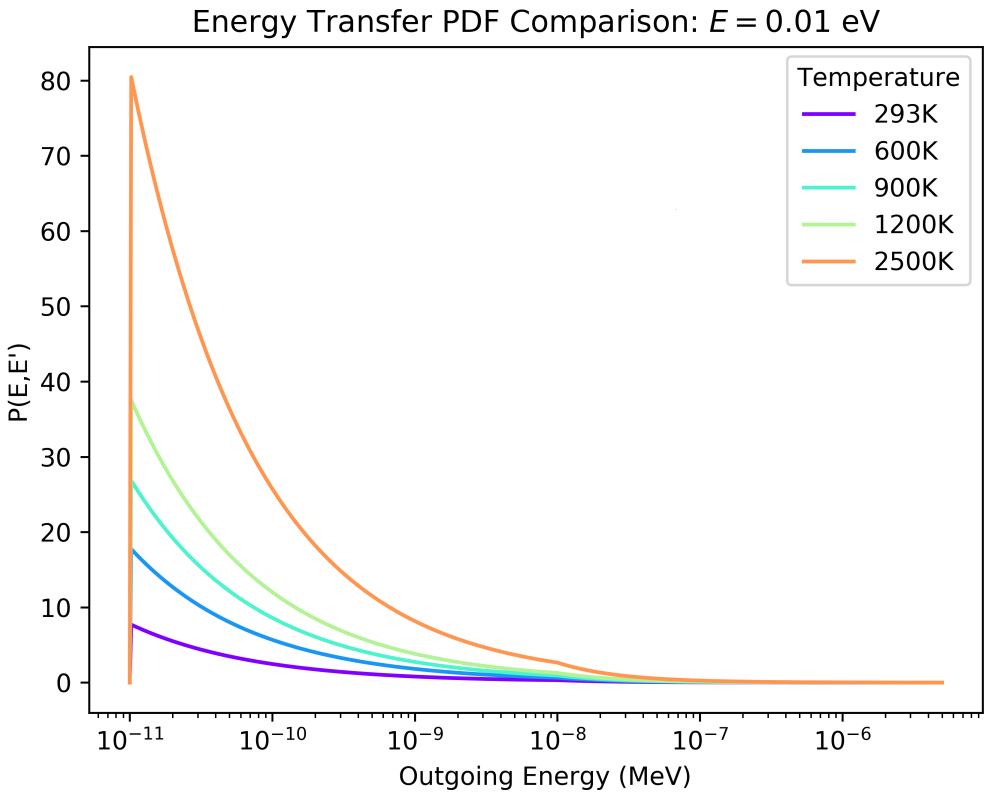

Figure F.6: **FRENSIE Adjoint Free Gas Energy Transfer PDF at Varying Temperatures for Incident Energy of 0.01 eV.** *The free gas energy transfer PDF is plotted for various temperatures with a fixed incident neutron energy of 0.01 eV.*

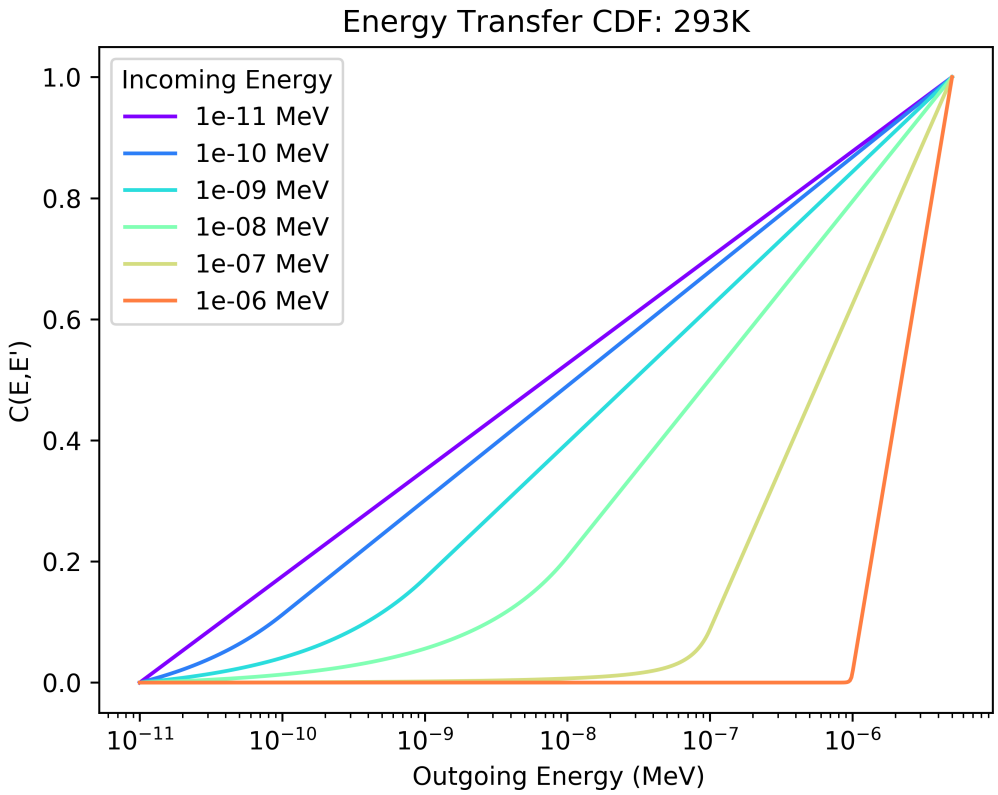

Figure F.7: **FRENSIE Adjoint Free Gas Energy Transfer CDF at 293K.** *The free gas energy transfer CDF is plotted for various incoming neutron energies incident on a monatomic hydrogen gas a temperature of 293K.*

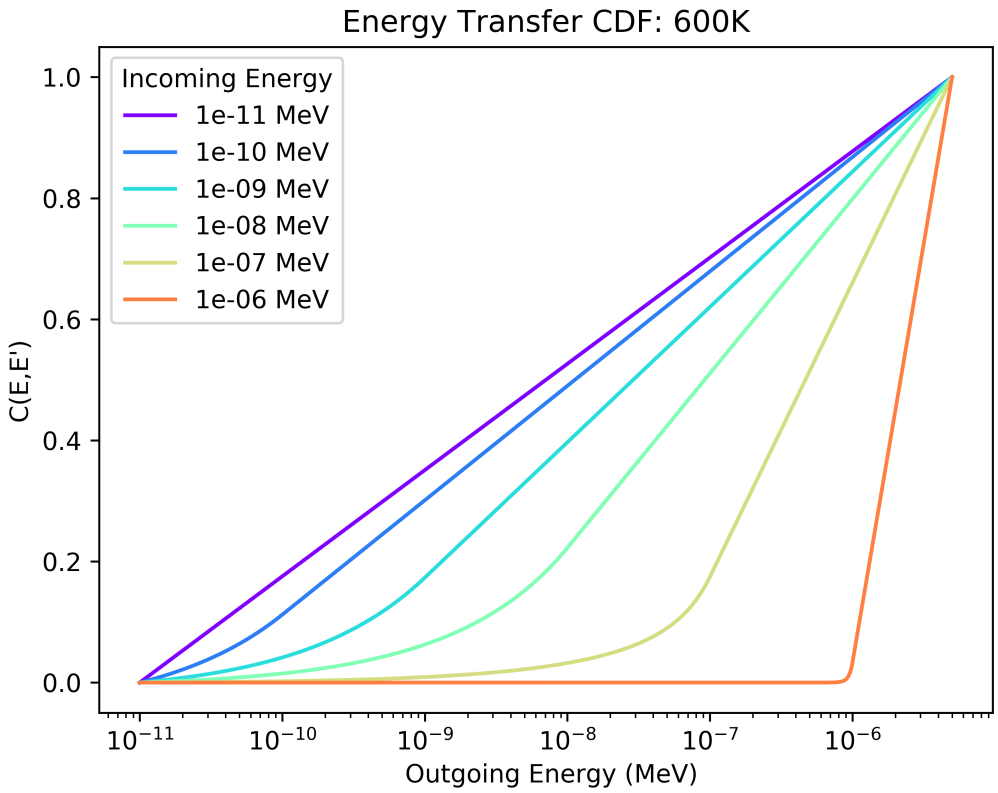

Figure F.8: **FRENSIE Adjoint Free Gas Energy Transfer CDF at 600K.** *The free gas energy transfer CDF is plotted for various incoming neutron energies incident on a monatomic hydrogen gas a temperature of 600K.*

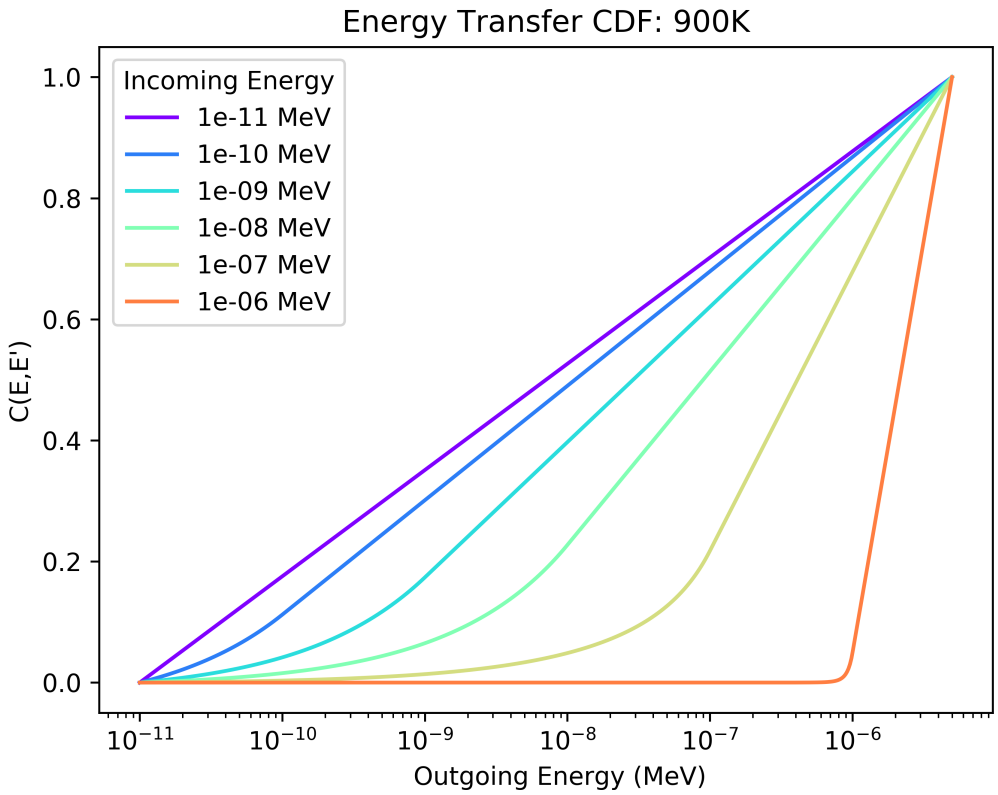

Figure F.9: **FRENSIE Adjoint Free Gas Energy Transfer CDF at 900K.** *The free gas energy transfer CDF is plotted for various incoming neutron energies incident on a monatomic hydrogen gas a temperature of 900K.*

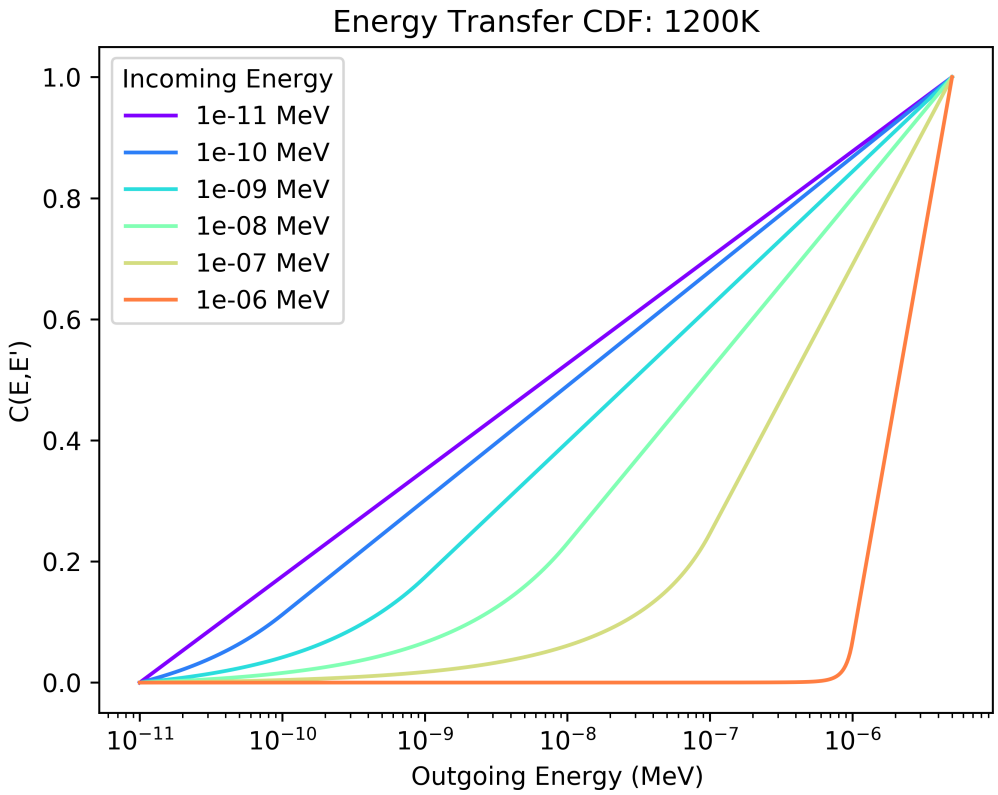

Figure F.10: **FRENSIE Adjoint Free Gas Energy Transfer CDF at 1200K.** *The free gas energy transfer CDF is plotted for various incoming neutron energies incident on a monatomic hydrogen gas a temperature of 1200K.*

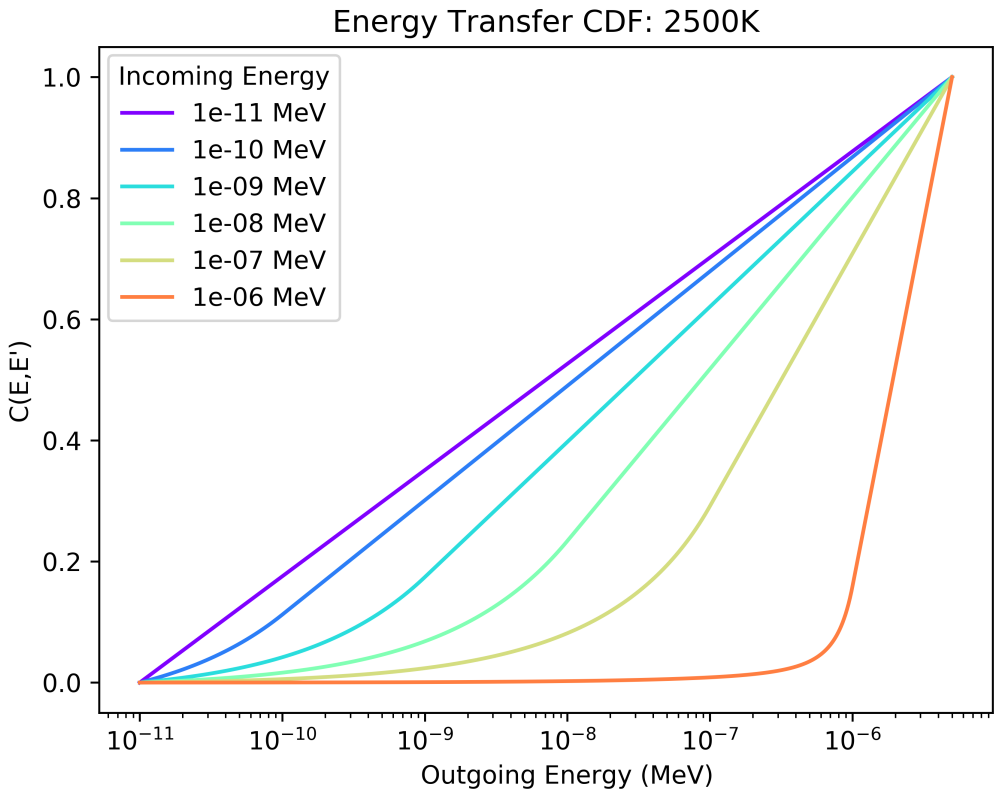

Figure F.11: **FRENSIE Adjoint Free Gas Energy Transfer CDF at 2500K.** *The free gas energy transfer CDF is plotted for various incoming neutron energies incident on a monatomic hydrogen gas a temperature of 2500K.*

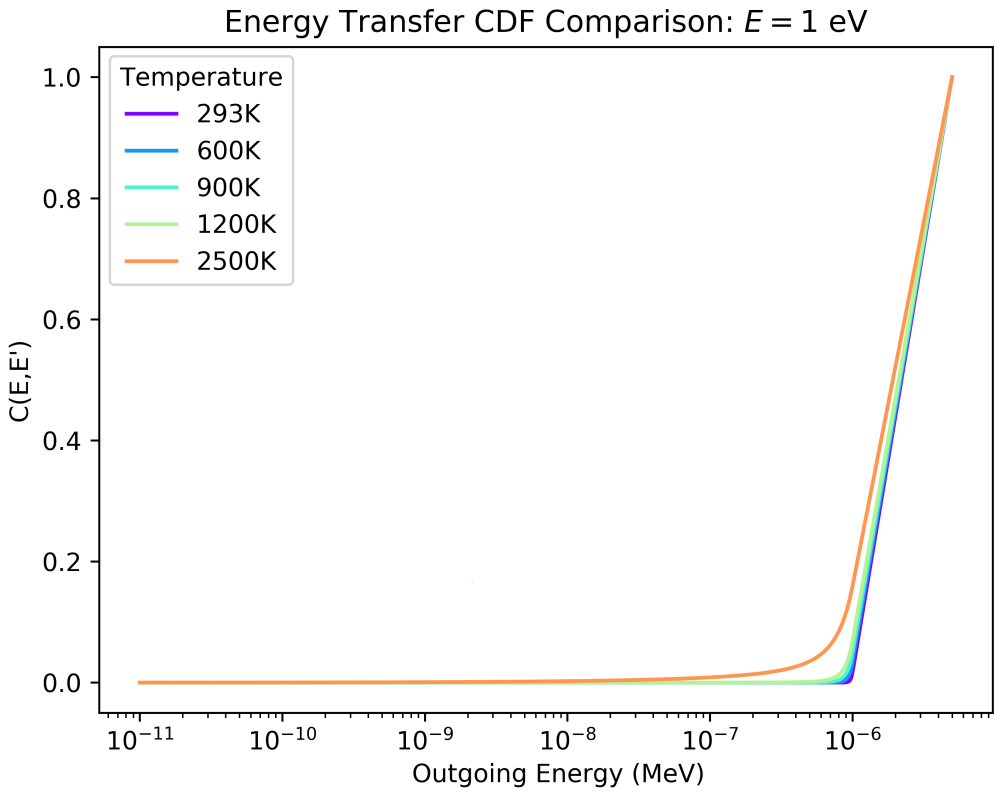

Figure F.12: **FRENSIE Adjoint Free Gas Energy Transfer CDF at Varying Temperatures for Incident Energy of 1.0 eV.** *The free gas energy transfer CDF is plotted for various temperatures with a fixed incident neutron energy of 1.0 eV.*

Appendix G

FRENSIE Forward Free Gas Scattering Cross Section Comparison

Appendix G includes the plots of the FRENSIE forward free gas scattering cross section in comparison with MCNP6.2 when utilizing the MCNP definition for the zero-temperature cross section as derived from the ACE data tables.

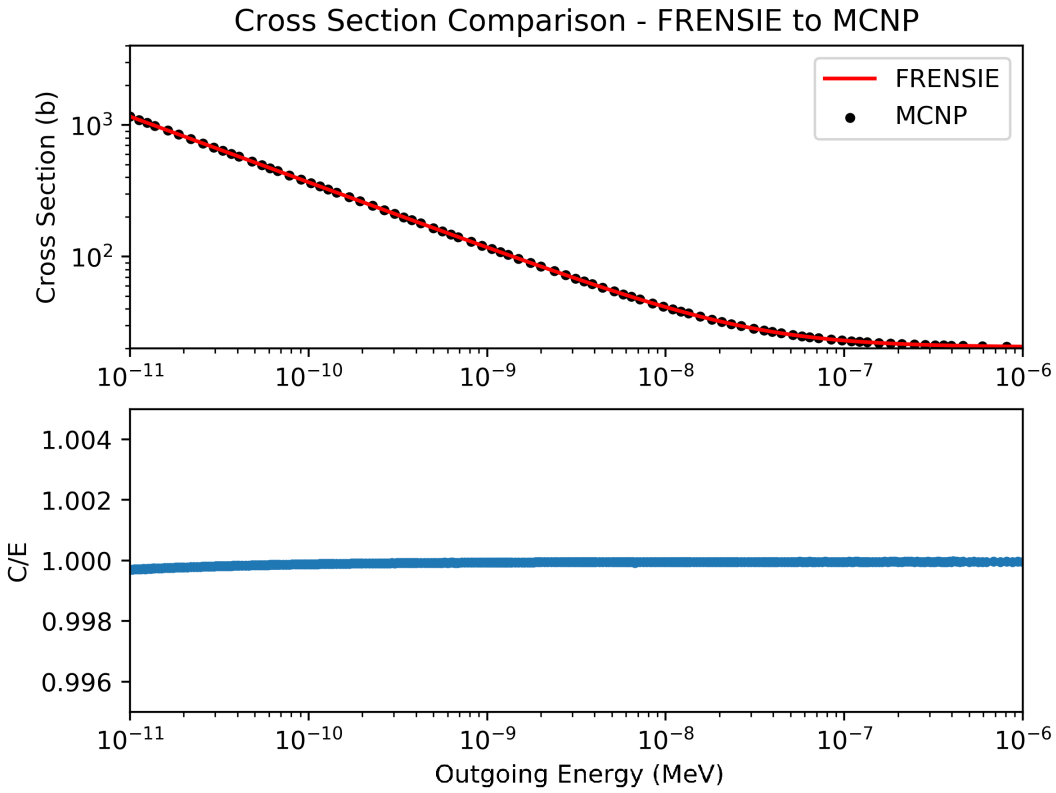

Figure G.1: **Comparison of FRENSIE vs. MCNP for the Free Gas Cross Section at 293.6K.** *(Above) FRENSIE and MCNP free gas cross sections for monatomic hydrogen at 293.6K are plotted. (Below) C/E ratio for FRENSIE vs. MCNP showing good agreement between the two models. The only deviations are now on the order of* 1×10^{-4} *relative and are caused by the numerical integration.*

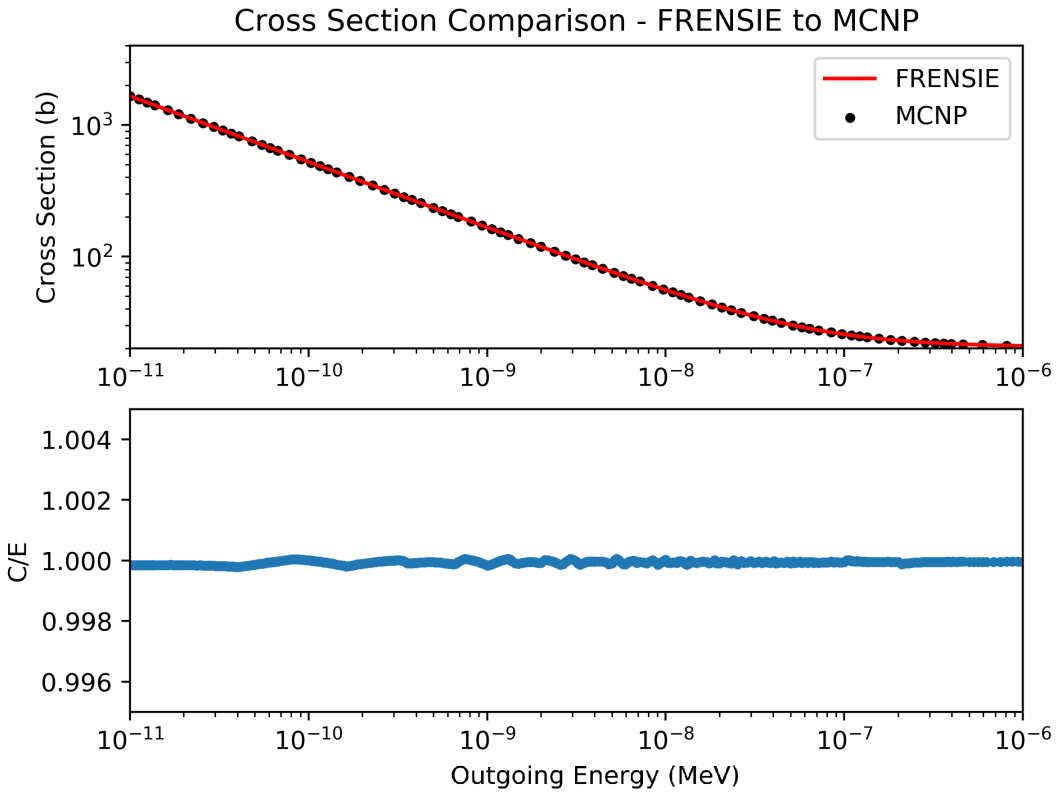

Figure G.2: **Comparison of FRENSIE vs. MCNP for the Free Gas Cross Section at 600K.** *(Above) FRENSIE and MCNP free gas cross sections for monatomic hydrogen at 600K are plotted. (Below) C/E ratio for FRENSIE vs. MCNP showing good agreement between the two models. The only deviations are now on the order of* 1×10^{-4} *relative and are caused by the numerical integration.*

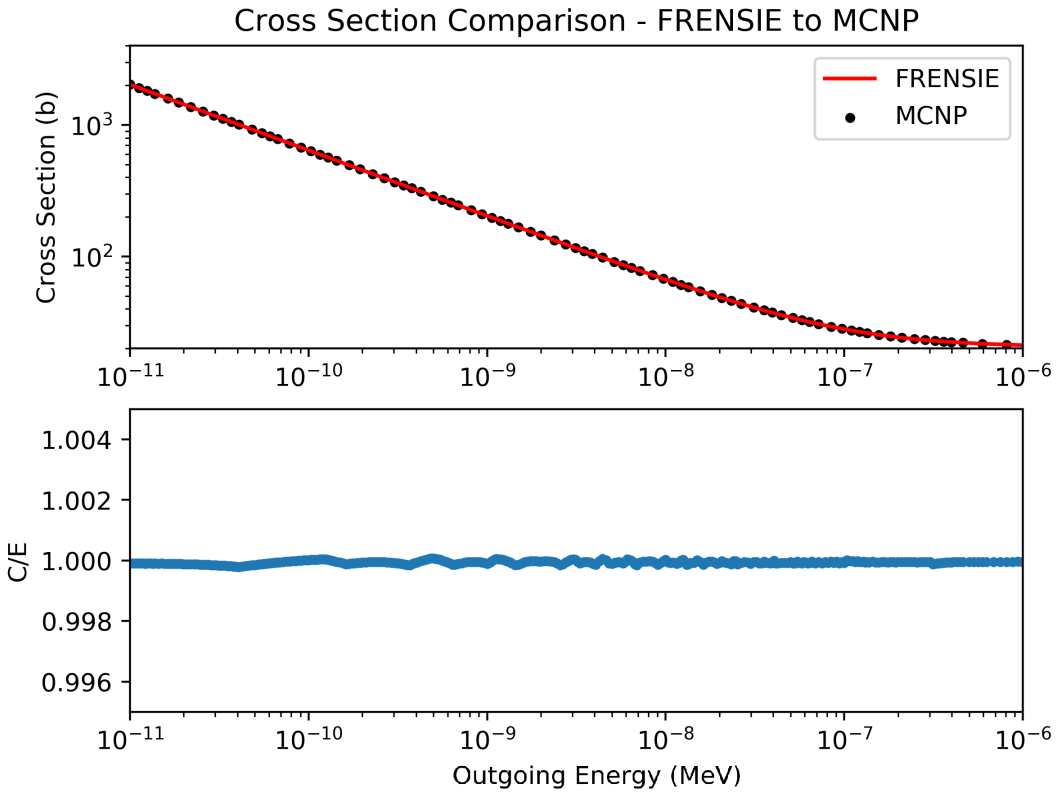

Figure G.3: **Comparison of FRENSIE vs. MCNP for the Free Gas Cross Section at 900K.** *(Above) FRENSIE and MCNP free gas cross sections for monatomic hydrogen at 900K are plotted. (Below) C/E ratio for FRENSIE vs. MCNP showing good agreement between the two models. The only deviations are now on the order of* 1×10^{-4} *relative and are caused by the numerical integration.*

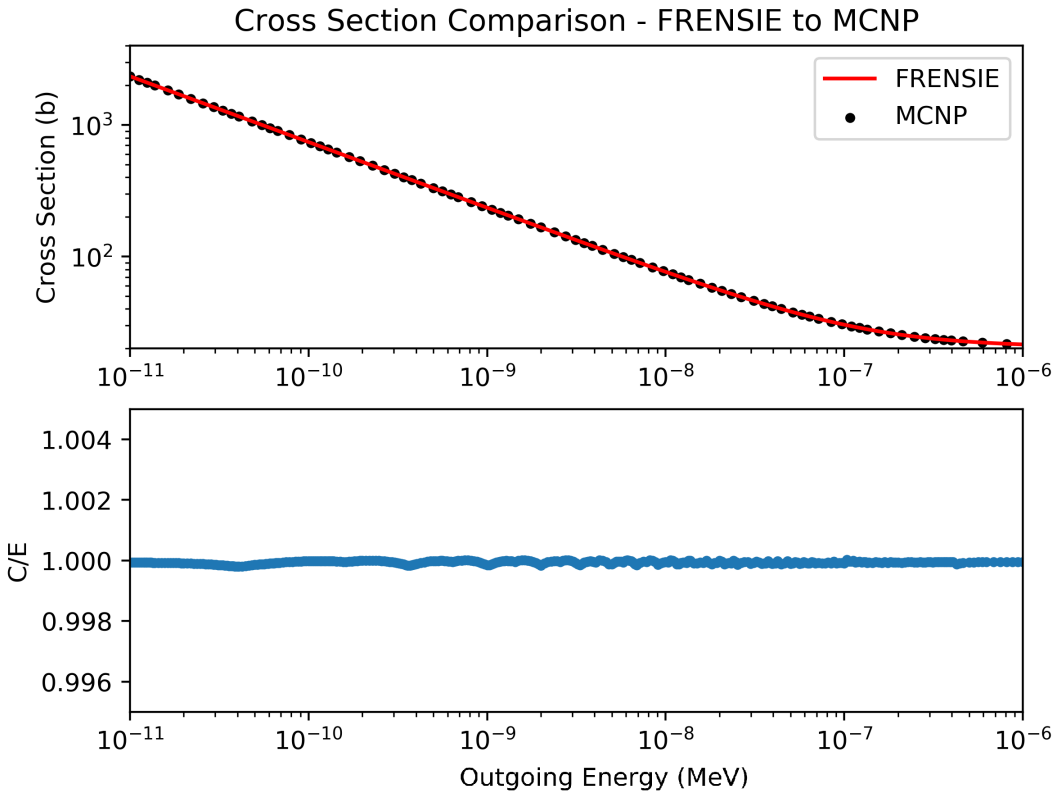

Figure G.4: **Comparison of FRENSIE vs. MCNP for the Free Gas Cross Section at 1200K.** *(Above) FRENSIE and MCNP free gas cross sections for monatomic hydrogen at 1200K are plotted. (Below) C/E ratio for FRENSIE vs. MCNP showing good agreement between the two models. The only deviations are now on the order of* 1×10^{-4} *relative and are caused by the numerical integration.*

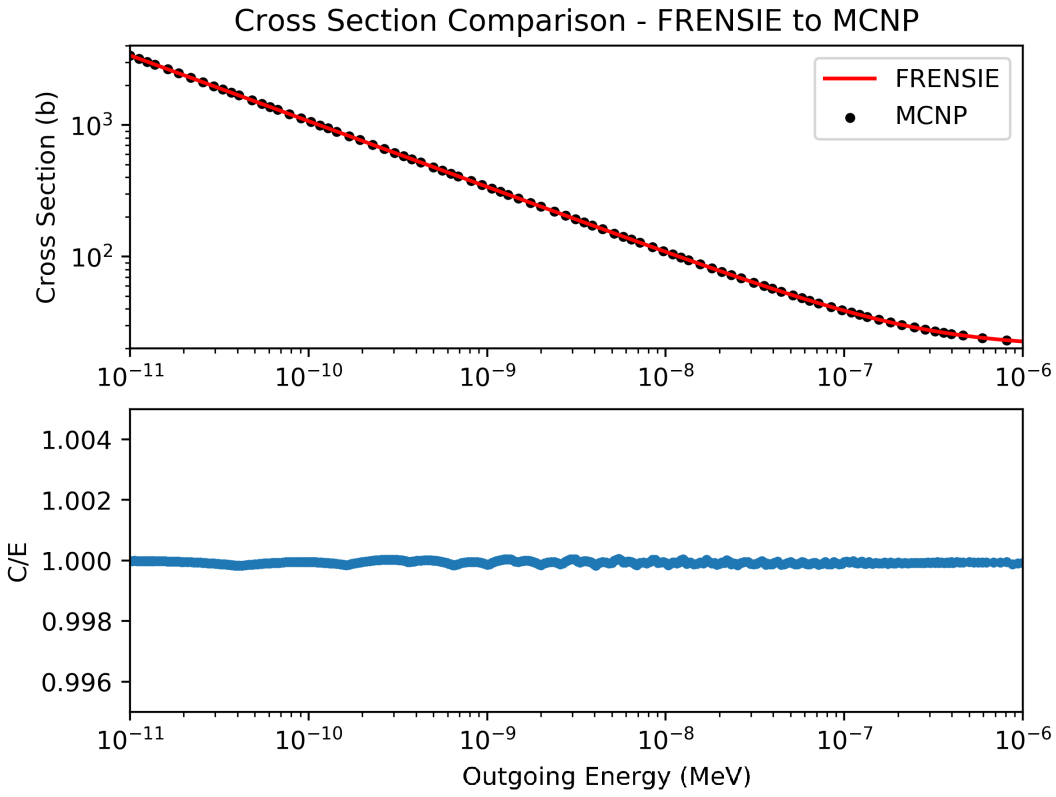

Figure G.5: **Comparison of FRENSIE vs. MCNP for the Free Gas Cross Section at 2500K.** *(Above) FRENSIE and MCNP free gas cross sections for monatomic hydrogen at 2500K are plotted. (Below) C/E ratio for FRENSIE vs. MCNP showing good agreement between the two models. The only deviations are now on the order of* 1×10^{-4} *relative and are caused by the numerical integration.*

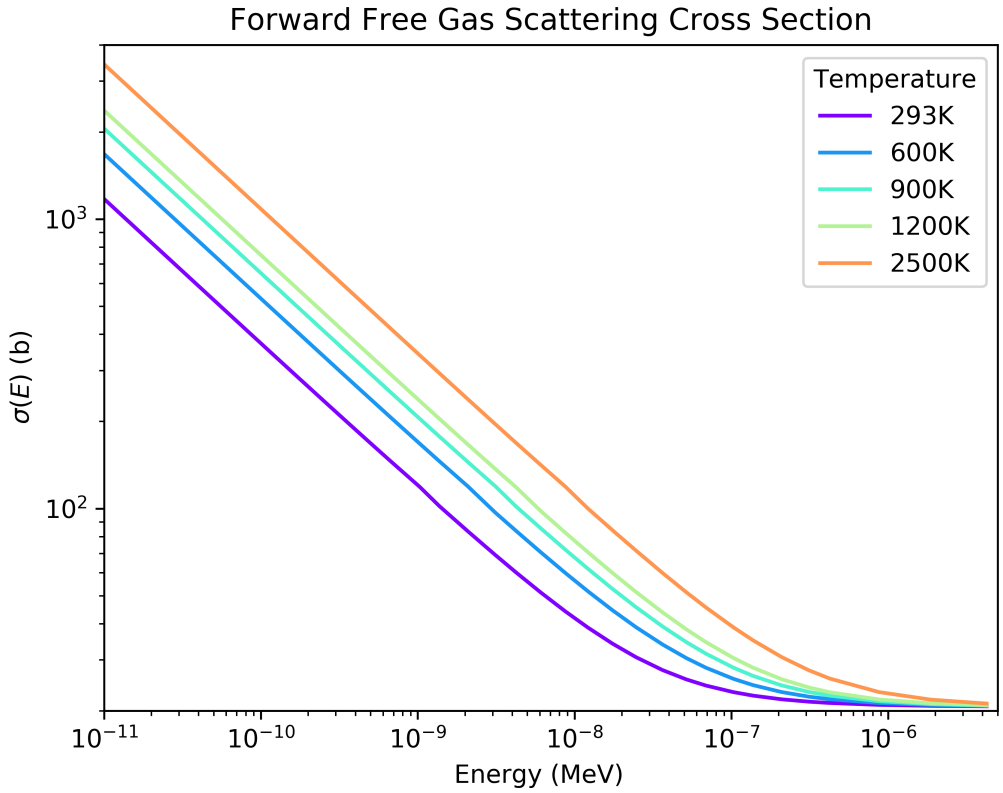

Figure G.6: **Comparison of FRENSIE Free Gas Cross Sections at Various Temperatures.** *The FRENSIE free gas cross section has been plotted at temperatures* $\mathsf{T} = [293.6, 600, 900, 1200, 2500]K$.

Appendix H

FRENSIE Forward Free Gas Transport Results

Appendix H includes the plots of the FRENSIE forward free gas transport. The neutron energy distribution is plotted as a function of collision number to understand the evolution and progression toward equilibrium.

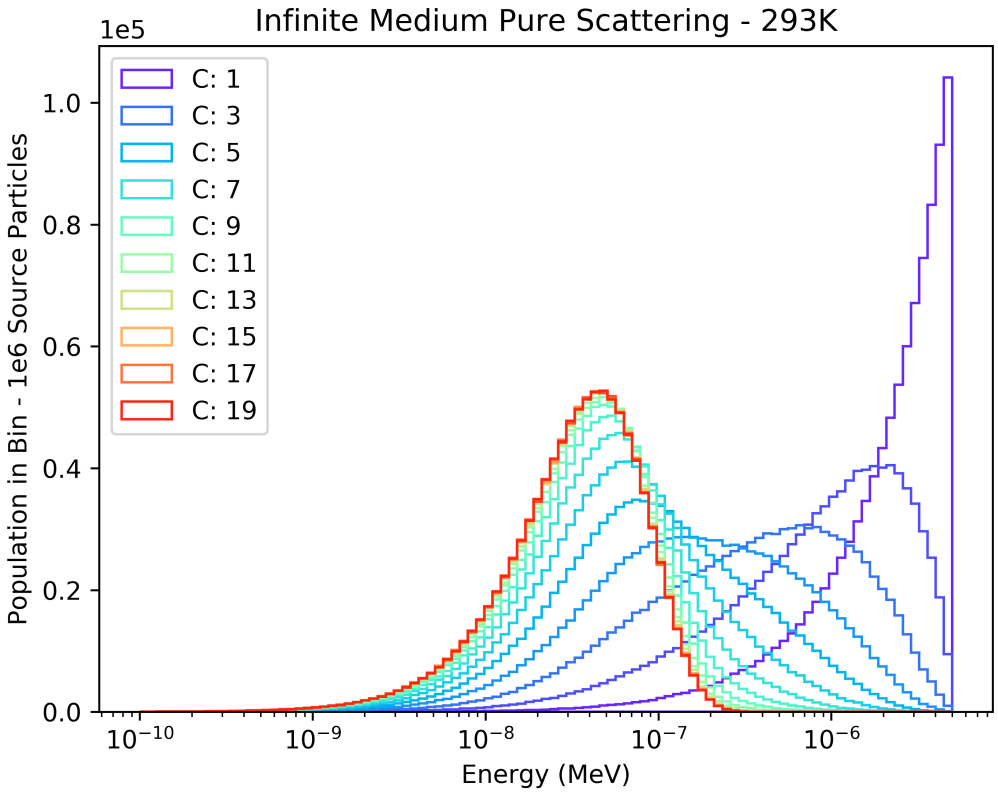

Figure H.1: **Forward Free Gas Neutron Transport at 293K.** *In order to construct a comparative test for the adjoint, a forward model was constructed. Neutrons are born at 5 eV and are scattered through elastic interactions on an infinite medium of monatomic hydrogen gas. The neutrons approach equilibrium after roughly 20 scattering events.*

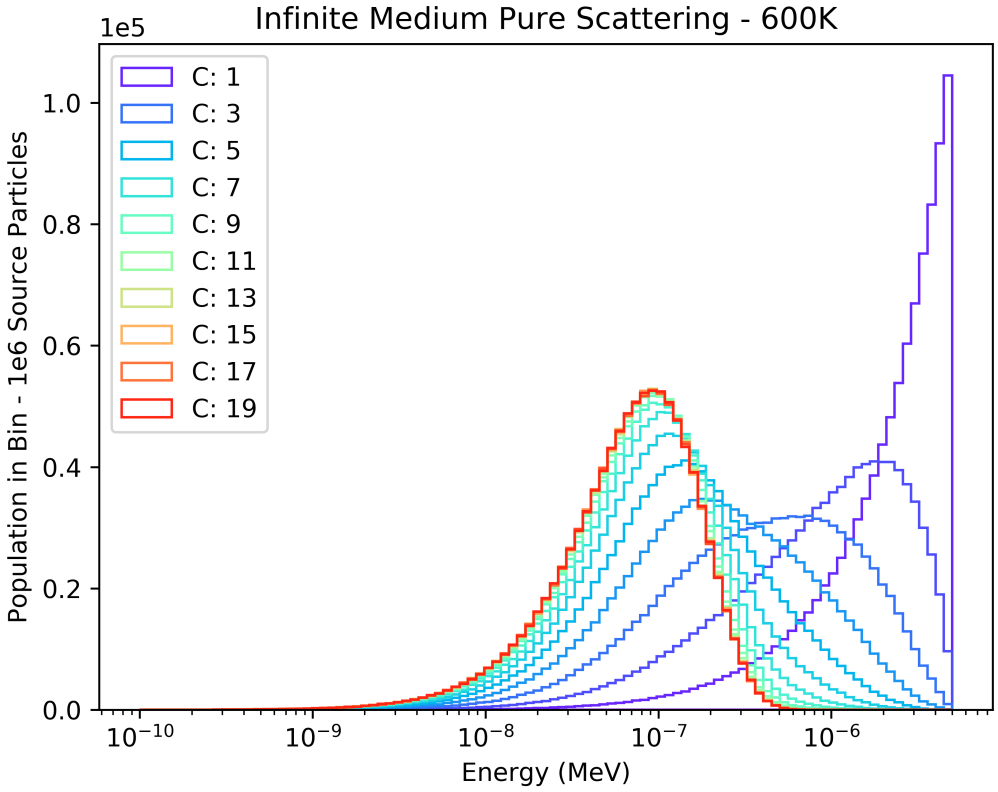

Figure H.2: **Forward Free Gas Neutron Transport at 600K.** *In order to construct a comparative test for the adjoint, a forward model was constructed. Neutrons are born at 5 eV and are scattered through elastic interactions on an infinite medium of monatomic hydrogen gas. The neutrons approach equilibrium after roughly 20 scattering events.*

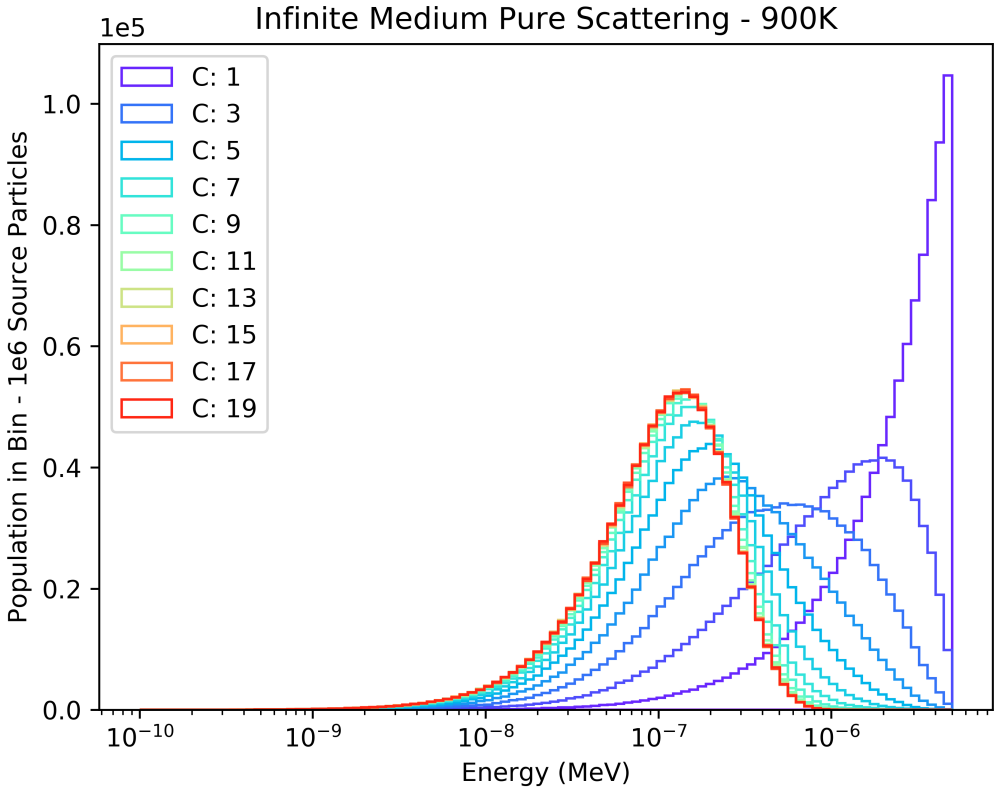

Figure H.3: **Forward Free Gas Neutron Transport at 900K.** *In order to construct a comparative test for the adjoint, a forward model was constructed. Neutrons are born at 5 eV and are scattered through elastic interactions on an infinite medium of monatomic hydrogen gas. The neutrons approach equilibrium after roughly 20 scattering events.*

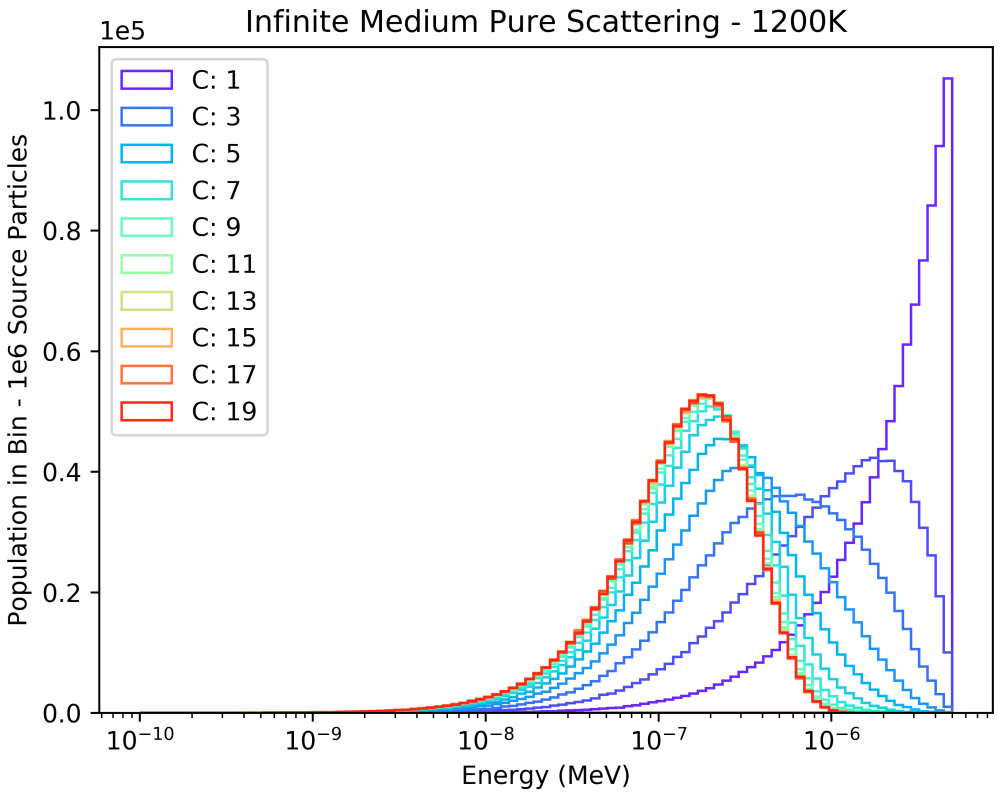

Figure H.4: **Forward Free Gas Neutron Transport at 1200K.** *In order to construct a comparative test for the adjoint, a forward model was constructed. Neutrons are born at 5 eV and are scattered through elastic interactions on an infinite medium of monatomic hydrogen gas. The neutrons approach equilibrium after roughly 20 scattering events.*

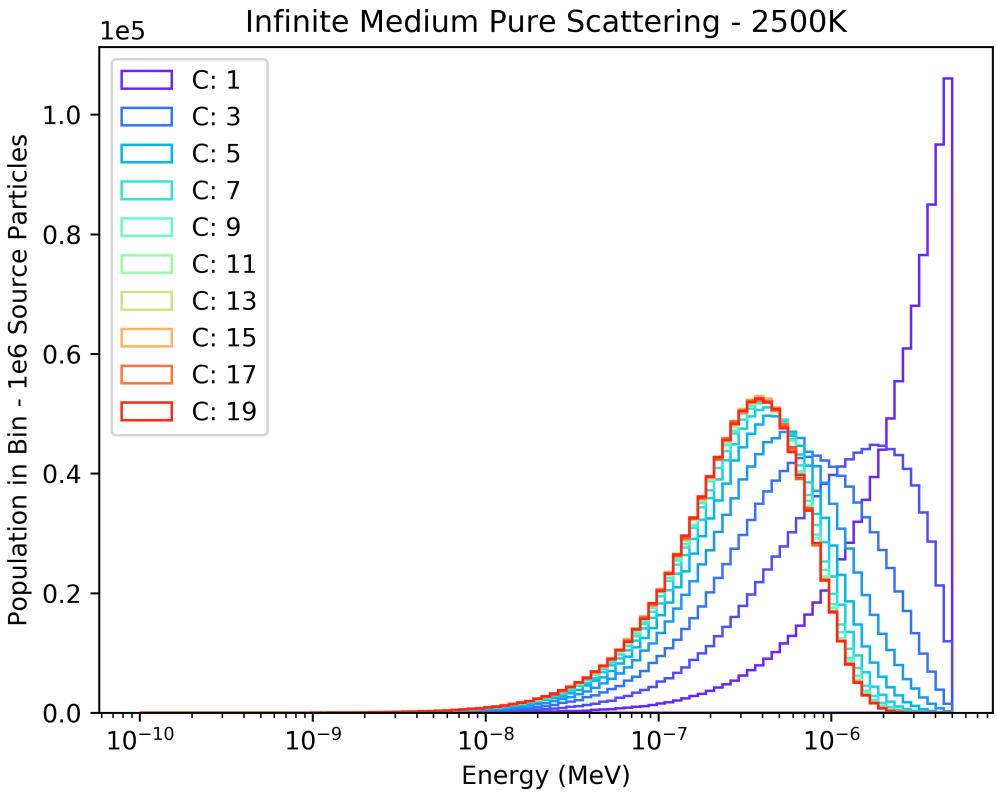

Figure H.5: **Forward Free Gas Neutron Transport at 2500K.** *In order to construct a comparative test for the adjoint, a forward model was constructed. Neutrons are born at 5 eV and are scattered through elastic interactions on an infinite medium of monatomic hydrogen gas. The neutrons approach equilibrium after roughly 20 scattering events.*

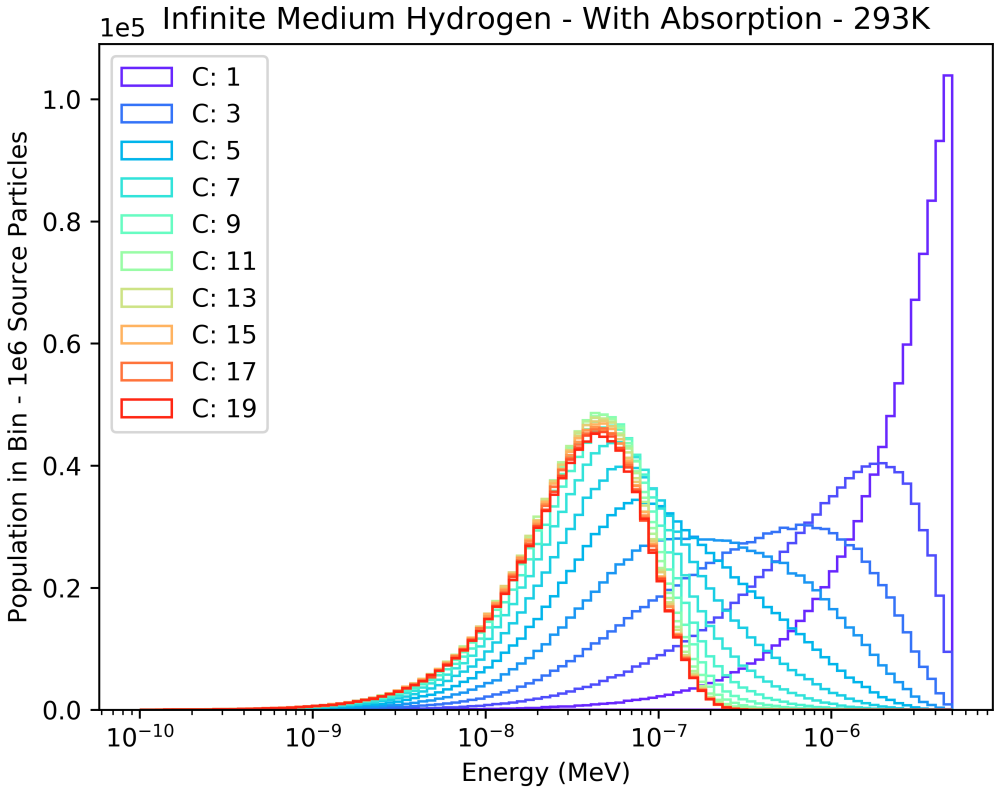

Figure H.6: **Forward Free Gas Neutron Transport at 293K with Absorption.** *In order to construct a comparative test for the adjoint, a forward model was constructed. Neutrons are born at 5 eV and are scattered through elastic interactions and absorption on an infinite medium of monatomic hydrogen gas. The neutrons approach equilibrium after roughly 20 scattering events.*

Appendix I

FRENSIE Adjoint Free Gas Transport Results

Appendix I includes the plots of the FRENSIE adjoint free gas transport. The neutron energy distribution is plotted as a function of collision number to understand the evolution and progression toward equilibrium.

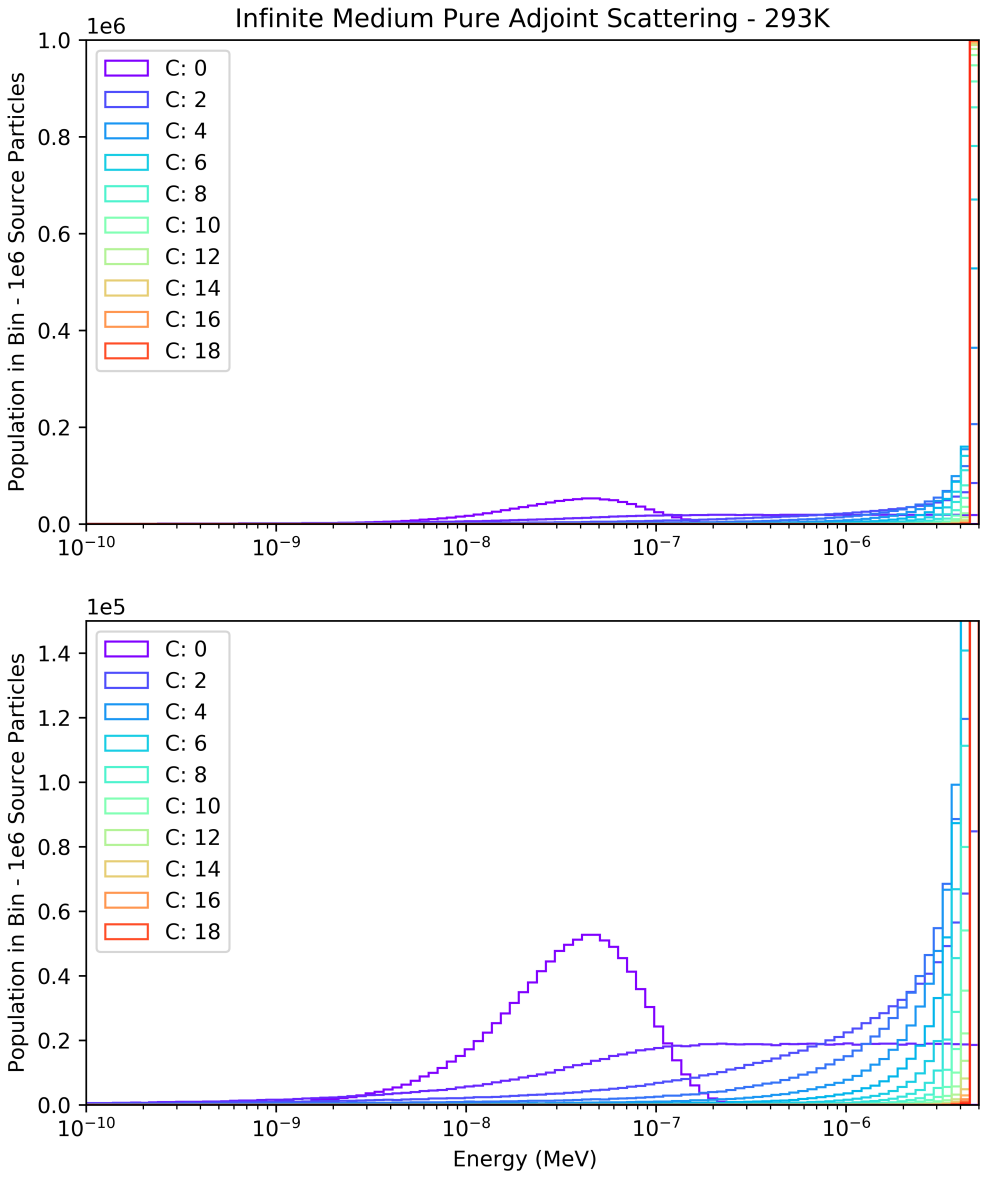

Figure I.1: **Adjoint Free Gas Neutron Transport at 293K.** *Neutrons are born at the forward equilibrium distribution and are scattered through elastic interactions on an infinite medium of monatomic hydrogen gas. The neutrons the maximum problem energy equilibrium after roughly 20 scattering events.*

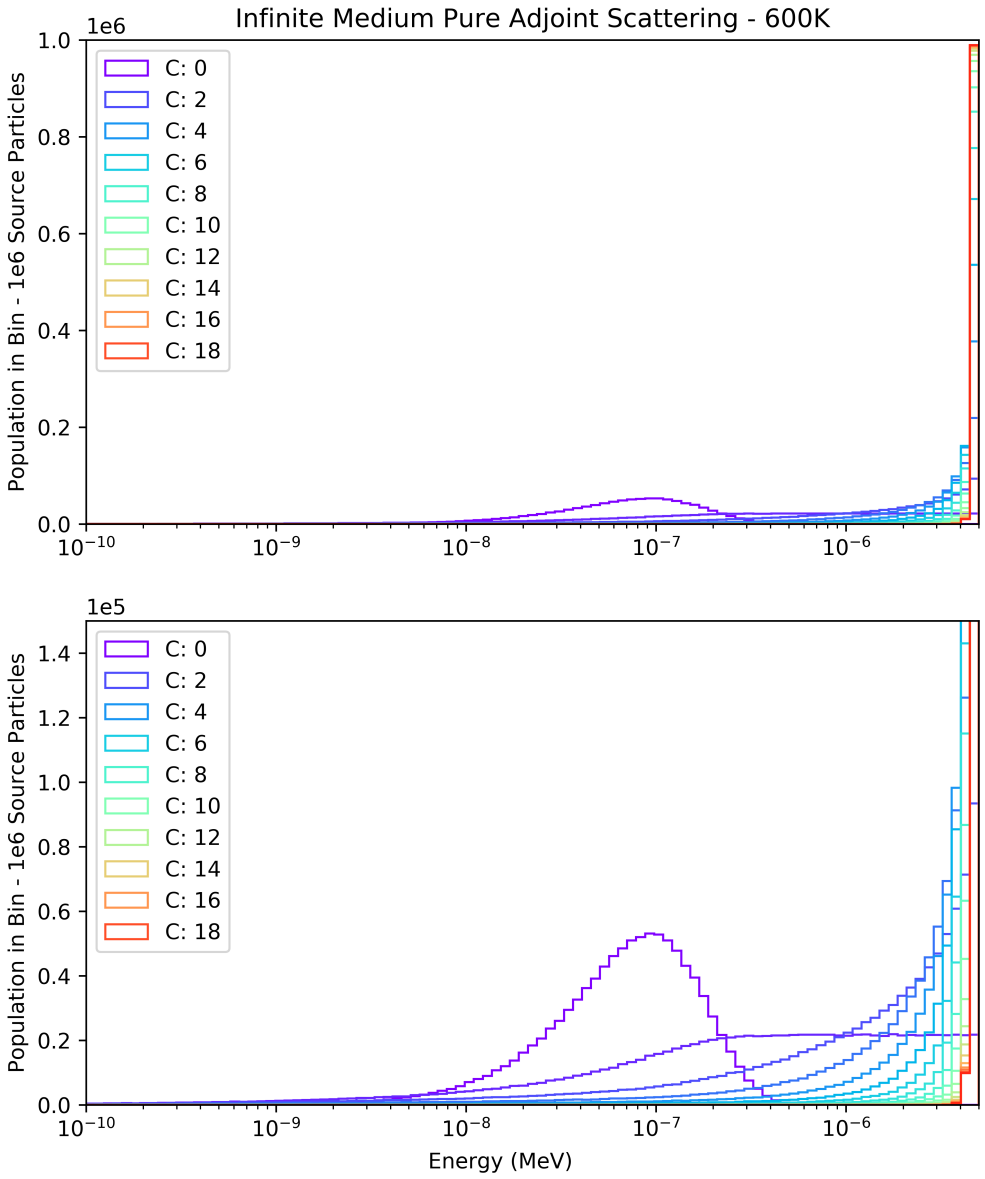

Figure I.2: **Adjoint Free Gas Neutron Transport at 600K.** *Neutrons are born at the forward equilibrium distribution and are scattered through elastic interactions on an infinite medium of monatomic hydrogen gas. The neutrons the maximum problem energy equilibrium after roughly 20 scattering events.*

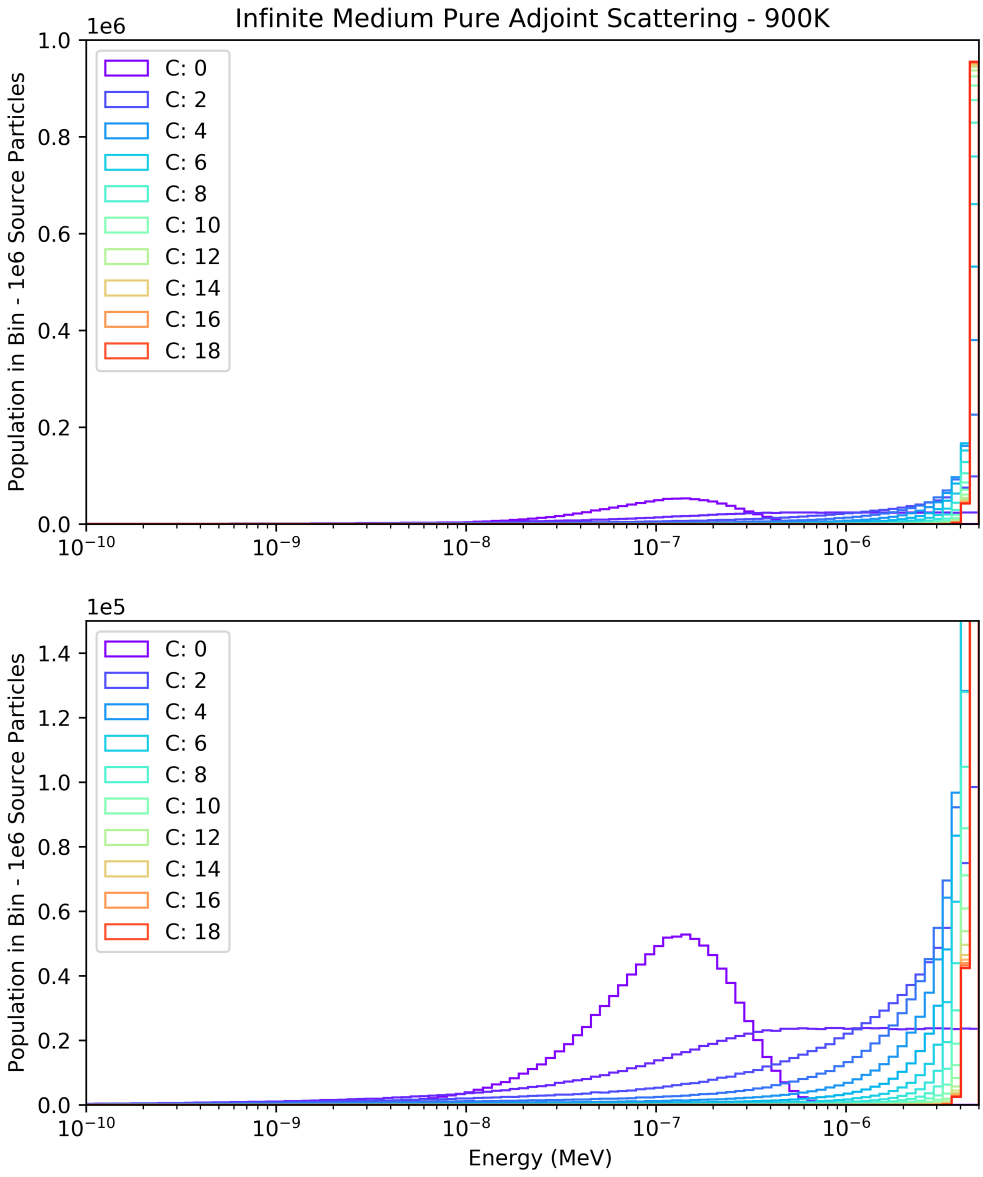

Figure I.3: **Adjoint Free Gas Neutron Transport at 900K.** *Neutrons are born at the forward equilibrium distribution and are scattered through elastic interactions on an infinite medium of monatomic hydrogen gas. The neutrons the maximum problem energy equilibrium after roughly 20 scattering events.*

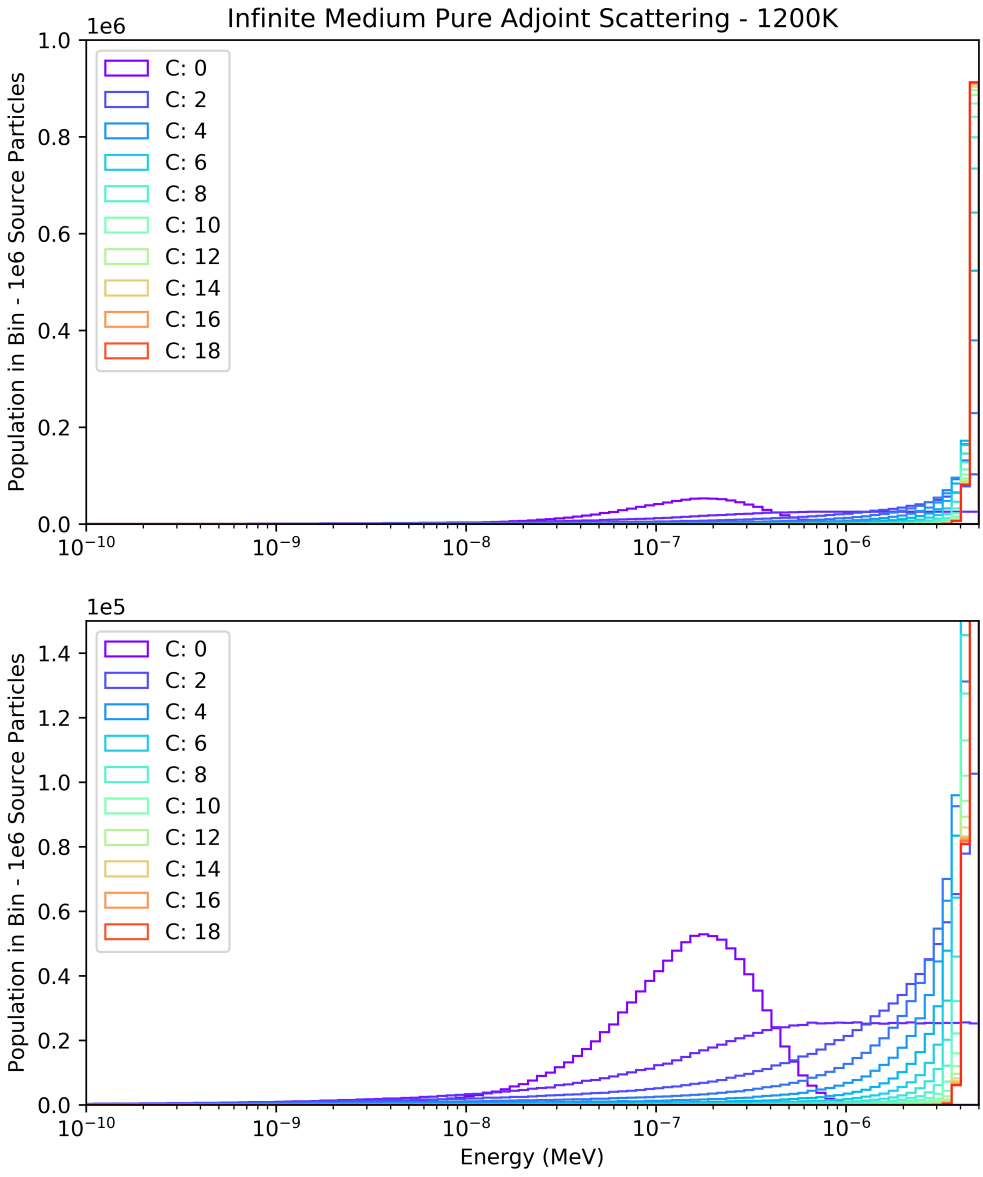

Figure I.4: **Adjoint Free Gas Neutron Transport at 1200K.** *Neutrons are born at the forward equilibrium distribution and are scattered through elastic interactions on an infinite medium of monatomic hydrogen gas. The neutrons the maximum problem energy equilibrium after roughly 20 scattering events.*

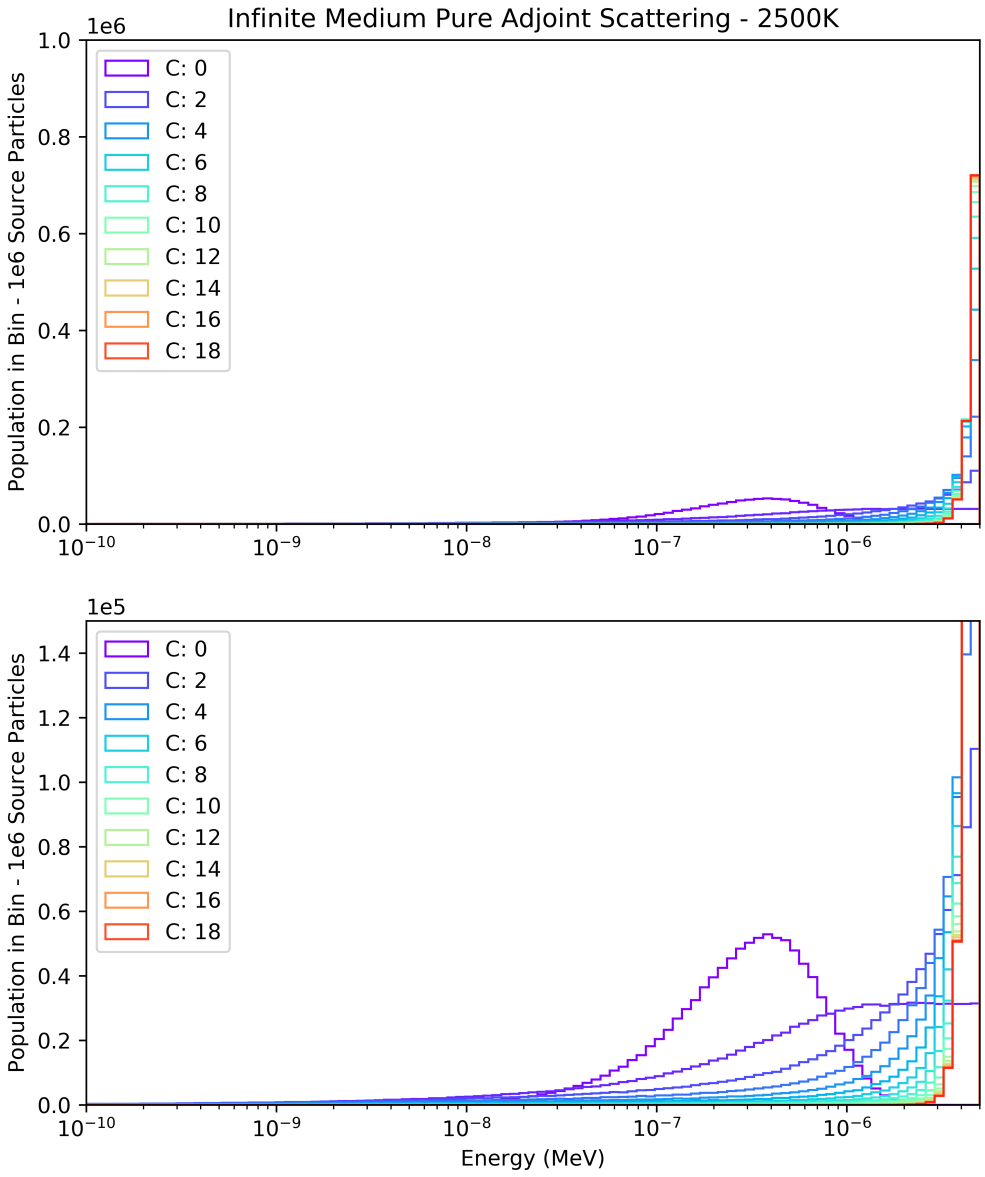

Figure I.5: **Adjoint Free Gas Neutron Transport at 2500K.** *Neutrons are born at the forward equilibrium distribution and are scattered through elastic interactions on an infinite medium of monatomic hydrogen gas. The neutrons the maximum problem energy equilibrium after roughly 20 scattering events.*

Appendix J

Overview of FRENSIE

One of the most common questions regarding FRENSIE (Framework for REsearch in Nuclear ScIence and Engineering) is the reason for developing yet another Monte Carlo code and software framework. This chapter will seek to answer that question by providing a brief description of the ethos and methodology behind the work. Further, it will briefly discuss the road toward open source licensing, an overview of FACEMC (Forward-Adjoint Continuous Energy Monte Carlo) and its capabilities, and areas that require further attention and collaboration with individuals with more expertise.

J.1 Methodology

While there exist many Monte Carlo radiation transport packages available today, very few of them have been developed with modern software practices in mind. Thus, the legacy debt associated with most of these codes is enormous. Compounding this effect is the fact that many of these codes were written before thorough unit testing of each individual component was common practice. This leads to difficulty in development and debugging, as one cannot run rigorous regression tests. The final issue is that many of these codes have been written primarily for production, not continued development. Their goal has been to obtain a solution as efficiently as possible, and often in doing so the high-level software design and maintainability have lost priority. For these reasons and many more it became apparent that there was a need for FRENSIE. FRENSIE aims to be a framework that allows developers to build and test new functionality for nuclear research in an academic setting.

To combat these issues FRENSIE has been developed from the ground up the C++11 standard and modern software design practices. The design strategy for FRENSIE may be generally broken into these broad rules:

- FRENSIE must allow for easy interfacing with external packages.
  - This consists of implementing black-box interface designs.
- Object-oriented programming (OOP) must be used for native (internal) code for easier design and maintenance.

  - The C++11 standard allows FRENSIE to utilize the power of OOP.
  - Some of the key benefits of OOP include the grouping of common functionality, the ability to create a single point of control, and the lack of code duplication required.

- FRENSIE must utilize quality assurance and collaboration techniques.
  - For quality assurance, all classes and functionality in classes must be unit tested to ensure that the primary and edge cases all function as expected with mock inputs.
  - Git must be utilized to allow users in various locations to work collaboratively on the code.

External Packages and Interfaces

As stated, one of the goals of FRENSIE is to create a software framework which allows for easy interfacing with external packages. There are incredible software libraries and resources which have already been developed for most of the Monte Carlo radiation transport components. Rather than attempting to redevelop these components from the ground up, it was decided that the ability to efficiently utilize existing capabilities would be optimal. Further, some users and developers may which to change a component of FRENSIE to utilize their own software. In this way FRENSIE must be easily extensible and must allow for the inclusion of external software packages.

In order to achieve this goal FRENSIE has been designed with a black-box design strategy. For the purposes of this discussion the design in FACEMC will be discussed. The general requirements of a MC radiation transport code could be broken into these groups:

- Utility functions (interpolation, distributions, etc.),
- Data (data handling, parsing, modification),
- Estimation (estimators),
- Geometry (ray firing, surface collisions),
- Monte Carlo (transport, collision sampling).

In FACEMC each of these *modules* will is connected to the whole by an interface. An interface acts much like a wall socket does in a house. Assuming an electronic device is designed properly internally and is able to fit the socket, it may be plugged into any socket in the house and be provided with the electricity it requires. The analogous case in FACEMC is that any module may be plugged into FACEMC assuming it can match the requirements of the interface.

The geometry module is a perfect example of this methodology. Initial work was done to create a rudimentary combinatorial geometry package, but it was found that to construct anything with substantial error checking (as is done in MCNP) would take more work than available for the small development team. Thus, the geometry interface was designed. In order for a geometry package to be utilized by FRENSIE it must be capable of providing FRENSIE with the results from various queries such as ray fires, surface crossing locations, current cell id, etc. As long as a package is capable of completing these tasks it may be utilized. All that must be done is to write a specific interface which translates the results of these queries into information which FRENSIE is capable of utilizing.

The original geometry package that this model was tested with was DagMC [38]. With very little work it was found that DagMC could be implemented to handle all of the geometry requirements of FRENSIE. This author also implemented the combinatorial geometry package ROOT from CERN [39]. The inclusion of each of these geometry packages required less than 500 lines of newly generated code, all of which was designed to translate the function calls from FRENSIE into ones in the geometry package, as well as to translate the outgoing data from the geometry package into the format expected by FRENSIE. In this way it was shown that the black-box approach allows one to utilize fully developed libraries with very little development effort. It is hoped that this will promote other collaboration between developers to utilize FRENSIE as a common framework for testing and development.

Object Oriented Programming (OOP)

FRENSIE has been written and updated to be in accordance with the C++11 standard. As stated previously, object oriented programming is a key feature of modern software languages and one which completely changes the way in which one thinks about software design. The goal of OOP is to allow the user create powerful entities which interact with one another in specific ways. Further, it assists in the management of code and in creating a single point of control for specific functionality.

For those unfamiliar with OOP, a very simple example of an object in the context of radiation transport would be a particle. Every particle must have a position, direction, and associated energy. However, certain particles like neutrons and electrons have an associated mass, whereas photons do not. Thus, photons, neutrons, and electrons are all generic particles, but each requires its own treatment. Therefore one might define the *base class* to be a generic particle which is a class which stores a position, direction, and energy with the ability to update and retrieve those values. At this point, one might define *derived classes* which implement additional functionality for each specific particle type. However, the *derived classes* in this model would still utilize the generic particle functions for updating and retrieving the position, direction, and energy. While this is a very simple example, it provides the reader with an understanding of how OOP can be used to mimic real entities and create shared functionality.

Recall that FRENSIE is truly a research framework, and not a production level code. Thus, the motivation behind all of the software design done on FRENSIE can be broken into three main streams:

- To improve the clarity of the code for developers.
- To allow easy modification and maintenance of functionality through a single point of control.
- To thoroughly test functionality.

The event (or estimator) module is a good example of how the software hierarchy and OOP are designed in FRENSIE. As there are various types of estimators, one would not wish to develop and maintain the shared functionality for every estimator separately. Thus, the event module was designed in such a way as to have one additional layer of specificity added to the estimators at each new set of derived classes. For example, the surface flux estimator is a child of the surface estimator, which is a child of the entity estimator, which is a child of the base class estimator. In this way all of the common functionality is included as one proceeds toward the base class. Figure J.1 shows a general structure of the event module to assist in understanding how OOP plays a role in FRENSIE development.

Quality Assurance and Collaboration

Another common practice in modern programming is the inclusion of unit tests. Unit tests are designed to test a specific component of functionality in the code. For

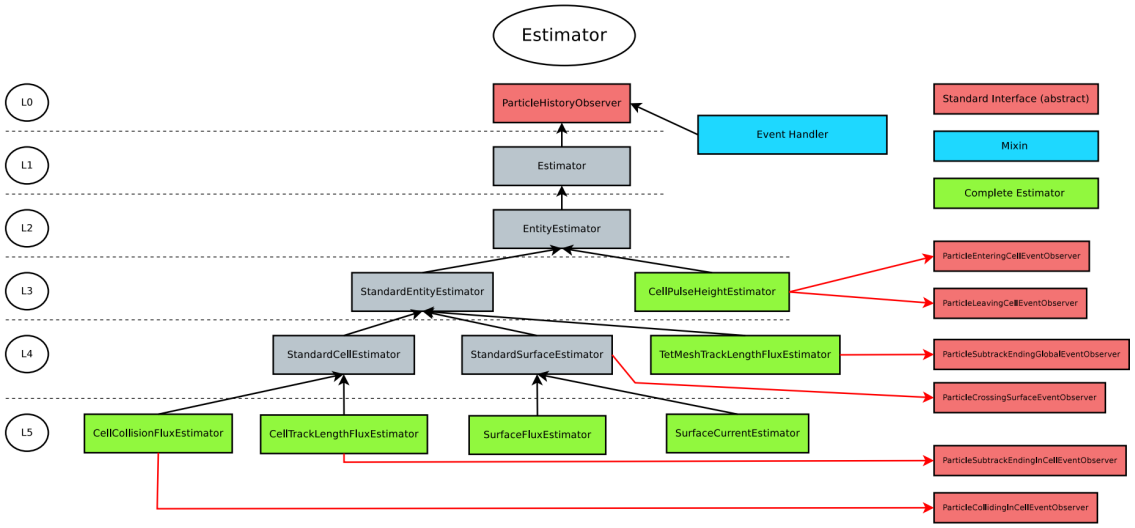

Figure J.1: **Event (estimator) module structure in FACEMC.** *The event module has been designed to create single points of control for all common functionality. Thus, developers need only implement, test, and maintain functionality at a single point in the code.*

example, returning to the earlier discussion of the particle class, one must test that the functions to set the particle energy work appropriately. A unit test would then be written which attempts to utilize the function for setting the particle energy. The particle energy would then be requested and compared against the expected value to ensure that the `setEnergy()` function was working as expected.

Currently over 95% of the lines of code in FRENSIE are unit tested, resulting in several hundred tests. These may be run when the code is compiled to check for any errors. Not only do these help when actively developing new classes to test that the functionality is behaving as expected, they also assist in regression testing. If one is required to refactor an existing class, the unit tests already written for that class will ensure that the refactor has not caused the class to exhibit unexpected or erroneous behavior.

In terms of collaboration, all FRENSIE developers are required to use git. Currently the repository is hosted privately on Github until it is ready for full release. The utilization of git allows developers from all over the world to work on the code simultaneously. Further, one can create their own forks, and from those branches which deal with specific issues. In this way specific components of the code can be handled in isolation, and the resulting code may then be brought back into the working master version when the changes are proven stable. This allows for one

to always have a working version of the code, even when significant development efforts are underway.

J.2 Licensing and Ethos

Open source software is a primary concern for the FRENSIE development team. The nuclear engineering community has been plagued with radiation transport codes which are commercial, export-controlled, or entirely in-house at laboratories and companies. While this has a fragmenting effect on the user base, it is even more noticeable in the fragmentation of developer efforts. Often efforts are duplicated on various projects, when the same developer efforts might be used collaboratively. Thus, the goal with FRENSIE is to create a research framework and MC radiation transport code which can be freely utilized and developed on by any individual.

In accordance with this goal, steps have been taken with the UW-Madison legal department to apply the BSD-3 license to the FRENSIE code. All students in the research group will be required to assign their copyright to the UW-Madison for all modifications on the code. The only major modification to the BSD-3 license that will be required for avoiding export control is that the UW-Madison will maintain the master repository for FRENSIE, and any derivative work not contained in the master branch will not be covered under the no-export control clause. FRENSIE has yet to be released publicly, but the licensing work has been done and as of this writing only internal development milestones are preventing the release.

J.3 FACEMC - Forward-Adjoint Continuous Energy Monte Carlo

The FACEMC code is the primary software component in FRENSIE currently. There is also the Transport Planning Optimization Routines (TPOR) package, as well as a rudimentary transmutation package, but FACEMC is the primary focus of current FRENSIE development. The current capabilities of FACEMC are as follows:

- **Geometry Modeling**: Ray tracing is done on CAD models using DagMC or combinatorial geometry models using ROOT.

- **Data**: ACE tables are supported. ENDL tables are mostly supported. Only a small subset of ENDF tables are supported. For electrons some EEDL tables are also supported.

- **Estimators**: Surface flux, surface current, cell collision flux, cell track-length flux, cell pulse height, tet mesh track length flux estimators, and hex mesh track length flux estimators are supported.

- **Parallelism**: A shared memory model, distributed memory model, and hybrid memory model have been implemented, which allows FACEMC to run on multiple cores.

- **Reproducibility**: All results are reproducible and independent of the machine and number of cores used.

In terms of physics, the following list describes the state of neutron, photon, and electron physics in FRENSIE:

- **Neutron Physics**: All forward neutron physics are implemented with the exception of the free gas thermal scattering model derived in this work. Adjoint elastic and inelastic level scattering, adjoint free gas thermal scattering, and adjoint ACE $S(\alpha, \beta)$ scattering are to be completed by Eli Moll.

- **Photon Physics**: All forward photon physics are implemented. The completion of the adjoint photon cross sections, transfer probabilities, and software implementation are to be completed by Alex Robinson, a fellow student under Dr. Henderson.

- **Photon Physics**: Analog and moment preserving forward electron physics are implemented. The completion of the adjoint electron physics for the analog and moment preserving methods are to be completed by Luke Kersting, a fellow student under Dr. Henderson.

J.4 Areas for Improvement and/or Collaboration

One of the primary areas for improvement is that of variance reduction. Discussions with Dr. Paul Romano of ORNL during his visit to the UW-Madison in 2017 highlighted the fact that FRENSIE will be incapable of solving high-level nuclear

transport problems without the variance reduction capabilities present in codes such as MCNP. However, Dr. Romano also mentioned that OpenMC, an open-source Fortran based MC code from MIT, is also looking to develop variance reduction methods. It is likely that going forward a student will need to be brought on to focus on the implementation of current variance reduction methods, as well as the development of further methods. It is the hope of this author that this work may be done in collaboration with developers from MIT.

J.5 Chapter Summary

- FRENSIE has been designed from the ground up to be a framework in which students and researchers are able to develop and utilize new functionality for nuclear research.
- Black-box interface design allows minimal development effort when including new software packages.
- The FRENSIE development team has placed a high value on clear and organized code, produced in accordance with the C++11 standard, and utilizing high level OOP.
- Over 95% of the several hundred thousand lines of code in FRENSIE are unit tested to ensure that the code performs as expected.
- Work with the UW-Madison legal department has ensured that the code can be released as non-export controlled and under a BSD-3 license to promote open use and collaborative development.
- All forward physics for neutrons, photons, and electrons have been implemented and current work is being done on the adjoint for each of these.

Bibliography

[1] N. Metropolis and S. Ulam, "The monte carlo method," *Journal of the American Statistical Association*, vol. 44, no. 247, pp. 335–341, Sep. 1949.

[2] P. Boyle, M. Broadie, and P. Glasserman, "Monte carlo methods for security pricing," *Journal of Economic Dynamics and Control*, vol. 21, pp. 1267–1321, 1997.

[3] J. H. Halton, "A retrospective and prospective survey of the monte carlo method," *SIAM Review*, vol. 12, no. 1, pp. 1–63, Jan. 1970.

[4] S. J. Chucas and et al, "Preparing the monte carlo code MCBEND for the 21st century," Arlington, Texas, 1994.

[5] E. E. Lewis and W. F. Miller, *Computational methods of neutron transport*. Wiley, 1993.

[6] J. J. Duderstadt and L. J. Hamilton, *Nuclear Reactor Analysis*, 1st ed. Wiley, Jan. 1976.

[7] C. L. L. and C. E. D., "Particle-transport simulation with monte carlo method," National Technical Information Service, Springfield, Tech. Rep., 1975.

[8] J. Spanier and E. M. Gelbard, *Monte Carlo Principles and Neutron Transport Problems*. Addison-Wesley, 1969.

[9] E. Moll and A. Robinson, "Presentation of facemc capabilities," University of Wisconsin-Madison, Tech. Rep.

[10] S. Yoo, "Optimization of brachytherapy treatment planning using adjoint functions," PhD, University of Wisconsin-Madison, 2003.

[11] V. Chaswal, "Adjoint based treatment planning for brachytherapy: Novel techniques and further developments," PhD, University of Wisconsin-Madison, 2007.

[12] B. Wang, M. Goldstein, X. G. Xu, and N. Sahoo, "Adjoint monte carlo method for prostate external photon beam treatment planning: an application to 3D patient anatomy," *Physics in Medicine and Biology*, vol. 50, no. 5, pp. 923–935, Mar. 2005.

[13] L. Desorgher, F. Lei, and G. Santin, "Implementation of the reverse/adjoint Monte Carlo method into Geant4," *Nuclear Instruments and Methods in Physics Research Section A: Accelerators, Spectrometers, Detectors and Associated Equipment*, vol. 621, no. 1-3, pp. 247–257, 2010.

[14] K. S. Krane, *Introductory Nuclear Physics*, 1st ed. Wiley, 1988.

[15] M. B. Chadwick, M. Herman, P. Oblozinsky, M. E. Dunn, Y. Danon, A. C. Kahler, D. L. Smith, B. Pritychenko, G. Arbanas, R. Arcilla, R. Brewer, D. A. Brown, R. Capote, A. D. Carlson, Y. S. Cho, H. Derrien, K. Guber, G. M. Hale, and others, "ENDF/B-VII.1 nuclear data for science and technology: Cross sections, covariances, fission product yields and decay data," *Nuclear Data Sheets*, vol. 112, no. 12, pp. 2887–2996, 2011.

[16] G. L. Blackshaw and R. L. Murray, "Scattering functions for low-energy neutron collisions in a maxwellian monatomic gas," *Nuclear Science and Engineering*, vol. 27, pp. 520–532, May 1967.

[17] R. E. MacFarlane, "New thermal neutron scattering files for endf/b-vi release 2," Los Alamos National Laboratory, Los Alamos, N.M., Technical Report, 1994.

[18] A. Robinson, "Development of a monte carlo code system with continuous energy adjoint transport capabilities for neutrons and photons," Ph.D. dissertation, 2013.

[19] M. Grimstone, "Extension of the mcbend monte carlo code to perform adjoint calculations using point energy data," *Radiation Protection and Shielding Division Conference*, 1998.

[20] J. Hoogenboom, "Adjoint monte carlo photon transport in continuous energy mode with discrete photons from annihilation," in *PHYSOR*, 2000, pp. 50–62.

[21] M. Rahman, *Integral Equations and their Applications*. WIT Press / Computational Mechanics, Jun. 2007.

[22] P. M. Morse and H. Feshbach, *Methods of Theoretical Physics, Part I*. McGraw-Hill Science/Engineering/Math, Jun. 1953.

[23] J. E. Hoogenboom, "Adjoint monte carlo methods in neutron transport calculations," PhD Thesis, Technishe Hogeschool Delft, 1977.

[24] D. C. Irving, "The adjoint boltzmann equation and its simulation by monte carlo," *Nuclear Engineering and Design*, vol. 15, pp. 273–292, 1971.

[25] G. I. Bell and S. Glasstone, *Nuclear Reactor Theory*. Krieger Pub Co, Jun. 1979.

[26] X-5 Monte Carlo Team, "MCNP - a general monte carlo n-particle transport code, version 5," Los Alamos National Laboratory, Technical Report LA-UR-03-1987, 2003.

[27] H. Kahn, "Applications of monte carlo," Technical Report AECU-3259, 1956.

[28] N. Mohamed, "Efficient algorithm for generating maxwell random variables," *Journal of Statistical Physics*, vol. 145, no. 6, pp. 1653–1660, Dec. 2011.

[29] C. J. Everett, "A third monte carlo sampler: (a revision and extension of samplers i and II)," Los Alamos National Laboratory ; available from NTIS, Los Alamos, N.M. : Springfield, VA, Technical Report LA-9721-MS, 1983.

[30] R. Sartor and N. Glazener, "An investigation of mcnp6.1 beryllium oxide s(a,b) cross sections," Jun. 2016, pp. 491 –494.

[31] X-5 Monte Carlo Team, "MCNP - a general monte carlo n-particle transport code, version 5 - manual volume ii," Los Alamos National Laboratory, Technical Report LA-UR-03-1987, 2003.

[32] A. Robinson and E. Moll, "Development of monte carlo tools for active interrogation modeling," University of Wisconsin-Madison, Tech. Rep.

[33] J. Conlin, "Personal communication," Los Alamos National Laboratory, Tech. Rep., 2016.

[34] R. Osborn, "Some characteristics of the thermal neutron scattering probability," *Nuclear Science and Engineering*, vol. 3, pp. 29–37, 1957.

[35] B. Davison, "On the spectrum of thermal neutrons in monatomic hydrogen gas," 1953.

[36] D. P. Laurie, "Calculation of gauss kronrod quadrature rules," *Mathematics of Computation*, pp. 1133–1145, 1997.

[37] B. Davison, "Neutron transport theory," pp. 19–20, 1958.

[38] M. Sawan, P. Wilson, T. Tautges, L. El-Guebaly, D. Henderson, T. Bohm, E. Marriott, B. Kiedrowski, B. Smith, A. Ibrahim, and R. Slaybaugh, "Application of CAD-neutronics coupling to geometrically complex fusion systems," in *2009 23rd IEEE/NPSS Symposium on Fusion Engineering, SOFE 2009, June 1, 2009 - June 5, 2009*, ser. Proceedings - Symposium on Fusion Engineering. San Diego, CA, United states: Institute of Electrical and Electronics Engineers Inc., 2009.

[39] R. Brun, A. Gheata, and M. Gheata, "The root geometry package," *Nuclear Instruments and Methods in Physics Research*, vol. 502, pp. 676–680, 2003.